The University of Nottingham

UNITED KINGDOM · CHINA · MALAYSIA

Investigating native and exogenous compounds within skin tissue

Nichola Jayne Starr MSci

Thesis submitted to the University of Nottingham for the degree of Doctor of Philosophy

September 2016

Abstract

The skin is the most extensive and accessible organ in the human body. It efficiently provides a barrier to an external hostile environment whilst maintaining and regulating fundamental physiological functions. The sophisticated and complex nature of this natural barrier requires continued analytical advancement to offer further insight into both its biological mechanisms and how to target the delivery of compounds through it. This work presents the use of a recently emerging technique in the field of skin research, time of flight - secondary ion mass spectrometry (ToF-SIMS), to investigate the presence of both native and exogenous compounds in skin tissue from samples collected both *in vivo* and *ex vivo*.

Subtle changes to the *stratum corneum* lipid composition have been shown to exert significant effects on the barrier properties of the skin and are associated with numerous skin disorders. The analysis of these lipid species and factors affecting their composition, both internal and external, is therefore a vital area of research. Using ToF-SIMS, this work has conducted an examination of changes to this lipid composition that have resulted from aging of the skin. This has been achieved by undertaking extensive development of a recently proposed surface analysis method to analyse sequential tape strips of *stratum corneum.* This study was unprecedented in demonstrating that ToF-SIMS could obtain information on human skin from samples collected *in vivo*. Changes in the levels of both cholesterol sulfate and long chain fatty acids were observed as a consequence of both intrinsic and extrinsic aging, offering confirmatory evidence to previously theorised skin aging mechanisms.

Research relating to the effective permeation of compounds across this skin barrier is also of upmost importance, both to the pharmaceutical and cosmetic industries, to enable the design of new topical formulations for skin delivery. Currently employed methods to assess the permeation of a compound are heavily focused on dermal delivery, with limited information obtained on the effectiveness of a compound to permeate into the upper layers of the skin. This research has therefore pioneered a dynamic SIMS method to conduct depth

profile analysis of *ex vivo* porcine skin tissue, enabling the permeation of exogenous compounds to be monitored as a function of skin depth.

This work is novel in successfully producing 3D spatially resolved chemical profiles of exogenous compounds within biological tissue using ToF-SIMS. The permeation of four different vitamin C related compounds, popular ingredients in anti-aging cosmetic formulations, were assessed using this method, highlighting a significant difference in permeation efficiency between them. An investigation into the delivery of ascorbic acid to the skin from various different formulations was also achieved, highlighting a permeation enhancing effect from delivery via a novel supramolecular gel formulation. The method developed for surface analysis was also successfully applied to monitor the permeation of ascorbic acid through human *stratum corneum* following *in vivo* application of an ‘off-the-shelf’ cosmetic product.

Acknowledgements

I would firstly like to acknowledge the funding provided by the University of Nottingham School of Pharmacy, the Centre for Doctoral Training in Targeted Therapeutics and Formulation Science and Walgreens Boots Alliance in coordination with the EPSRC (EP/I01375X/1). Special thanks to my industrial supervisors Dr. Mike Bell, Ian Marlow and Dr. Judata Wibawa for all of their support and guidance over the last three and a half years.

I would like to thank everyone at the School of Pharmacy, especially those within the LBSA, who have contributed their knowledge and experience to this project. I am extremely grateful for all of the technical support I have received. In particular, Christine Grainger-Boultby for her SEM expertise and Cath Ortori, whose wealth of knowledge, experience and willingness to help has proved invaluable. A huge thank you also to both Dr. Daniel Johnson at the University of Swansea and Dr. Lluïsa Pérez-García at the University of Barcelona for their collaboration on this project.

I would like to thank all of my friends for their support, in particular Laura and Guðrún. They have been a continued source of advice and encouragement when I needed it the most and I could not have got through this final stage of the PhD without them. Huge thanks to my mum, dad, Emma and of course Matt who have been pillars of support throughout the whole PhD, always pushing me to be the best I can be and showing unwavering belief in me.

I would finally like to thank both of my academic supervisors Professor David Barrett and Dr. David Scurr, who have both taught me so much throughout this project. I am extremely grateful for their continued support and guidance. I am especially indebted to the time and effort that has been dedicated to this PhD project by my primary supervisor Dr. David Scurr. I have been extremely lucky to have worked with someone so committed and compassionate.

Table of Contents

Figures

Tables

Abbreviations

AA – ascorbic acid

AFM – atomic force microscopy

AG – ascorbyl glucoside

BA – burst alignment

CLSM – confocal laser scanning microscopy

DESI – desorption electrospray surface ionisation

DMSO – dimethyl sulfoxide

EAA – ethyl ascorbic acid

ER – electrical resistance

FFA – free fatty acid

FWHM – full width at half maximum

HPLC – high performance liquid chromatography

GCIB – gas cluster ion beam

HC-BU – high current bunched

H & E – haemotoxylin and eosin

HS – heat separated

LHS – left hand side

LMIG – liquid metal ion gun

MALDI – matrix assisted laser desorption ioninsation

MVA – multivariate data analysis

MW – molecular weight

m/z – mass-to-charge ratio

NMF – natural moisturising factor

OA – old arm

OCT – optimal cutting temperature

OECD – The Organisation for Economic Co-operation and Development

OH – old hand

OPLSDA – orthogonal partial least squares discriminant analysis

PBS – phosphate buffered saline

PCA – principal component analysis

RHS – right hand side

RT – room temperature

SAP – sodium ascorbyl phosphate

SCCS – The Scientific Committee on Consumer Safety

SEM – scanning electron microscopy

SIMS – secondary ion mass spectrometry

SLS – sodium lauryl sulfate

TEWL – trans-epidermal water loss

ToF – time of flight

ToF-SIMS – time of flight – secondary ion mass spectrometry

TWF – tritiated water flux

TC – target current

UV – ultraviolet

YA – young arm

YH – young hand

Chapter 1: General introduction

The skin is the most extensive and accessible organ in the human body yet only measures several millimetres thick. Despite this, it plays a vital role in both regulating the body and providing sensory capabilities, whilst efficiently protecting it from an external hostile environment. It is known that the complex chemical composition of the uppermost layer, the *stratum corneum,* contributes to many protective functions of the skin and subtle changes to this composition have been implicated in many skin disorders and diseases. However, the complexity of this tissue means that the mechanisms behind many of these functions are still largely unknown. Further understanding regarding the barrier function and the permeation efficiency of compounds across this tissue is of upmost importance to both the pharmaceutical and cosmetic industries in the design of new topical formulations. Therefore, continued analytical advancements are needed to provide new insights in the field of skin research.

1.1 The anatomy of the skin

The skin is a complex, multi-layered structure containing several specialised appendages, such as hair follicles, sweat glands and sebaceous glands, numerous different cell types and various extracellular components. The anatomical structure of the skin consists of three different layers (as illustrated schematically in Fig. 1.1), namely the epidermis, dermis and the hypodermis. The deepest of these layers is the hypodermis, often termed ‘subcutaneous fat’ as it consists primarily of adipose tissue which acts to insulate and cushion the body. The dermis is the central region of the skin and provides both mechanical support and elasticity through the presence of fibrous connective tissue with high collagen and elastin content. It also contains structural components such as blood vessels, hair follicles, sweat glands and nerve endings, which provide the skin with touch and heat sensitivity [1,2].

The most superficial region of the skin is the epidermis, which is a keratinised stratified squamous epithelium [1]. This region consists primarily of

keratinocytes and can be split into 5 distinct layers defined by the differentiation stage of these cells (illustrated schematically in Fig. 1.2). There are smaller quantities of other epithelial cells present, namely melanocytes, Langerhans cells and Merkel cells which play a role in immune response, skin pigmentation and cutaneous sensation respectively. Of the five epidermal layers, the *stratum basale* is the deepest and predominantly contains mitotically active keratinocytes, which are columnar in shape and anchored to the basal membrane by structures called hemidesmosomes. These keratinocytes then differentiate into the *stratum spinosum* and change their morphology into a polygonal shape. In the *stratum spinosum* the cells continue to synthesise keratin, which is responsible for providing structural resistance against mechanical stress. The keratinocytes in this layer are attached through a network of intercellular bridges, called desmosomes, which have given this layer the name 'prickle cell layer', due to their histological appearance [1,2].

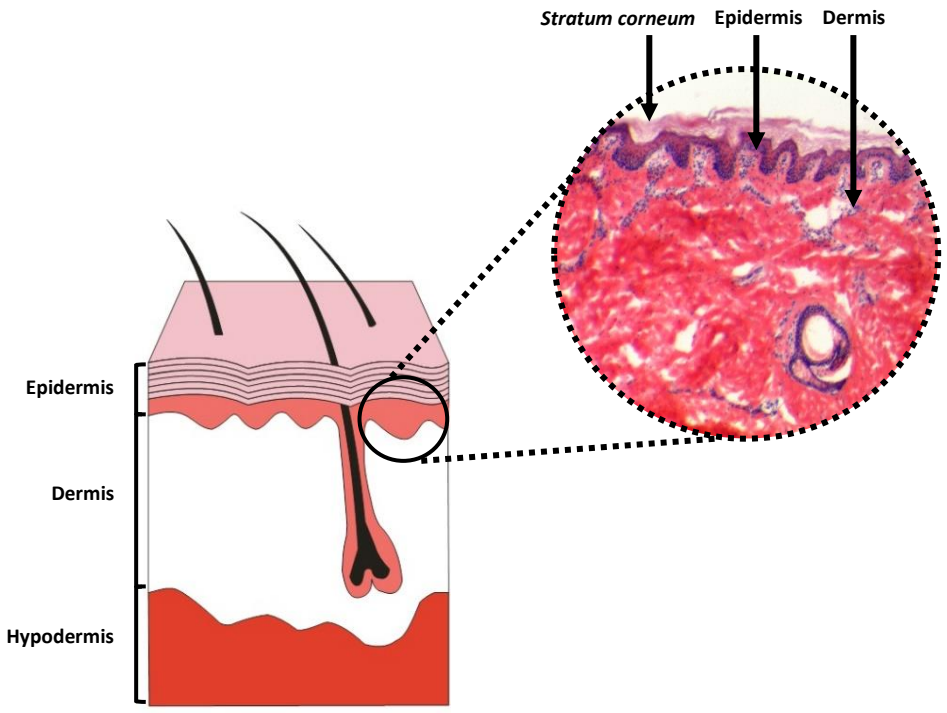

Figure 1.1 A schematic illustrating the three anatomical layers of the skin. Inset: A H&E stained porcine ear tissue slice acquired during this project, with the observed stratum corneum, epidermis and dermis layers indicated.

The next differentiation stage occurs in the *stratum granulosum*, which is known as the 'granular layer' due to the two types of granules formed within the keratinocyte cells. These are keratohyalin granules, structural proteins that form fibrous aggregates and lamellar granules, which deliver lipids into the intercellular space, forming precursors to the *stratum corneum* lipids. In the upper region of this layer, structural disintegration of the cell nucleus and cytoplasm facilitates the terminal differentiation of keratinocyte cells into the corneocytes found in the *stratum corneum*. In particularly thick skin there is also an extra, narrow layer of compact keratin, called the *stratum lucidum* [1,2].

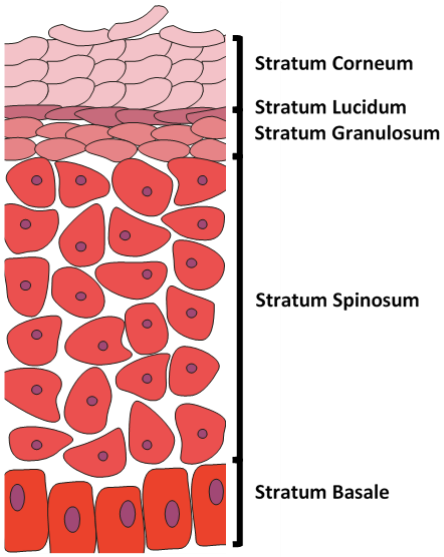

Figure 1.2 A schematic illustrating the five distinct layers of the epidermis region. These are defined by the differentiation stage of the epithelial keratinocyte cells.

1.2 The *stratum corneum*

1.2.1 Structure and function

The *stratum corneum* is the outermost layer of the skin, containing terminally differentiated keratinocytes, termed corneocytes. Kligman *et al.* [3] first demonstrated the presence of these cells, elucidating their polygonal shape and coherent layer arrangement (Fig. 1.3). Numerous studies have shown that the size of these corneocyte cells vary as a result of several different factors including age [4-8], body site [4,7-10], disease [4,11] and extrinsic influences such as

UV exposure [6,12]. These factors, plus a diversity in the measurement techniques used, have resulted in a variation in reported corneocyte surface area. However, recent studies using different techniques to analyse middle-aged, human *stratum corneum* collected from the arm region all present corneocyte surface areas in the region of 900-1000 μm^2 [4,9,13]. Reported corneocyte thickness measurements also vary due to both differences in analysis techniques and the difficulty associated with measuring this parameter. As such, there are limited studies available reporting a wide variation in values. Recent studies have reported variations between 0.2 µm and 1 µm [4,13-15]. The most recent measurements, acquired by Fredonnet *et al.* in 2014, calculated the corneocyte thickness directly from a tape stripped sample with no prior sample preparation, producing mean values of ~ 900 nm [14]. The work also demonstrated how chemical pre-treatment of corneocytes prior to analysis resulted in denaturation and a reduction in the measured thickness values by a factor of between 2-3. Therefore, it may be that the chemical removal methods typically employed prior to thickness measurements are producing inaccurate results for this parameter. The number of corneocyte layers [9,16-19] (~10-20) is also acknowledged to vary with body site and measured values for this parameter and the *stratum corneum* thickness [18,20-24] (~10-20 µm) again demonstrate variation between different studies. This prevents the accurate calculation of a 'theoretical' corneocyte thickness.

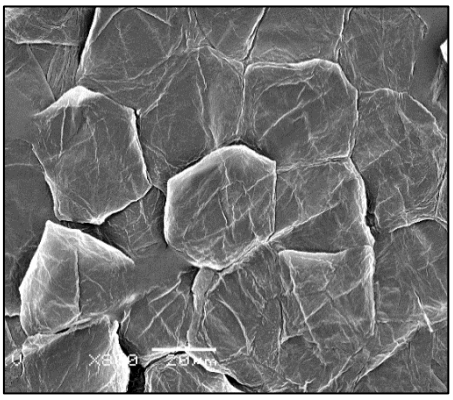

Figure 1.3 A scanning electron microscopy image of a tape stripped human stratum corneum sample collected in this project, highlighting the coherent layer of polygonal cells.

The 'bricks and mortar' structure now widely associated with the *stratum corneum* was first described by Elias in 1983 [25]. This analogy describes the presence of multiple layers of stacked corneocytes ('bricks') which lie parallel to the skin surface surrounded by a lipid matrix ('mortar'), as illustrated in Figure 1.4. However, although the 'bricks and mortar' analogy provides a reasonable visual description of the *stratum corneum*, it could be argued that it oversimplifies the intricate chemical nature of this structure. Although the corneocytes themselves are metabolically inactive, they are encased in complex cornified envelopes consisting of both protein and lipid structures, the functions of which are still being investigated [26,27]. Corneocytes also contain high concentrations of 'natural moisturizing factor' (NMF) compounds [28]. NMF is found exclusively in the *stratum corneum* and consists of a combination of free amino acids, amino acid derivatives such as pyrrolidone carboxylic acid and urocanic acid and small amounts of lactic acid, urea, citrate and sugars. The hygroscopic NMF acts as a humectant by absorbing atmospheric water, therefore maintaining *stratum corneum* hydration [28].

The term 'mortar' is also misleading as it suggests a homogeneous substance holding a structure together. Yet the intercellular lipid-rich domain is in fact a highly organised, multi-component arrangement that does not function to stabilise the corneocytes. Instead they are bound to each other through corneodermosomes, structures which are enzymatically digested before desquamation [1,2]. Prior to the discovery of an intercellular lipid matrix, it was believed that the *stratum corneum* provided a structural barrier to the body through the fibrillar-matrix of cornified cells. However, Elias *et al.* revolutionised the perception of the *stratum corneum* barrier function by highlighting the significant role played by the *stratum corneum* lipids in preventing the permeation of exogenous substances [29-32].

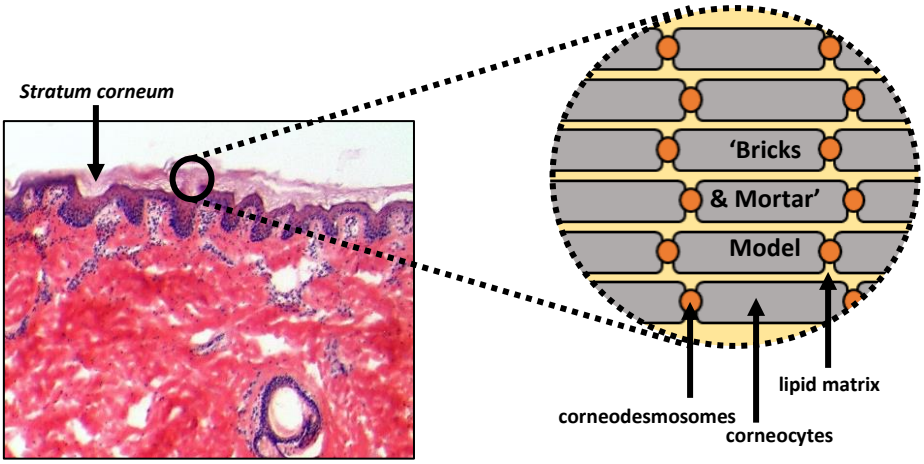

Figure 1.4 A schematic highlighting the architecture of the stratum corneum layer. This layer consists of stacks of corneocytes aligned parallel to the skin surface surrounded by a lipid matrix. Main image: A H&E stained porcine ear tissue slice acquired during this project. Inset: a representation of the 'bricks and mortar' anaology.

It is now known that the *stratum corneum* is predominately responsible for the barrier function of the skin, a protective role incorporating water and heat loss regulation, antimicrobial defence, resistance against mechanical stress, protection against UV exposure and much more [33,34]. Although once thought to be the by-product of keratinocyte differentiation, this anucleate layer is actually a sophisticated 'biosensor', exhibiting metabolic activity in response to external stimuli, as summarised in Table 1.1 [33].

Table 1.1 A summary of the known stratum corneum signalling mechanisms and responses. Adapted from Elias et al., The Stratum Corneum as a Biosensor, In Dermal Absorption and Toxicity Assessment, 2007, 79-87 [33].

Cause	Signal	Response
Acute barrier disruption	Cytokine and growth factor generation	Lipid and DNA synthesis and a cytokine cascade
	↓ Extracellular Ca^{++}/K^{+}	↑ Secretion of preformed lamellar bodies
	↑ pH leads to ↑ serine protease activity	Terminal differentiation and ↓ lamellar body secretion
	↓ O_2 leads to ↑ vascular endothelial growth factor	Vasodilation and angiogenesis
↑ or ↓ in humidity	Water gradient	↑ or ↓ in lipid synthesis respectively

1.2.2 Lipid composition

The lipids present in the intercellular domain of the *stratum corneum* demonstrate a unique lamellar arrangement which is crucial to the barrier function of the skin. The basis for this structure involves lipid bilayer sheets stacked on top of one another in a regular arrangement parallel to the corneocyte walls, as illustrated in Figure 1.5 [35,36].

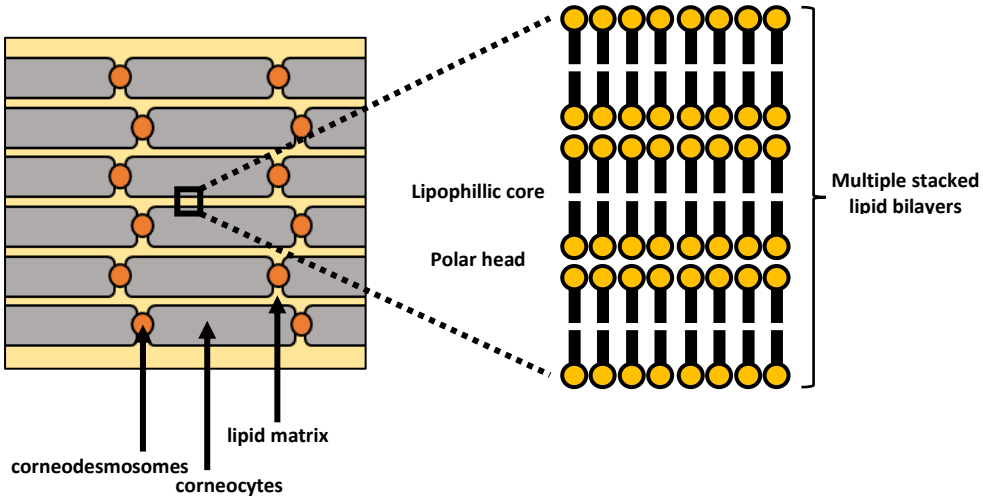

Figure 1.5 A schematic illustrating the 'bricks and mortar' model of the stratum corneum and the lamellar stacked bilayer structure of the intercellular lipid matrix.

The lipid composition of the *stratum corneum* is also unique, displaying significant differences to other biological membranes. Typical keratinocyte plasma membranes contain high levels of phospholipids, yet it has been shown that the *stratum corneum* contains virtually none, as depletion of these lipids accompanies cornification [37]. It is widely acknowledged that the lipid composition consists predominately of three main species, ceramides, cholesterol and free fatty acids (FFAs), the structures of which are illustrated in Figure 1.6. There are also small quantities of cholesterol sulfate, which increases in concentration with increasing depth [38]. The *stratum corneum* surface differs in lipid composition due to a dominance of lipids produced by the sebaceous glands, predominantly triacylglycerols, short chain fatty acids and small amounts of wax esters, cholesterol esters and squalene [39,40].

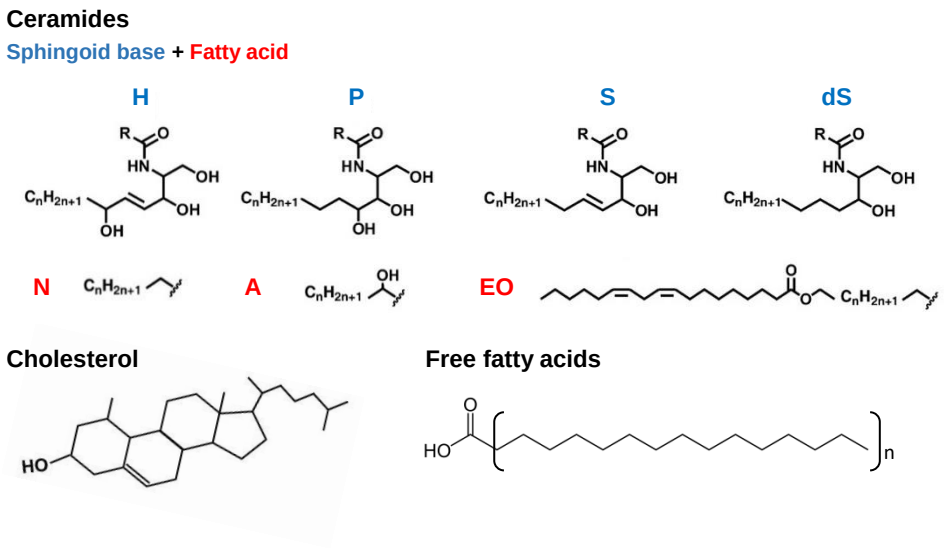

Figure 1.6 The chemical structures of the three main lipid species present in the stratum corneum, cholesterol, fatty acids and ceramides. 12 subclasses of ceramides have been identified in ex vivo human stratum corneum, resulting from a combination of 4 sphingoid bases and 3 fatty acids. Adapted from van Smeden et al., J. Lipid Res. 2011, 52, 1211-21 [41].

Of the three main *stratum corneum* lipid species, the most predominant by percentage weight are the ceramides compounds. These compounds consist of a sphingoid base linked to a fatty acid through an amide bond and there are theoretically twelve known subclasses of ceramides resulting from bonds between 4 types of sphingoid base and 3 different fatty acid components (Fig. 1.6). The presence of all twelve in human *stratum corneum* was only recently demonstrated by van Smeden *et al.* in 2011 through the use of a new liquid chromatography method [41]. This illustrates the complex nature of this lipid domain and highlights the importance of analytical advancement to further understand this tissue.

The reported relative amounts of both fatty acids and cholesterol in the *stratum corneum* differs between studies, highlighted by Weerheim *et al.* [42], most likely due to variation in skin sampling and analysis techniques. The presence of cholesterol has been proposed to regulate the fluidity of the *stratum corneum* lipid matrix [43]. Approximately 30 known species of fatty acids have been detected in *ex vivo* human *stratum corneum,* ranging from chain lengths of 14 to 34 and consisting of a mix of saturated and unsaturated compounds [44,45]. Unsaturated species, however, have been shown to be present

at very low levels [45]. The saturated population consists predominately of FFAs with a chain length ≥ 20, with C24:0 and C26:0 demonstrated to be the most prominent [44,45]. Shorter chain lengths, mainly C16:0 and C18:0, have been shown to be present in the *stratum corneum* at significant levels [44,46,47]. However, there is some debate as to whether these FFAs are actually sebaceous lipids that have been integrated into the upper layers. Norlen *et al.* suggests that both are of sebaceous origin due to the significant variation observed between individuals [44]. Rogers *et al.* demonstrated that palmitic acid (C16:0) exhibited a decreased level in the *stratum corneum* during winter, correlating to the decrease in sebum production. However, stearic acid (C18:0) levels remained constant, suggesting that these may be part of the original *stratum corneum* composition [46].

The minor sterol cholesterol sulfate is found in smaller quantities, present at ~ 1 % of the total *stratum corneum* lipid content in the most superficial layers but increasing to 5 % in the deeper layers, before reaching an epidermal maximum in the *stratum granulosum* [37,48]. The possibility of an epidermal cholesterol sulfate cycle was first proposed by Epstein *et al.* in 1984, based on the observed levels of two related enzymes, cholesterol sulfotransferase (SULT2B1b) and steroid sulfatase (SSase) [38]. This cycle describes the sulfurylation of cholesterol by SULT2B1b in the nucleated epidermial layers, producing a peak in cholesterol sulfate levels in the *stratum granulosum,* which is then desulfated by SSase to form a pool of cholesterol within the *stratum corneum.* Despite its presence at a low level, Sato *et al.* has demonstrated that cholesterol sulfate is crucial for the regulation of corneocyte desquamation, through inhibition of proteases which facilitate corneocyte loss [49] and both Elias *et al.* [48] and Sato *et al.* [49] have induced scaling of murine skin through topical cholesterol sulfate application. It has also been shown to accumulate in skin associated with X-linked ichthyosis [50], a disease which causes extreme scaling of the skin.

It is well established that the *stratum corneum* plays a very significant role in the protective barrier function of the skin (Table 1.1) and therefore it is not surprising that changes to these important lipid species are associated with many different skin disorders [51-63], which are summarised in Table 1.2.

Although differences in lipids have been detected for these diseases, the mechanisms behind these changes are still not fully understood. This highlights the continued need for analytical advancement and continued investigation into this complex structure.

Table 1.2 A summary of the detected changes to stratum corneum lipids associated with skin disorders. Adapted from van Smeden et. al, J. Invest. Dermatol. (2014) [56].

Disease	Change in lipid composition
Lamellar ichthyosis	CER [NP] [EOS] ↓
Psoriasis	CER [NP] [EOS] [AP] ↓ CER [AS] [NS] ↑
Netherton	CER [EOS] [EOP] [EOH] [EOdS] [NP] ↓ Short chain lipids ↑ Unsaturated lipids ↑
Atopic dermatitis	CER [EOS] [EOP] [EOH] [EOdS] ↓ CER [AS] [AH] [AP] [AdS] ↑
Chanarin - Dorfman	Acyl-CERs ↓ TAG ↑
X-linked ichthyosis	↑ cholesterol sulfate

1.2.3 Sampling methods

There are several techniques which can be used to remove lipids from the *stratum corneum* prior to analysis, all which possess their own particular advantages and disadvantages. The main techniques currently employed are solvent extraction, skin scraping or skin stripping using cyanoacrylate resin or adhesive tape, all of which can be used to collect samples *ex vivo* or *in vivo.*

1.2.3.1 Solvent extraction

Solvent extraction is commonly employed to extract lipids from a range of different biological tissue samples. One of the most widely followed protocols, described by Folch *et al.* [64] in 1957, uses a chloroform/methanol solvent mix. This method has been adapted numerous times, with the most renowned being procedures published by Bligh and Dyer (1959) [65] and Sheppard (1963) [66] which use a chloroform/methanol and ethanol/diethyl ether mix respectively. Previously, these methods have been used to perform surface extraction of

lipids from skin tissue *in vivo*. However, the now established toxicity of chloroform restricts the use of the most efficient chloroform/methanol extraction mixture. Chloroform has been highlighted as a potentially carcinogenic compound which when applied to the skin in particular can cause irritation and burns with the potential to cause systemic damage following prolonged exposure. The protocol described by Sheppard [66] instead uses an alternative ethanol/diethyl ether mix. However, although this omits the use of chloroform it is impractical for lipid extraction from the skin surface as the volatility of diethyl ether makes it difficult to acquire quantitative data. Recent publications have demonstrated the successful use of safer, less volatile alternatives, such as mixtures of hexane and short chain alcohols [44,67,68]. One major disadvantage of this technique for *stratum corneum* analysis is that it only extracts lipids from the skin surface, preventing analysis as a function of *stratum corneum* depth, unless combined with a *stratum corneum* layer removal technique such as cyanoacrylate resin or adhesive tape stripping.

1.2.3.2 Skin scraping

Small quantities of *stratum corneum* can also be removed by scraping the application site with a scalpel or dermal curette. Skin scraping is a technique more commonly employed for diagnostic reasons in the medical field. It is still employed in some research studies [69] but its use is far more limited compared to the other sampling techniques. This is most likely due to the fact that it is the most invasive technique to employ *in vivo* and also there is less control over the depth of skin tissue that is removed. This technique can therefore not provide information as a function of *stratum corneum* depth.

1.2.3.3 Cyanoacrylate resin

There are two commonly used skin stripping techniques, using cyanoacrylate resin or adhesive tape. Unlike solvent extraction, neither pose any safety issues *in vivo*, omitting the use of harmful chemicals on the skin. The use of cyanoacrylate resin, first published by Marks and Dawber in 1971 [70], has been termed the “skin surface biopsy” as it removes a thin sheet of *stratum corneum*

in one step using a rapidly polymerising cyanoacrylate adhesive. This technique is still widely used for both *in vitro* and *in vivo* analysis [71-73]. Of the two stripping techniques, the use of cyanoacrylate resin offers a shorter acquisition time, yet is slightly more invasive, as it removes multiple layers of the *stratum corneum* at once. Multiple strips can be collected to enable analysis as a function of *stratum corneum* depth. However, this technique does not offer the layer-by-layer analysis which can be gained from tape stripping. For chromatographic analysis of lipids this method also has to be combined with a solvent extraction procedure, to separate the lipids from the resin material.

1.2.3.4 Tape stripping

Stripping of the *stratum corneum* can also be conducted using adhesive tape (Fig. 1.7), a method first described by Wolf in 1940 [74]. Pinkus *et al.* then demonstrated how repeated stripping of the skin at the same point on the tissue could remove sequential layers of the *stratum corneum* [75]. This offers the potential to collect information as function of *stratum corneum* depth, providing an advantage over the other sampling methods described.

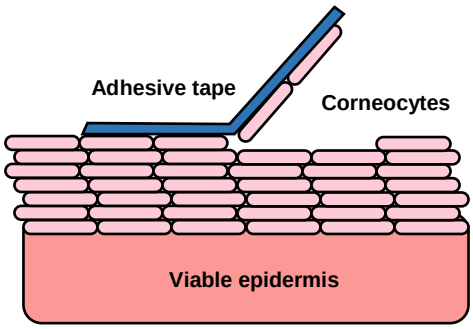

Figure 1.7 A schematic illustrating the tape stripping process. The process uses adhesive tape to sequentially remove layers of corneocyte cells from the stratum corneum.

This quick and minimally invasive technique has been widely used to collect *stratum corneum in vivo* [41,42,76-80] and *in vitro* [41,81-84] from human [41,42,76-82] and animal skin [80,83-85] for the analysis of both native and exogenous compounds.

Although this technique is simple in principle, there are various factors that have been shown to influence the amount of *stratum corneum* removed by the stripping process. These include both external factors, such as the type of tape used [86,87], the pressure applied [86,88] and the application of a formulation [89,90] and inherent influences such as skin hydration [91], the anatomical site [86], the presence of hair follicles [92,93] and the depth of skin [75,94]. Without a universal standardised protocol, these are all factors to consider regulating when conducting tape strip analysis. These variations also prove problematic when trying to assess the permeation of a compound using this technique. One way to account for this is to quantify the amount of *stratum corneum* present on each strip and use this to normalise the concentration of compound detected.

There are several different methods to measure the amount *stratum corneum* removed during tape stripping but the most widely used are differential weighing and protein quantification. Differential weighing is the simplest method, but is time consuming and can be subject to variation from a number of sources. These include, static electricity on the tape, moisture content from the environment, or following application of a product, and imprecisions due to the small weight of *stratum corneum* removed relative to the weight of the tape [95]. The amount of protein present can also be used as a normalising factor, by conducting modified protein assays [96]. However, these assays typically require extraction of the protein content from the tape strip and are therefore a destructive technique. Recently, novel imaging methods have been applied to estimate protein content, yet they often require specialist equipment/methods and increase the complexity of the simple tape stripping procedure [97-100]. It has also been demonstrated that the presence of skin furrows can result in unstripped skin from one layer being subsequently removed by the following strip, meaning that the compounds detected from a single tape strip may actually originate from multiple layers [101]. Despite these issues, tape stripping still remains the most widely used *stratum corneum* sampling method due to the simple nature and opportunity to collect information as a function of depth.

1.3 Monitoring skin permeation

1.3.1 Skin permeation pathways

An exogenous compound has three potential pathways by which it can permeate through the skin barrier, either using an appendageal route, intercellularly through the *stratum corneum*, or intracellularly through the *stratum corneum* (Fig. 1.8) [2,102,103]. Permeation can also occur through a combination of these pathways depending on the physiochemical properties of the compound. The appendageal route successfully bypasses the *stratum corneum* and epidermis, providing direct and rapid access to the dermis and hence systemic circulation. This includes permeation through sweat ducts, hair follicles and associated sebum glands. However, these appendages only cover between 0.1-1 % of the total surface area of the skin [2,104] limiting the amount of compound that can utilise this route. Due to these limitations, this route had been considered negligible, but recent studies have shown rapid systemic delivery of compounds through follicular appendages [105] and they have also been highlighted as an effective long term storage reservoir for drug delivery [106].

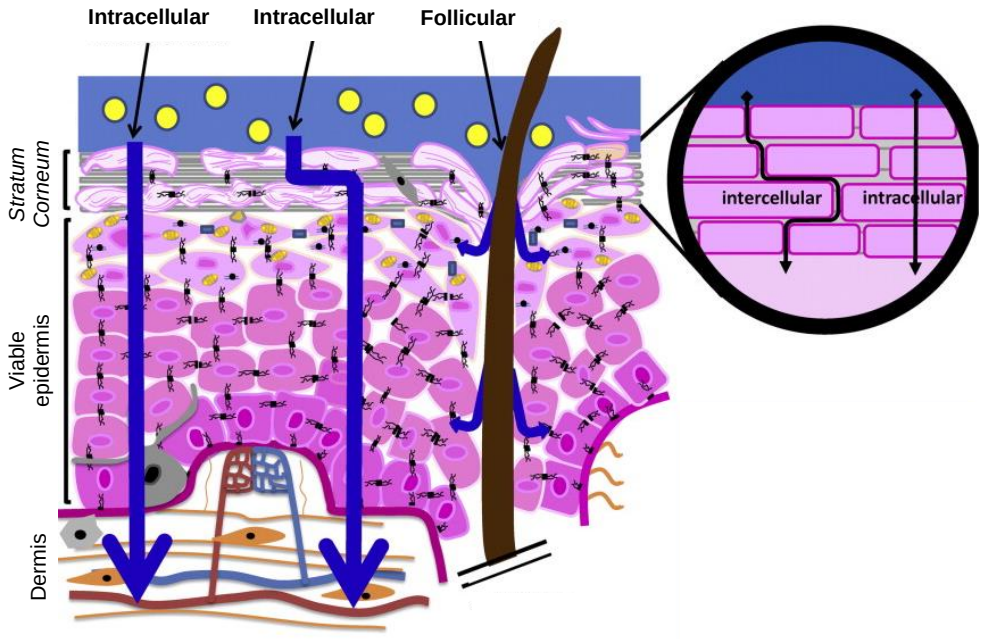

Figure 1.8 A schematic illustrating the three skin permeation pathways. Reprinted from 'Penetration of drugs through skin, a complex rate-controlling membrane', Bolzinger et al., Curr. Opin. Colloid Interface Sci., 17(3), Copyright (2012), with permission from Elsevier [103].

The intracellular pathway is the shortest route through the *stratum corneum*. Although the corneocytes contain a keratin matrix, which is relatively hydrated and would therefore favour polar compounds, the intracellular route involves the repeated partition between this polar environment and the more lipophilic surrounding domain. Conversely, the intercellular route provides a continuous route through the *stratum corneum* and is therefore widely acknowledged as the preferred pathway for most compounds [2,102]. Despite a *stratum corneum* thickness in the region of 20 µm, the intercellular pathway is estimated to be much longer ~ 150 µm and is therefore a less direct route than the other two pathways [2]. However, transport can take place through diffusion via the lipid core or the polar head group, which enables this pathway to be utilised by a wider range of compounds compared to the intracellular route [2].

1.3.2 *In vitro* permeation studies

In vitro permeation studies are often referred to as 'Franz cell' studies, due to the use of a glass diffusion cell set-up first designed by Thomas Franz in 1975 [107]. This system involves monitoring the permeation of compounds through a skin tissue section mounted between two glass compartments, a donor and a receptor compartment (Fig. 1.9). *In vitro* studies are crucial to assessing human skin permeation. This method can provide a platform for the initial assessment of topical actives and formulations, especially those containing pharmaceuticals that may have not yet proved toxicologically safe for human application. It is also extensively applied to conduct risk assessments for many pesticides and industrially used chemicals. This method is favourable as it allows quick, large scale investigations to be carried out on multiple repeat samples without the need to recruit large numbers of human volunteers.

'Static' vertically arranged cells are typically employed, however a horizontal arrangement can also be considered. Alternative flow-through Franz cell systems are also popular. These involve a continuous flow of receptor solution underneath the skin surface, which aims to mimic the blood supply carrying the exogenous compound away from the site of absorption. This type of cell

requires more attention to set up and manage compared to the static system and also, as all the cells in one experiment are interconnected, a failure in experimental set up can affect the whole batch. Therefore the use of static cells are often preferred for practical reasons. In both types of cell the parameters of the receptor solution are specifically controlled to mimic physiological conditions as closely as possible, including the choice of solvent, temperature and in static cells, the stirring mechanism.

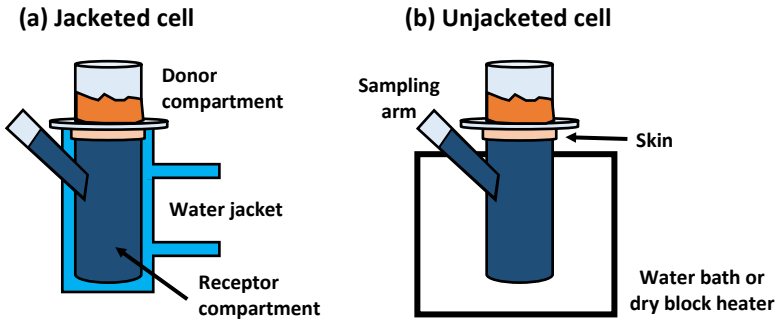

Figure 1.9 A schematic of a typical 'Franz' cell. (a) Jacketed Franz cell (b) Unjacketed Franz cell.

They key principle with regards to the receptor solution is that solubility of the compound must not be the rate determining factor for permeation. Hence the compound should exhibit adequate solubility in the chosen receptor solution. It is generally agreed that sink conditions are maintained if the compound does not exceed 10% of its saturation concentration in the receptor solution [108-110]. Failure to maintain these conditions would result in an underestimation of permeation. For the evaluation of water soluble compounds, the Organisation for Economic Co-operation and Development (OECD) guidelines on skin absorption studies [111] recommend saline solutions of pH 7.4, which closely mimics physiological conditions. Whereas, for the assessment of lipophilic compounds, it is acknowledged that organic solvents must be used to aid solubility. However, when using organic solvents, damage to the integrity of the skin barrier may occur and hence enhanced permeation effects must be taken into consideration.

In order to maintain sink conditions, an effective continuous stirring mechanism is required to prevent the accumulation of a concentration gradient within the receptor solution and both the type and speed of magnetic stirrer have been shown to effect this [110]. OECD guidelines also specify that the skin is maintained at a constant temperature as fluctuations can alter the permeation. The temperature is chosen to mimic the physiological conditions, typically 37 °C in the receptor solution giving a skin surface temperature of 32 °C [104,108,111]. The temperature of static cells is typically controlled either by the encasing of the cell in a jacket through which water is circulated or through submergence of the cells in a water bath, illustrated in Figure 1.9a and b respectively. In addition, most cells will possess a sampling arm, to allow the removal of small volumes of receptor solution for analysis at designed time points throughout the experiment. These volumes are then typically replaced with fresh receptor solution.

Both a 'finite' and 'infinite' dose, where the concentration of compound in the donor compartment is not diminished, can be applied depending on the aim of the study. Both OECD guidelines and guidelines produced by the Scientific Committee on Consumer Safety (SCCS) for *in vitro* assessment of cosmetic ingredients recommend a 24 hour exposure period [108,111]. Following the termination of the experiment 'skin fractionation' is conducted for samples applied with a finite dose, typically using high performance liquid chromatography (HPLC) [111]. This involves measurement of the concentration of compound that resides in the following compartments: donor solution, dislodged from the skin surface using a wash, the *stratum corneum*, the remaining tissue and the receptor solution. The *stratum corneum* can be analysed using one of the sampling methods described in 1.2.3, however, typically tape strip analysis is employed.

1.3.3 The use of *ex vivo* tissue

1.3.3.1 Human vs. animal tissue

Although *ex vivo* human tissue is considered as the 'gold standard' for the assessment of human skin permeation, e*x vivo* animal tissue is often employed

in Franz cell permeation experiments. Animal tissue is more readily available and raises less ethical issues compared to human tissue. The most commonly used species for skin tissue analysis are pigs, small rodents and rabbits. There are advantages and limitations associated with each species, an area which has been broadly researched and recently reviewed in detail by Jung and Maibach in 2015 [112]. The main limitations regarding the use of small rodents, such as rats and mice, include a thinner total skin thickness (Table 1.3) and a huge difference in both hair follicle density and diameter (Table 1.4). Both the OECD [111] and SCCS [108] acknowledge that rodent skin is invariably more permeable than human skin. For this reason the SCCS guidelines for cosmetic ingredient permeation advise against the use of rodent skin and instead recommend porcine skin.

Table 1.3 A summary of the differences in skin layer thickness between different species. Adapted from Jung and Maibach, J. Appl. Toxicol. 2015, 35, 1-10 [112].

Species, anatomical site	*Stratum corneum* (µm)	Epidermis (µm)	Whole skin (mm)
Human, forearm	17	36	1.5
Pig, ear	10	50	1.3
Pig, back	26	66	3.4
Mouse, back	5	13	0.8

Porcine skin is considered to be one of the closest matches to human skin, offering similarities in both morphological and biochemical properties. These include total and individual layer thickness (Table 1.3), density of hair follicles (Table 1.4) and a similarity in epidermal lipid composition not observed in rodents [113]. A recent review of the literature by Barbero and Frasch (2009) [114] found that there was a correlation efficiency between porcine and human permeation data of 0.88 with a p value < 0.0001. Interestingly, they also highlighted that pigs offered a lower intra species variation compared to human samples, reducing the number of repeats needed to obtain statistically significant results. Both porcine ear and flank are typically employed as a model for human skin. However, porcine ear exhibits a more

comparable layer thicknesses to human forearm skin (Table 1.3) and has demonstrated a good correlation in *in vitro* experiments [115-119].

Table 1.4 A summary of the differences in the density and diameter of hair follicles in different species. Adapted from Bronaugh et al., Toxicol. Appl. Pharmacol. 1982, 62, 481-8 [120].

Species	Area of skin	No. of follicles /cm^3	Diameter of follicles (µm)
Human	Abdomen	11 ± 01	97 ± 01
Pig	Back	11 ± 01	177 ± 04
Rat	Back	289 ± 21	25 ± 01
Mouse	Back	658 ± 38	26 ± 01
Hairless mouse	Back	75 ± 06	46 ± 01

1.3.3.2 Choice of skin thickness

Both the OECD and SCCS accept the use of both full thickness skin and split-thickness skin [108,111]. Split-thickness skin can be achieved through the use of a dermatome or by the removal of the epidermal membrane. A dermatome is typically used to produce skin sections between 200 – 400 µm thick. The epidermal membrane can be removed using either heat, chemical or enzymatic separation methods. Updated guidance notes from the OECD (2010) advise that split thickness tissue is preferred over full thickness skin, except when justified by the experimental expectations [121]. The SCCS agrees that split-thickness skin should be used for human tissue, but recognises the difficulties of achieving split thickness skin with porcine tissue may allow the use of full thickness skin [108].

1.3.3.3 Testing the skin integrity

In order to confidently use *ex vivo* skin tissue to accurately assess the permeation of a compound, the integrity of the skin must be evaluated. This can either be done before, during or after the permeation study. Concurrent integrity evaluation requires the addition of a reference material to the test solution and so is not typically employed due to practical reasons. OECD guidelines [111] recommend only conducting the integrity test after exposure to

the test solution in short-exposure studies, e.g. to test hair products, as for longer studies damage to the *stratum corneum* cannot be ruled out. The OECD guidelines report three acceptable methods to check skin integrity prior to permeation studies, specifically the measurement of three parameters, electrical resistance (ER), trans-epidermal water loss (TEWL) and tritiated water flux (TWF). Checking the integrity of the skin prior to the study enables the elimination of any damaged skin immediately, minimising time and material wasted on ineligible samples. Measuring the permeation of a reference material, such as tritiated water, is time consuming and the TEWL measurements require a controlled temperature and humidity environment. Therefore, an ER measurement is the most practical of the three. Davies *et al.* have reported 'acceptable' values for ER measurements for the skin of six different species, which can be used as guidelines [122]. However, it is important to realise that variations in the way the integrity check is conducted, such as the type of instrument used, the receptor solution, the exposed skin area etc., can affect the ER values produced.

1.4 Analytical techniques for *stratum corneum* chemical analysis

1.4.1 Chromatographic techniques

The most commonly employed technique for chemical analysis of the *stratum corneum* is liquid chromatography coupled with mass spectrometry. This technique is typically employed to analyse tape strips collected both *in vivo* [76,77,79] and *in vitro* following Franz cell studies [82,123 124-126] to determine the concentration of a compound that has permeated into the *stratum corneum.* Chromatographic mass spectrometry analysis of tape stripped samples has also been widely demonstrated for the detection and quantification of native *stratum corneum* compounds [41,46,127-129].

However, although this technique can be used to determine the exact concentration of a specific compound, the combination of this technique with tape stripping does have some disadvantages. Liquid chromatography requires a sample which is in solution, so for tape strip analysis this ultimately means

that any chemicals of interest, either exogenous or native in origin, will have to be extracted from the adhesive material. This requires an extraction process which can be both complicated and time consuming and if not done correctly can complicate the chromatographic analysis with the presence of co-extracted adhesive components. In addition, the tape stripping process offers the potential to monitor the presence of a compound as a function of *stratum corneum* depth, through sequential stripping. However, if the compound is present at a low concentration, multiple strips have to be pooled for chromatographic analysis, resulting in the loss of depth information. As chromatographic analysis does not offer any imaging capabilities it is also unable to provide any information about the spatial distribution of a compound within the *stratum corneum*, which would be of particular interest for compounds which have been applied topically to the skin.

1.4.2 Emerging analytical techniques

The field of skin research has seen recent analytical developments, particularly in techniques which offer imaging capabilities, both for analysis of native skin species and the permeation of exogenous compounds. Confocal laser scanning microscopy (CLSM) [130-134] can be applied *in vivo* to obtain 3D images, but is restricted by the fact that compounds of interest must contain a fluorophore. This therefore limits the number of species that can be imaged or introduces the complication of fluorescent 'tagging' of compounds, which can also impact their localisation in biological tissue. Vibrational spectroscopy methods can provide both species specific and label free imaging. Both infrared [135-144] and Raman spectroscopy based techniques [23,145-150] [151-154] are emerging in popularity as they have the ability to image the skin *in vivo.* However, the spatial resolution of infrared spectroscopy is limited by the diffraction limit of light and can suffer from interference from a strong water absorption signal. In contrast, Raman spectroscopy based techniques are not affected by water absorption bands and have recently shown the ability to provide 3D chemical information up to 100 µm, with a depth resolution of ~ 2 µm and a spatial resolution of 1 µm [147,148,152,153,155]. However, ultimately these

techniques cannot match the high chemical specificity of mass spectrometry techniques.

Matrix assisted laser desorption ionisation (MALDI) spectroscopy is a popular technique for the analysis of biological materials and is often favoured over other mass spectrometry techniques due to its ability to detect intact high mass ions, such as proteins and peptides. Numerous studies have therefore applied this technique to skin tissue analysis [156-160]. However, this technique requires the deposition of a matrix onto the sample surface and the spatial resolution is typically ~20 µm. In addition, due to interference from matrix ions, lower mass ions of typically < 500 *m/z* are harder to detect using this technique. Desorption electrospray surface ionisation (DESI) spectroscopy offers the advantage of ambient conditions for biological tissue analysis. However, the spatial resolution is much poorer (at ~ 100 µm) which limits the applications of this technique [161].

Time of flight - secondary ion mass spectrometry (ToF-SIMS) is a technique which is relatively new in the field of skin analysis. This is a mass spectrometry technique that can provide both high mass resolution spectra and high spatial resolution images. By employing a highly focused ion beam (section 1.5.3) this technique has the ability to achieve a spatial resolution lower than 1 µm and the newly developed gas cluster source beams (section 1.5.9) have the potential to provide depth profiles of organic materials with a depth resolution in the nanometer range. A limited number of studies have demonstrated the ability of this technique to detect both native and exogenous compounds from skin tissue [83,159,162-166]. Analysis of both tape stripped *stratum corneum* and microtomed tissue slices have shown the use of this technique to obtain chemical information as a function of skin depth. Interestingly, the depth profiling capabilities of this technique have not been employed for skin tissue analysis to date.

1.5 Time of flight - secondary ion mass spectrometry

Secondary ion mass spectrometry (SIMS) was first developed in the 1950s [167] and 1960s [168] and is a technique which involves the bombardment of a sample

surface in order to emit ionised particles, which are then separated and measured according to their mass. This ultra-high vacuum technique uses a high energy, primary ion beam to bombard the sample surface, which causes a collision cascade resulting in the ejection of 'secondary' particles (Fig. 1.10). These can be electrons, neutral species, ions or photons. Only secondary ions can be detected using this technique, however, they represent a small proportion of the sputtered material as the vast majority is neutral (> 99 %) [169]. The output of this technique is therefore a mass spectrum, providing detailed chemical information about the species present on the surface.

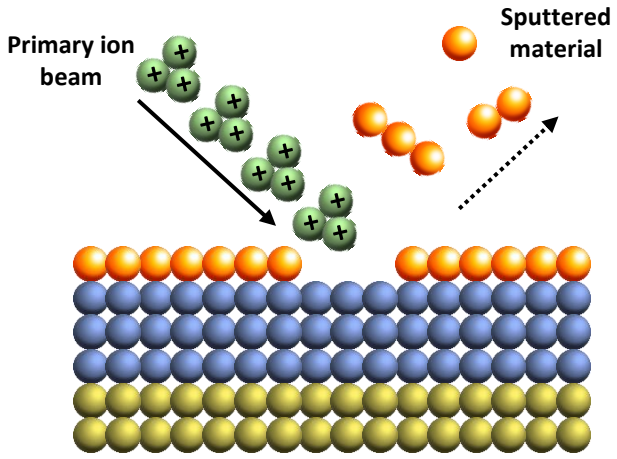

Figure 1.10 A schematic illustrating the primary ion bombardment of a sample surface in SIMS analysis. This process emits sputtered material containing secondary ions.

1.5.1 Static SIMS

Until the 1980s, the primary use of SIMS was as a destructive technique, employed to analyse the elemental composition of materials below the sample surface. This method is now known as dynamic SIMS (section 1.5.9). Benninghoven and his group in Münster (Germany) [170] were the first to demonstrate that, by using a low primary ion dose, mass spectral data could be acquired faster than the lifetime of the surface layer. This method is now termed 'static' SIMS and requires the primary ion dose to be $\leq 10^{12}$ ions per cm^2 (static limit) to enable the acquisition of ions representative of the true surface of a sample [169]. It has been estimated that each primary ion impacts an area on the surface of 10 nm^2 and therefore it would take 10^{13} impacts per cm^2

to damage all of the sample surface [169]. Therefore, keeping the primary ion dose under the static limit ensures that statistically no area on the sample will be impacted twice during the acquisition time. The use of a lower primary ion dose ultimately produces a lower secondary ion yield, which has resulted in the advancement of highly sensitive detection equipment.

Typical ToF-SIMS instruments all consist of the following primary components for static analysis: an airlock, main analysis chamber, primary ion gun, mass analyser and electron flood gun as illustrated in Figure 1.11 [171]. The airlock system preserves the main chamber pressure, which typically reaches pressures in the region of 10^{-7} Torr.

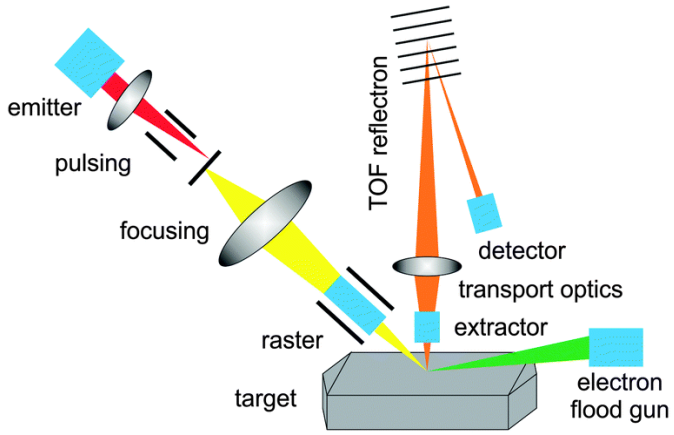

Figure 1.11 A schematic illustrating the primary components of a ToF-SIMS instrument. Taken from Hofmann et al., Phys. Chem. Chem. Phys. 2014, 16, 5465-74. Published by the PCCP Owner Societies [170].

1.5.2 Primary ion sources

There are four types of primary beam source which differ in the way that they produce the positive primary ions, specifically surface ionisation, plasma, field ionisation and electron bombardment [169]. Surface ionisation sources use thermal stimulation to produce ions from an absorbed layer of material, whereas a plasma source employs a heating method to produce primary ions from a gaseous source.

Field ionisation sources work by using a very high electric field to strip electrons from source atoms. This method is not appropriate for gaseous sources but is typically employed for liquid metals. In this case a thin 'skin' of liquid metal, such as bismuth, flows over a tungsten tip with a radius < 1 µm in the vicinity of an extraction field. This creates a 'Taylor cone' and plasma ball structure on the probe tip, from which primary ions are stripped away [169]. These sources are often referred to as liquid metal ion guns (LMIG). The ion volume produced by the tip is small and the energy distribution is narrow, enabling LMIG sources to be focused to small areas with high current densities. At a given beam current, the LMIG source has a focusing capability one order of magnitude better than gas-phase sources [172], therefore offering much higher spatial resolution for imaging (section 1.5.7). LMIG sources are therefore the preferred source type for static SIMS analysis.

Electron bombardment sources work by using high energy electrons to ionise the primary gas source. This method is used for the production of gas cluster ion beams (GCIB), which are becoming increasingly popular both as sputter beams in dynamic SIMS and for the analysis of intact high mass ions in static SIMS (section 1.5.3). Neutral clusters are first formed through high pressure expansion of the source gas and then subjected to electron bombardment [173].

1.5.3 Monatomic vs. cluster ion beams

The original primary ion beams employed for SIMS analysis consisted of positively charged monatomic species, such as Ga^+ and Cs^+. However, the breakthrough for biological sample analysis came following the development of polyatomic, or cluster ion beam sources. Examples of these include widely used LMIG sources, such as Bi_n^+, the carbon based buckminsterfullerene C_{60}^+ source and GCIB sources, such as Ar_n^+ which are now becoming increasingly popular. As demonstrated by molecular simulations [174] primary ions from monatomic sources and cluster sources exhibit very different behaviours when impacting a sample surface. Due to their small size and high energy, monatomic species cause considerable disruption deep into the sample on impact. This dispersion of energy into the sample also results in only a small

amount of material being desorbed from the surface. In contrast, the energy associated with the cluster ion is distributed between all the atoms in the cluster. It has been shown that this results in an energy deposition that remains closer to the sample surface, hence increasing desorption of ions at the surface, producing a higher ion yield and reducing damage deeper in the sample [174,175]. Weibel *et al.* demonstrated that for certain organic materials this yield enhancement was between 30-100 fold when a C_{60}^+ ion source was employed over a Ga^+ source [176]. This enhancement in ion yield is particularly important for the analysis of biological species, which do not ionise as readily as inorganic materials.

In addition, the high spatial resolution achieved with an LMIG source (section 1.5.2) coupled with the enhanced ion yields produced by cluster ion beams, allows unprecedented analysis of the spatial distribution of specific substances in biological tissues and cells, as detailed in section 1.5.10. Large cluster sources, such as C_{60}^+ and the recently developed Ar_n^+, have also revolutionised the use of dynamic SIMS (section 1.5.9), enabling chemical analysis of a sample as a function of depth. In addition, the recent development of Ar_n^+ sources has shown potential to enhance the surface analysis of biological samples. These primary ion sources consist of much larger clusters (> 1,000 atoms) and have demonstrated not only reduced damage accumulation but also a 'gentler' ionisation process, causing an increase in the number of intact molecular species observed. This has led to the analysis of larger biological molecules such as lipids and peptides, which could only previously be identified by fragmentation patterns [177-179].

1.5.4 Charge compensation

The bombardment of the sample surface with a positively charged primary ion beam increases the surface potential due to both an increase in positive ions and the ejection of secondary electrons. This increase in surface potential can result in the repulsion of positive ions from the surface, accelerating them past the acceptance window of the analyser, which results in the loss of positive data. In addition, an increased surface potential can prevent the emission of

negative ions from the sample, resulting in a loss of negative data [169]. To compensate for this, an electron gun is widely used, which floods the surface with low energy electrons to neutralise any positively charged regions [169,180]. However, it has been demonstrated that the use of an electron flood gun can cause damage to the sample surface and so a recommended limit of 6.3×10^{18} electrons/m^2 is typically adhered to [181].

1.5.5 Mass analysers

There are several different types of mass analysers that can be employed. Originally, a quadrupole analyser was widely used as its small size enabled incorporation into a high vacuum system. A quadrupole mass analyser uses four parallel rods to which equal and opposite potentials are applied. The application of specific voltages to the rods affects the trajectory of ions with specific mass-to-charge ratios (*m/z*), which pass through a mass filter. However, as this analyser uses a scanning method to detect the ions, not all the sputtered ions are collected and analysed, which reduces the ion yield of the experiment. Therefore, especially for 'static' SIMS when the ion yield is already low, a more sensitive detector is preferred. The most commonly employed mass analyser for static SIMS analysis is therefore a time-of-flight (ToF) analyser. In ToF analysis, secondary ions are generated by pulses of a primary ion beam and all ions emitted from a single pulse are accelerated to a given potential to produce ions which all possess the same kinetic energy. The time taken for the ions to drift along a 'flight tube', with a known path length, to the detector is measured. Ions with a higher *m/z* will take longer to reach the detector than ions with the same kinetic energy that possess a lower *m/z*. This parallel detection of ions therefore means that a ToF analyser has a sensitivity 10^4 times that of a quadrupole analyser [169]. It also offers the detection of ions from a greater mass range, higher mass resolution and the pulsed nature of the analysis allows for the addition of effective charge compensation [169,182].

1.5.6 Ionisation efficiency and matrix effects

The ionisation process occurs during, or close to, the emission of particles from the sample surface. This means that the sample matrix will strongly influence the electron exchange processes that occur and hence the formation of secondary ions is strongly affected by the electronic state of the surface. This is a phenomenon termed the matrix effect [169,182,183]. Therefore, the ionisation efficiency for a particular ion will depend on the interactions with the remaining material and hence a variation in both ion formation and yield may occur for the same species present in different materials. In particular for organic samples, it has been demonstrated that the co-localisation of other species present in the sample can have a profound effect on ionisation and can result in both ion enhancement and suppression effects [184]. The matrix effect therefore prevents the use of ToF-SIMS as a fully quantitative technique and needs to be accounted for when conducting analysis of complex samples.

For organic materials, secondary ions can be produced through a number of different mechanisms, specifically ionisation or cationisation of a neutral molecule, ejection of an electron to form an $M^{\cdot +}$ species or polar molecules can undergo acid base reactions to form $(M+H)^+$ or $(M-H)^{\pm}$ ions. Fragment ions most likely occur through collision of molecular ions with either the primary ions directly or energetic atoms within the sample. These fragments can often offer important insight into chemical structure.[169]

1.5.7 Imaging capabilities

The ToF-SIMS technique also has the ability to produce secondary ion images, which map the spatial distribution of ions present in the sample. The instrument has the capability to record every ion that is detected as both a function of its *m/z* value and its x, y coordinates on the sample surface. Therefore, every pixel in a ToF-SIMS ion image contains a full mass spectrum at that point, allowing the spatial distribution of specific ions to be analysed. Using an LMIG source, as described in section 1.5.2, a beam diameter and hence spatial resolution of 50 nm is possible, although typically a range of 200 nm – 1 µm is achieved.

1.5.8 Primary ion focusing mode

The spatial resolution achievable is dependent on the primary ion focusing mode and a high spatial resolution is balanced with a high mass resolution. The typically employed focusing mode for spectral analysis is called 'high current bunched mode' (HC-BU) and enables the production of spectra with high mass resolution. This mode uses a buncher to reduce the primary ion pulse width so that all primary ions created in one pulse will impact the sample in quick succession. A bunched primary ion beam therefore produces a stream of ion pulses that impact the surface in succession at a known distance apart. This increases the energy deposition rate at the surface, which increases particle ejection and reduces the extraction and detection time of ions with the same *m/z*, which improves mass resolution. However, the use of a buncher impairs the focusing ability of the primary ion source and so reduces the spatial resolution. Therefore, ToF-SIMS images are usually acquired using another mode, termed burst alignment (BA). A buncher is not employed, which means that the pulse width is comparatively long and therefore the mass resolution and total ion count of the spectra will be reduced. However, it does enable a high focused beam, which results in high spatial resolution [169,182], as illustrated in Figure 1.12.

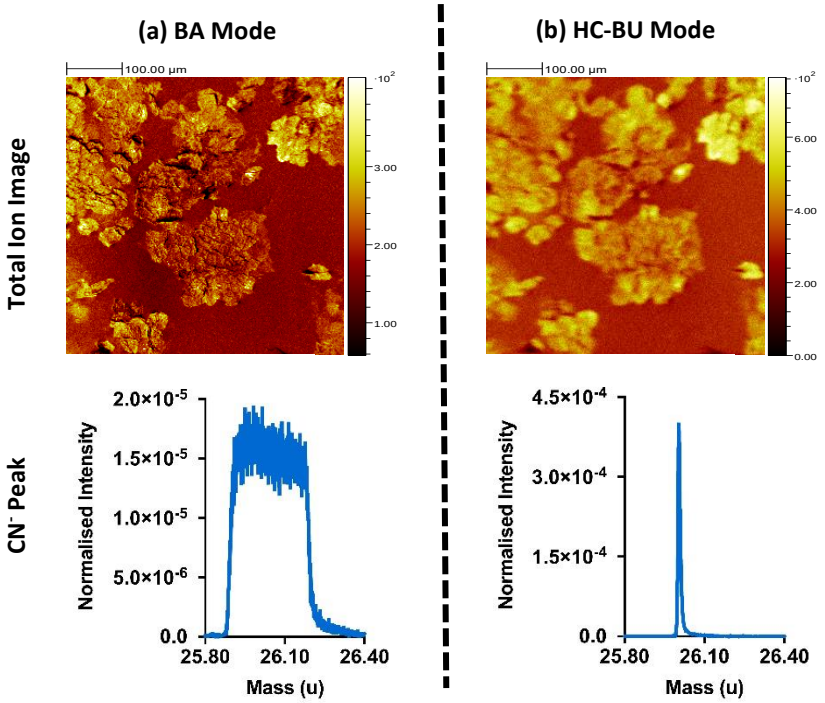

Figure 1.12 ToF-SIMS secondary ion images and spectra of human tape stripped corneocytes, illustrating the improvement in spatial resolution (images) but reduction in mass resolution (spectra) produced in (a) burst alignment mode compared to (b) high current bunched mode.

1.5.9 Dynamic SIMS

Dynamic SIMS is a term used to describe the operation of the primary ion beam at a dose which exceeds the 'static' limit, hence causing damage to the sample surface. This mode can therefore be employed specifically to collect information from the underlying sample. The development of cluster ion beams revolutionised the use of dynamic SIMS by greatly improving the depth resolution that could be achieved. As previously described (section 1.5.3) monatomic ion sources cause damage much deeper into the sample on impact compared to cluster ion sources, subsequently removing much less material from the surface. Monatomic ions are therefore less efficient for sample sputtering and can cause inter-mixing of sputtered material from different layers, which reduces the depth resolution that can be achieved [175]. Cluster ions beams, however, distribute the beam energy equally between the atoms in the cluster, resulting in a 'softer' impact, which restricts damage to the

underlying sample but removes surface material more efficiently. This offers a more uniform sputtering of the sample, with distinct layers removed and a greater depth resolution [175]. This is crucial for samples that differ chemically as a function of depth, including biological materials.

Dynamic SIMS analysis can be conducted using a single beam or dual beam method. Dual beam analysis is conducted by regularly interchanging two beams, one to sputter through the material and one to conduct surface analysis on the recently uncovered layer (Fig. 1.13). Dual beam analysis is typically employed over single beam analysis for several reasons. Single beam analysis requires the primary ion beam settings to be changed between each sputter and analysis cycle, which is less practical to operate and more time consuming. Whereas, the use of a separate beam for sputtering and analysis allows each beam setting to be specifically chosen and maintained throughout the experiment. Dual beam analysis also allows the optimisation of both the sputter process and analysis parameters. This allows the employment of a sputter beam that can produce a relatively high depth resolution, such as C_{60}^{+}, with an analysis beam that can offer high spatial resolution, such as an LMIG source. The dual beam mode therefore offers the opportunity to produce 3D chemical images with both high lateral and depth resolution.

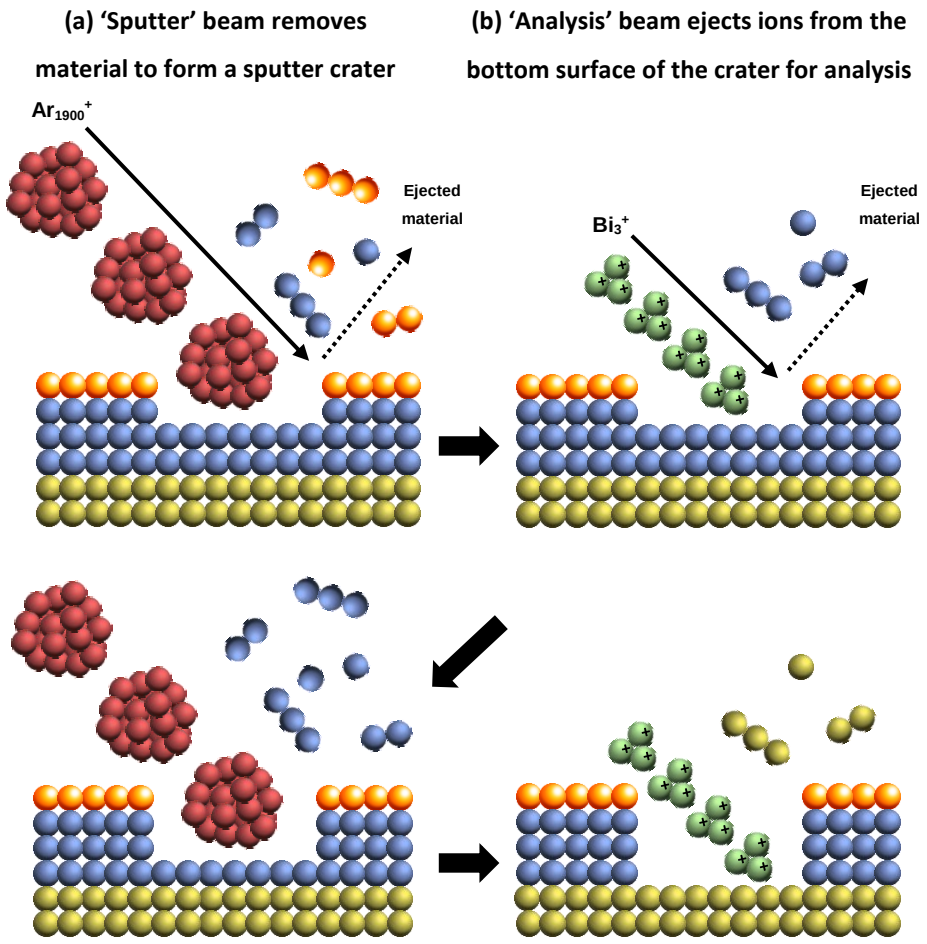

Figure 1.13 A schematic illustrating the process of dual beam dynamic SIMS for depth profile analysis. The interchanging of (a) a sputter beam with (b) an analysis beam enables chemical information to be collected as a function of sample depth.

A C_{60}^+ sputter beam has been widely employed in the depth profile analysis of a wide range of materials, both inorganic and organic, including biological tissue [185-193]. However, recent developments in cluster ion beams have seen the emergence of large argon clusters (> 1,000 atoms). Due to their larger cluster size they have been shown to offer enhanced depth resolution in comparison to a C_{60}^+ source [194-196]. These beams therefore offer huge potential in the acquisition of depth profile data with both high lateral and depth resolution from multicomponent systems, illustrated by the example data in Figure 1.14 showing the nanometer depth resolution achieved through analysis of a multi-layered polymer structure using an Ar_{2000}^+ GCIB [195].

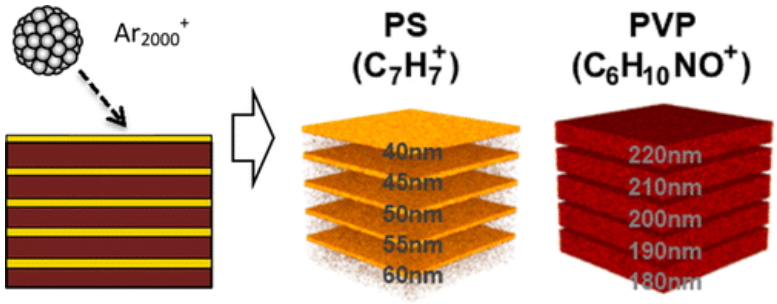

Figure 1.14 ToF-SIMS secondary ion 3D images showing depth profile analysis of a multi-layered polymer structure using an Ar_{2000}^+ beam to achieve nanometer depth resolution. Reprinted with permission from Bailey et al., ACS Appl. Mater. Interfaces 2015, 7, 2654-9. Copyright © 2015 American Chemical Society [194].

1.5.10 Biological tissue analysis

Numerous studies have shown the successful application of ToF-SIMS for the analysis of biological material, demonstrating the detection of important biomolecules, such as proteins [197,198] and lipids [159,199-203], from a variety of both healthy [83,163,199,202,204,205] and diseased [159,206-208] tissues and other biological substrates, such as individual cells [193,209-212] and bacteria [213-215]. However, although this technique has great potential in the application of skin tissue analysis, this is an area which has been relatively unexplored with only a limited number of studies to date [83,159,162-165].

As previously eluded to, the emergence of gas cluster ion beams has placed ToF-SIMS in an advantageous position to study biological material. The technique provides high mass resolution and chemical specificity, which is crucial in discriminating between the array of complex structures present in biological samples. The reduction in surface damage and fragmentation offered by these cluster sources has also allowed enhanced detection of biomolecules, by preserving their intact structures, aiding in compound identification. The advantages provided by cluster ions for sample sputtering has further advanced the field of bioanalysis, producing relevant chemical profiles as well as high spatial and depth resolution images for complex multi-layered structures, such as biological tissues and cells.

The recent development of argon GCIB (section 1.5.9) has provided enhanced depth resolution for ToF-SIMS depth profile analysis. This technique now has the potential to provide huge analytical advancements in the field of drug delivery, through analysis of the 3D distribution of exogenous compounds within biological tissue, which before could only be achieved through 2D surface analysis of vertical tissue slices. The detection of pharmaceutical compounds within cells has been recently demonstrated using dynamic SIMS [212,216-218], but to date this has not yet been achieved for whole tissue sections.

1.6 The scope of this thesis

This thesis looks to address some of the current issues surrounding skin research through the employment of both emerging and established analytical techniques. The first part of the project will focus on the analysis of native *stratum corneum*, collected *in vivo* from human volunteers. The aim of this work will be to develop suitable methods to study both chemical and physical parameters of the *stratum corneum* and then use these to study age-related changes to this tissue. Changes to the lipid composition in particular are relatively unexplored, due to both the complex nature and the issues associated with extracting and distinguishing between the numerous species present. ToF-SIMS offers the opportunity to conduct simultaneous analysis on all lipid species directly from tape stripped samples, providing high chemical specificity and imaging capabilities which can provide new insights into this area. The second part of the project will focus on the development and use of a dynamic SIMS method to enable the permeation of exogenous compounds to be monitored from *ex vivo* tissue sections as a function of skin depth. There is a current need for analytical techniques to provide more detailed information about the permeation of compounds across the *stratum corneum* layer, to enable better design of both pharmaceutical and cosmetic topical products. No other technique is currently able to match the combination of high chemical specificity, mass resolution and both lateral and axial resolution. Therefore, this project looks to utilise these capabilities to enhance the field of permeation analysis.

Chapter 2: Materials and methods

2.1 Materials

10 % neutral buffered formalin, xylene (histological grade), paraffin wax, haematoxylin and eosin Y (H&E) were purchased from Sigma Aldrich, UK. Optimal cutting temperature compound was purchased from VWR Chemicals, UK. Dimethyl sulfoxide (HPLC grade), ethanol (ACS reagent grade) and phosphate buffered saline tablets were purchased from Fischer Scientific, UK. Vitamin C 10 Day Glow Boosting Concentrate was purchased from The Body Shop®, UK.

1,3-bis[(3-octadecyl-1-imidazolio)methyl]benzene dibromide was synthesised and provided by the group of Dr. Lluïsa Pérez-García at the University of Barcelona, Spain.

D-Squame skin sampling discs (CuDerm, Texas, U.S.A.), D-Squame pressure disc applicator (CuDerm), ascorbic acid, ascorbyl glucoside, ethyl ascorbic acid and sodium ascorbyl phosphate were supplied by Walgreens Boots Alliance.

2.2 Tissue collection and preparation

2.2.1 Human tape stripped *stratum corneum*

Tape stripped *stratum corneum* was collected from human volunteers for both native analysis (chapters 3 and 4) and following the application of a topical product (relevant to results discussed in chapter 6). Ethical approval for these studies was granted from the University of Nottingham Research Ethics Committee (reference no. 003-2016).

2.2.1.1 Volunteer population

All samples were collected from healthy, female volunteers above 20 years of age with a Fitzpatrick skin type [219] of II/III. This is a numerical classification system for human skin colour, based on the reaction of different skin types to UV exposure. Therefore, especially for the aging study (chapter 4), a

controlled population of volunteers with a similar skin type was needed. All volunteers participated after providing consent and confirmed they were free from skin conditions and medication.

For the skin aging study (results discussed in chapter 4) the volunteers were selected from two age categories, 'young' i.e. < 27 years and 'old' i.e. > 60 years old (post-menopausal). This comparison represented changes related to intrinsic aging. For each volunteer, samples from two different body locations were collected in order to assess extrinsic aging. Samples were taken from an area of expected high UV exposure, the dorsal hand, and an area of lower UV exposure, the flexor forearm. For these samples the following abbreviations will be used: post-menopausal (old or O), under 27 years old (young or Y), arm (A) and hand (H).

2.2.1.2 Tape stripping protocol

Tape stripping experiments were performed using D-Squame skin sampling discs (CuDerm, Texas, U.S.A.). The circular discs have a diameter of 22 mm and consist of a fully cured, medical grade, synthetic polyacrylate ester adhesive. Following application of the disc to the skin, a constant pressure was applied using a pressure disc applicator (CuDerm) and the disc removed in one fluent motion. A series of 15 consecutive tape strips were taken per sampling site and the data reported is specified as strip 1 being the uppermost layer and strip 15 being the deepest. Any samples used as part of a comparative study (chapters 4 and 6) were collected by the same practitioner to prevent variability in technique. All samples not immediately analysed were stored in individual Eppendorf® tubes at – 20 °C.

2.2.2 Porcine *ex vivo* tissue

2.2.2.1 Sample collection

The *ex vivo* tissue used in the project was exclusively of porcine origin. All skin tissue was collected as a secondary use of the animal, in accordance with the NC3R framework on the reduction and refinement of animals in research.

Preliminary studies were conducted on porcine flank tissue. However the majority of the samples in this project were prepared using porcine ear tissue. The skin was obtained from a local abattoir, from 5 month old pigs which were specifically reared for food and not experimentation. The gender of the pigs was undefined, but samples within a single experiment were taken from a single ear to minimise variability. The acquisition of tissue from a local abattoir ensured a regular supply, which reduced the need to store samples for long time periods. In order to preserve the integrity of the skin, it was taken immediately after the pigs were slaughtered, prior to any cleaning or hair removal procedures. The tissue was then kept at 4 °C for approximately 24 hours until collection from a local butchers, upon which it was prepared immediately.

2.2.2.2 Skin preparation

The porcine tissue was first washed using deionised water and the hair was trimmed as short as possible using scissors only.

The porcine flank tissue was sectioned to a 400 µm thickness using an electric dermatome. The tissue was then stored at -20 °C until used. The dermatome process was carried out by a colleague with prior experience in the technique.

For the porcine ear tissue, a scalpel was used to detach the skin from the underlying cartilage and any excess subcutaneous fat was removed. The resulting full thickness skin sections were then kept at -20 °C until used.

For the preparation of heat separated (HS) epidermis sections, prior to freezing the full thickness ear skin was cut into smaller squares of approximately 2-4 cm^2. These were placed into a water bath at 60 °C and the skin was submerged for 60 seconds, after which the epidermal layer was carefully peeled away from the dermis using tweezers. This epidermal membrane was then stored at – 20 °C until used.

In accordance with the Organisation for Economic Co-operation and Development (OECD) guidelines on skin absorption studies [111], tissue was

stored at – 20 °C and used within 3 months of preparation. Once defrosted, any unused tissue was discarded and not refrozen.

2.2.2.3 Microtome sectioning

Prior to microtoming, 1 cm × 1 cm squares of dermatomed porcine flank skin (400 µm thick) were fixed in a 10 % (v/v) formalin solution for 20 minutes. After washing in phosphate buffered saline (PBS), the skin samples were then dehydrated using a series of ethanol solutions. The samples were soaked in each solution for 30 minutes, increasing in ethanol concentration from 25-100 % (v/v). The samples were then twice submerged in xylene (2 × 1 hour) and lastly twice in paraffin wax (2 × 1 hour) ensuring that the skin sample was embedded with the *stratum corneum* facing upwards. This dehydration and embedding process was conducted automatically using a tissue processor (Leica TP1020, Milton Keynes, UK). The samples embedded in paraffin were then cut vertically into sections of varying thickness (8, 10 and 15 µm) using a microtome (Leica RM 2165 microtome, Leica Microsystems Ltd.) and mounted onto glass slides. The sectioning was conducted in my presence by a colleague with prior experience in this technique.

2.2.2.4 Histological imaging

Porcine ear tissue, 1 cm × 1 cm squares, were embedded using the inert support medium, optimal cutting temperature (OCT) compound. The OCT compound is initially a slurry, which allows embedding of the skin material, but then rapidly solidifies once cooled below –10 °C. The embedded skin was cut vertically into 20 µm sections using a cryostat (Thermo Fischer Scientific) set at – 20 °C and then mounted onto glass slides. The samples were then subjected to H&E staining before being imaged using an optical microscope (Leica DM5000B microscope). The sectioning and staining was conducted by a colleague with prior experience in this technique.

2.2.2.5 Homogenised tissue samples

Full thickness porcine ear skin was cut into sections using scissors. The sections were cut as small as physically possible, with a maximum area of 1 mm^2, as the smaller the size the more efficient the homogenisation process. The skin was then left to hydrate in deionised water for 1 hour, before being homogenised using a rotor-stator homogeniser (Ultra-Turrax T25, IKA, Germany). Once fully homogenised, the skin homogenate was dispersed onto a petri dish and left to air dry.

To prepare the skin homogenate/compound reference samples (chapter 6), 50 mg of homogenate was added to 200 µL of a 2% compound (w/v) solution in dimethyl sulfoxide (DMSO). A probe sonicator (Bandelin Sonoplus, Germany) was used to aid dissolution of the skin homogenate in the compound/DMSO solution. This was done for the four different vitamin C compounds, ascorbic acid, ascorbyl glucoside, ethyl ascorbic acid and sodium ascorbyl phosphate and a blank sample containing only DMSO and the skin homogenate was also prepared. 10 µL spots were the pipetted onto a glass slide and left at room temperature to facilitate the evaporation of DMSO before loading into the ToF-SIMS instrument.

2.3 Analytical methods

2.3.1 Time of flight - secondary ion mass spectrometry (ToF-SIMS)

All analysis was conducted using a ToF-SIMS IV instrument (IONTOF, GmbH) equipped with a single-stage reflectron analyser. Charge compensation of the sample was achieved using a low energy (< 20 eV) electron flood gun. All ToF-SIMS data was acquired and analysed using SurfaceLab 6 software (IONTOF, GmbH) and all exported peak intensities were normalised to the total ion count of the spectra.

2.3.1.1 Sample preparation

Prior to analysis, tape strips were fixed to glass slides, using adhesive tape, and loaded directly into the instrument, unless specified otherwise.

The microtomed sections were paraffin-stripped in xylene and left to air dry before loading into the instrument on glass slides.

Heat separated (HS) epidermis and full thickness samples were loaded using the ToF-SIMS 'backmount' stage. This allows samples to be mounted on the underside of the stage and the surface of the sample presented through 1 cm × 1 cm openings. HS epidermis samples were loaded into the instrument with no prior sample preparation. Full thickness samples were clamped between two cling film wrapped glass slides and dried under vacuum at room temperature for ~ 12 hours prior to loading into the instrument.

Due to the reliability of the ToF-SIMS instrument and the ability to normalise each ion peak to the total ion count of the individual spectra, it was not necessary to randomise the samples for ToF-SIMS analysis.

2.3.1.2 Static SIMS analysis of tape strips

Static analysis was conducted using a bismuth liquid metal ion gun (LMIG), unless specified, with Bi_3^+ clusters chosen as the primary ion source. A 25 keV beam energy, ~ 0.3 pA pulsed target current and 10 keV post-acceleration energy were employed. High current bunched (HC-BU) mode was used throughout, unless specified otherwise, and the primary ion dose density was always maintained at $\leq 1\times10^{12}$ ions/cm^2 to ensure static conditions. The primary ion beam was directed at the sample at an angle of 45 °C and in HC-BU mode the bismuth LMIG had a focused beam size of 1−2 μm.

For most samples, data was acquired over 4 mm × 4 mm area in both positive and negative polarity at a resolution of 100 pixels/mm. Each 4 mm × 4 mm area was scanned using the macroraster stage function, using a random raster pattern. A total of 64 separate 0.5 mm × 0.5 mm patches were scanned, with 15 scans acquired per patch.

For the primary ion beam focusing mode comparison (section 3.3.1.1) and the homogenised skin reference samples (section 6.3.1) data was acquired from 15 scans of a 500 μm × 500 μm patch, at a resolution of 256 × 256 pixels.

2.3.1.3 Dual beam dynamic SIMS of ex vivo tissue

Dual beam dynamic SIMS was conducted using both a Bi_3^+ LMIG beam and an argon (Ar_n^+) gas cluster ion beam (GCIB). The Bi_3^+ LMIG beam was employed as the analysis beam, using the settings described in section 2.3.1.2 with the exception of a 128 × 128 pixel resolution used. The argon GCIB was used as the sputter beam and the settings were optimised throughout the project, varying the beam energy, cluster size and target current. The final optimised settings employed a 20 keV Ar_{1900} beam set to a target current of 10 nA. A non-interlaced sputter mode was employed, consisting of a continuous cycle of 10 seconds sputtering, followed a 0.5 second pause and then 3.25 seconds of analysis. A sputter region of 500 µm × 500 µm was employed for all samples and a 200 µm × 200 µm region within the centre of the sputtered crater was analysed.

2.3.1.4 Frozen hydrated sample analysis

A 2 cm × 2 cm HS epidermis sample was attached to the cyrostage and loaded into the ToF-SIMS airlock chamber. Using liquid nitrogen the temperature of this chamber was then cooled to – 80 °C over a 5 minute period. Once the pressure in the airlock had reached 1×10^{-6} mbar, the cryostage was introduced into the precooled main chamber for analysis. Depth profile analysis was then conducted using the settings described in section 2.3.1.3, ensuring that the temperature was maintained at < - 80 °C.

2.3.2 Scanning electron microscopy (SEM)

2.3.2.1 Basic principles

SEM is an imaging technique that functions by scanning a sample with a focused beam of electrons and records both emitted secondary electrons and backscattered electrons in order to elucidate the sample topography. Non-conductive samples require coating with a thin layer of metal to prevent sample surface charging. Conventional SEM works under high vacuum to prevent the deflection of electrons by atmospheric particles. However, this

requires biological samples to undergo a fixation or dehydration process, which may damage structural integrity. A low vacuum SEM mode has therefore been established which typically allows a lower accelerating voltage. This reduces the effects of sample charging and therefore metal coating of the sample is not required. However, as a lower voltage is employed compared to the high vacuum mode, image resolution is typically lower.

2.3.2.2 General settings

The tape stripped samples were mounted onto aluminum SEM stubs of 12.5 mm diameter, using carbon-based, electrically conductive, doublesided adhesive discs. All analysis was conducted using a JEOL 6060LV variable pressure SEM (JEOL, UK). Initial analysis was attempted using both low vacuum (48 Pa, 9 mm working distance) and high vacuum mode (10^{-2} – 10^{-4} Pa, working distance 20 mm) using an accelerating voltage of 10 keV and a spot size of 45. High vacuum mode required samples to be metal coated, which was achieved by sputter coating with gold for 3 minutes to give a surface coverage of approximately 20 nm. All SEM images were processed using ImageJ software (W. Rasband, National Institute of Health, U.S.A).

2.3.2.3 Aging comparison

SEM analysis was used to investigate age-related changes to corneocyte surface area (chapter 4). Analysis was conducted on tape strip no. 6 for three volunteers from each age category. Tape strip 6 was chosen due to its median *stratum corneum* position within the collected samples. The samples were analysed in high vacuum mode using the initial settings detailed in section 2.3.2.2, but the beam energy and spot size were varied slightly between samples to optimize the individual image resolution. Samples were imaged at × 800 magnification. Image J software was used to outline each corneocyte and calculate the surface area using the scale bar provided on the image as a reference measurement. For each sample, six repeat measurements were collected from different areas across the sample.

2.3.3 Optical profilometry

2.3.3.1 Basic principles

Optical profilometry provides a non-contact method to measure surface topography and height variation across a sample. The sample is typically scanned over a user specified vertical (or Z) range, recording the XY location and precise Z height of the pixels. Traditional white light interferometers work by calculating the variation in optical path length of light reflected from the sample compared to light reflected from an inbuilt reference surface. However, this results in splitting of the initial light source, which limits the amount of light available for imaging. In addition, due to a relative motion created by splitting the light source, the vertical resolution can be susceptible to vibrational interference. The optical design employed in the Zeta-20 optical microscope used in this project allows these issues to be overcome. The instrument does not use a split light source, which provides high light throughput for imaging. This enables true colour images to be acquired for a wide range of sample types, including very dark surfaces and those with low reflectivity. The other advantage provided by the Zeta-20 instrument is the ZDot^{TM} technology, an advanced precision focusing pattern based on a confocal grid illumination. This generates contrast irrespective of the sample type and therefore allows the system to accurately detect and provide height measurements for virtually all surfaces, including those that are transparent, tilted or display large variations in height. The instrument uses this focusing pattern to accurately map multiple focal planes across the user specified Z range, which can then be rebuilt to create an accurate 3D profile of the sample.

2.3.3.2 General settings

Samples were imaged using a Zeta-20 optical microscope (Zeta Instruments, CA, U.S.A). The sample was vertically scanned at regular depth intervals between user-defined upper and lower reference surfaces. The Z resolution was defined as the total depth scanned divided by the number of vertical scans acquired. The maximum number of scans possible is defined by the computer memory, which was 1000 for the instrument used in this project. Both 2D and

3D optical images were produced and accurate step height measurements could then be acquired for any feature in the image respective to the underlying flat substrate.

Tape stripped samples were placed onto glass slides for analysis with the adhesive side facing upwards. Images were collected at × 50 magnification, which equated to a working distance of 1 mm and an XY resolution of 0.18 µm. The adhesive material was defined as the lower surface and the *stratum corneum* layer as the upper surface. The maximum Z resolution achievable for these samples was approximately 0.04 µm.

Heat separated epidermis sections adhered to silicon wafers were gently compressed between two glass slides and imaged with the *stratum corneum* side facing upwards. Images were collected at × 20 magnification, which equated to a working distance of 3.1 mm and an XY resolution of 0.45 µm. The silicon wafer was defined as the lower surface and the top of the skin as the upper surface. The maximum Z resolution achievable for these samples was approximately 0.25 µm.

2.3.4 Atomic force microscopy (AFM)

2.3.4.1 Basic principles

AFM analysis involves the scanning of a probe along a sample surface in order to elucidate the topography. The probe consists of a cantilever with a sharp integrated tip and a fixed distance between the tip and the surface is maintained. Forces acting on the tip therefore result in a deflection of the cantilever in the Z direction, which is converted into topographical information. There are several different modes in which AFM analysis can be conducted. Tapping mode in particular is useful to prevent the tip sticking to the surface of the sample. In this mode the cantilever is set to oscillate up and down at a fixed amplitude and any topographical changes in the surface therefore cause a change in amplitude.

2.3.4.2 General settings

All AFM measurements were carried out by Dr. Daniel Johnson in collaboration with Swansea University. AFM measurements were performed on a Multimode AFM with NanoScope IIIa controller (Bruker, U.S.A.) using manufacturer-supplied software. All measurements were carried out using tapping mode under ambient laboratory conditions (humidity ~60%, temperature ~22 °C) using TESP probes (nominal spring constant 20−80 N/m). Data was analysed using instrument control software (NanoScope software version 5.31R1 was used throughout). Tape stripped samples were fixed to metal sample stubs prior to imaging. For sample height measurements, images were taken with approximately equal areas of skin and substrate visible. Line profiles were then taken across the surface and the maximum height of the corneocyte layer above the substrate plane was measured. Three images were taken from different areas of each sample, with three line profiles taken from each image, making all average step height values the mean of nine individual measurements.

2.3.4.3 Aging comparison

Analysis was conducted on both the arm and hand samples of one < 27 year old volunteer and one post-menopausal volunteer. Alternate tape strips 2−14 were used for analysis.

2.4 Permeation studies

2.4.1 *In vitro* studies

2.4.1.1 Preparation of PBS solutions

5% (w/v) solutions in phosphate buffered saline (PBS) were prepared for the four vitamin C compounds, namely ascorbic acid (AA), ascorbyl glucoside (AG), ethyl ascorbic acid (EAA) and sodium ascorbyl phosphate (SAP). The solutions were prepared fresh prior to each Franz cell experiment. The PBS solution was also prepared fresh before each Franz cell experiment, by

dissolving one PBS tablet in 100 mL of deionised water to give a pH 7.4 solution.

2.4.1.2 Preparation of ascorbic acid gel formulation

The supramolecular gelator used was 1,3-bis[(3-octadecyl-1-imidazolio)methyl]benzene dibromide [220]. To prepare the gel formulation 5 mg of gelator was dissolved in 0.4 mL of ethanol. In a separate vial 50 mg of ascorbic acid was dissolved in 0.6 mL of deionised water. The ascorbic acid solution was then added to the gelator solution and stirred manually for 60 seconds. The mixture was then left undisturbed until gelation had occurred, which was confirmed using the inverted vial method [220]. The gelation process took ~ 1 hour, however this varied between samples which was likely due to laboratory conditions.

2.4.1.3 Franz cell experimental set up

Circular samples of full thickness porcine ear skin approximately 2.5 cm in diameter were prepared. Porcine ear tissue was chosen due to the reported similarity in skin layer thickness compared to human tissue [112,221,222]. This therefore allowed the use of full thickness skin, rather than risk damage to the skin integrity through the preparation of split thickness tissue. The skin samples were then mounted between a donor and receptor chamber in a Franz-type static diffusion cell set up, as illustrated in Figure 2.1. The discs were mounted dermal side down and had an exposed surface area of 2.54 cm^2. Prior to the permeation experiment, the integrity of each skin sample was assessed using electrical resistance measurements, as detailed in section 2.4.1.4. For the permeation experiment, a recorded volume of freshly prepared PBS solution (pH 7.4) and a stirrer bar were added to each receptor chamber. The cells were mounted into an aluminium stand and placed into the centre of a stirring water bath at 36 °C, equipped with a built-in magnetic stirrer plate.

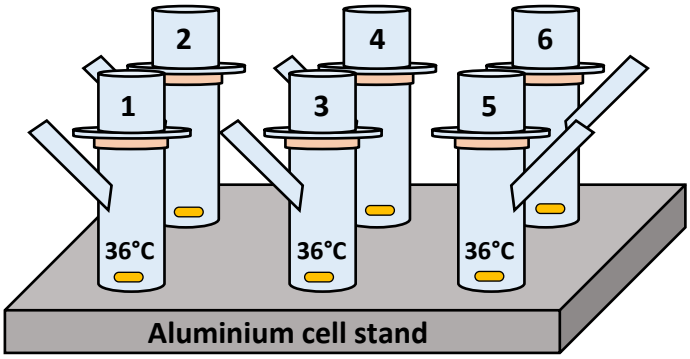

Figure 2.1 A schematic illustrating the Franz cell experimental set up.

Six cells were available for each Franz cell experiment. One cell was assigned to a blank skin sample and the rest were available for application of the compounds of interest. Each comparative study was conducted by running the compounds/formulations of interest in parallel in one Franz cell experiment. For example, for the comparison of the vitamin C compounds the Franz cell set up would be as follows: (1) Blank (2) PBS solution only (3) AA in PBS (4) AG in PBS (5) EAA in PBS and (6) SAP in PBS. Where possible three separate Franz cell experiments were run for each comparative study. For each Franz cell experiment one porcine ear tissue was used to prepare all 6 skin samples. Therefore, three different pig ears were used for the three experimental repeats, to account for any variability in permeation resulting from biological variance. Where possible, three repeat ToF-SIMS data sets were collected from different areas on each of the three repeat samples. This therefore produced nine depth profiles for each compound of interest.

A 1 mL volume was applied for all tested solutions, including the cosmetic product from The Body Shop®. The meniscus of the solution in each donor chamber was marked on the outside of the glass and checked at the end of the experiment to monitor any possible evaporation or leakage of the solution. For the gel formulation, 200 mg was applied and a uniform coverage of the exposed skin area was ensured. On termination of the experiment the excess donor solution or gel layer was removed and the samples were prepared for ToF-SIMS analysis as described in section 2.3.1.1.

2.4.1.4 Skin integrity testing

The skin integrity was initially visually checked and discarded if obvious signs of damage or defects were present. Electrical resistance measurements were also taken prior to Franz cell experiments. The skin samples were set up in the Franz cells as described in section 2.4.1.3 using physiological saline solution (aq. 0.9 % w/v) as both the receptor and donor solution. The skin was then allowed to equilibrate in a water bath at 36 °C for 30 minutes. Measurements were taken using an EVOM2 Voltohmmeter (World Precision Instruments, U.S.A) connected to two stainless steel electrodes. Resistance values were measured for an exposed skin surface area of 2.54 cm^2. To record the resistance, one electrode was inserted into the receptor chamber via the side arm and the other electrode immersed in the saline in the donor chamber. The recorded value was taken once the resistance had stabilised.

Typical resistance values for different species have been documented by Davies *et al.* [122], who specify that intact full thickness porcine skin should produce a resistance > 4 kΩ. However, this value is based on specific experimental parameters and Davies *et al.* also noted that values ranged between 2-10 kΩ relating to both the porcine breed and seasonal variation. Therefore, an internal study was conducted to distinguish the difference in resistance between 'visibly intact' native samples and deliberately perforated samples. Based on this study a cut off value of > 10 kΩ was used to determine intact samples.

2.4.2 *In vivo* studies

The *in vivo* permeation study was conducted under guidance from Walgreens Boots Alliance. Three volunteers were employed for the study, which involved the application of a cosmetic product from The Body Shop® containing 5% (w/v) ascorbic acid, specifically 'Vitamin C 10 Day Glow Boosting Concentrate'. Prior to use, this product requires a powder material to be thoroughly dissolved into a base solution within a sealed container. This procedure was performed 30 minutes before application. Prior to product application two 'pre-tapes' were taken and discarded. This involved a minimal

pressure application and removal of two sequential strips in order to remove any partly detached corneocytes, which are termed *stratum disjunctum*. A glass donor chamber with an exposed surface area of 2.54 cm^2 was secured to the forearm and an infinite dose (1 mL) of the product was applied and left for 30 minutes. At the end of the application period the remaining solution was removed, the skin was wiped with both an alcohol wipe and a dry tissue and 15 sequential tape strips were collected. An adjacent site on the skin was also stripped to use as a blank control site.

2.5 Statistical analysis

Statistical analysis was carried out using Graphpad Prism 7.0. Prior to analysis a D'Agostino-Pearson omnibus test was conducted to confirm that the data exhibited a normal distribution, allowing parametric analysis methods to be used. An unpaired, Welch's unequal variance t test was used throughout to determine whether two groups of data presented a statistical difference. P values ≤ 0.05 were considered statistically significant and are represented by asterisks. The following asterisk format is used throughout; * $p \leq 0.05$, ** $p \leq 0.01$, *** $p \leq 0.001$, **** $p \leq 0.0001$.

2.6 Multivariate data analysis (MVA)

2.6.1 Basic principles

Multivariate data analysis (MVA) is a statistical tool which is used to find patterns and relationships in data containing several interdependent simultaneously measured variables. A typical ToF-SIMS spectrum can contain hundreds of peaks and often data sets contain multiple spectra from multiple samples, which results in a large data matrix for analysis. Manual assessment of peak variation between samples for these large data sets would therefore prove impractical and time consuming. Therefore, MVA techniques can help to elucidate both the variation between sample types and the identity of peaks which contribute to these differences. However, it must be noted that MVA is a statistical tool which analyses the data purely from a numerical basis.

Therefore, the original source of the data, i.e. the ToF-SIMS spectra, must always be consulted to confirm any trends highlighted using MVA. There are numerous MVA techniques all which offer their own advantages and disadvantages depending on the type of data set to be analysed. For the purpose of this project two different techniques will be discussed, principal component analysis (PCA) and orthogonal partial least squares discriminant analysis (OPLSDA).

2.6.2 Principal component analysis

Principal component analysis (PCA) operates by viewing the overall variance within a data set, which is defined as a matrix with 'sample' rows and column 'variables'. For a ToF-SIMS data set, the 'samples' are the individual spectra and the 'variables' are the *m/z* values of the peaks in the spectra, with the data matrix containing the measured peak intensities. The PCA analysis is then calculated from the covariance matrix of the original data and involves an axis rotation that aligns a new set of axes, called principal components (PC). The new axes are aligned with the maximal directions of variance within the data set. PCA then produces three new matrices termed the scores, loadings, and residuals. The residuals are assumed to contain random noise and no useful sample information. The scores and the loadings together present a summary of the variance within the data set and must be viewed together to gain meaningful information. The scores plot indicates the projection of the original data points on the new given PC axes and a split along the axes highlights variance between the samples. The loadings indicate which of the variables are responsible for the separation between samples highlighted in the scores plot. It must be noted that as PCA is designed to find the greatest directions of variance within a data set, the largest variation between samples may rise from contamination and not more subtle native changes in chemistry [223]. PCA is a popular starting choice for most data sets due to its simple and unsupervised nature. However, this method only produces good class separation when the variation within a single class is sufficiently less than the variation between the two classes [224]. This therefore posed a problem for the aging study (chapter 4), as the aim was to detect subtle differences in

human samples, which invariably suffer from significant variability between volunteers.

2.6.3 Orthogonal partial least squares discriminant analysis

Most biological data analysis aims to compare data taken from different class types and to discriminate between them. Typically, this type of data is highly multivariate, with the number of variables much greater than the number of observations. Predictive models based on latent variables, such as partial least squares (PLS) regression, are well suited to these types of data sets. Applying an orthogonal correction filter to these models (OPLS) can help to distinguish between variations in the data that are useful for the prediction of a quantitative response and variations that are orthogonal to this prediction. OPLSDA is a further extension of these models, which has proven useful to highlight unexpected variability related to biological variation. This analysis technique focuses on the predictive component of the model, rather than the orthogonal component which contains variation unrelated to class response. OPLSDA is known as a supervised multivariate method, which utilises user-inputted information on the class identity of a sample. However, it serves to maximise class separation within a data set, which is important when analysing subtle differences between samples [225,226].

2.6.4 General settings

All multivariate data analysis was conducted using SIMCA-P software (version 13.1, Umetrics, MKS Instruments Inc.). The models produced are evaluated using R^2 and Q^2 values. The R^2 value measures the goodness of fit of the model, with values closer to 1 indicating a more reliable model. Whereas the Q^2 value indicates the predictability of the model, with values > 0.5 considered acceptable. Numerically close R^2 and Q^2 values confirms that overfitting of the model has not occurred [3].

All ToF-SIMS data was exported as peak intensities which had been normalised to the total ion count of the spectra. The peaks were selected using

the automatic peak picking tool in the ToF-SIMS software, ensuring the same peak list was applied for all samples. Prior to selection it was ensured that all the spectra were calibrated using the same calibration list.

For PCA the exported data was mean centred and scaled using the software recommended scaling, unit variance. This method uses the standard deviation as the scaling factor. For the aging study using OPLSDA (chapter 4), the data was mean centered and Pareto scaled. This involves the division of each variable by the square root of its standard deviation. This scaling method can help to emphasise subtle variations between samples [227].

Chapter 3: Characterisation of tape stripped, native human *stratum corneum*

3.1 Introduction

Tape stripping is the most popular method to remove, and hence facilitate analysis of, the *stratum corneum.* The simplicity and non-invasive nature of this technique allows easy application to human volunteers and sequential stripping allows information to be acquired as a function of *stratum corneum* depth. The analysis of tape stripped samples has therefore been widely utilised, using numerous techniques to assess both the physical and chemical properties of the *stratum corneum.*

The *stratum corneum* is a complex structure with a highly organised, sophisticated lipid matrix that has been shown to play an important role in many of the protective functions of the skin (section 1.2.2). Characterisation of this lipid composition and the influence of both intrinsic and extrinsic factors is therefore a highly researched area. As discussed in section 1.4.1, liquid chromatography mass spectrometry methods are typically employed to analyse the chemical composition of the *stratum corneum*. However, chromatographic methods suffer from several disadvantages in the analysis of tape stripped samples. Extraction of the tissue components from the tape strip involves a laborious process and a poor extraction method can result in contamination of the sample from adhesive components. In addition, analysis of native species requires a multi-step gradient method to separate the numerous lipid and other chemical components present in the *stratum corneum,* which can be complicated and time consuming.

Chromatography based methods also provide no information regarding the spatial distribution of compounds present in the *stratum corneum*. Recent analytical developments in *stratum corneum* analysis have seen the emergence of both imaging and spectroscopy based techniques, such as confocal microscopy, infra-red and Raman spectroscopy. These techniques all provide advantages and disadvantages, as discussed in section 1.4.2. However, none provide the chemical sensitivity and specificity offered by mass spectrometry

techniques. Matrix assisted laser desorption ionisation (MALDI) and desorption electrospray ionisation (DESI) are both mass spectrometry techniques that have shown potential for skin analysis (section 1.4.2). Although DESI offers analysis under ambient conditions, which are ideal for biological samples, it cannot produce high spatial resolution images and MALDI requires a chemical modification of the surface, which is not preferred for biological sample analysis.

Time of flight - secondary ion mass spectrometry (ToF-SIMS) offers unparalleled sensitivity and excellent mass and spatial resolution. As discussed in section 1.5.10, ToF-SIMS analysis has been applied to a wide range of biological tissues, demonstrating huge potential for the detection of both native and exogenous species. The use of this technique for skin tissue analysis, however, remains relatively unexplored, especially for the detection of native species. Judd *et al.* has demonstrated successful analysis of sequentially stripped porcine *stratum corneum*, with the aim of detecting an exogenous compound [83]. This therefore highlights the potential of this technique to provide relevant depth information about the native chemical composition of this layer, especially as tape stripping can easily be applied to collect human *stratum corneum in vivo.*

3.2 Chapter aims

The initial aim of this chapter is to further develop the method applied by Judd *et al.* [83] for ToF-SIMS analysis of tape stripped *stratum corneum.* The optimisation of several instrumental parameters will be explored, such as the chosen analysis region, the choice of primary ion beam and the beam focusing mode, in order to maximise the information gained from this sample type.

Once the instrumental parameters have been optimised, the aim is then to determine whether ToF-SIMS can be used to provide relevant information regarding the lipid composition of tape stripped *stratum corneum* samples. In particular, this will be assessed using samples collected from human volunteers *in vivo* in order to utilise the non-invasive nature of the tape stripping procedure.

Before this technique can be applied to cross compare samples and investigate physiological properties, several important experimental factors need to be addressed. Therefore, effects on the *stratum corneum* morphology and lipid composition resulting from different sample preparation methods will be examined, as well as investigating the correct storage conditions to prevent sample degradation.

This work will also look to establish suitable protocols to measure known physical properties of the *stratum corneum* that are subject to variation, such as the corneocyte surface area and layer thickness. Measurement of these properties in any future cross comparative studies will ensure that the chemical analysis provided by ToF-SIMS agrees with physiologically relevant changes to the *stratum corneum.*

3.3 Results and discussion

3.3.1 Method development for ToF-SIMS chemical analysis of tape stripped *stratum corneum*

3.3.1.1 Primary ion focusing mode selection

There are two possible primary ion focusing modes commonly employed in ToF-SIMS analysis (section 1.5.8), high current-bunched (HC-BU) and burst alignment (BA). Both offer their own advantages and disadvantages. BA mode produces high resolution images (< 500 nm) but can only achieve a nominal mass resolution, whereas HC-BU mode offers a much greater mass resolution ($M/\Delta M$ = 7000 (FWHM) at *m/z* = 29) but poorer spatial resolution (> 2 µm). Figure 3.1 demonstrates the differences observed when analysis was conducted on a tape stripped sample using each mode. To ensure a direct comparison the same 500 µm × 500 µm area was analysed. The BA mode (Fig. 3.1a) offers superior spatial resolution, with the total ion image showing clearly defined boundaries for the corneocyte cells and even highlighting the uneven surface morphology. However, as demonstrated by the example CN^- peak, which is a generic marker for organic material, the mass resolution is poor and ultimately would not prove sufficient for chemical characterisation of the *stratum corneum*. The presence of many different components, all with very similar structures, would make peak identification with this mode impossible. In contrast, the mass resolution produced by the HC-BU mode (Fig. 3.1b) is excellent, demonstrated by the narrow peak width. In addition this mode produces a much higher total ion count, which is vital for the detection of native compounds that may be present at lower concentrations. The spatial resolution of the HC-BU mode (Fig. 3.1b) is visibly poorer than the BA mode (Fig. 3.1a). However, the distribution of the tissue on the adhesive tape is still well defined, in both the total and CN^- ion images. Therefore, it was decided that the HC-BU mode alone would be sufficient for the characterisation of native tape stripped skin and therefore the rest of the data shown in this study has been analysed using this mode.

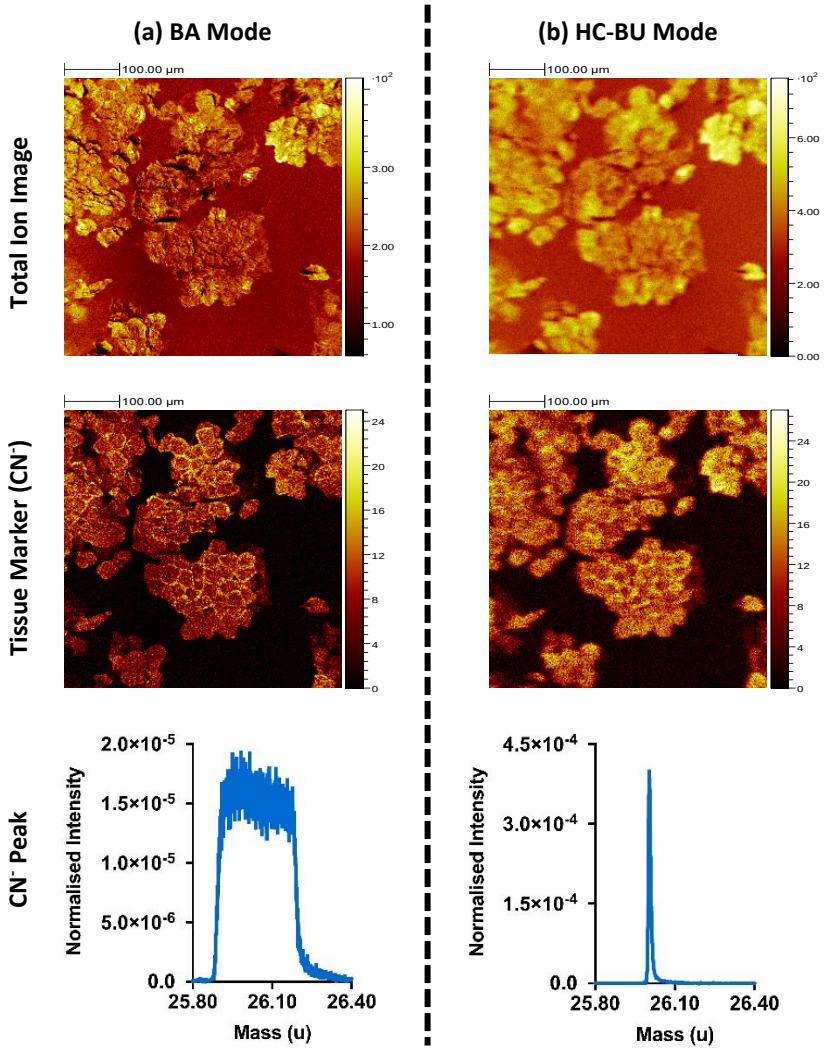

Figure 3.1 ToF-SIMS secondary ion images and spectra of a tape stripped sample analysed in (a) burst alignment (BA) mode and (b) high current bunched (HC-BU) mode.

3.3.1.2 Choice of primary ion beam

Argon gas cluster ion beams are a recent development in ToF-SIMS instrumentation. As described in section 1.5.3, their large cluster size is favourable as it reduces the impact energy per atom, resulting in less sample damage and reduced fragmentation. Several groups have therefore demonstrated the advantage of using this type of beam for surface analysis of biological samples, in order to detect intact structures for higher mass species, such as proteins and lipids [177-179]. An initial comparison was therefore made between the commonly used Bi_3^+ beam and an Ar_{1000}^+ primary ion beam for the analysis of a tape stripped sample. The same 4 mm × 4 mm area was analysed using both beams in negative and positive polarity. Visual

comparison of the spectra was then conducted, which interestingly did not show any significant differences, with no additional or absent peaks present for either beam. This is illustrated by the example negative spectra shown in Figure 3.2, but this was also true for the positive polarity data (Fig. A-1). One theoretical advantage of the large cluster size provided by the Ar_{1000}^+ beam is a reduction in fragmentation and therefore this beam was expected to produce more peaks in the higher mass region of the spectra. However, like the spectrum produced by the Bi_3^+ beam (Fig. 3.2a) the Ar_{1000}^+ spectrum (Fig. 3.2b) was also dominated by peaks at *m/z* < 200 and there was no significant increase in the intensity of higher mass ions or any new peaks produced at *m/z* > 500.

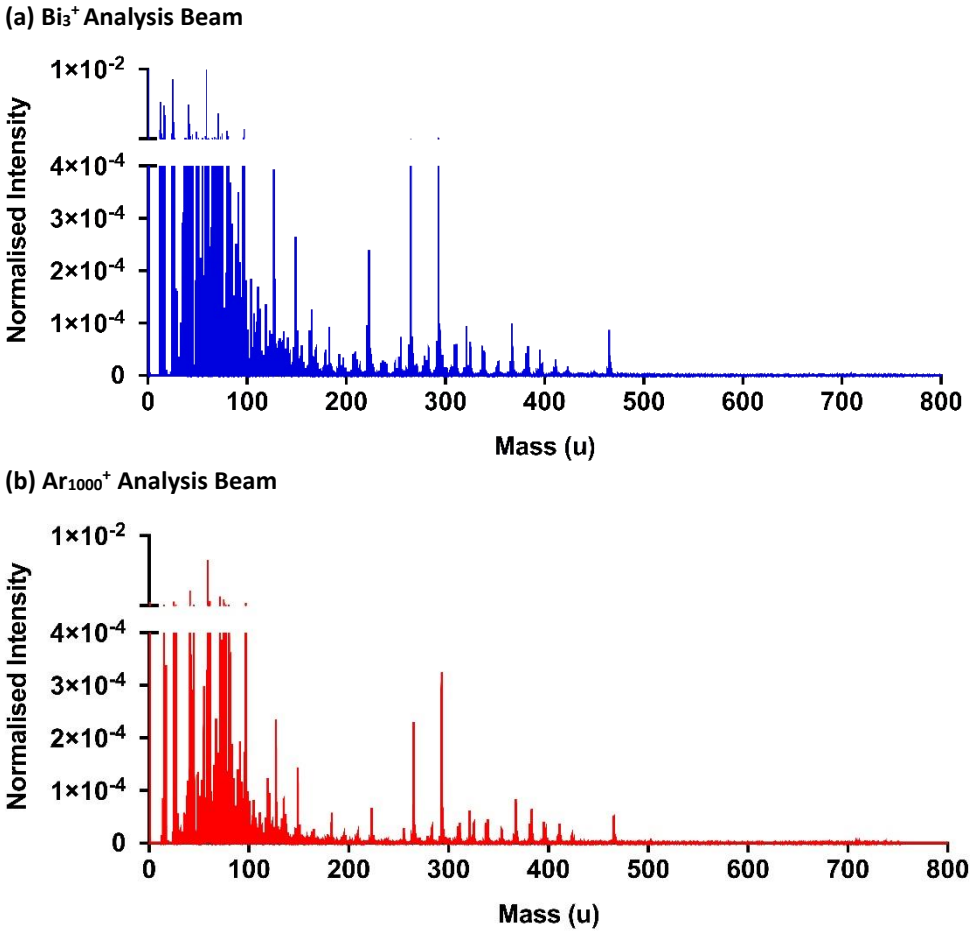

Figure 3.2 ToF-SIMS negative spectra of a tape stripped sample analysed using (a) a Bi_3^+ analysis beam and (b) an Ar_{1000}^+ analysis beam.

The main differences between the two beams were observed in both the total ion count and the mass and spatial resolution. As illustrated in Figure 3.3b, the Ar_{1000}^+ analysis beam produced a significantly poorer mass and spatial resolution data set compared to the Bi_3^+ analysis beam (Fig. 3.3a). The total ion count of the spectra was also reduced and hence the individual peak intensity was lower.

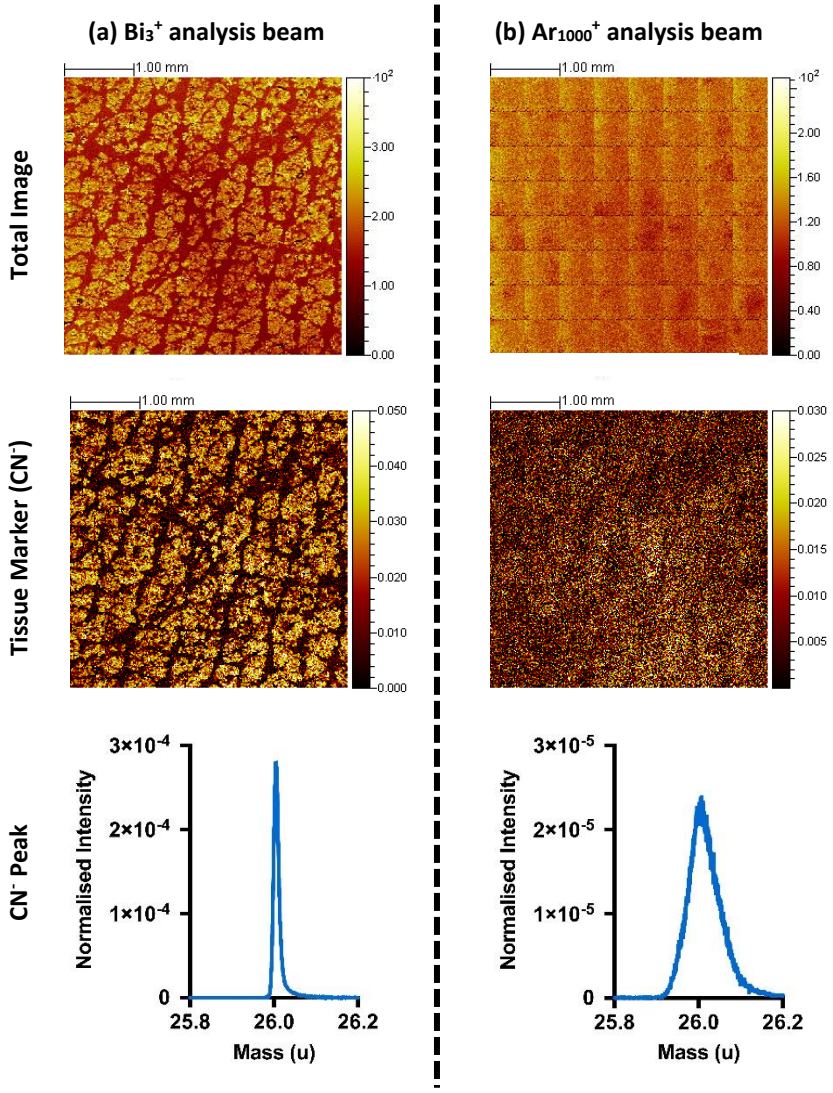

Figure 3.3 ToF-SIMS secondary ion images and spectra of a tape stripped sample analysed using both (a) a Bi_3^+ analysis beam and (b) an Ar_{1000}^+ analysis beam.

Due to the larger cluster size of the Ar_{1000}^+ beam in comparison to the Bi_3^+ beam, the focused diameter of the Ar_{1000}^+ beam is evidently larger, typically ~ 10 µm [228] compared to the 1-2 µm diameter achievable for Bi_3^+. This partly

explains the poorer spatial resolution observed for the Ar_{1000}^+ beam in Figure 3.3. However, the furrows in the skin appear larger than 10 µm, therefore the larger Ar_{1000}^+ beam diameter does not fully account for the observed lack of skin structure in the secondary ion images (Fig. 3.3b). It is possible that the spatial resolution could be improved through further optimisation of several parameters. Yet as there were no significant improvements in the spectral data it was decided that, for these samples, the Bi_3^+ beam provided the most useful information.

3.3.1.3 Data processing to improve spectral quality

Unlike traditional chromatographic analysis, ToF-SIMS has the ability to both simultaneously analyse ions from multicomponent systems and map the spatial distribution of specific ions across a sample surface. Both these capabilities offer advantages for the analysis of tape stripped *stratum corneum*.

Tape stripped samples typically consist of a non-confluent layer of cornecoytes, as the removal of these cells relies heavily on the morphology of the skin and can be hindered by hair follicles or skin furrows. Therefore, a sample may contain areas consisting of only adhesive tape material, contributing to the presence of unwanted peaks in the overall ToF-SIMS spectrum. However, by mapping the distribution of ions indicative of both organic tissue and adhesive material, ToF-SIMS is able to elucidate the areas on the sample where no tissue is present. Example ToF-SIMS secondary ion images of a tape stripped sample are illustrated in Figure 3.4, which show both the total ion image and distribution maps for tissue (CN^-/Na^+) and adhesive tape ($C_2H_3O_2^-/C_4H_9^+$) markers in both negative (Fig. 3.4a) and positive (Fig. 3.4b) polarity.

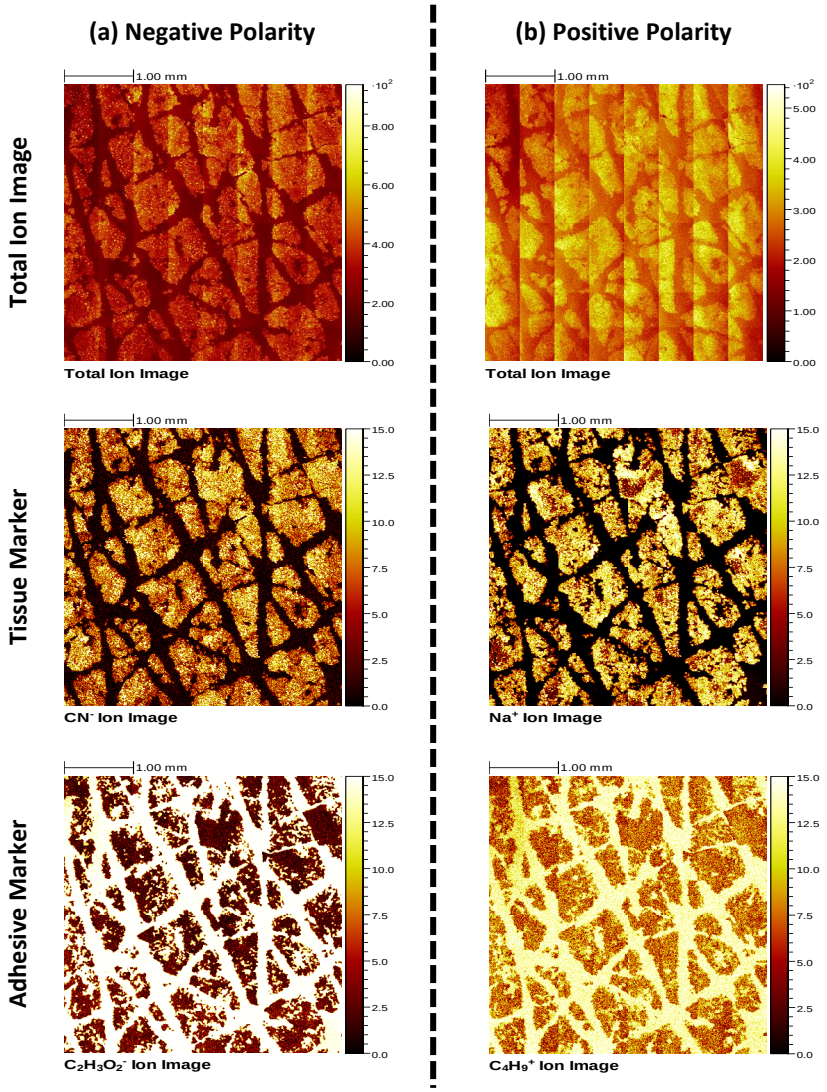

Figure 3.4 ToF-SIMS (a) negative and (b) positive secondary ion images of a tape stripped stratum corneum sample, highlighting the ability to map the spatial distribution of both tissue (CN^-/Na^+) and adhesive material ($C_2H_3O_2^-/C_4H_9^+$).

Judd *et al.* demonstrated the first use of ToF-SIMS for the analysis of tape stripped *stratum corneum* and recognised that the secondary ion images could be used to retrospectively threshold the data [83]. Figure 3.5 illustrates the stages of the thresholding process. The total ion image for the tape stripped sample (Fig. 3.5a) demonstrates that the initial spectrum consists of data from all across the sample, although the furrows in the skin can be identified due to an overall lower ion count for these areas. Figure 3.5b shows the distribution of CN^-, indicating the regions on the sample containing skin tissue. This image is then used to create a region of interest, highlighted in blue (Fig. 3.5c), which

enables thresholding of the data to exclude the contribution from ions that are present in the furrows. The post-threshold total ion image (Fig. 3.5d) demonstrates that ions relating to the adhesive only regions have been predominately removed from the overall data set. The effect of the thresholding process on the spectra is illustrated in Figure 3.5e, which highlights a significant decrease in peaks relating to adhesive material and an increase in organic tissue related peaks.

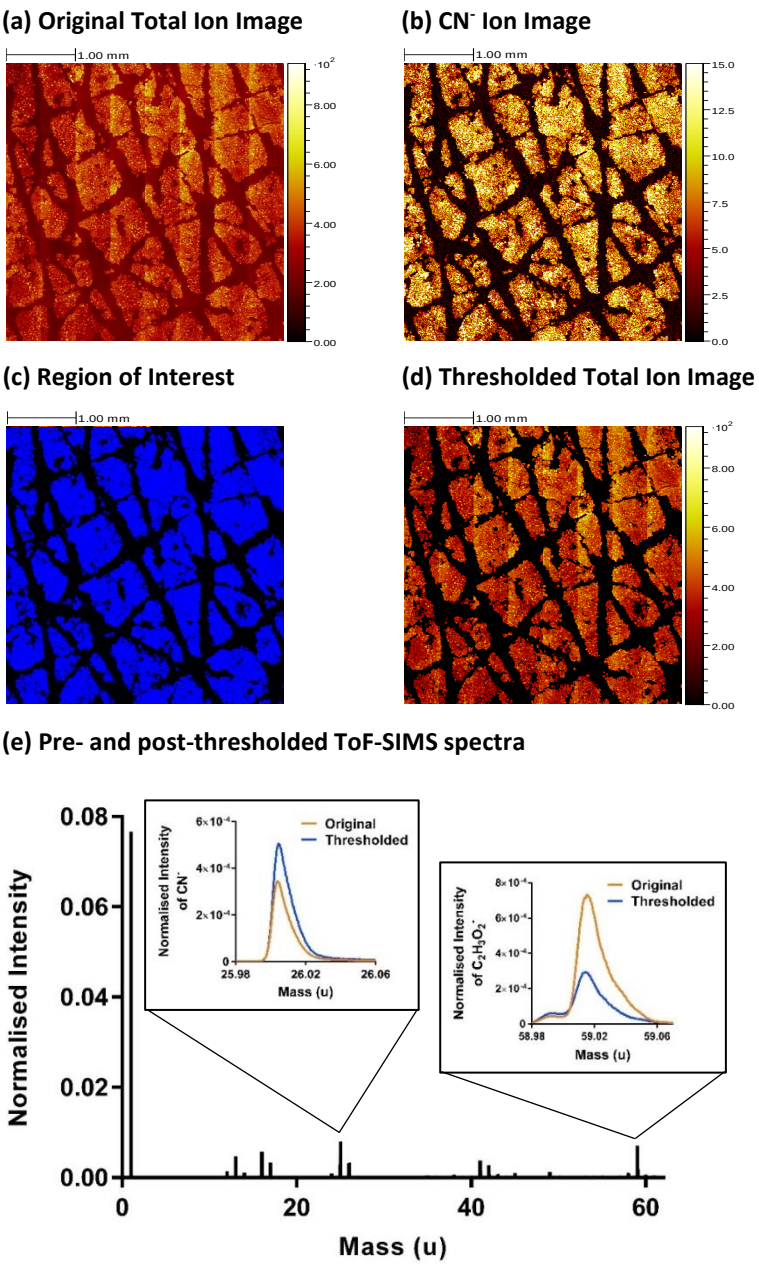

Figure 3.5 ToF-SIMS data for an example tape stripped sample showing the thresholding process (a – d) secondary ion images illustrating the removal of ions from adhesive only regions and (e) spectra showing the intensity reduction in adhesive related peaks and subsequent enhancement in tissue related peaks.

The tape strip analysis conducted by Judd *et al.* employed an analysis region between 100-500 µm^2. This size area was adequate to achieve their main aim, which was to produce a semi-quantitative depth profile for chlorhexidine permeation [83]. However, to fully utilise the spatial information that can be gained from ToF-SIMS and examine the distribution of both native and

topically applied compounds, a larger analysis area is more appropriate. For this study an analysis area of 4 mm × 4 mm was therefore chosen, which produces a more representative image of the skin surface, incorporating features such as furrows and potentially hair follicles. Once thresholded, this area can then be retrospectively sectioned into four smaller 2 mm × 2 mm areas, illustrated in Figure 3.6a. This process enables repeat data sets to be collected whilst still maintaining a large enough analysis area to examine the spatial distribution of compounds across the surface. In addition, the heterogeneous nature of biological tissue results in a variation in morphology across the sample surface. Therefore, dividing the 4 mm × 4 mm area into four smaller 2 mm × 2 mm areas also improves the mass resolution, as demonstrated by the reduced peak width in Figure 3.6b.

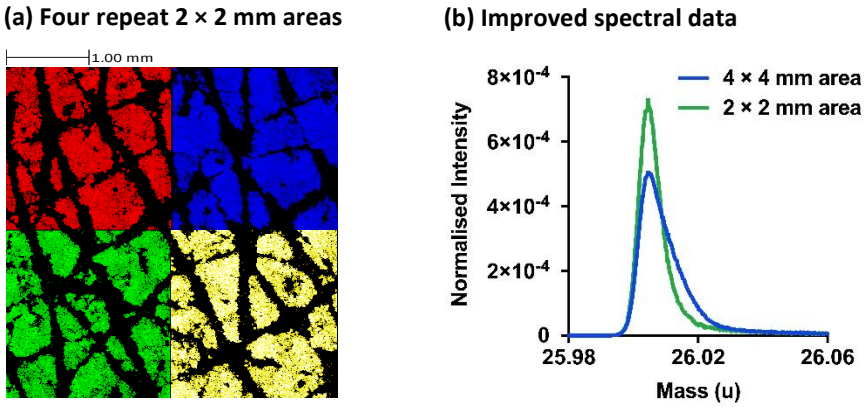

Figure 3.6 ToF-SIMS retrospective data processing (a) secondary ion images demonstrating the creation of four 2 mm × 2 mm analysis regions and (b) spectra highlighting the consequent improvement in mass resolution.

3.3.1.4 Detection of stratum corneum lipids

Although several groups have used ToF-SIMS to examine the presence of biomolecules in skin tissue sections [162,166,229,230], no one has yet attempted detailed analysis of native *stratum corneum* from tape stripped samples. Therefore, preliminary analysis was conducted to determine if it was feasible to gain relevant information on the *stratum corneum* lipid composition from individual tape stripped layers. As the ToF-SIMS analyser collects positive and negative ions separately, it was also important to determine if one polarity

was more favourable for lipid analysis. Figure 3.7a and b show example ToF-SIMS spectra for negative and positive polarity respectively, illustrating that in both cases the spectra are dominated by high intensity peaks within the 0-100 *m/z* region, which corresponds to small, generic ions common in biological sample analysis, such as CN^-, CNO^-, SO_4H^-, Na^+, $C_4H_9O^+$ etc.

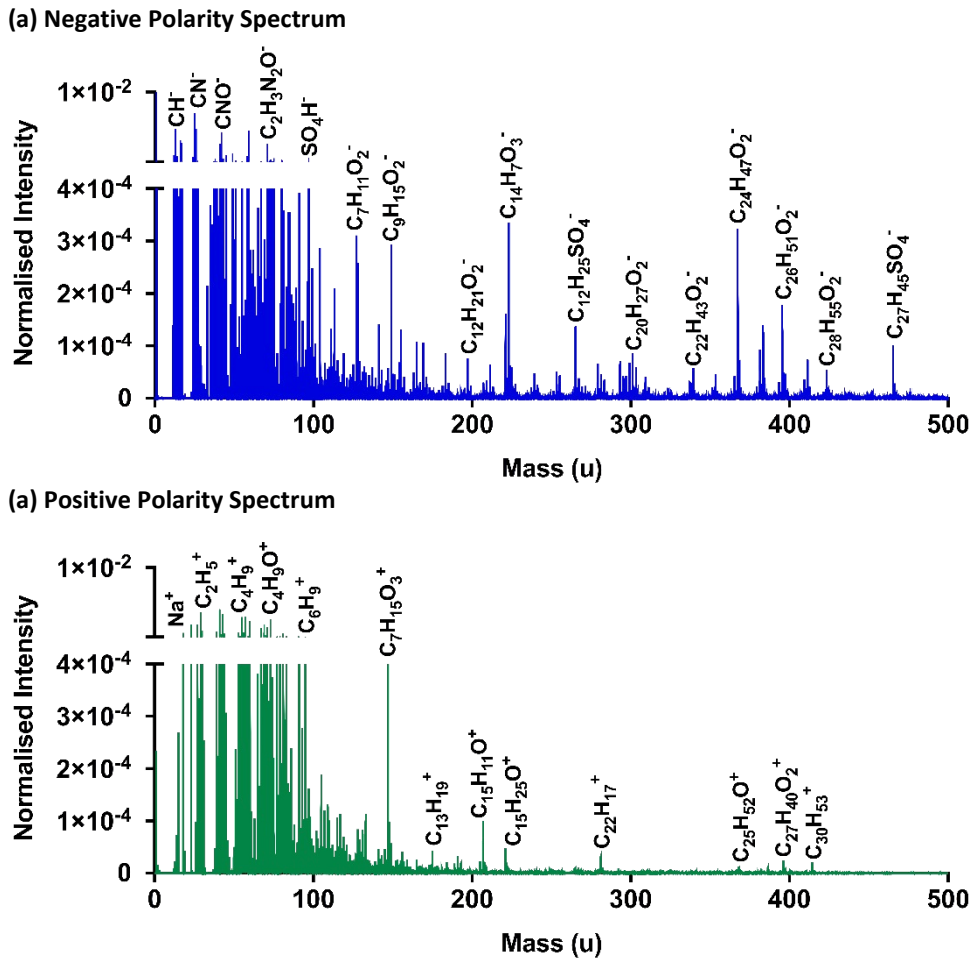

Figure 3.7 ToF-SIMS spectral data for a tape stripped stratum corneum sample in both (a) negative and (b) positive polarity.

Owing to the wide range of compounds present in the *stratum corneum* and their similarity in structure, these low mass, high intensity ions cannot be uniquely attributed to a given lipid species. The more important peaks for characterisation of this tissue are therefore those with a higher *m/z* value, which are more diagnostic of intact structures. A comparison of the negative

and positive spectra shows that the negative polarity contains more of these higher mass ions at significant intensities.

The three primary species present in the *stratum corneum*, ceramides, free fatty acids and cholesterol are all based around a similar backbone structure, consisting mainly of long carbon chains ending in carboxyl or alcohol groups. It is therefore not surprising that both the negative and positive mass spectra are dominated by fragments with the general formula $C_xH_yO_z$, as illustrated in Figure 3.7. Both polarity spectra contain similar fragmented structures, yet the intensities for these fragments are significantly higher in the negative spectra. This is expected due to the favourable loss of a hydrogen to form carboxylate and alkoxide ions.

The similarity in lipid structure makes it difficult to uniquely assign even some of the higher mass ions, as the fragmentation process can cause the production of identical ions from multiple species. However, some intact structures were detected, particularly in the negative polarity, where fragments with the formula $C_nH_{2n-1}O_2^-$ correspond to the $[M-H]^-$ ions of fatty acid species. Ceramides, which are formed from sphingolipids and fatty acids are much larger species and as there are no significant peaks at $m/z > 500$ present in the spectra, these lipids are likely to be fragmented into their precursor compounds. A recent study by Sjövall *et al.* demonstrated the localisation of ceramide compounds in the *stratum corneum* of mouse skin [229]. The predominant ceramide ions detected were fragments in the positive spectra, but they also demonstrated the presence of low intensity intact molecular ions. However, this analysis was conducted on *ex vivo* tissue slices and hence the whole *stratum corneum* layer was available for analysis. It may be therefore that the ceramide concentration available for analysis of intact molecular species is too low from a single stripped *stratum corneum* layer.

Unusually, despite being acknowledged in the field as a "mass spectrometry-friendly lipid species" [231] and numerous publications demonstrating its detection from a range of tissue types using ToF-SIMS [199-203,205,229], no distinctive cholesterol peak was detected. This lipid produces a characteristic fragment pattern in the positive polarity, illustrated in Figure 3.8a, with

significant peaks at *m/z* = 369 and 385 relating to the $[M\text{-}OH]^+$ and $[M\text{-}H]^+$ ions respectively.

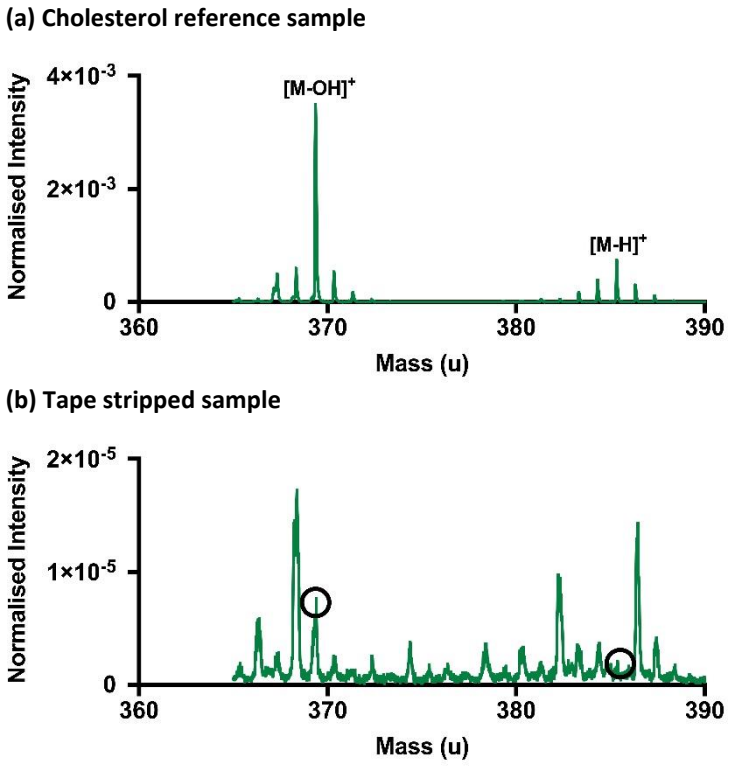

Figure 3.8 ToF-SIMS spectra comparing the presence of characteristic cholesterol peaks in the positive polarity for (a) a cholesterol reference sample, highlighting the $[M\text{-}OH]^+$ and $[M\text{-}H]^+$ peaks and (b) a tape stripped stratum corneum sample demonstrating the apparent absence of these peaks possibly due to cholesterol migration effects.

Although there was a peak present at *m/z* = 369 in the tape stripped samples, it did not match the pattern or peak ratio produced in the reference spectrum and there was no peak visible at *m/z* = 385, as demonstrated in Figure 3.8b. The absence of this lipid, which is one of the three main species present in the *stratum corneum* cannot be reasonably explained. Previous work by Sjövall *et al.* [199] demonstrated the migration of cholesterol to the surface of mouse brain tissue under vacuum conditions at ambient temperature. Although these samples were significantly different to tape stripped *stratum corneum*, both in tissue structure and thickness, it does indicate unusual behaviour under vacuum for this lipid in biological tissue. Another explanation may be the result of the matrix effect, which has been described in detail in section 1.5.6. There are currently no other studies that have combined ToF-SIMS with tape

strip analysis to study the lipid composition of the *stratum corneum*. Therefore, effects on the ionisation of this lipid species in this specific environment cannot be ruled out. It is also possible that the distinctive cholesterol peaks have been obscured by other fragments with similar structures. However, typically this would affect the ratio between the cholesterol peaks or alter the characteristic pattern, not cause an absence in the peak, as observed for the $[M-H]^+$ ion. In order to elucidate the reason for this absence in cholesterol, a more detailed study of these samples would be required, however, this is outside the scope of this project.

Overall, this preliminary analysis produced unprecedented data, which demonstrated that ToF-SIMS could successfully detect ions relating to native *stratum corneum* lipid species detected from human samples collected *in vivo.* Importantly, this could be achieved from individual tape stripped samples, enabling analysis as a function of *stratum corneum* depth and demonstrating the excellent sensitivity of the technique.

Another important advantage of ToF-SIMS is the ability to map the spatial distribution of ions of interest. Recent studies have demonstrated the use of both ToF-SIMS [229,230] and matrix assisted laser desorption ionisation mass spectrometry (MALDI-MS) [158] to study the distribution of lipids within the *stratum corneum.* However, these techniques were used to analyse *ex vivo* skin tissue. Raman spectroscopy methods have emerged as a popular technique to image the skin *in vivo* and monitor the distribution of lipid components as a function of depth [151,232,233]. However, this method cannot match the specificity offered by mass spectrometry and therefore cannot map the specific distribution of individual lipids. The preliminary data in this study, however, has demonstrated the ability of ToF-SIMS to elucidate the distribution of native compounds within a single *stratum corneum* layer from samples collected *in vivo*. Example ToF-SIMS secondary ion images for both common biological fragments, such as CN^- (Fig. 3.9a) and SO_4H^- (Fig. 3.9b) and intact lipid structures, such as $C_{18}H_{35}O_2^-$ (Fig. 3.9c) and $C_{24}H_{47}O_2^-$ (Fig. 3.9d) demonstrate a varied spatial distribution between fragment ions. A variation in spatial distribution between ions confirms that these differences are physiologically relevant and not merely artefacts of the data. These example

images demonstrate an apparent difference even between fatty acid components, with lignoceric acid (Fig. 3.9d) exhibiting a more uniform distribution across the tissue compared to stearic acid (Fig. 3.9c). This may be associated with the fact that stearic acid is present at high levels in sebum [44,46], whereas lignoceric acid has been shown to be contained within the *stratum corneum* [229]. An in-depth examination of the spatial distribution of *stratum corneum* lipids is outside the scope of this work. However, the imaging capability of ToF-SIMS has elucidated interesting findings for both the aging study (Chapter 4) and the *in vivo* permeation work (Chapter 6).

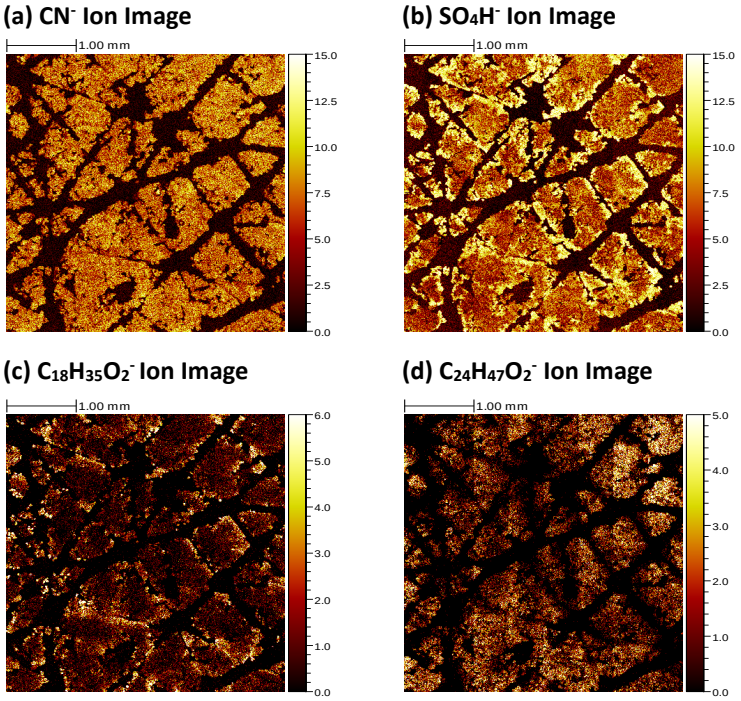

Figure 3.9 ToF-SIMS secondary ion images highlighting the varied spatial distribution for example negative ions (a) CN^-, a generic tissue marker (b) SO_4^-, a common biological fragment (c) $C_{18}H_{35}O_2^-$, C18:0 fatty acid (d) $C_{24}H_{47}O_2^-$, C24:0 fatty acid.

3.3.2 Analysis of *stratum corneum* morphology using scanning electron microscopy

Scanning electron microscopy (SEM) is an imaging technique which provides increased spatial resolution over optical microscopes. It was therefore employed throughout this project to analyse the morphology of both the *stratum corneum* layer as a whole and the individual corneocyte cells. As

discussed in section 2.3.2.1, both low and high vacuum modes can be employed and although the low vacuum mode offers analysis of biological samples in their original state, the high vacuum mode typically produces better resolution images. It was therefore important to conduct preliminary analysis of tape stripped samples using both modes, to determine which one was most suitable for studying the *stratum corneum* morphology. Figure 3.10 shows SEM images collected from the same tape stripped sample in both low (Fig. 3.10a) and high (Fig. 3.10b) vacuum mode at three different magnifications, specifically × 50, × 200 and × 800.

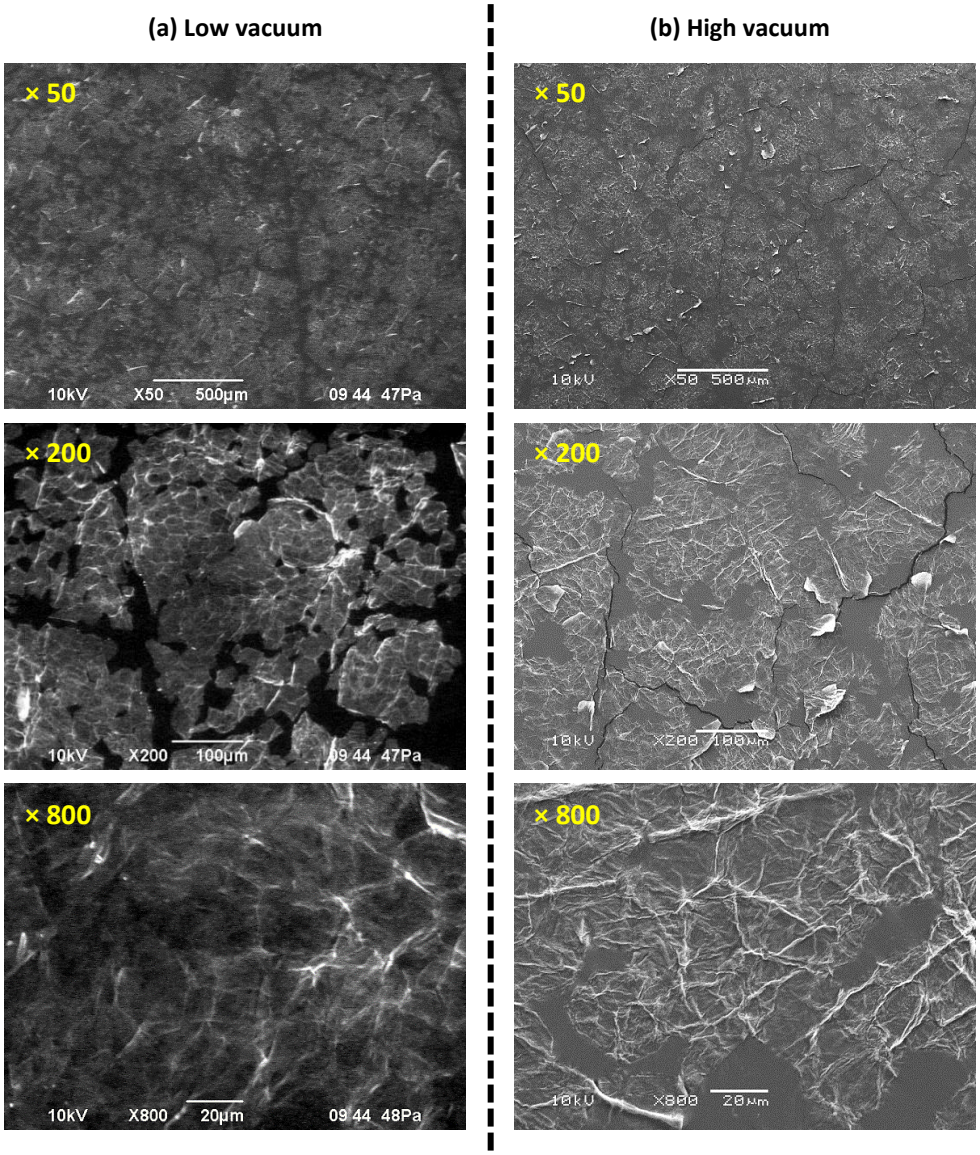

Figure 3.10 SEM images of tape stripped stratum corneum in both (a) low vacuum and (b) high vacuum mode at three different magnifications.

It is clearly apparent that, as expected, the high vacuum images offer much better resolution. Yet for the × 50 and × 200 magnifications, similar information can be gained from the low vacuum images. The × 50 images highlight the general pattern of the skin (light grey regions) on the adhesive material (dark grey regions) and indicate areas where no *stratum corneum* has been removed, due to furrows in the skin. The low vacuum × 200 image actually provides much better contrast between the skin and the adhesive, and corneocyte boundaries are also visible in parts of the image. This appears to be

due to electron charging of the sample, localised to the areas between the corneocytes. These boundaries between individual cells are harder to visualise in the high vacuum × 200 image. The higher resolution of the high vacuum mode produces a more detailed view of the individual cell morphology and at this magnification the uneven surface of the cells are obstructing the visibility of the cell boundaries. However, for the × 800 images the difference between the two modes is significantly different. Both the individual cell surface morphology and cell boundaries are clearly defined in the high vacuum image. Whereas, the low vacuum image loses the contrast observed for the × 200 image, with no individual cell morphology visible and indistinct cell boundaries. Therefore, the high vacuum mode proved to be the most useful to observe both the overall morphology of the tape stripped samples and the surface morphology of individual corneocytes. This mode was therefore employed for the rest of the SEM analysis conducted.

3.3.3 Investigating the physical and chemical effects of sample preparation

ToF-SIMS is a high vacuum technique, causing dehydration of the sample prior to analysis. Therefore, samples typically undergo some form of dehydration process before being placed into the instrument. Two types of dehydration method were therefore evaluated to establish whether either proved favourable in regards to both physical and chemical effects on the tape stripped *stratum corneum* samples. The use of a freeze dryer and vacuum oven were tested and compared to a 'control' sample which underwent no prior sample preparation. Both SEM and ToF-SIMS were used to analyse the physical and chemical effects respectively. However, as both techniques require the samples to be analysed under vacuum, a typical before and after comparison could not be made. Therefore, to try and minimise any variability caused by differences in the initial samples rather than the preparation method, one tape stripped sample was cut into thirds and each section was subjected to a different method prior to analysis.

3.3.3.1 Analysis of structural changes in stratum corneum morphology using SEM

The surface morphology of the samples was assessed by conducting SEM analysis using the high vacuum mode settings. Images were collected at both × 50 (Fig. 3.11a) and × 800 (Fig. 3.11b) magnification in order to assess both the surface coverage and the individual corneocyte morphology. Comparison of the × 800 images illustrates that there is no significant difference in the surface structure of the individual corneocyte cells between the three samples. However, comparison of the × 50 images highlights a significantly decreased surface coverage for the freeze dried sample. The cause of this is unlikely to be the dehydration process itself, but instead the method of first plunge freezing the sample in liquid nitrogen. This process results in a temporary contraction of the tape, which might result in the loss of corneocytes from the adhesive strip. This loss of skin material is also evident in the × 800 image, where absent patches are visible. Although this method appears to decrease the amount of *stratum corneum* present on the sample, it doesn't appear to affect the morphology of the corneocytes themselves.

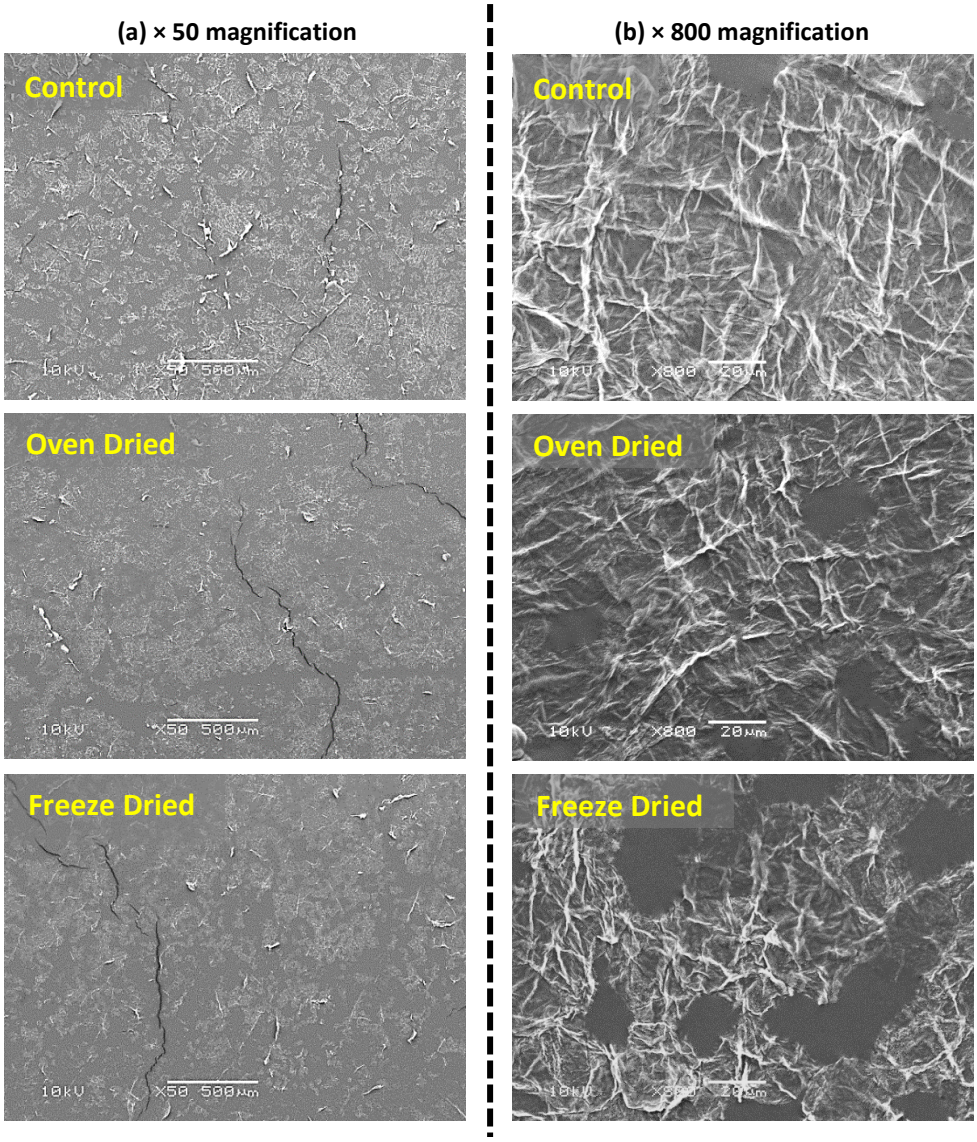

Figure 3.11 SEM images of tape stripped stratum corneum prepared using different dehydration methods at both (a) × 50 and (b) × 800 magnification.

3.3.3.2 Analysis of changes to stratum corneum lipids using ToF-SIMS

The three sample types, specifically vacuum oven dried, freeze dried and a control sample, were also subjected to ToF-SIMS analysis. Chemical differences were examined through visual comparison of the spectra, which revealed that all three samples contained similar peaks, with no new or absent peaks produced for any sample type. There was also little difference between the intensities of most peaks, with the exception of the vacuum oven dried sample, which showed differences in high intensity peaks relating to intact lipid structures. There was a noticeable reduction in peak intensity specifically

for the $[M-H]^-$ ions of some fatty acids. An example of this is illustrated by the spectra (Fig. 3.12a) and exported peak intensities (Fig. 3.12c) for the C24:0 fatty acid ($C_{24}H_{47}O_2^-$). However, the reason for this is unclear. One explanation would be a degradation of these species relating to the sample being subjected to an increased temperature of 40 °C. However, this seems unlikely given that this temperature is similar to the natural skin temperature (~ 34 °C). The vacuum oven dried sample also appeared to show an increase in the presence of other lipids, for example the molecular marker for cholesterol sulfate ($C_{25}H_{47}SO_4^-$), as highlighted by the spectra and exported peak intensities shown in Figure 3.12b and d respectively. Interestingly, the freeze dried sample appears to show a decrease in this lipid compared to the control, but again there is no rational explanation for this observation. To confirm these differences and further elucidate the reason behind them, repeat data analysis would need to be conducted, which is outside the scope of this study.

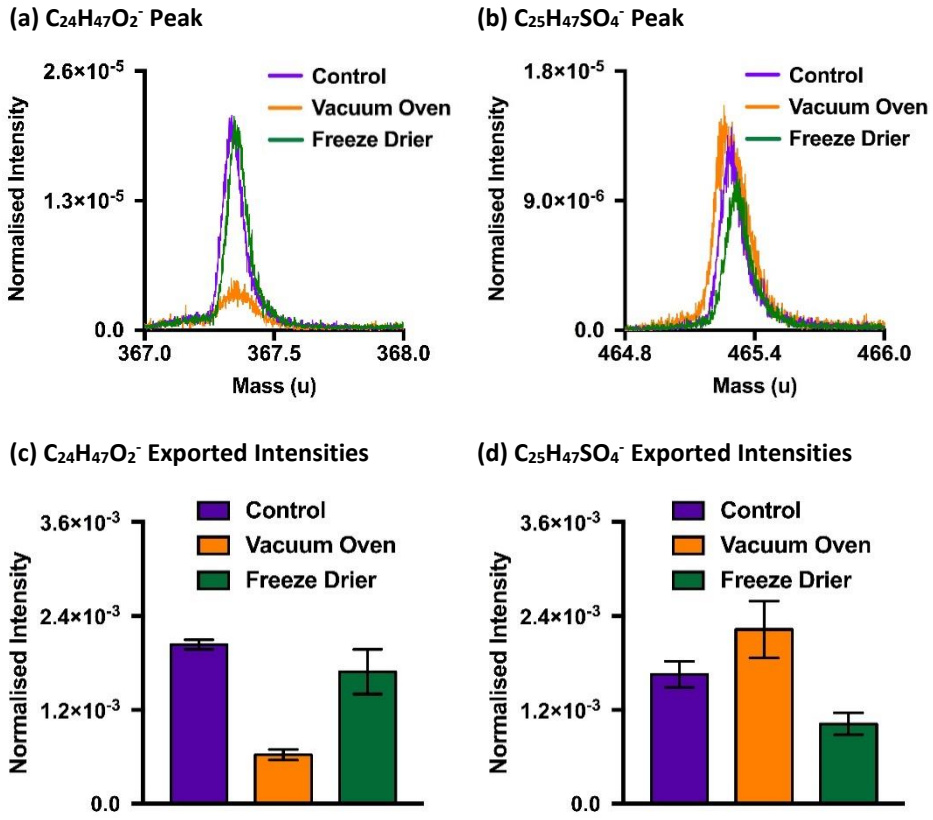

Figure 3.12 ToF-SIMS data highlighting the differences in $C_{24}H_{47}O_2^-$ and $C_{25}H_{47}SO_4^-$ for different sample preparation methods (a-b) example spectra showing peak intensities for a single data set and (c-d) exported average peak intensities for each sample type.

Overall, the SEM analysis highlighted a slight reduction in surface coverage for the freeze dried samples and the ToF-SIMS indicates an intensity difference in several lipid components, specifically for the vacuum oven dried samples. It therefore appears that direct placement into the instrument is the best sample preparation method. As these tape strips contain a minimal amount of moisture this should not negatively affect the ToF-SIMS vacuum system. Importantly, this comparative study highlights the need to keep the sample preparation method constant when cross comparing different tape stripped samples. If there is no variation in the preparation method then any differences observed between these samples can be assumed to be the result of physiologically relevant changes.

3.3.4 Assessing sample degradation over time and the effect of storage temperature

Due to the large volume of tape stripped samples collected for *in vivo* studies, it is not always possible to analyse all of the samples immediately after they are stripped. Therefore, it was important to assess the best temperature to store these samples at and evaluate whether there was any significant chemical degradation over time. Three different tape stripped samples were analysed immediately after stripping and then stored at three different temperatures, specifically at room temperature (laboratory bench), at 4 °C (refrigerator) and at -20 °C (freezer). ToF-SIMS analysis was conducted after 1, 2, 3, 4 and 6 months. For each storage temperature the samples were compared to the initial data collected immediately after stripping, referred to hereon in as month ‘0’. As each spectrum contained over 500 peaks, visual comparison for these samples was difficult. Therefore, multivariate data analysis, specifically principal component analysis (PCA), was used to highlight any differences in ion intensity between the sample types. This method is discussed in detail in section 2.6. The PCA produces scores plots, which indicate the largest variance between samples, and the variables which contribute to this variance are highlighted in the corresponding scatter loadings plots.

The data for the room temperature (RT) stored samples proved very interesting as the scores plot (Fig. 3.13a) demonstrated that the samples divided into three distinct groups, 0-1 months, 2-3 months and 4-6 months. This suggests that there is a definite change in the chemical composition of these samples over time when stored at RT. The corresponding loadings plot (Fig. 3.13b) highlights which ions are associated with each sample type and the variables furthest away from the plot origin are described as the most significant contributors to the variance. Principal component 1 highlights a split between the 4-6 month samples and the rest. As indicated by the scatter plot, this difference can be attributed to a reduction in high mass ions, highlighted by the *m/z* values labelled in Figure 3.13b, which relate to intact lipid structures including fatty acid components. The exported spectra for example ions $C_{16}H_{31}O_2^-$ (*m/z* = 255) and $C_{24}H_{47}O_2^-$ (*m/z* = 367) for the 0 and 6 month samples can be observed in Figure 3.12c and d respectively, confirming a visible difference in the peak intensities. This data therefore indicates sample degradation over time at RT, which suggests long term storage is not ideal at this temperature.

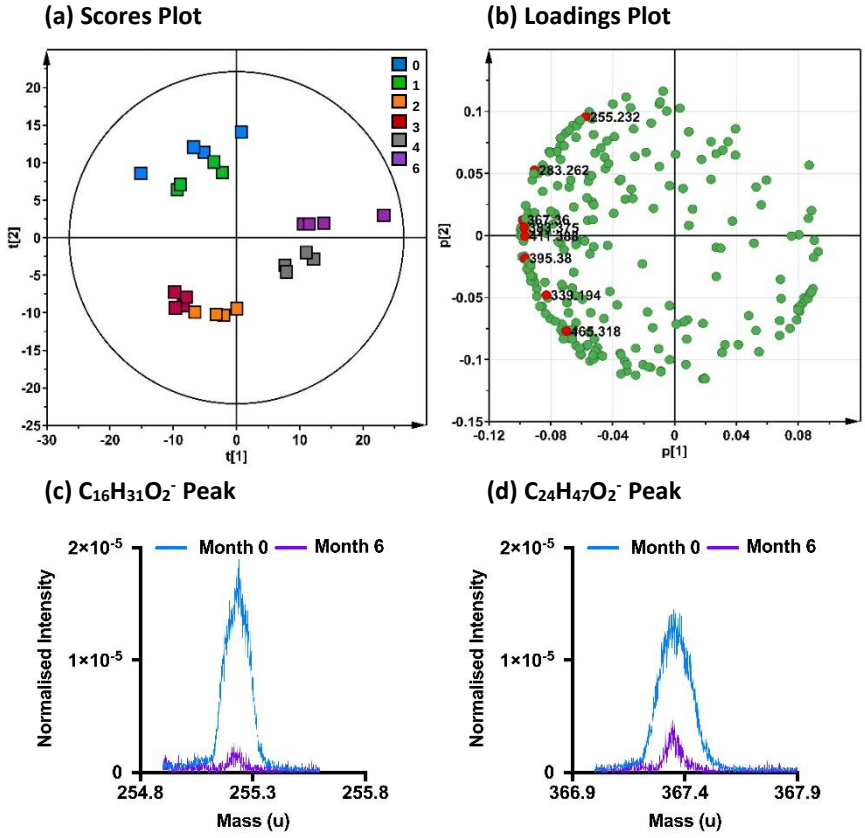

Figure 3.13 PCA results for a RT stored tape stripped sample showing (a) the scores plot (b) the scatter loadings plot with significant variables labelled (c-d) spectra highlighting the decrease in peak intensity observed for the 6 month time point compared to the original sample for $C_{16}H_{31}O_2^-$ and $C_{24}H_{47}O_2^-$.

In contrast, the data obtained for the samples stored at 4 °C, specifically the scores plot illustrated in Figure 3.14a, shows no significant difference between the sample types. This suggests that long term storage of the samples at a lower temperature eliminates the degradation observed for the RT conditions.

Interestingly, the -20 °C storage temperature, which was expected to keep the samples stable for the longest, shows a split along principal component 1 for the 0-1 month samples, highlighted in Figure 3.14b. However, on examination of the loadings plot (Fig. 3.14c) it appears that this split is largely due to a difference in low mass ions, labelled in Figure 3.14c, which relate to common, generic fragments. The fact that these are at a higher level in the initial 0-1 month samples therefore does not point to degradation. Instead this variance is likely to be caused by the presence of an increased level of surface

contaminants on the 0-1 month samples. Both the loadings plot (Fig. 3.14c) and spectra also show some differences in ions relating to fatty acid components, but only those with a chain length of 18 and less. Figure 3.14d shows spectra relating to the C16:0 fatty acid peak ($C_{16}H_{31}O_2^-$) which highlights a higher intensity for this lipid in the original sample compared to the 6 month time point. However, shorter chain fatty acids are known to be common environmental contaminants in mass spectrometry [234] and therefore these differences could again be due to external contamination rather than variation in the native samples. To confirm and elucidate the nature of these differences further exploration and repeat sample analysis would be needed, but this is outside the scope of this project.

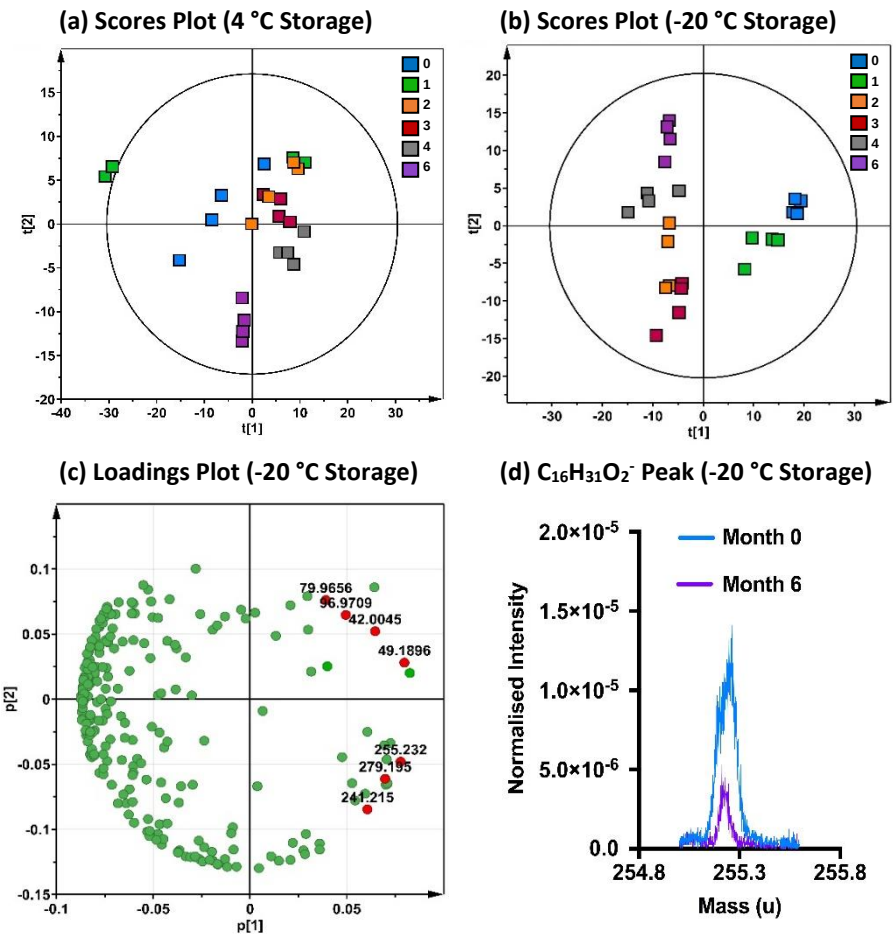

Figure 3.14 PCA results for the 4 °C and -20 °C stored tape stripped samples (a) the scores plot for the 4 °C stored sample (b) the scores plot for the -20 °C stored sample (c) the scatter loadings plot for the -20 °C stored sample, with significant variables labelled (d) spectra highlighting the decrease in $C_{16}H_{31}O_2^-$ peak intensity observed for the -20 °C stored 6 month time point compared to the original sample.

Overall, the samples stored at RT appeared to show a clear degradation of lipid components over the 6 month period. However, there were no apparent differences observed for high mass, intact lipid components for the fridge or freezer samples, which confirms that either of these conditions are suitable for long term storage of these samples.

3.3.5 Investigating the depth of *stratum corneum* removed per tape strip

The measured thickness of a corneocyte layer has been shown to vary considerably between studies, and there is also conflicting data reporting the

total *stratum corneum* thickness and number of layers present (section 1.2.1). This variation is likely to be a combination of influencing factors, both experimental and physiological, hence the depth of *stratum corneum* removed by sequential stripping is an unknown entity that has to be measured. Two different techniques, optical profilometry and atomic force microscopy (AFM), were therefore employed to try and attain an accurate depth measurement for a tape stripped *stratum corneum* layer.

3.3.5.1 Depth measurements acquired using an optical profilometer

A single tape stripped sample was analysed using the optical profilometer. The magnification chosen enabled the visualisation of individual corneocytes whilst still providing a large enough area to obtain a representative measurement. Several different areas on the sample were scanned and example images and line profile graphs are displayed in Figure 3.15. Both the 3D (Fig. 3.15a) and 2D (Fig. 3.15b) morphology of the sample can be examined using this technique and the depth calculations are obtained retrospectively using the 2D image to define the measurement area. Initial height measurements across the sample are relative to the start and end points of the scan, as defined by the user. However, as these are somewhat arbitrary, the height value of features across the sample are not meaningful unless a reference surface is defined. For tape stripped samples, the reference surface used to define the height of the *stratum corneum* layer is therefore the underlying adhesive substrate. Example measurement parameters are displayed on the 2D image in Figure 3.15b. The two sets of orange parallel lines indicate the areas which have been defined as the ‘flat’ reference surface and the measurement area is defined by the region along the red line between the two terminal arrows. Figure 3.15c illustrates example line profile graphs taken using different measurement and reference areas on the tape stripped sample. These graphs contain the step height measurements of features on the sample relative to the underlying adhesive substrate.

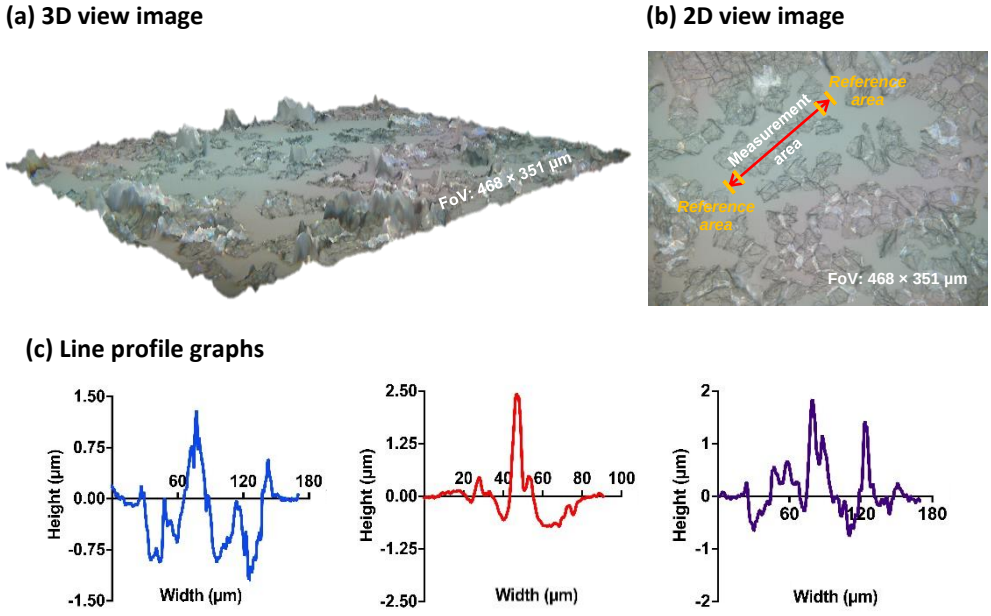

Figure 3.15 Optical profilometry data analysis of a tape stripped sample showing (a) an example 3D image (b) an example 2D image, with a representative measurement area indicated by the red line and the selected reference areas highlighted in orange and (c) example line profile graphs showing the step height values across different measurement areas.

It quickly became apparent that there were some limiting factors associated with using this technique to analyse tape stripped *stratum corneum*. As demonstrated in the examples shown in Figure 3.15c, the step height graphs contained unexpected troughs and also a significant variation in the positive step height values, both within a single measurement area and also between different regions on the sample.

There are several possible factors that may have contributed to these inconsistent surface profiles. Firstly, the underlying adhesive used as a 'flat' reference substrate may not be completely 'flat'. Adhesive material is designed to be flexible and the process of peeling the tape strip away from the skin will ultimately disrupt the uniformity of the surface. Secondly, the method of applying pressure to the tape strip before removal may have caused the corneocytes to become partially embedded into the adhesive material. These two issues may therefore be contributing to both the negative values observed and the significant variation in positive step height values across the sample.

The positive step height values recorded ranged from as little as 0.2 µm to over 3 µm, which is triple the maximum measured thickness of a corneocyte layer (section 1.2.1). One explanation for these larger values may be that the tape stripping process is removing multiple layers with a single strip. However, it would be expected that this would cause a general increase in depth values across the whole sample, which is not evident. Visual observation of both the 2D and 3D images highlights corneocytes which are not fully adhered and are protruding from the surface. Therefore a non-uniformity in corneocyte flatness may be a more likely explanation for both the excessive step height values observed and the significant variation across the sample. Given this variation, it was decided that this method was not suitable to measure the depth of *stratum corneum*.

3.3.5.2 Depth measurements acquired using atomic force microscopy

Atomic force microscopy (AFM) was also used to take step height measurements between the underlying adhesive substrate and the corneocyte layer. However, these measurements differed from the ones calculated with the optical profilometer, as AFM relies on physical contact between the tip and the surface to obtain the measurement. Line profile scans were taken across an area that contained equal amounts of both the corneocyte layer and the adhesive material, as shown in Figure 3.16b. The step height measurement was then calculated by taking the difference between the highest point on the corneocyte and a point on the adhesive material, as illustrated in Figure 3.16a. AFM has the potential to provide a more accurate reading than the optical profilometer as the actual height of the substrate is being accounted for through contact with the AFM tip, rather than the use of a projected ‘flat’ reference surface.

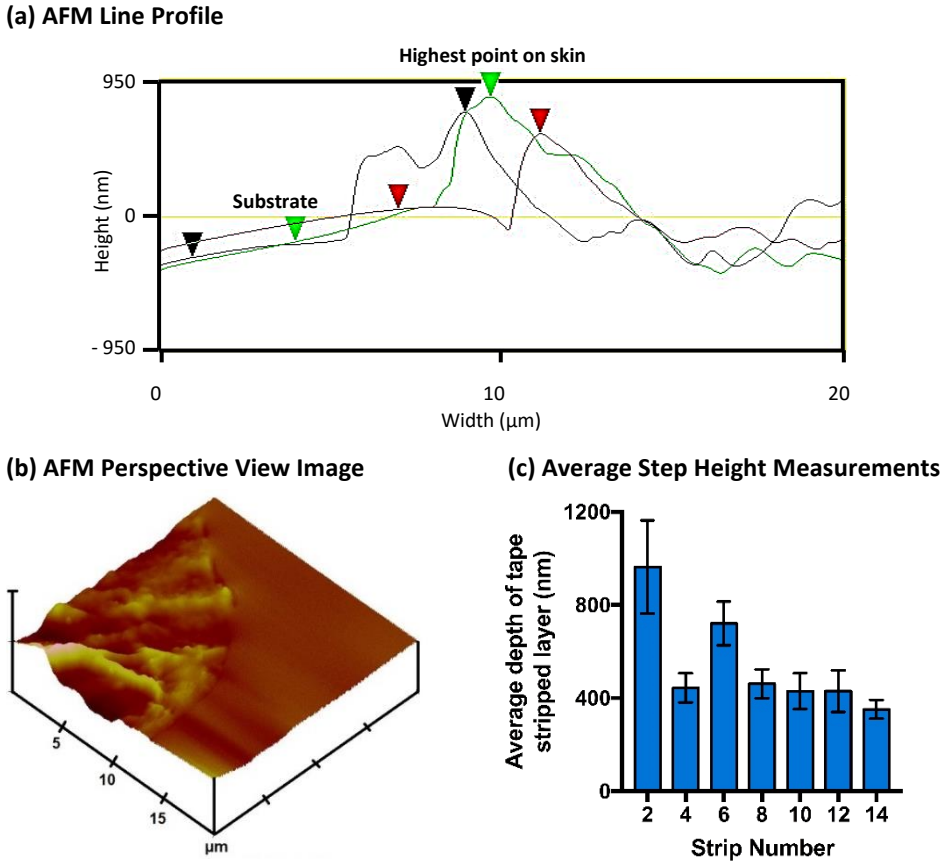

Figure 3.16 AFM data for tape stripped stratum corneum (a) an example line profile graph indicating the height of the corneocyte layer (b) an example perspective view image incorporating areas of both tissue and adhesive material and (c) average step height measurements for each alternate strip 2-14 for one volunteer.

Analysis was conducted on alternate strips 2-14 taken from the arm of one volunteer and 9 repeat measurements were acquired per sample. The average height measured per strip was ~500 nm, illustrated in Figure 3.16c, which is within the range of measurements produced by other studies [4,13-15] (section 1.2.1). However, a recent study by Fredonnet *et al.* [14] also demonstrated AFM analysis of individual tape stripped samples, producing an average height value of ~ 900 nm across all tape strip numbers. The thickness values produced in this study of ~500 nm are therefore significantly lower using the same measurement technique. However, this may indicate partial embedding of the corneocytes into the adhesive layer, as previously suggested, resulting from the pressure applied before strip removal. In addition, the study conducted by Fredonnet *et al.* [14] used an alternative type of tape for the

stripping process and the pressure applied before removal was not stated, parameters which have both shown to be influential on the depth of *stratum corneum* removed (section 1.2.3.4). Therefore, differences in experimental parameters may have resulted in a variation in measured corneocyte thickness. As the pressure disc applicator used in this study ensures that a constant pressure is applied to all samples, it can be assumed that the amount of *stratum corneum* embedded in the adhesive is consistent. Therefore, although this technique may not be able to provide an absolute value for the thickness of a removed *stratum corneum* layer, it does have the potential to assess any changes in the depth of *stratum corneum* associated with differences in volunteer parameters.

3.4 Conclusions

This work has demonstrated the first use of ToF-SIMS to detect lipid components from tape stripped human *stratum corneum*. Intact structures relating to several fatty acid species and cholesterol sulfate could be easily identified, although no intact ceramides were detected, due to proposed fragmentation of these larger species. An unexpected absence of cholesterol was observed, despite numerous studies demonstrating the detection of this molecule in other biological tissues using ToF-SIMS. The reason for this absence is unknown, although previous research has demonstrated an unpredictability in the behaviour of this molecule under vacuum conditions.

The imaging capabilities of the technique proved advantageous over typically used chromatographic methods, enabling effortless separation of sample regions relating to tissue and adhesive tape and highlighting differences in the spatial distribution of several chemical components within the tissue. Although the use of argon GCIBs are proposed to reduce fragmentation and therefore elucidate larger intact structures, this was not observed for analysis of a tape stripped sample and the liquid metal ion gun (LMIG) Bi_3^+ primary ion source demonstrated enhanced mass and spatial resolution. As expected the BA focusing mode produced higher resolution images than the HC-BU mode. However, the HC-BU mode provided superior mass resolution, crucial for deconvolution of the complex spectra created by the abundance of similarly structured lipid species.

SEM and ToF-SIMS analysis demonstrated a difference in the morphology and chemical composition of the samples respectively, relating to different sample preparation methods. The cause of this variation needs further investigation, but does highlight the need to keep the preparation method constant when conducting a comparative study. ToF-SIMS analysis also highlighted the degradation of samples kept at room temperature within a six month time period, which was prevented by the storage of samples at ≤ 4 °C.

SEM proved to be a suitable technique to study the morphology of both the *stratum corneum* layer and the individual corneocytes. Optical profilometry was unable to provide meaningful thickness measurements for a tape stripped

sample. However, AFM did succeed in providing consistent values that were within the range of previously reported corneocyte thicknesses. The measured values, however, were still significantly different from those previously reported using AFM analysis. The proposed reason for this is a variation in the experimental parameters used and a possible partial embedding of the corneocytes into the adhesive tape. This emphasises the inconsistencies encountered in measuring corneocyte properties, resulting in the variations observed between different studies. It therefore highlights the importance of conducting an internal assessment of these properties when cross comparing tape stripped samples.

Chapter 4: Age-related changes to human *stratum corneum* collected *in vivo*

4.1 Introduction

4.1.1 Skin aging pathways

Research into aging skin is becoming increasingly popular, a consequence of both an aging population and an increased awareness of UV damage. The skin aging process occurs through two pathways, intrinsic and extrinsic, both of which produce phenotypic changes to the skin [235]. Intrinsic, or chronological aging, is a consequence of the inevitable degenerative process the body undergoes over time. Extrinsic aging, however, becomes apparent in people from a much younger age and is determined by environmental factors, such as lifestyle, diet and exposure to cigarette smoke, pollution, and UV radiation [235]. Prolonged UV exposure is the main extrinsic aging factor and has been shown to cause significant damage to skin DNA (photodamage), which can ultimately lead to skin cancer [236,237]. Clinical manifestations of skin aging are well documented, including wrinkles, xerosis, cutaneous infection, mottled and hyperpigmentation and loss of cutaneous structure, resulting in sagging of the skin [235,238]. However, research is still ongoing to try and determine the mechanisms behind these clinical outcomes. Due to the complex nature of the *stratum corneum* and its known involvement in numerous protective roles (section 1.2.2), aging effects on this structure have been highly investigated.

4.1.2 Age-related changes to the *stratum corneum*

A large proportion of the research surrounding the effects of aging on human *stratum corneum* have focused on changes to physical parameters, such as trans-epidermal water loss (TEWL) [145,239-243], surface pH [239,240,244,245], levels of sebum production [239,240,244,246,247] and skin hydration [145,239,240,244]. These parameters are easy to measure *in vivo* and indicate a disruption to the barrier properties of the *stratum corneum.*

Aging effects on corneocyte morphology have also been extensively studied. In particular, corneocyte surface area has been shown to both increase and decrease as a result of intrinsic and extrinsic aging respectively [4-6,10,12,248,249]. The increased corneocyte size associated with aged skin is believed to be a consequence of a decrease in proliferative activity in the epidermis [250-253]. This is proposed to reduce the number of corneocyte cells present in a layer, resulting in an increase in corneocyte size to maintain surface coverage. It has also been demonstrated that UV radiation causes an increase in epidermal proliferation, which further supports the theory behind an observed aging variation in corneocyte size [254,255].

Reported age-related changes in *stratum corneum* thickness are contradictory between different studies. Both Boireau-Adamezyk *et al.* [145] and Tagami *et al.* [248] report an increase in thickness related to intrinsic aging by conducting *in vivo* measurements using confocal Raman microspectroscopy and Raman spectroscopy respectively. Whereas, Lock-Andersen *et al.* [256] used light microscopy on skin biopsies to demonstrate no age-related change in *stratum corneum* thickness. With respect to extrinsic aging, several groups have demonstrated a decreased *stratum corneum* thickness *in vivo* relating to body locations with a proposed higher UV exposure [145,248,257], yet Pearse *et al.* show an increase in thickness following *in vivo* irradiation with both UVA and UVB [258].

In order to elucidate the fundamental mechanisms relating to skin aging, changes to the chemical composition of the *stratum corneum* need to be investigated. Due to both the complex nature of this layer and the problems associated with extracting chemical information *in vivo*, age-related changes to human lipid composition are less documented and present variation between reported results. The majority of research focuses on a change in ceramide content. Both Jungersted *et al.* [259] and Imokawa *et al.* [58] used the cyanoacrylate method to remove human *stratum corneum* and conducted analysis using thin-layer chromatography. Yet while Jungersted *et al.* noted no significant change in any of the individual ceramide classes, Imokawa *et al.* reported a significant

decrease in total ceramide content with age. Denda *et al.* [128] used solvent extraction coupled with thin-layer chromatography to reveal both an age-related increase and decrease in individual ceramide subclasses, but only for female volunteers. This study highlighted the significant influence of age-related female hormones on the presence of sphingolipids in the *stratum corneum*. Rogers *et al.* [46] used thin-layer chromatography to report an age-related decrease in all three major lipid classes, but this analysis was conducted using pooled tape stripped samples. Similarly, Boireau-Adamezyk *et al.* [145] reported a decrease in total ceramide and cholesterol content related to intrinsic aging, using *in vivo* confocal Raman microspectroscopy.

There is also limited information regarding the effect of environmental exposure on *stratum corneum* lipids. Bak *et al.* [260] demonstrated a significant decrease in murine *stratum corneum* ceramide content following long-term UV exposure, and Boireau-Adamezyk *et al.* [145] reported a decrease in cholesterol levels when comparing an exposed arm site to a protected one. Despite its proposed importance in desquamation, only one group to date has focused on a change in cholesterol sulfate levels with age. Haratake *et al.* [261] conducted thin-layer chromatographic analysis of extracted lipids from murine *stratum corneum* to demonstrate that cholesterol sulfate and cholesterol levels were increased and decreased, respectively, in aged mice.

Despite the presence of a lipid gradient within the *stratum corneum* [47] there is limited research assessing both lipid composition in general and age-related changes as a function of *stratum corneum* depth. Typical *stratum corneum* sampling methods, such as surface extraction and cyanoacrylate resin, sample the *stratum corneum* as a whole, and until recently instrument sensitivity required sequential tape strips to be pooled. Both Egawa and Tagami [146] and Boireau-Adamezyk *et al.* [145] have recently demonstrated the ability to record measurements at varying depths within the *stratum corneum in vivo* using Raman spectroscopy techniques, at depths of 2 and 4 μm apart, respectively. However, this technique cannot provide the chemical specificity that is offered by mass spectrometry techniques.

4.2 Chapter aims

The aim of this study is to determine whether the methods developed in chapter 3 can be applied to detect age-related changes to human *stratum corneum* collected *in vivo* using tape stripping.

Samples from two different age groups, < 27 years old and post-menopausal > 60 years old, will be assessed to establish whether intrinsic aging effects can be detected. In addition, samples from the dorsal hand and flexor forearm will be analysed as areas of proposed high and low UV exposure respectively, in order to investigate extrinsic aging effects.

Both scanning electron microscopy (SEM) and atomic force microscopy (AFM) will be employed to establish whether aging effects on the morphology of the *stratum corneum* are present in these samples.

Time of flight - secondary ion mass spectrometry (ToF-SIMS) will be used to investigate age-related changes to the *stratum corneum* lipid matrix. This technique has the capability to assess changes to both the lipid composition and spatial distribution of compounds and 15 sequential strips will be collected per sample to enable analysis as a function of *stratum corneum* depth.

4.3 Results and discussion

4.3.1 Aging effects on corneocyte surface area

It is well established that both intrinsic and extrinsic aging affect corneocyte surface area, causing an increase and decrease respectively [4-6,10,12,248,249]. SEM analysis was therefore conducted to explore whether the tape stripped samples collected displayed known morphological age-related changes. Representative SEM images of each sample type are displayed in Figure 4.1, with individual corneocyte cells outlined in black. Three volunteers per age category were sampled and image analysis was performed using ImageJ, as described in section 2.3.2.2, to quantify the surface area for 6 corneocytes per sample. The average corneocyte area for each sample type is displayed in Figure 4.2.

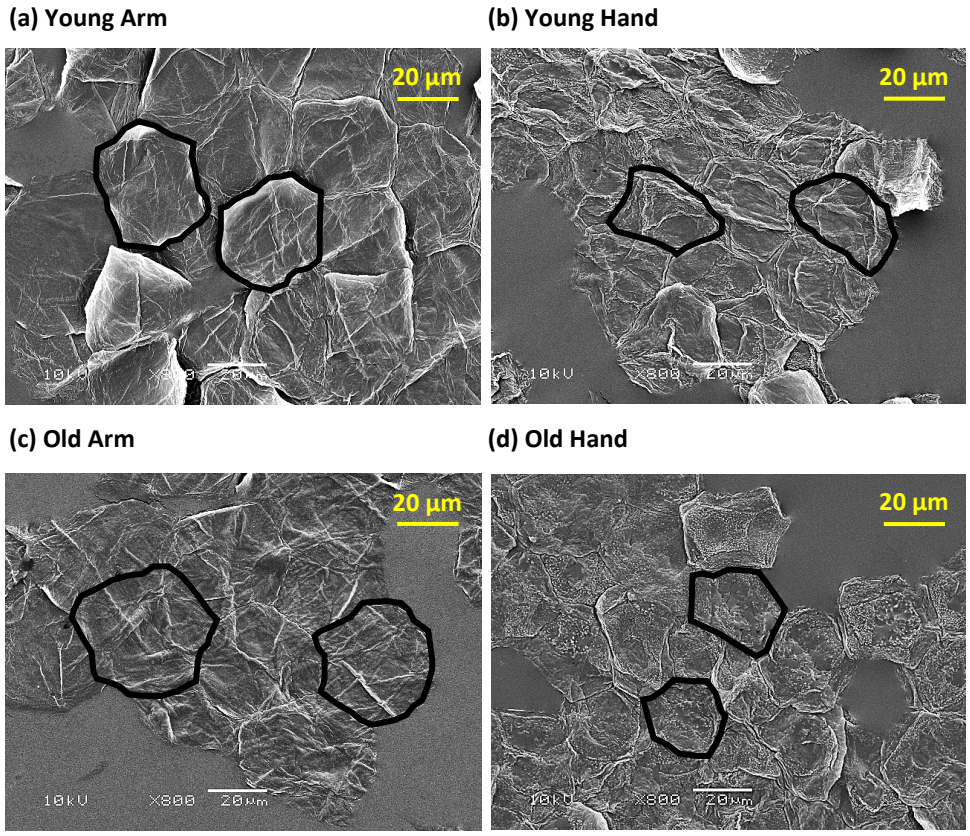

Figure 4.1 SEM images of tape stripped stratum corneum highlighting the variation in corneocyte surface area for different sample types (a) a young arm (b) a young hand (c) an old arm and (d) an old hand sample.

As discussed in section 1.2.1, there is a variation in reported corneocyte surface area measurements due to numerous factors. However, several recent studies have produced comparable values for the surface area of middle-aged human forearm corneocytes, between 900 -1000 μm^2 [4,9,13]. The surface area measurements produced in this study were therefore all within an acceptable range, confirming the suitability of the SEM method to measure this parameter. For both age categories, the hand corneocytes (Fig. 4.1b and d) show a statistically significant decrease in surface area compared to the corresponding arm samples (Fig. 4.1a and c). This demonstrates a decrease in surface area related to UV exposure. There is also a statistically significant increase in corneocyte surface area for the post-menopausal arm samples (Fig. 4.1c) compared to the < 27 year olds (Fig. 4.1a). This highlights an increase in surface area related to intrinsic aging. Interestingly, the two opposing aging effects result in no statistically significant difference between the hand samples (Fig. 4.1b and d) of the two age groups. These trends in surface area therefore agree with previously published data and demonstrate that both intrinsic and extrinsic aging can be evaluated through comparison of individual tape stripped layers. This therefore validates the use of these samples to study the chemical effects of aging using ToF-SIMS.

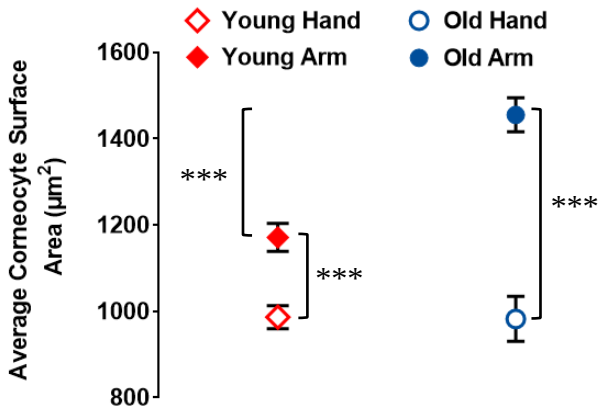

Figure 4.2 The average corneocyte surface area for each sample type calculated from SEM image analysis.

4.3.2 Aging effects on the depth of *stratum corneum* removed

Reports on age-related changes to the thickness of the *stratum corneum* are contradictory, both for intrinsic and extrinsic aging. However, in order to accurately cross compare the chemical composition as a function of depth between the two age groups, it was first important to determine whether the same depth of *stratum corneum* was being analysed. The depth of *stratum corneum* removed per tape strip has also proved to be a variable factor, impacted greatly by both experimental and physiological parameters, as discussed in section 1.2.3.4. The AFM analysis conducted in chapter 3 (section 3.3.5.2) provided consistent thickness values across a range of tape strip numbers for an example forearm sample. However, these values varied from recently reported measurements by Fredonnet *et al.* [14], despite using the same analysis technique. This therefore highlighted the need to conduct internal analysis to monitor the depth of *stratum corneum* removed when cross comparing different sample types.

Consequently, prior to chemical analysis, AFM was conducted to compare the average thickness of the corneocyte layer removed per strip for each of the four sample groups. Step height measurements were taken to quantify the thickness of the corneocyte layer protruding above the adhesive tape material. As eluded to in section 3.3.5, due to the pressure applied when collecting a tape stripped sample, it is believed that part of the removed corneocyte layer becomes embedded into the adhesive material. Therefore, it is possible that the AFM step height measurement does not provide an absolute value for the thickness of a removed *stratum corneum* layer. However, as the pressure disc applicator ensures that a constant pressure is applied to all samples, it can be assumed that the amount of *stratum corneum* embedded into the adhesive is equal across all samples. Therefore, the step height value can provide an accurate comparison of thickness between different sample types.

Figure 4.3 shows the average depth of *stratum corneum* removed for each alternate strip (strip 2-14) for every sample type. This graph illustrates a

similarity in variation between the individual strips of one sample type and between different sample groups.

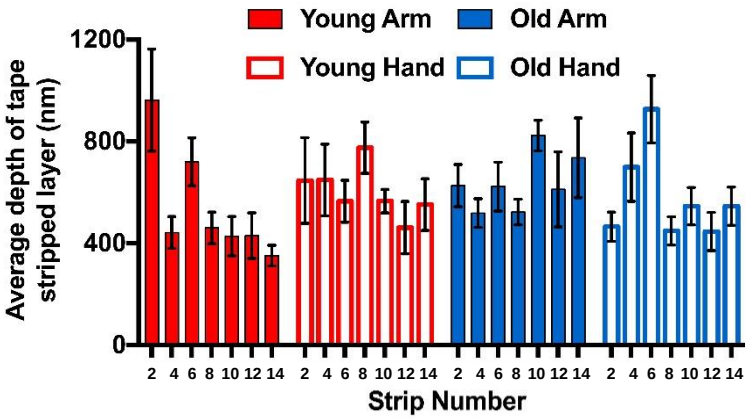

Figure 4.3 The average depth of stratum corneum removed for each alternate strip (2-14) for each sample type, calculated from AFM step height measurements.

The average depth removed per strip for each sample type is shown in Figure 4.4 and is calculated as the average across all strip numbers. This data suggests that there is no statistically significant difference in depth between any of the sample types. This disagrees with results of previous studies that have also used AFM analysis to examine aging effects on corneocyte thickness. Kashibuchi *et al.* [4] described a decrease related to both intrinsic and extrinsic aging but an increase with increasing strip number. However, Kashibuchi *et al.* used xylene to extract the corneocyte cells from the tape strip, which has been shown by Fredonnet *et al.* [14] to dramatically affect corneocyte thickness. The data published by Fredonnet *et al.* agrees with Kashibuchi *et al.* with regards to the decrease in corneocyte thickness associated with extrinsic aging, but contradicts the trend observed with increasing strip number, instead demonstrating a decrease in corneocyte thickness [14]. The measurements produced in this study therefore do not follow the trends of either of these previously published results and in addition the values produced are lower than those published by Fredonnet *et al.* [14], despite using the same technique. However, as discussed in section 3.3.5.2, it is

proposed that this may be due to differences in experimental parameters, such as the type of tape used and the pressure applied.

Importantly, identical preparation and analysis was employed in this study for all four sample types. This ensures that although the depth values may not be absolute, the method is suitable as a comparative measure. Therefore, for the samples acquired in this study it can be assumed that there is no significant difference in sampling depth between the different sample types and hence any age-related chemical differences observed can be confidently attributed to real physiological effects.

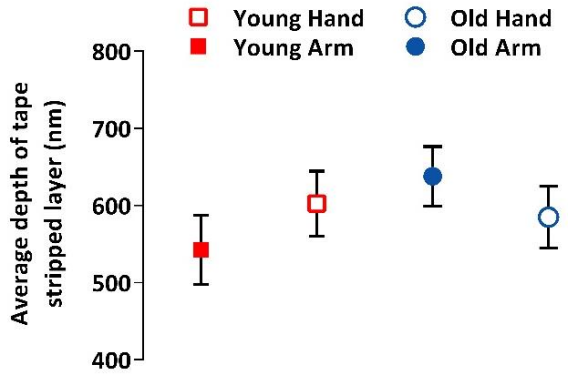

Figure 4.4 The average depth of stratum corneum removed per strip for each sample type, calculated from AFM step height measurements. No significant difference was observed between any of the sample types.

4.3.3 Age-related changes to *stratum corneum* lipids

4.3.3.1 Preliminary screening of the data

Initial ToF-SIMS analysis of native tape stripped samples, outlined in section 3.3.1.2, demonstrated that it was possible to detect lipid components of the *stratum corneum* from individual strips. However, in order to determine whether it was possible to detect changes to this lipid composition between different sample types, preliminary ToF-SIMS analysis was conducted on alternate strips 1-15 for one volunteer per age category. Figure 4.5 shows example ion intensity data from the hand samples of both volunteers,

illustrating the change in intensity as a function of tape strip number. Observed differences in ion intensities between the two volunteers demonstrates the novel application of ToF-SIMS to successfully differentiate between human skin samples collected *in vivo*. Importantly, these differences can be detected from individual tape stripped layers and therefore as a function of *stratum corneum* depth.

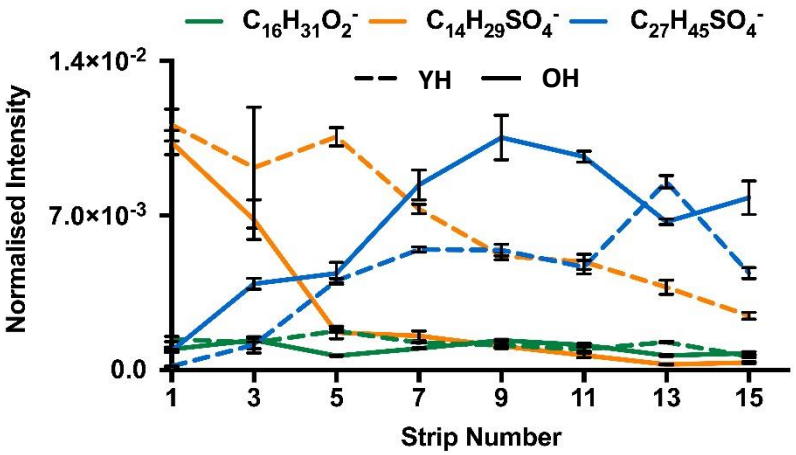

Figure 4.5 ToF-SIMS exported peak intensities as a function of increasing tape strip number for one young and one old hand sample, demonstrating varying trends with depth for three different ions $C_{16}H_{31}O_2^-$, $C_{14}H_{29}SO_4^-$ and $C_{27}H_{45}SO_4^-$.

Examination of this data also demonstrates that various trends in ion intensity can be identified as a function of *stratum corneum* depth within a single data set. Figure 4.5 illustrates example ions which display different trends with *stratum corneum* depth, specifically $C_{27}H_{45}SO_4^-$ (increases with depth), $C_{16}H_{31}O_2^-$ (remains constant) and $C_{14}H_{29}SO_4^-$ (decreases with depth). Trends in these ions were identified by manually exporting and analysing the data for both high intensity peaks and previously observed (section 3.3.1.2) high mass peaks related to intact lipid structures. The presence of conflicting trends both within a single data set and between different volunteers confirms that the differences observed are physiologically relevant and not merely experimental artefacts. In addition, the presence of varying trends in lipids as a function of *stratum corneum* depth supports the presence of a previously demonstrated

stratum corneum lipid gradient [47]. This variation with depth is discussed in more detail in section 4.3.3.7.

Due to the number of volunteers and samples collected, it was not possible within the scope and timescale of the study to conduct analysis on all 15 strips for each sample. Therefore, in order to compare the chemical composition across all volunteers, a single tape strip number was used for analysis. Due to its median position within the *stratum corneum* samples collected, tape strip 7 was chosen for cross-comparison. This ensures that the chemical composition analysed does not include lipids originating from surface sebum. The concentration of these lipids is highly variable between volunteers and largely dependent on short-term environmental factors, such as the season [46], lifestyle of the volunteer, in particular their diet [39] and most importantly age [246].

4.3.3.2 Chemical differentiation between sample types using multivariate data analysis (MVA)

Each individual tape stripped sample produced a spectrum containing > 500 ion peaks. This large number is due to both the complexity of the *stratum corneum* lipid composition and the ToF-SIMS fragmentation process. The vast number of peaks present in each spectrum prevents the employment of a visual comparison between all samples within a reasonable timescale. Therefore, differences between samples were identified using multivariate data analysis, as described in section 2.6.4.1.

Due to its unsupervised nature, principal component analysis (PCA) was used to conduct initial analysis of the data and confirm the presence of variation between the sample types. However, this was followed by detailed orthogonal partial least squares discriminant analysis (OPLSDA), as this method enhances class separation, as discussed in detail in section 2.6.1.3.

For both PCA (Fig. 4.6) and OPLSDA (Fig. 4.7) analysis, four individual comparisons were made. Extrinsic aging effects were examined through comparison of body sites for both the post-menopausal (Fig. 4.6a and Fig.

4.7a) and < 27 years volunteers (Fig. 4.6b and 4.7b). Effects of intrinsic aging were examined through comparison of both arm samples (Fig. 4.6c and 4.7c) and hand samples (Fig. 4.6d and 4.7d) between the post-menopausal and < 27 years volunteers.

As shown in Figure 4.6, the PCA score plots did show some separation between groups for all four comparisons, which confirmed that it was acceptable to use OPLSDA to enhance this separation. Caution must be taken when using supervised methods to ensure that overfitting of the data does not occur, producing false results. However, any differences observed using multivariate methods can be confirmed by revisiting and assessing the ToF-SIMS spectra.

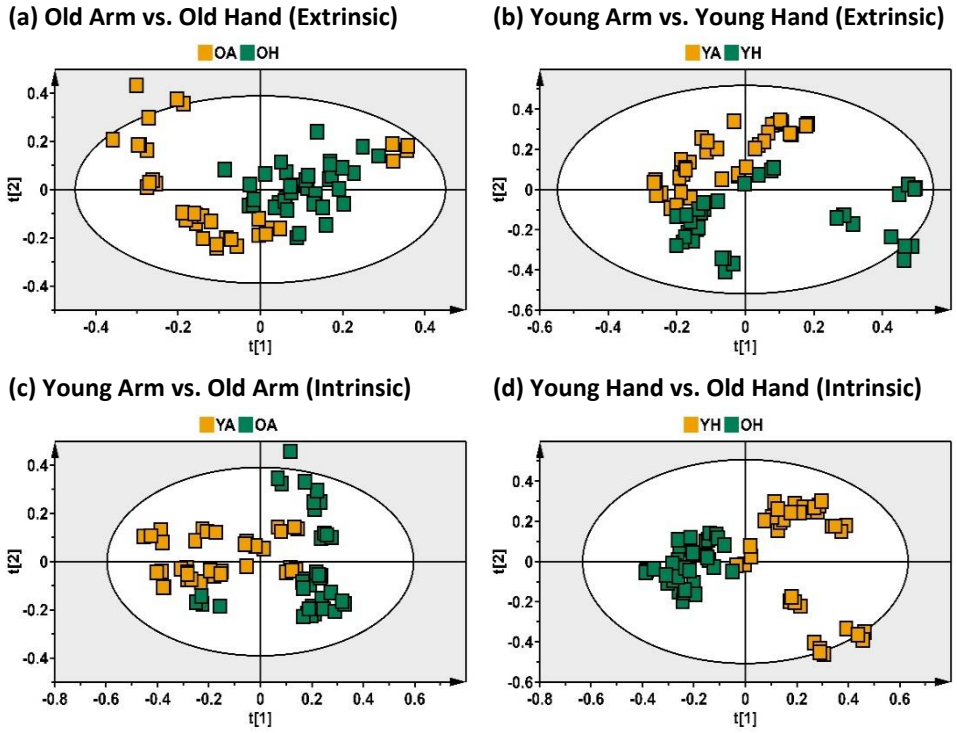

Figure 4.6 Score plots produced from PCA analysis of ToF-SIMS data, highlighting separation between sample types for all four aging comparisons.

The OPLSDA output is presented as both score plots and corresponding 'S' loadings plots, shown in Figure 4.7 on the left and right respectively. The scores plots visualise both the inter-class (x axis) and intra-class variance (y axis). The 'S' loadings plots display the variables as a function of both the magnitude of contribution to the variance (x axis) and the reliability of the ion as a biomarker (y axis). In this study a biomarker is defined as an ion that is present in one sample type at a level significantly different to another. Ions with a low reliability value, p(corr), are considered too close to the spectrum noise to be considered a reliable biomarker, with possible values between -1 and 1. For this study a p(corr) 'cut off' value of ± 0.5 was applied and so an ion was considered as a potential biomarker if it had a p(corr) value in the range $0.5 < p(corr) < -0.5$.

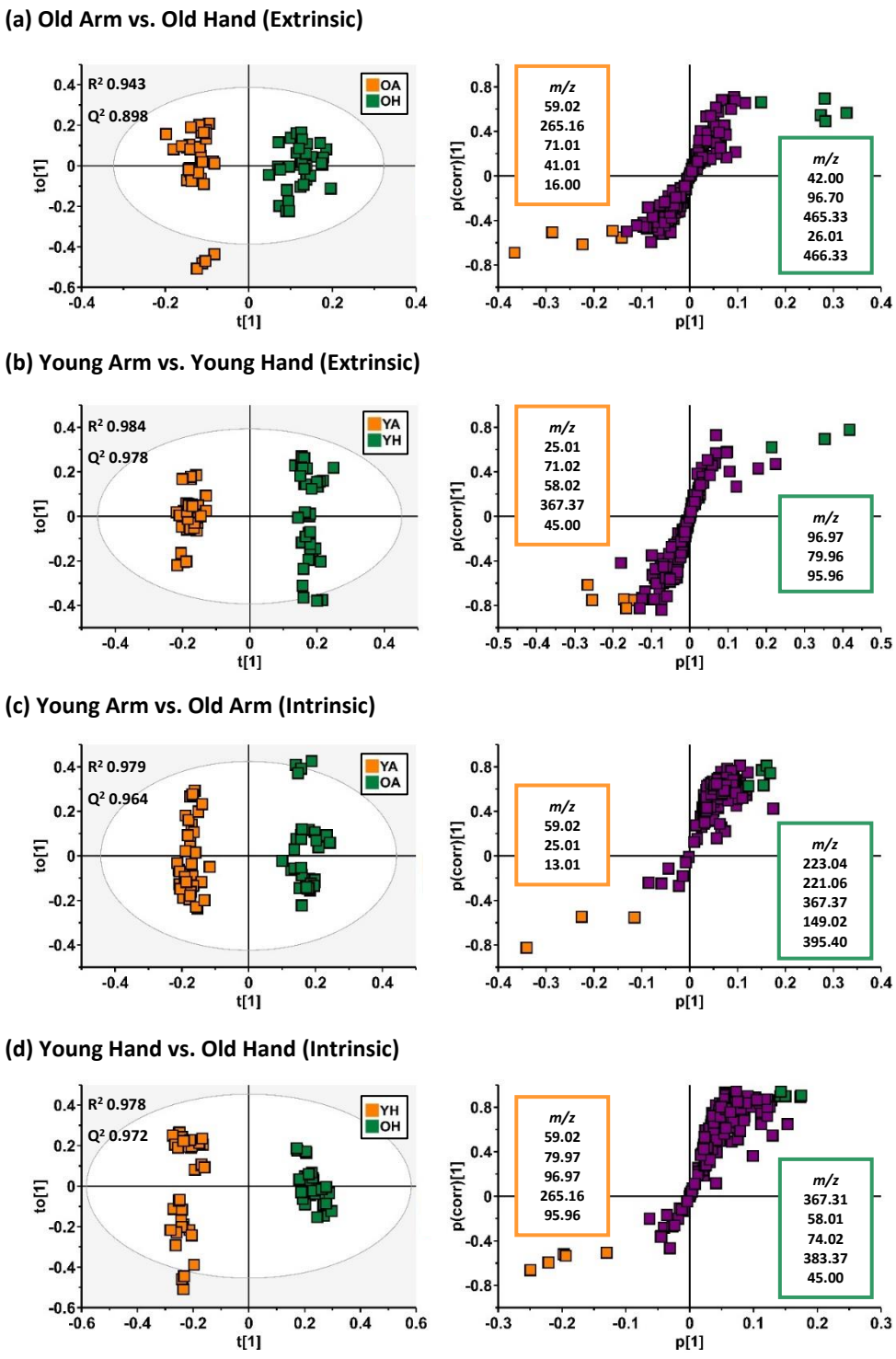

Figure 4.7 Score plots (left) and 'S' loadings plots (right) produced from OPLSDA analysis of ToF-SIMS data, showing enhanced separation between sample types for all four aging comparisons and highlighting the most significant variables that are present at higher levels in the colour coordinated sample group.

All four OPLSDA scores plots illustrated in Figure 4.7 (left) show enhanced separation between classes compared to the scores plots produced by the PCA analysis (Fig. 4.6). The OPLSDA 'S' loadings plots illustrated in Figure 4.7 (right) highlight which ions are responsible for this class separation. The variables with the highest magnitude (p[1]) and hence highest contribution to the class variance which also have a $0.5 < p(corr)[1] < -0.5$ are highlighted in the loadings plots and colour coded to demonstrate their class association.

Due to the similarity in structure of lipids present in the *stratum corneum*, the origin of many fragment ions could not be uniquely identified. Low mass ions ($m/z < 100$) can be attributed to generic common fragments, such as CN^- ($m/z = 26$) and CNO^- ($m/z = 42$) characteristic protein fragments indicative of organic material, the acetate ion $C_2H_3O_2^-$ ($m/z = 59$) which is present in both adhesive tape and biological material, and ions at $m/z = 80$ and 97, which can be attributed to popular biological fragments SO_3^-/PO_3H^- and $SO_4H^-/H_2PO_4^-$ respectively. The 'S' loadings plots shown in Figure 4.7 (right) all highlight some of these low mass ions as significant contributors to the separation between sample types observed in the scores plots. As these ions relate to generic fragments it is impossible to determine their origin. They may be fragments produced from native lipid species but they could also have originated from exogenous substances, such as surface contaminants or advantageous hydrocarbons. If these small mass ions were the only ions highlighted in the 'S' loadings plots then it could be argued that the OPLSDA analysis is merely finding a difference between sample types that purely relates to the level of contaminants. However, the 'S' loadings plots also highlight some high mass ions diagnostic of intact lipid species, which confirms that the separation observed between the different sample types is due to actual physiological differences and not merely an inconsistency in contaminants. It is therefore likely that the small mass ions are a fragmentation product of native lipid species. As the high mass ions can be uniquely related to specific lipid species they are much more informative than the lower mass ions and will therefore be the focus for the rest of this study.

4.3.3.3 Variation in cholesterol sulfate levels

Several high mass ions highlighted in the 'S' loadings plots could be attributed to lipid $[M-H]^-$ molecular markers. One ion at *m/z* = 465 was easily identified as the molecular marker for cholesterol sulfate, $C_{27}H_{45}SO_4^-$. This ion was highlighted in the 'S' loadings plot for the post-menopausal body site comparison (Fig. 4.7a) due to both a high biomarker reliability and a high contribution to class variance. However, although it wasn't highlighted as one of the highest variables for the other comparisons it did show good reliability as a biomarker for all except the < 27 years body site comparison (Fig. 4.7b). The difference in this ion between sample types was clearly apparent both from visual inspection of the normalised spectra, illustrated in Figure 4.8a, and examination of the exported peak intensities (Fig. 4.8b). Comparison of the average peak intensity for the cholesterol sulfate ion between the four sample types highlights a statistically significant difference for all aging comparisons.

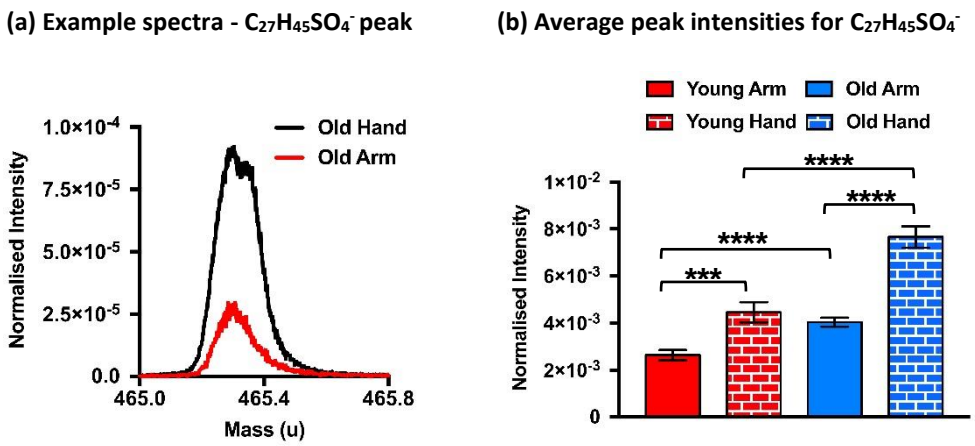

Figure 4.8 Example ToF-SIMS data for the cholesterol sulfate ion $C_{27}H_{45}SO_4^-$ present in the tape stripped samples, highlighting (a) a visible intensity change in the normalised spectra between sample types and (b) a statistically significant difference in the average exported peak intensities for all four aging comparisons.

The change in the presence of the cholesterol sulfate molecule is of particular interest because, as discussed in section 1.2.2, this molecule is present at low levels within the *stratum corneum* but has been shown to play an important

role in regulating desquamation [49]. As shown in Figure 4.8b, the intensity of cholesterol sulfate is increased in both the post-menopausal samples compared to the < 27 years samples and in the hand samples compared to the corresponding arm samples, indicating an increase in this molecule related to both intrinsic and extrinsic aging. The extrinsic aging effect is more significant in the post-menopausal volunteers compared to the < 27 years, which is proposed to be due to an accumulation effect caused by prolonged UV exposure. A change in the concentration of cholesterol sulfate due to aging has been previously demonstrated in murine skin [261] but has not yet been reported for human *stratum corneum* analysis. However, it does correlate to what is currently known about this molecule, whereby an increase in cholesterol sulfate has been associated with diseases, such as recessive X-linked ichthyosis, that cause heightened desquamation, producing symptoms of scaly and peeling skin [63]. These are both symptoms observed in skin which is suffering from xerosis, a commonly observed clinical manifestation of aging skin (section 4.1.1) and skin which has suffered prolonged UV exposure.

As mentioned previously, it is important to remember that two different body sites are being compared, therefore inherent differences in the *stratum corneum* lipid composition due to body location cannot be completely excluded. However, if the differences in cholesterol sulfate observed were solely an effect of body site and not UV exposure, then a similar variance between the sites would be expected for both age groups. However, the difference in cholesterol sulfate levels between the two body sites is much greater for the post-menopausal volunteers, indicating an accumulative effect caused by prolonged UV exposure over time.

4.3.3.4 Variation in fatty acids levels

Multivariate data analysis also highlighted ions that could be attributed to the $[M\text{-}H]^-$ molecular markers of fatty acids. Ions at *m/z* = 367 and 395 correspond to the saturated fatty acids, lignoceric acid (C24:0) and hexacosanoic acid

(C26:0) respectively. These peaks are not highlighted as the highest contributors to class variance in all of the 'S' loadings plots. However, they both exhibit good reliability as a biomarker for all classes and the exported average peak intensities (Fig. 4.9) show a statistically significant difference for all four aging comparisons.

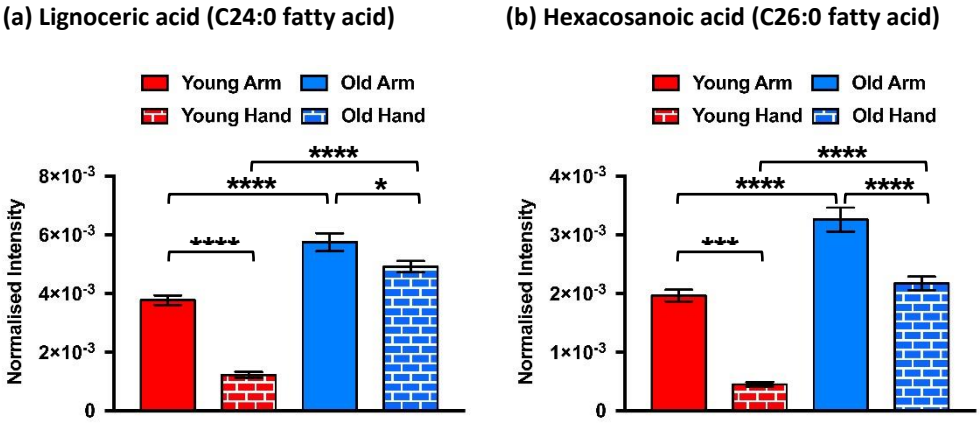

Figure 4.9 Exported ToF-SIMS data showing the average peak intensities for each sample type for (a) lignoceric acid and (b) hexacosanoic acid.

The endogenous fatty acid fraction of the *stratum corneum* has been characterized by Norlén *et al.* as "a stable population with low interindividual variation, dominated by saturated lignoceric and hexacosanoic acid" [44]. In addition, Sjövall *et al.* [229] recently reported that these two fatty acids were the most abundant in mouse *stratum corneum*, using ToF-SIMS, and demonstrated a localisation of these compounds within the *stratum corneum* layer. It is therefore not surprising that these two fatty acids, above others, show variance between the different classes. Interestingly, these lipids show opposite trends for intrinsic and extrinsic aging. An increase in intensity is observed for the post-menopausal samples in comparison to the corresponding < 27 years samples, suggesting an increase in these two fatty acids related to intrinsic aging. This appears to contradict data previously published by Rogers *et al.* [46], which suggests a decrease in all major lipid classes with age. However, the study by Rogers *et al.* [46] only included fatty acids up to a

maximum chain length of 24 and closer inspection of the data highlights that lignoceric acid (C24:0) did show elevated levels in the aged volunteers. This therefore correlates with the intrinsic aging increase in lignoceric acid observed in this study. However, there appears to be no other study which has examined intrinsic aging effects on the levels of *stratum corneum* fatty acids. By monitoring the spatial distribution of these fatty acid compounds (C24:0 and C26:0) in mouse *stratum corneum* using ToF-SIMS, Sjövall *et al.* [229] demonstrated co-localisation of these ions with both sphingosine base fragments, d17:1 and d18:1, and also ceramide molecular ions resulting from the combination of these sphingosine bases with the C24:0 and C26:0 fatty acids. Sjövall *et al.* therefore proposed that the abundance of these two fatty acids may actually relate to the levels of ceramides present in the *stratum corneum* and not the free fatty acid component. If this was the case for the samples in this study, then an increase in the presence of these two ions would disagree with typically reported decreases in ceramide content relating to intrinsic aging [46,58,145].

These two fatty acids appear to show the opposite trend for extrinsic aging. A decrease in intensity is observed in the hand samples compared to the corresponding arm samples for both age groups, indicating a decrease in these fatty acids relating to UV exposure and photoaging effects. As discussed in section 4.1.2, there are few reported studies which investigate the effect of extrinsic aging on *stratum corneum* lipids. Research into the effects of extrinsic aging on *stratum corneum* fatty acid levels has not been previously reported and therefore this finding is believed to be unprecedented. However, it does correlates with work published by Kim *et al.* [262], which describes a decrease in total fatty acid content in human epidermis relating to both acute UV exposure and long term photoaging effects.

4.3.3.5 Variation in the spatial distribution of cholesterol sulfate

ToF-SIMS has proven capable of detecting subtle changes in native lipid levels between different sample types. However, in addition to the excellent sensitivity provided by the technique, it also has the ability to map the spatial distribution of specific ions of interest. As demonstrated in chapter 3 (section 3.3.1.4), ToF-SIMS can therefore be used to investigate the distribution of lipid species within an individual *stratum corneum* layer. By mapping the spatial distribution for ions highlighted by the previous multivariate analysis, a significant age-related localisation in the spatial distribution of cholesterol sulfate was revealed.

Representative secondary ion images for each sample group illustrating the spatial distribution of cholesterol sulfate ($C_{27}H_{45}SO_4^-$), lignoceric acid ($C_{24}H_{47}O_2^-$) and hexacosanoic acid ($C_{26}H_{51}O_2^-$) are shown in Figure 4.10b, c and d respectively. The distribution of a generic tissue marker, CN^-, is also shown (Fig. 4.10a) and all images for a particular ion are displayed on the same intensity scale. A comparison of image intensity visually confirms the age-related differences in lipid levels observed between sample groups in the spectral data. However, the more important observation is that age-related variations in the spatial distribution can be detected for specific lipids. This is information that cannot be gained from the spectral data alone, which highlights one advantage of using ToF-SIMS over typically used chromatographic methods for tape strip analysis.

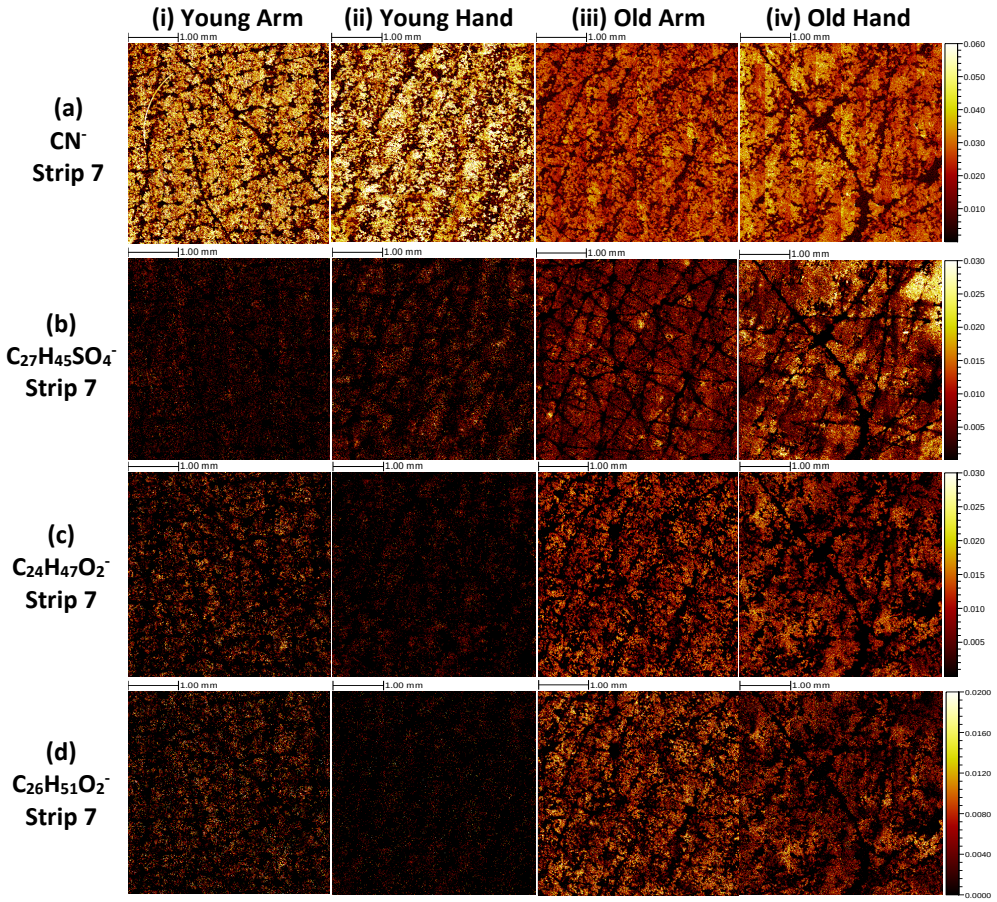

Figure 4.10 Representative ToF-SIMS secondary ion images of tape strip number 7 for the four sample types, highlighting the spatial distribution of (a) a generic tissue marker CN^- (b) cholesterol sulfate $C_{27}H_{45}SO_4^-$ (c) lignoceric acid $C_{24}H_{47}O_2^-$ and (d) hexacosanoic acid $C_{26}H_{51}O_2^-$

Although the intensity of the two fatty acids (Fig. 4.10c and d) differs between sample types, the spatial distribution matches the skin pattern highlighted in the CN^- image (Fig. 4.10a) and remains homogeneous across all samples. In contrast, the spatial distribution of cholesterol sulfate (Fig. 4.10b) is varied. The post-menopausal images, illustrated in Figure 4.10b(iii) and 4.10b(iv), indicate a localised increase in this molecule resulting in 'pools' of higher ion intensity. These observed 'pools' of increased intensity vary in size, with the diameter of the small circular shaped areas evident in the post-menopausal arm sample, Figure 4.10b(iii), measuring in the region of ~200 µm. The SEM images produced in section 4.3.1 indicate that the corneocyte diameter for a

post-menopausal arm sample is between 30-40 µm. Therefore, these 200 µm wide areas of intensity appear to correlate to small clusters of corneocytes. The post-menopausal hand sample, Figure 4.10b(iv), displays much larger localised regions of increased intensity with the largest area apparent in the top right corner of the image, measuring over 1 mm in length. This suggests that the age-induced increase in cholesterol sulfate within the *stratum corneum* is a non-uniform process, initially affecting isolated areas rather than a homogeneous increase. In addition, the relative homogeneity of the fatty acid distribution confirms that this localisation of cholesterol sulfate is the result of a physiological effect and not an artefact of the data.

To further confirm the age-induced localised increase of cholesterol sulfate, the spatial distribution of this compound was also assessed as a function of *stratum corneum* depth. As part of the preliminary data analysis conducted in section 4.3.3.1, alternate strips 1-15 were analysed for one volunteer per age category. The ToF-SIMS secondary ion images from these samples highlight that the localised increase in cholesterol sulfate observed in the tape strip 7 samples is actually present throughout the *stratum corneum.* Representative images highlighting the distribution of cholesterol sulfate ($C_{27}H_{45}SO_4^-$) across strip numbers 1, 5, 9 and 13 are illustrated for the arm and hand sample of one post-menopausal volunteer, shown in Figure 4.11a and b respectively. This localised distribution is most pronounced for the post-menopausal hand samples (Fig. 4.11b), which even show 'pools' of increased cholesterol sulfate in the outermost layer, strip 1, illustrated in Figure 4.11b(i). The fact that this localisation is present in multiple layers of the *stratum corneum* confirms that it is the result of a non-uniform physiological change in cholesterol sulfate levels.

This age-related localised increase in *stratum corneum* cholesterol sulfate is an unprecedented phenomenon that has not been previously demonstrated and has been elucidated due to the excellent sensitivity and spatial resolution of the ToF-SIMS instrument. These findings also support the decision to scan a large analysis area, specifically 4 mm × 4 mm. The analysis areas originally

employed by Judd *et al.* [83], between 100-500 μm^2, may have elucidated the extreme cholesterol sulfate localisation seen for the post-menopausal hand samples, but would most likely have missed the smaller areas of localisation present in the post-menopausal arm samples. It may be that even the 4 mm × 4 mm area used in this study is inadvertently missing features that are more widespread across the sample surface. Therefore, in the future it might be useful to examine larger analysis regions to establish the most suitable size for these sample types. However, ultimately the chosen area size will be limited by the sample acquisition time, in order to retain a reasonable sample throughput for this method.

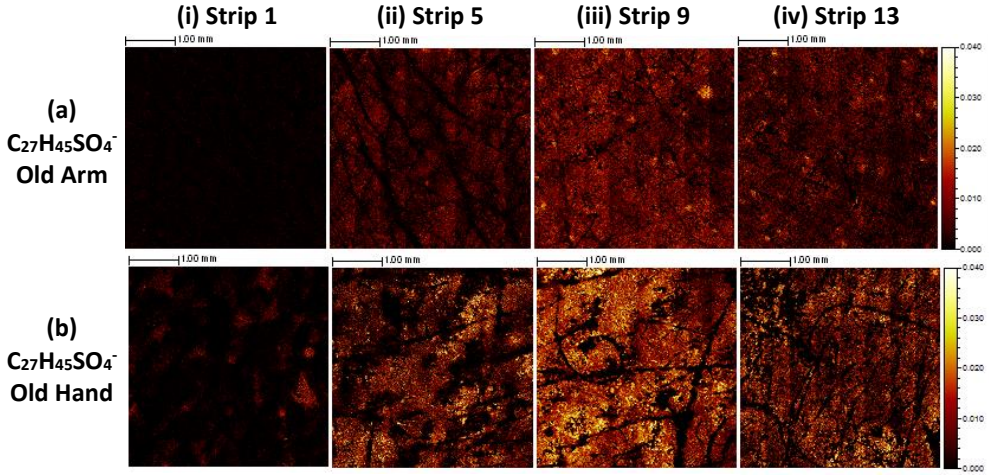

Figure 4.11 Representative ToF-SIMS secondary ion images for (a) an old arm sample and (b) an old hand sample highlighting the distribution of cholesterol sulfate with increasing stratum corneum depth.

4.3.3.6 Detection of sodium lauryl sulfate

One high mass ion highlighted in the 'S' loadings plots for several of the aging comparisons was an ion at *m/z* = 265. Visual inspection of the spectra and secondary ion images related to this ion highlighted both a high peak intensity and unusual spatial distribution. The exported peak intensities for this ion are shown in Figure 4.12 and highlight an inconsistent trend for this peak relating to aging effects. For the younger volunteers, the levels of this ion are

significantly greater in the hand samples compared to the arm samples. However, this is reversed for the older volunteers, who show an increased level in the arm samples over the hand samples. Therefore, there is no conclusive trend with respect to either intrinsic or extrinsic aging, despite the high intensity of this fragment in the tape stripped samples. One explanation may be that this is a common fragment which is simultaneously produced from several different lipid species that exhibit different aging trends. However, one of the possible assignments for this ion is $C_{12}H_{25}SO_4^-$, which corresponds to the $[M\text{-}Na]^-$ fragment of sodium lauryl sulfate (SLS), an anionic surfactant commonly used in many cleaning and hygiene products. This ion has previously been detected in ToF-SIMS analysis of hair samples treated with an SLS containing formulation [263,264]. Therefore, it may be possible that the origin of this ion is a xenobiotic substance, exposed to the skin most likely through the use of cosmetic or hygiene products. This may explain the inconsistent trend observed in the intensity of this ion across the volunteer types.

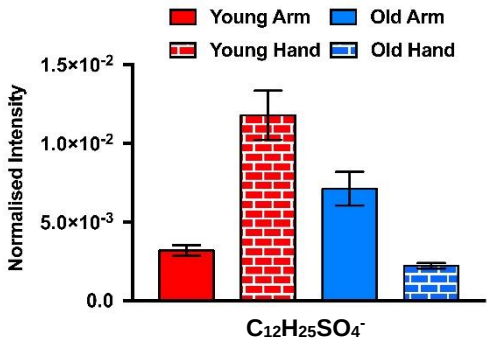

Figure 4.12 Exported ToF-SIMS data showing the average peak intensities across the four sample types for $C_{12}H_{25}SO_4^-$.

This ion also displayed an unusual spatial distribution, highlighted in the example ToF-SIMS secondary ion images shown in Figure 4.13. These are overlaid images with the distribution of the tissue marker CN^- shown in red and $C_{12}H_{25}SO_4^-$ in green. Unlike other skin related peaks this ion is not distributed in the same pattern as the tissue, suggesting it is not a native species. Yet it is also clearly not an adhesive related ion. Instead, this ion

appears to accumulate around the edges of the corneocyte cells, adjacent to the furrows. This suggests that this compound permeates through the skin via an intercellular route, supporting the theory that this ion is related to a xenobiotic substance and not a native lipid component. Volunteers were asked not to apply any cosmetic products to their skin prior to the sampling process. However, washing of the hands or body was not included in this and therefore for future studies it may be beneficial to specify this, to prevent the detection of surfactants or other compounds present in hygiene products. This ion was detected at high intensities in these tape stripped samples, which are theoretically related to the 7th layer of the *stratum corneum.* If this ion has originated from a hygiene product then this demonstrates that the components are not just acting on the superficial layers of the skin, but are actually successfully permeating into the *stratum corneum* and potentially the viable epidermis.

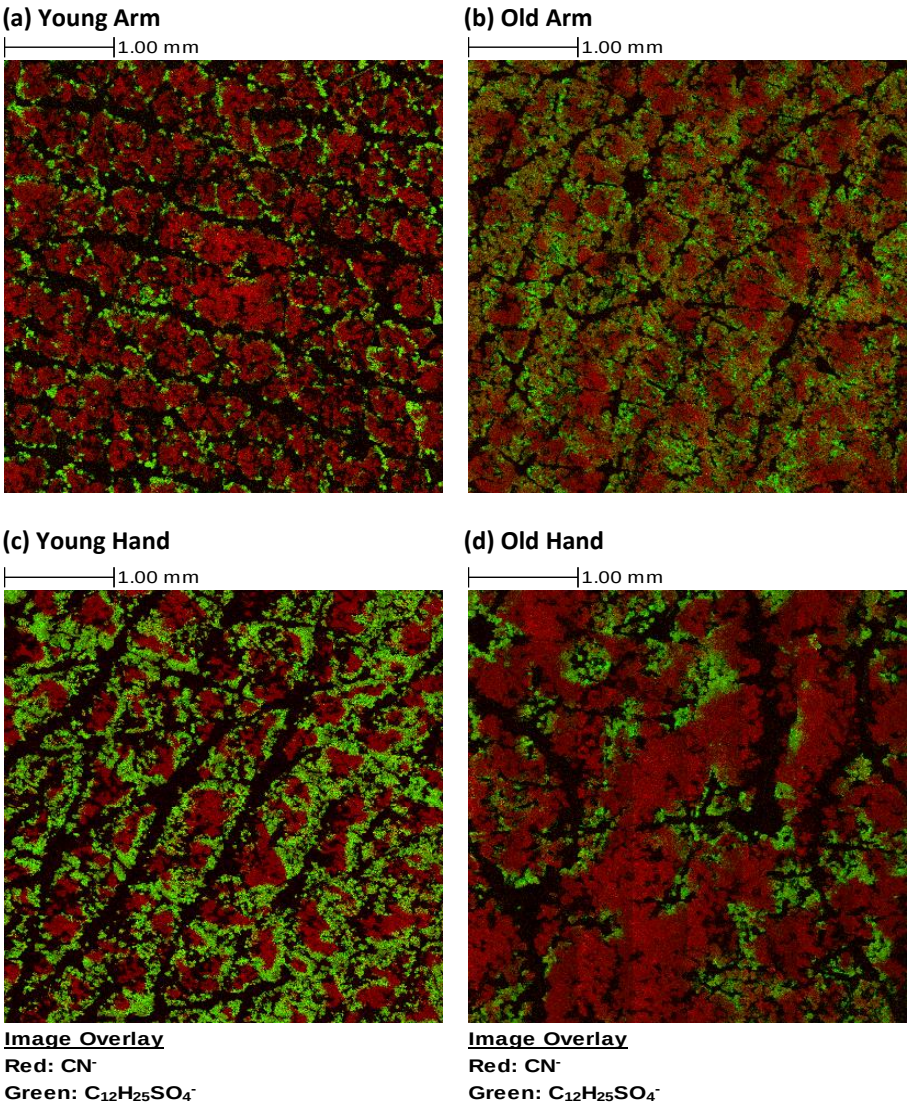

Figure 4.13 Representative ToF-SIMS secondary ion images for (a) a young arm (b) an old arm (c) a young hand and (d) an old hand sample, highlighting the non-uniform spatial distribution of $C_{12}H_{25}SO_4^-$.

4.3.3.7 Lipid variation as a function of stratum corneum depth

As previously mentioned, alternate strips 1-15 were analysed for one volunteer per age category, which allowed analysis as a function of *stratum corneum* depth for ions of interest (section 4.3.3.1). These results highlighted that ToF-SIMS is able to detect differences between individual strip numbers and elucidate trends in *stratum corneum* components relating to skin depth. Figure

4.14 shows the exported ion intensities as a function of tape strip number for the four ions relating to lignoceric acid, hexacosanoic acid, cholesterol sulfate and sodium lauryl sulfate (SLS). It is important to note that as these results are from samples taken from one volunteer per age category they do not represent the average trends previously observed between sample types. However, they can provide insight into physiological changes in these compounds with increasing depth into the skin.

Both cholesterol sulfate and SLS show a significant increase and decrease with depth respectively. The increase in levels of cholesterol sulfate with depth (Fig. 4.14c) agrees with data previously published by both Bonte *et al.* and [47] Bouwstra *et al.* [265] and supports the idea of the cholesterol sulfate gradient eluded to in the proposed epidermal cholesterol sulfate cycle [38] (discussed in section 1.2.2). In contrast, the ion believed to be related to SLS exhibits an almost immediate decline in intensity (Fig. 4.14d), which would correlate with the assignment of this ion to a xenobiotic compound that has permeated into the *stratum corneum.*

Both fatty acid compounds (Fig. 4.14 a and b) show an initial sharp increase with depth, which correlates to data reported by Bonte *et al.* [47], who used chromatographic methods to demonstrate a consistent decline in short chain fatty acids but an increase in lignoceric acid (C24:0) between tape strips 1-5. However, no analysis was conducted by Bonte *et al.* past tape strip number 5. For the samples in this study, the trends for the two fatty acids appear to differ after tape strip 7, with a constant intensity maintained for the young volunteer compared to a sharp increase followed by a sharp decline exhibited for the old volunteer. However, as stated these results are only representative of one volunteer and therefore further investigation on repeat samples would be needed to confirm these trends.

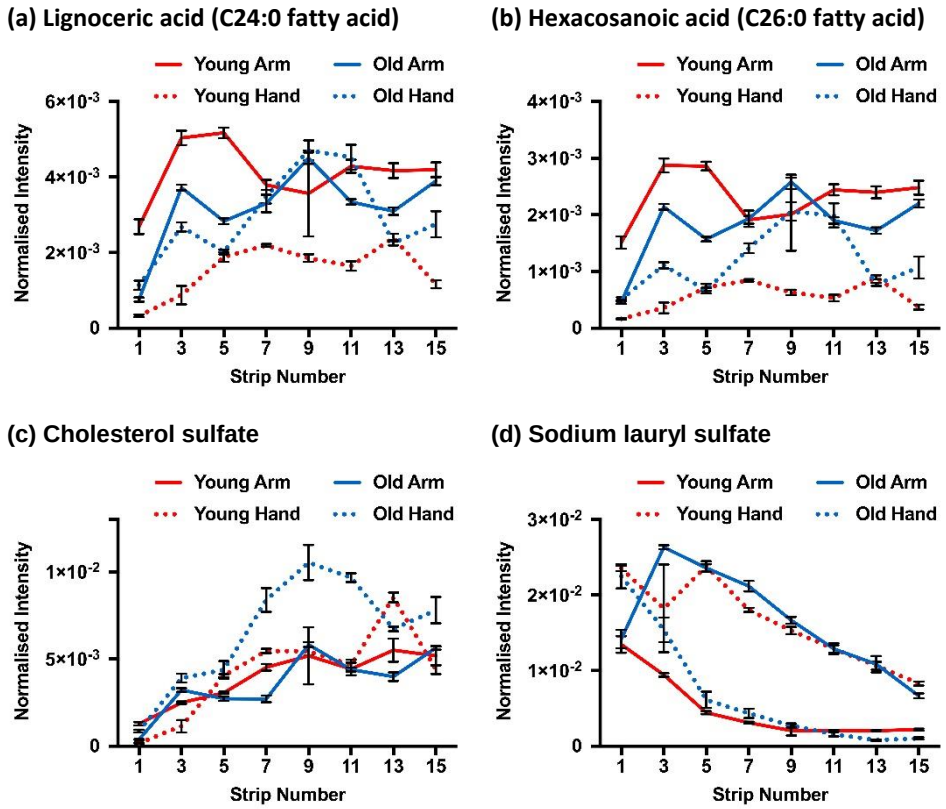

Figure 4.14 Exported ToF-SIMS data showing the change in ion intensity as a function of stratum corneum depth for (a) lignoceric acid (b) hexacosanoic acid (c) cholesterol sulfate and (d) sodium lauryl sulfate.

4.4 Conclusions

The tape stripped *stratum corneum* samples collected *in vivo* from human volunteers exhibited known age-related changes to corneocyte surface area, with an increase and decrease related to intrinsic and extrinsic aging respectively demonstrated through SEM analysis. This validated the use of these samples to detect age-related chemical changes using ToF-SIMS.

AFM analysis established that there was no statistically significant difference in the depth of *stratum corneum* removed per strip for all sample types. This ensured that any age-related variation in chemical composition observed through cross comparison of individual tape strips could be confidently attributed to actual physiological differences rather than a variation in sample depth.

This study has produced unprecedented data demonstrating the ability of ToF-SIMS to successfully detect subtle changes in the *stratum corneum* lipid composition between different sample types. Using this technique, the presence of several lipid species were shown to vary as a result of both intrinsic and extrinsic aging, specifically cholesterol sulfate and both lignoceric acid and hexacosanoic acid. In addition, ToF-SIMS was also able to elucidate the spatial distribution of these compounds within an individual *stratum corneum* layer, highlighting a previously unreported localised age-related increase in cholesterol sulfate. Analysis of sequential strips also elucidated trends in these *stratum corneum* lipids as a function of depth, confirming the presence of a previously reported *stratum corneum* lipid gradient.

Chapter 5: Method development of dual beam dynamic SIMS for depth profile analysis of *ex vivo* skin

5.1 Introduction

Dual beam dynamic SIMS can be used to conduct depth profile analysis, providing chemical information as a function of sample depth, as described in section 1.5.9. Although this technique has been applied to a wide range of biological tissue analysis it has not yet been utilised for the analysis of skin tissue. ToF-SIMS has previously been shown to be an effective technique for monitoring the permeation of an exogenous compound into the skin, through analysis of both tape stripped samples and microtomed tissue sections [83,159,162-165]. The high chemical specificity and sensitivity of the technique and the ability to map the spatial distribution of compounds has proved invaluable for skin permeation analysis. Therefore, the use of dynamic SIMS to create a 3D chemical depth profile of skin would offer a huge advancement in this field.

Prior to this technique being applied to skin tissue analysis, sufficient method development is required. In order to produce an accurate 3D chemical profile, the rate at which the ion beam sputters through the material must be known. The sputter rate for a particular sample type therefore has to be determined. It is obvious that the structural nature of the sample will play a significant role, specifically the density of the material. Research into the variation between sample types has shown that the sputter rate is a complex entity that is not easily predicted. Cumpson *et al.* [266] highlighted variance in the sputter rate between 19 types of polymer, indicating that even samples with similar material properties can sputter differently depending on their chemical composition. It has also been shown that fundamental choices regarding the ion beam parameters have an impact on the sputter rate, such as the ion beam choice, cluster size and beam energy [177,266-269]. Cumpson *et al.* also demonstrated that changes in sputter rate were non-linear in relation to the beam energy, cluster size or energy per atom within the cluster. This study also demonstrated that different polymers responded differently to changes in these beam parameters. In addition, various studies have demonstrated the complications that can arise with regards to the sputter rates for multi-layered

samples [195,270,271]. In particular, Taylor *et al.* [270] demonstrated that the sputter rate for a bilayer structure containing two different polymers could not accurately be predicted by combining the individual polymer sputter rates, highlighting a change in sputter rate related to the transition between the two layers. It is therefore apparent that an accurate sputter rate needs to be calculated for each specific sample type and cannot be predicted by previous work, in order to account for both experimental parameters and inherent sample variation.

One of the main disadvantages regarding ToF-SIMS analysis of organic materials is the ultra-high vacuum conditions required. Dehydration of samples, especially biological tissue, may result in damage to both the structural and chemical integrity. There are currently several popular fixation methods employed to try and preserve tissue integrity prior to ToF-SIMS analysis, both chemical and physical [209,272,273]. However, these all involve the removal of water content from the sample. The preparation of a frozen hydrated sample allows for the analysis of the sample without drying. In this method the sample is kept frozen throughout the experiment using a liquid nitrogen cooled stage within the instrument, which was first described by Chandra *et al.* [274]. As summarised by Passarelli and Winograd [231], this preparation method has shown an enhancement in the ion yield for several lipid species, with this enhancement arising from both a reduction in damage accumulation and the matrix effect of the surrounding water molecules. The key disadvantage, however, to using this method is the experimental set up, which is more complicated and time consuming. In addition, the cooling stage only allows the introduction of one sample at a time to the analysis chamber, which hugely decreases the sample throughput.

It is therefore apparent that although the dynamic SIMS technique offers huge potential in the field of skin analysis, it first requires the establishment of a suitable protocol following the exploration and optimisation of various experimental parameters.

5.2 Chapter aims

The aim of this study is to explore the potential of ToF-SIMS to produce accurate 3D chemical profiles of skin tissue, by developing a dynamic SIMS method. This study will look to optimise various experimental parameters, such as the applied beam energy, cluster size and sample preparation methods. An investigation into the sputter rate of *ex vivo* skin tissue will be conducted and the chemical composition of the tissue will also be examined for inherent markers that indicate tissue depth. The aim is to establish a suitable protocol that can be applied to provide relevant information regarding the permeation of exogenous compounds as a function of skin depth.

5.3 Results and discussion

5.3.1 Calibration of sputter rate

For depth profile analysis, in order to accurately provide chemical information as a function of sample depth, the sputter rate of the analysis material first needs to be calculated, as discussed in section 5.1. There are two possible ways that this can be achieved. A sample with known thickness can be profiled and the thickness then correlated to the sputter time taken. Alternatively, the sample can be profiled and the created sputter crater can then be measured.

The aim of this work was to develop a method for depth profile analysis of full thickness *ex vivo* porcine tissue, to be employed following Franz cell permeation studies. However, as biological tissue exhibits inevitable variability between individual samples, the depth of full thickness tissue is not a standard entity. It would therefore be impossible to calculate an accurate sputter rate simply by monitoring the time taken to profile through various full thickness skin samples. Therefore, for sputter rate calculations it was decided instead to use skin tissue which had been sectioned to a known thickness, specifically microtomed slices.

As an alternative method, depth profile analysis was also conducted on heat separated (HS) epidermis samples, with the aim of measuring the sputtered crater. The use of the epidermal layer ensures a much thinner tissue depth to profile through (~ 50-85 µm) compared to the substantial depth of full thickness tissue (~ 1-2 mm) [112,221,222]. The thickness of these epidermal layers could have been measured prior to profiling. However, both the non-uniform topography of the skin surface and the undulating nature of the dermoepidermal junction would have resulted in a variation in measured depth within an individual sample. Therefore, the aim was to instead measure the sputtered craters to more accurately correlate skin depth to sputter time.

5.3.1.1 Analysis of microtomed slices

It was chosen to produce microtomed slices of skin tissue rather than use tissue which had been dermatomed to a particular depth. The reason for this was twofold. Firstly, the microtome is able to produce much thinner sections than the dermatome, decreasing the profiling acquisition time. Secondly the microtome is able to slice the tissue vertically rather than horizontally, offering the ability to produce slices that contain multiple skin layers.

Due to a reduced thickness, dermatomed tissue is easier to microtome than full thickness tissue, therefore dermatomed porcine flank tissue (400 µm) was used for this study. The tissue was subjected to chemical fixation as described in section 2.2.2.3 and microtomed slices of 8, 10 and 15 µm were collected. As illustrated schematically in Figure 5.1a these slices were then positioned for ToF-SIMS analysis so that the depth of the tissue section to be profiled appeared as the microtomed thickness. The width of these microtomed slices were therefore known to be 400 µm, which meant that the sections contained regions from the *stratum corneum*, underlying epidermis and dermis.

Taking guidance from recent work by the Brunelle group [204], a 10 keV Ar_{1445} cluster beam was used for analysis. Brunelle *et al.* evaluated the use of argon sputtering for depth profile analysis of 14 µm rat brain sections, which were considered similar in structure and thickness to the microtomed skin samples employed in this study. As illustrated in Figure 5.1b-d the sputter area was 500 µm × 500 µm and the analysis area was a 200 µm × 200 µm region within the centre of the sputter area. The analysis area was purposely positioned to incorporate a section of underlying glass substrate, in order to highlight the edge of the skin tissue in the ToF-SIMS secondary ion images and the *stratum corneum* was positioned towards the upper edge of the analysis area. By assuming typical layer thickness for porcine tissue (section 1.3.3.1) [112,222] this 200 µm × 200 µm area should still include data from the *stratum corneum*, epidermis and dermis.

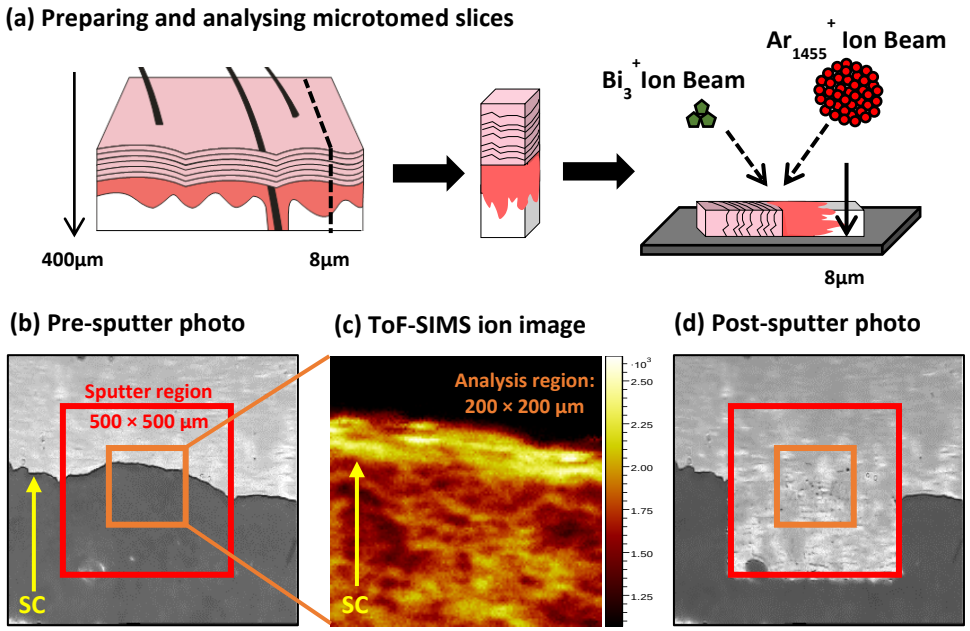

Figure 5.1 (a) A schematic illustrating the preparation and ToF-SIMS analysis of microtomed slices. (b-d) Optical and ToF-SIMS secondary ion images highlighting the ToF-SIMS sputter and analysis regions.

Depth profile analysis was conducted on the 8, 10 and 15 µm slices and the intensity of ions related to both tissue (CN^-) and underlying glass substrate (SiO_2^-) were monitored as a function of depth (Fig. 5.2a). Both the ToF-SIMS camera images in Figure 5.1, showing a pre- and post-sputtered microtomed slice, and the depth profile data displayed in Figure 5.2 demonstrates that successful profiling of skin tissue was achieved. This study is therefore thought to be novel in demonstrating the possibility of using dynamic SIMS to profile through skin tissue material.

The intensity decrease and increase of the CN^- and SiO_2^- ions respectively were used to indicate the tissue/substrate interface. Analysis was conducted on two different 200 µm × 200 µm areas for each of the 8, 10 and 15 µm slices. Although the depth profiles acquired for the 200 µm × 200 µm areas did show an intensity change for both the CN^- and SiO_2^- ions (Fig. 5.2a), they did not show the rapid change in intensity anticipated. Inspection of the 3D secondary ion images for these ions (Fig 5.2c and d) highlight a non-uniform intensity change within the 200 µm × 200 µm analysis area, indicating a variability in

tissue thickness. This is therefore the proposed reason behind the gradual intensity change observed in the depth profiles (Fig. 5.2a), preventing the conclusive assignment of a sputter time associated with the tissue/substrate interface. This was needed in order to produce an accurate sputter rate once the depth of the sputtered crater had been measured. It was therefore decided to select data from three smaller 12.5 µm × 12.5 µm areas within the original 200 µm × 200 µm region. These areas provided a more rapid intensity change, particularly for the SiO_2^- ion, as demonstrated in the example profiles shown in Figure 5.2b.

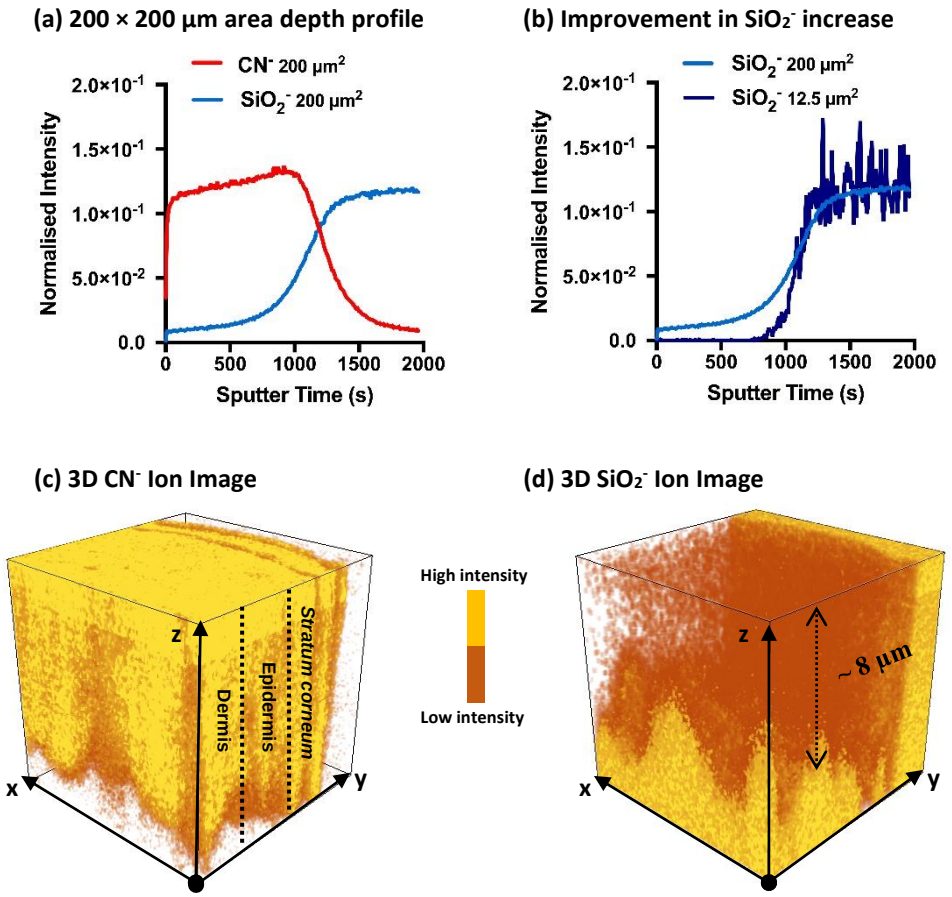

Figure 5.2 Example ToF-SIMS negative depth profile data from analysis of a microtomed slice showing (a) the change in CN^- (tissue) and SiO_2^- (glass) intensity for a 200 × 200 µm area (b) the more rapid SiO_2^- intensity increase observed for a 12.5 µm × 12.5 µm area (c-d) Secondary ion images showing the spatial distribution with depth for CN^- and SiO_2^- within a 200 µm × 200 µm area.

In order to assess whether there was any difference in sputter rate between the different skin layers, the three 12.5 µm ×12.5 µm analysis regions were taken from areas on the sample related to the *stratum corneum*, epidermis and dermis. These areas were originally assigned based on the typical porcine ear layer thicknesses (*stratum corneum* 10-28 µm, epidermis 50-85µm) [112,221,222] but were later confirmed as accurate through the identification of chemical biomarkers (section 5.3.2.1). As SiO_2^- demonstrated a more rapid change in intensity than CN^- and is a more distinct ion, originating only from the underlying substrate, only this ion was used to determine the tissue/substrate interface. The sputter time correlating to this interface was determined by the initial onset of the SiO_2^- intensity increase.

Depth profiles showing the increase in SiO_2^- intensity as a function of sputter time for each of the three layers, *stratum corneum*, epidermis and dermis, are shown in Figure 5.3. The data from the 8, 10 and 15 µm slices are colour coded. In general, the average sputter time does appear to show a positive correlation with increased thickness. However, this correlation is not linear and also appears to differ in magnitude between the three layers. Therefore, it is impossible to produce a linear calibration curve from this data. One possible reason for this variability may lie with the tissue embedding and slicing process. If the tissue was embedded into the paraffin block whilst not vertically and horizontally straight, then the microtome may have sliced the tissue at an angle, resulting in a non-uniform slice thickness.

One interesting observation is that within an individual slice, the *stratum corneum* layer (Fig. 5.3a) appears to show a significantly longer sputter time than the corresponding epidermis (Fig. 5.3b) and dermis (Fig. 5.3c) regions, with one *stratum corneum* area from the 10 µm slice showing no increase in SiO_2^- intensity within the duration of the experiment. As this trend is consistent for each of the 8, 10 and 15 µm slices it again may be due to a non-uniformity in thickness caused by the embedding process. However, as the 8, 10 and 15 µm slices were taken from the same embedded tissue, it would still be anticipated that a linear correlation between the three thicknesses for each analysed layer would be observed. Therefore, it is proposed that the *stratum corneum* requires a longer sputter time compared to the epidermal and dermal

regions. This may be explained by an increased level of paraffin entrapment in the *stratum corneum* compared to the other layers, due to a variation in tissue structure. However, it is likely that this increased sputter time is instead due to the native increase in tissue density associated with this layer, as the *stratum corneum* consists of tightly packed, keratin filled cells. Overall, this study has demonstrated that without evaluation and optimisation of certain parameters, this method cannot provide an accurate correlation between tissue depth and sputter time. However, even with optimisation, as the fixation process introduces the possibility of chemical changes to the tissue, this may not be the most effective method to use.

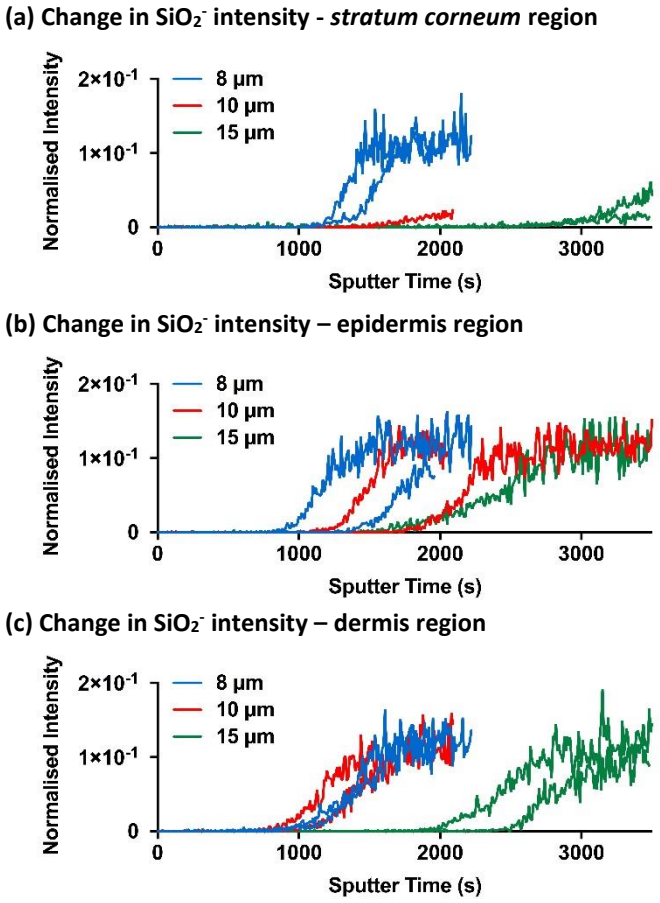

Figure 5.3 ToF-SIMS depth profile data aquired from microtomed slices showing the change in SiO_2^- intensity as a function of depth, indicating when the underlying glass substrate has been reached. The data was taken from three regions on each sample correlating to the (a) stratum corneum (b) epidermis and (c) dermis and data was aquired from three slice thicknesses, 8, 10 and 15 µm, which are coloured coded accordingly.

5.3.1.2 Optical profilometry analysis of sputtered craters

An alternative way to achieve a calibrated sputter rate is to measure the depth of a sputtered crater. To achieve this, optical profilometry was used to conduct depth measurements following dynamic profiling of porcine ear tissue. HS epidermis was used specifically for this analysis, as it retained its morphology better than full thickness tissue in the ToF-SIMS vacuum. This ensured a more uniform upper reference surface in the optical profilometer, minimising the error in calculated depth caused by variance in sample topography. Optimisation of the argon beam settings, detailed in section 5.3.3, resulted in profiling parameters that differed from those used for the microtomed slice analysis, specifically a 20 keV Ar_{1900} beam with a 10 nA specified target current.

In order to account for the large variability presented by biological samples, four different HS samples were prepared from four different pig ears. These samples were mounted onto silicon wafer substrates for analysis, which provided two key advantages. Firstly, the silicon substrate would produce a distinct, high intensity ion in the ToF-SIMS depth profile, to indicate when the tissue had been fully removed and secondly it would provide a flat lower reference surface for the optical profilometry analysis. An example of a sputtered region on a HS sample is illustrated in Figure 5.4.

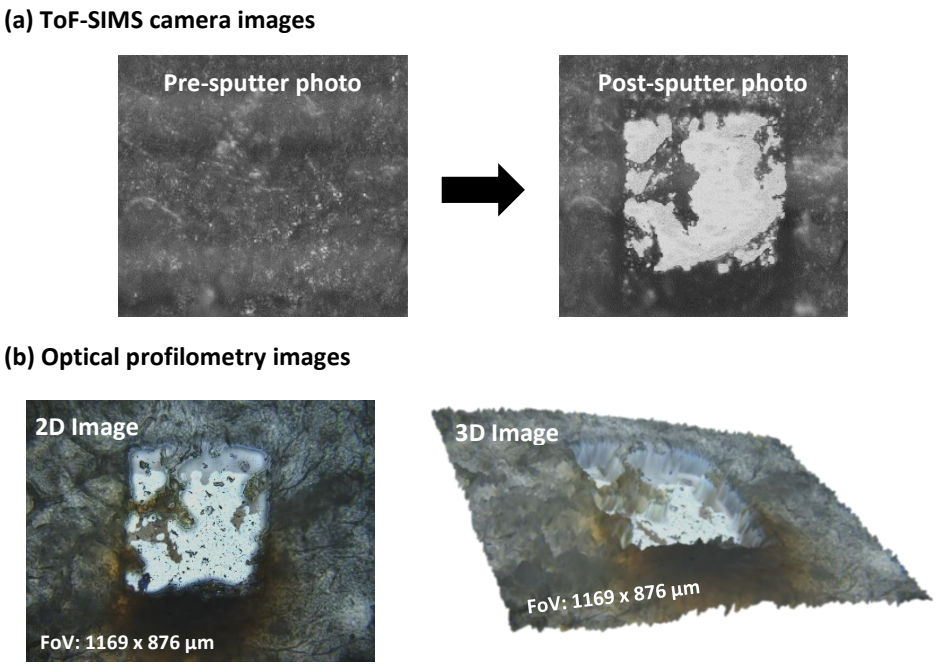

Figure 5.4 Example (a) ToF-SIMS camera images and (b) corresponding optical profilometry images of a sputtered region on a heat separated porcine skin sample.

The aim was to depth profile through the tissue section and again monitor the decrease in CN^- intensity and increase in SiO_2^- intensity to determine the sputter time for the tissue/substrate interface. However, although a definite decrease in CN^- intensity was observed, there was no accompanying increase in the SiO_2^- intensity (Fig. 5.5), despite the ToF-SIMS camera showing the emergence of the underlying silicon wafer (Fig. 5.4a).

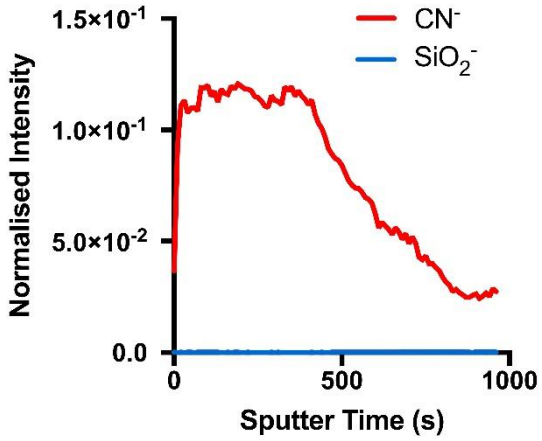

Figure 5.5 Example ToF-SIMS depth profile data acquired from a heat separated sample showing the decrease in CN^- as a function of depth, indicating the removal of tissue, but no corresponding increase in SiO_2^- to indicate the appearance of the underlying glass substrate.

This was observed for all four samples, which indicated a problem with the sample set up. This was confirmed when the samples were removed from the ToF-SIMS instrument as it became apparent that, due to the samples not being fully adhered to the silicon wafer, the drying process in the ToF-SIMS vacuum had delaminated the skin and the wafer. However, this did not detrimentally affect the analysis as the CN^- intensity alone was sufficient to indicate the tissue/substrate interface.

The change in CN^- intensity was again not as rapid as anticipated and examination of both the 2D (Fig. 5.6a) and 3D (Fig. 5.6b) secondary ion images highlighted a significant variation in topography within the 200 µm × 200 µm analysis area. It is important to note that the software reconstructs the depth profile images from the top surface downwards, which falsely represents the top of the skin as a flat surface. Therefore, the variation in topography observed for these HS samples may originate from either the surface of the skin, the dermoepidermal junction or a combination of both.

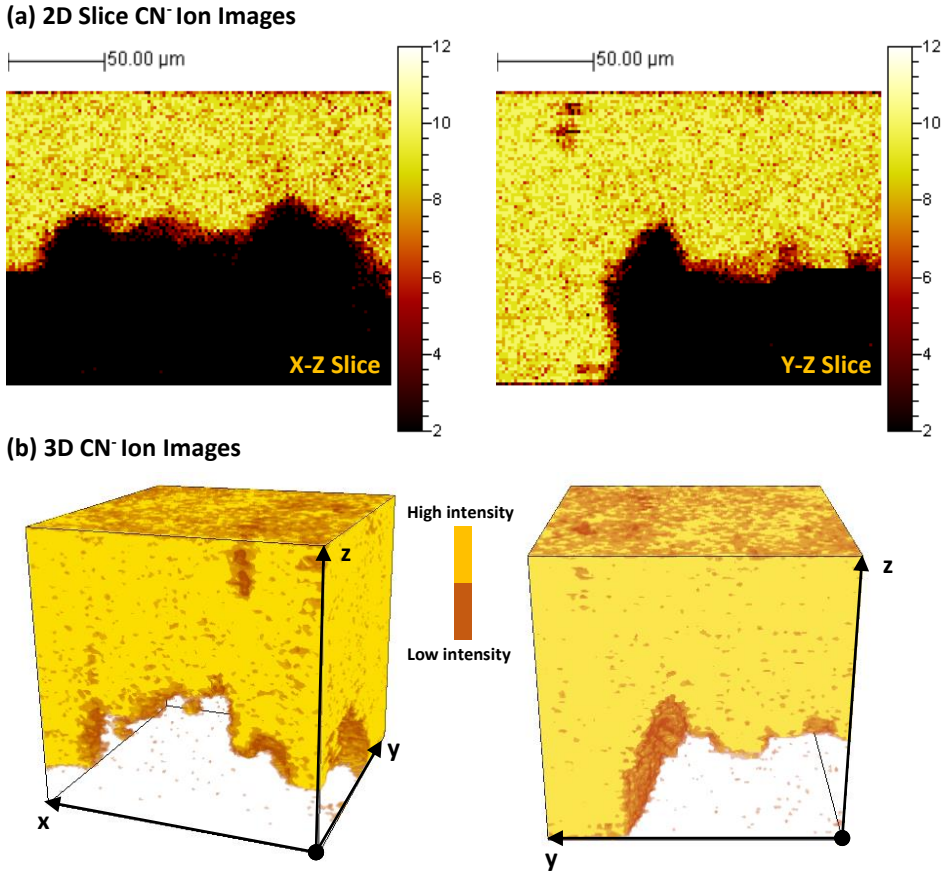

Figure 5.6 Example ToF-SIMS (a) 2D slice and (b) 3D secondary ion images aquired from depth profile analysis of a heat separated sample showing the non-uniform decrease in CN^- as a function of tissue depth within a 200 µm × 200 µm area.

Due to the variation in topography within the 200 µm × 200 µm area, data was again taken from three smaller 12.5 µm × 12.5 µm regions. The depth profiles from each sample are displayed in Figure 5.7. The sputter time correlating to the tissue/substrate interface was determined from the onset of the CN- ion intensity decrease.

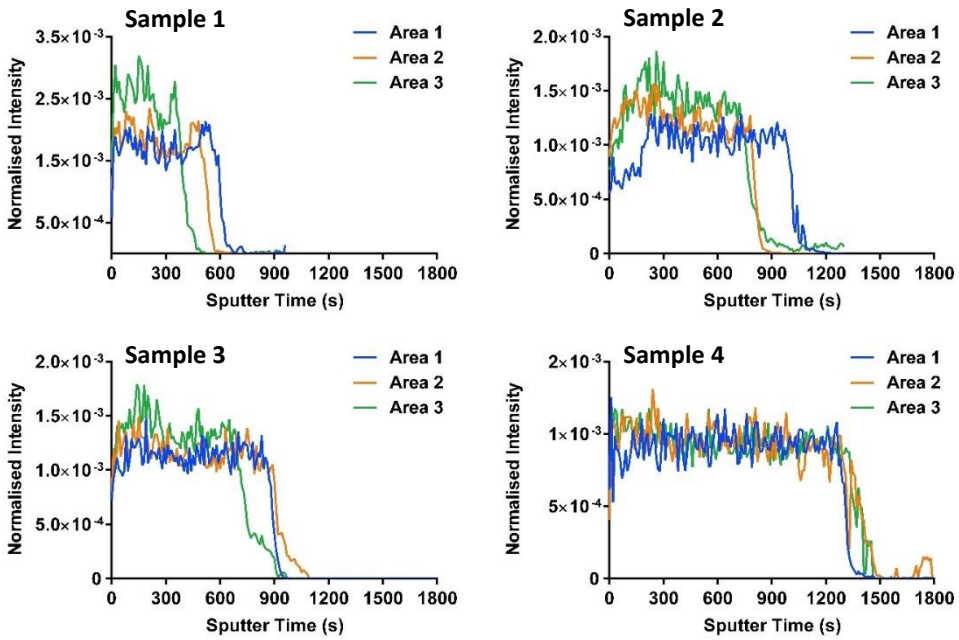

Figure 5.7 Example ToF-SIMS depth profile data for the four different heat separated samples displaying the decrease in CN^- intensity as a function of depth, the onset of which indicates when the tissue/substrate interface has been reached. Three repeat areas were analysed per sample.

The average sputter time per sample was calculated as the mean value of the three repeat areas. The average sputter time correlating to the tissue/substrate interface for each sample is displayed in Table 5.1. The average sputter time varies significantly between the four samples, which is assumed to be a consequence of the anticipated variability in epidermal depth. However, the analytical error between the three repeat areas was within an acceptable range (between 2-12 %), which supports the repeatability of the dynamic SIMS sputter process.

Table 5.1 The average sputter time required to reach the tissue/substrate interface for the four heat separated samples.

Sample No.	Average Sputter Time (s) ± SEM
1	457 ± 56
2	823 ± 75
3	810 ± 66
4	1310 ± 25

Once the sputter crater had been created, the depth was then measured using the optical profilometer. As the ToF-SIMS vacuum had caused the HS samples to become slightly elevated from the underlying silicon wafer, they first needed to be gently compressed to ensure that contact was re-established between the sample and the substrate. Failure to do this would have increased the depth values produced as these are calculated from a step height measurement between the top of the skin and the underlying substrate. Prior to analysis, the samples were therefore gently compressed between two glass slides. The optical profilometry 2D image for each sample is displayed in Figure 5.8 and it is apparent from these images that the sputtered craters demonstrate a random sputter pattern that is significantly different for each sample. This again demonstrates uneven sputtering across the sample, which is likely sample dependent and due to a non-uniformity in thickness across the sample.

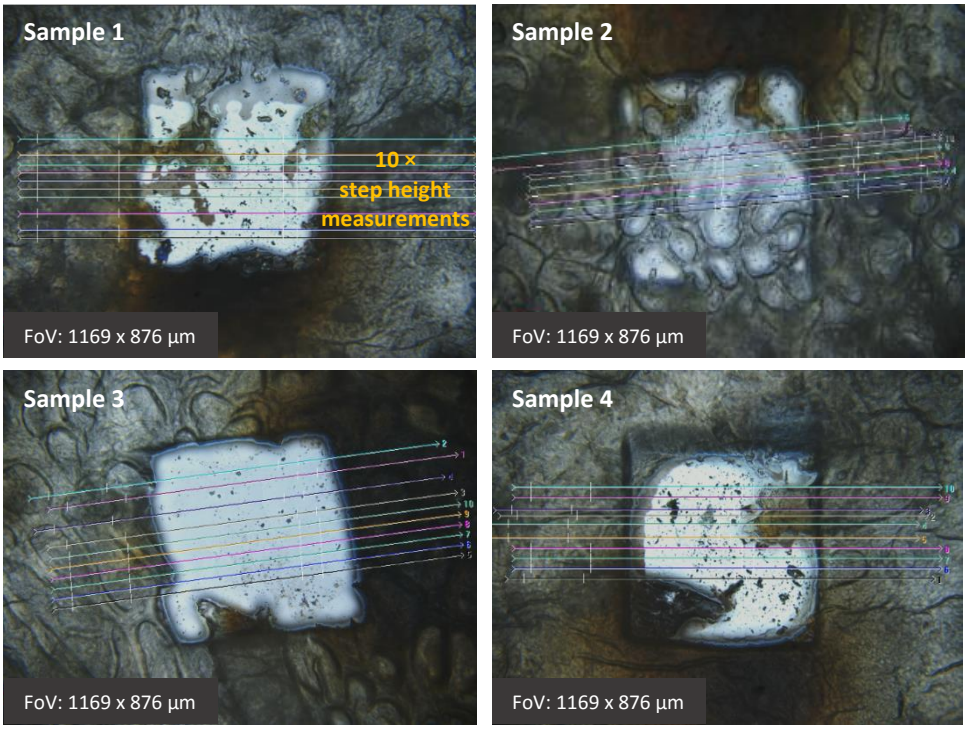

Figure 5.8 Optical profilometry 2D images of the sputtered crater for the four different heat separated samples. The horizontal lines indicate the measurement regions used to produce the ten step height measurements taken from either side of the sputtered crater.

The silicon substrate provides a flat, ideal lower reference surface. However, the inhomogeneity of the tissue surface proved problematic, as the step height measurement was significantly different depending on the specific area chosen as the upper reference surface. It was also observed that one side of the sputter region was noticeably higher than the other, which may be due to the ToF-SIMS sputter process. The beam is directed at the surface at an angle and therefore the material that is being removed will build up on one side of the sputtered crater. Therefore, in order to try and account for this variability, two different step height measurements were taken, using opposite sides of the sputter crater as the upper reference surface. In addition, to try to minimise the effects of an uneven tissue surface, ten different areas across the sputter region were sampled, as demonstrated by the horizontal lines shown in Figure 5.8. Therefore, the average step height values are calculated from twenty different measurements. For the samples with an incomplete sputter region, care was taken to only include step height measurements from areas where the

underlying silicon substrate was visible and to avoid areas with remaining skin tissue.

The total average step height values calculated for each sample are displayed in Table 5.2. The average step height values measured using opposite sides of the sputtered crater as the upper reference surface are also shown, highlighting the non-uniform topography. The average step height values produced by this method are significantly greater than reported porcine ear epidermal thicknesses (50-85µm) [112,221,222] This variation may arise from inaccuracy in the measurement technique, possibly caused by large variation in sample topography, or it may be a consequence of the sample preparation method.

Table 5.2 The average step height value, indicating the average depth of the sputtered crater, for the four heat separated samples.

Sample Number	Average step height Total (µm) ± SEM	Average step height LHS (µm) ± SEM	Average step height RHS (µm) ± SEM
1	112.40 ± 5.37	91.07	133.80
2	134.30 ± 3.42	130.50	138.0
3	124.30 ± 2.57	113.50	135.10
4	191.70 ± 2.49	181.50	201.90

The graph in Figure 5.9 displays the mean, minimum and maximum values for each sample, demonstrating that for all four samples the measured values are evenly distributed about the mean. This demonstrates the absence of large outliers in the data and, alongside a low analytical error of < 5 %, indicates high reproducibility for this method. Samples 1 and 2 displayed much greater variance in the data than samples 3 and 4. However, this is somewhat expected on examination of the optical profilometry 2D images in Figure 5.8, as samples 1 and 2 presented the most irregularly sputtered craters, indicating the greatest intra-sample variation in depth within the analysis region.

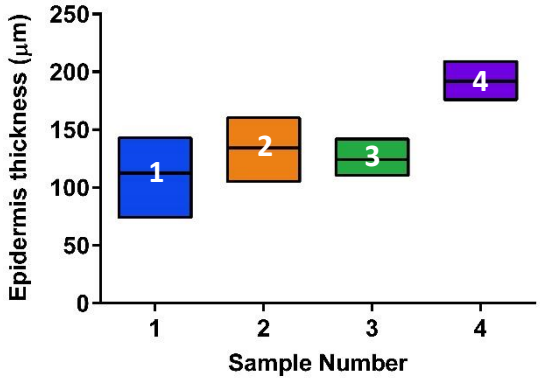

Figure 5.9 A boxplot highlighting the symmetrical distribution of the step height data acquired from the optical profilometry analysis of the heat separated samples. The upper and lower edges of the box represent the maximum and minimum step height values respectively and the horizontal line within the box represents the mean.

The step height measurements were then correlated to the acquired sputter times and an average sputter rate (µm/s) was calculated for each sample, which are shown in Table 5.3. Interestingly, despite the large variation in measured thickness, both within and between the samples, the calculated sputter rate for samples 2-4 is consistent. Although, the thickness measurements for the HS samples were much larger than expected for porcine ear tissue, this consistency in sputter rate suggests that the method has been successful in correlating sputter time with tissue depth. This may therefore point towards an issue with the sample preparation method, resulting in the observed increase in epidermal thickness.

However, both this study and the data acquired from the microtomed slices has proven that there is a huge variability in tissue depth associated with the porcine skin samples. The microtomed slice analysis also indicated a slower sputter time for the *stratum corneum* layer. Therefore, although the calculated sputter rate of ~ 0.15 µm/s can be used to roughly correlate ToF-SIMS sputter time with skin depth, there is not yet enough data to confidently adopt this as the standard sputter rate for all skin tissue. Due to the huge variability observed in tissue depth, a universal sputter rate for this variable thickness, multi-layered sample type may not be achievable.

Table 5.3 The average step height, required sputter time and subsequent sputter rate (µm/s) corresponding to the sputtered craters of the four heat separated samples.

Sample Number	Average step height (µm) ± SEM	Average Sputter Time (s) ± SEM	Average Rate (µm/s) ± SEM
1	112.40 ± 5.37	457 ± 56	0.25 ± 0.1
2	134.30 ± 3.42	823 ± 75	0.16 ± 0.05
3	124.30 ± 2.57	810 ± 66	0.15 ± 0.04
4	191.70 ± 2.49	1310 ± 25	0.15 ± 0.1

5.3.2 Chemical analysis as a function of skin depth

5.3.2.1 Microtomed slice analysis

Although the microtomed samples were prepared primarily to correlate skin depth with sputter time, they also allowed an investigation into chemical differences between the three skin layers. As eluded to in section 5.3.1.1, the 200 µm× 200 µm area chosen for analysis resulted in acquisition of data from the *stratum corneum,* underlying epidermis and dermis. The ToF-SIMS secondary ion images for these samples were therefore examined to determine whether any ions displayed a localised intensity in any of the three skin layers. This was investigated primarily by producing an ion image for every peak present in the spectra and comparing each distribution to that of the generic tissue marker, CN^-. However, the distribution of specific ions were also mapped if an obvious physiological difference in the chemistry of the skin layers was already known. For example, the distribution of phosphate related ions was predominately examined due to the known absence of phospholipids in the *stratum corneum* (section 1.2.2). These lipids are present at high levels in the epidermis, but decrease towards the skin surface as part of the keratinisation process.

Examination of the ToF-SIMS secondary ion images demonstrated that a localised distribution could be detected for several ions. The most significant of these was a phosphate fragment ion, PO_3^-, which despite its small structure

is believed to relate to the phospholipid class of compounds. Figure 5.10 shows example images from one microtomed sample, highlighting the distribution of CN^- (tissue), SiO_2^- (underlying glass substrate), PO_3^- (phospholipids) and an overlaid image of all three. The known physiological difference in phospholipid distribution is clearly revealed in the ToF-SIMS secondary ion images of the microtomed slice. The PO_3^- ion (Fig. 5.10c) is visibly absent from a band of tissue adjacent to the glass, which correlates to the top surface of the skin tissue. The ion intensity is then significantly increased in a band of tissue situated at an increased depth into the skin. It is therefore believed that these two regions relate to the *stratum corneum* and epidermis respectively, as highlighted on the overlaid image in Fig 5.10d. These proposed layers also exhibit thicknesses which correlate to the reported values for the *stratum corneum* (10-28 µm) and epidermis (50-85 µm) [112,221,222], ~ 30 µm and 50 µm respectively.

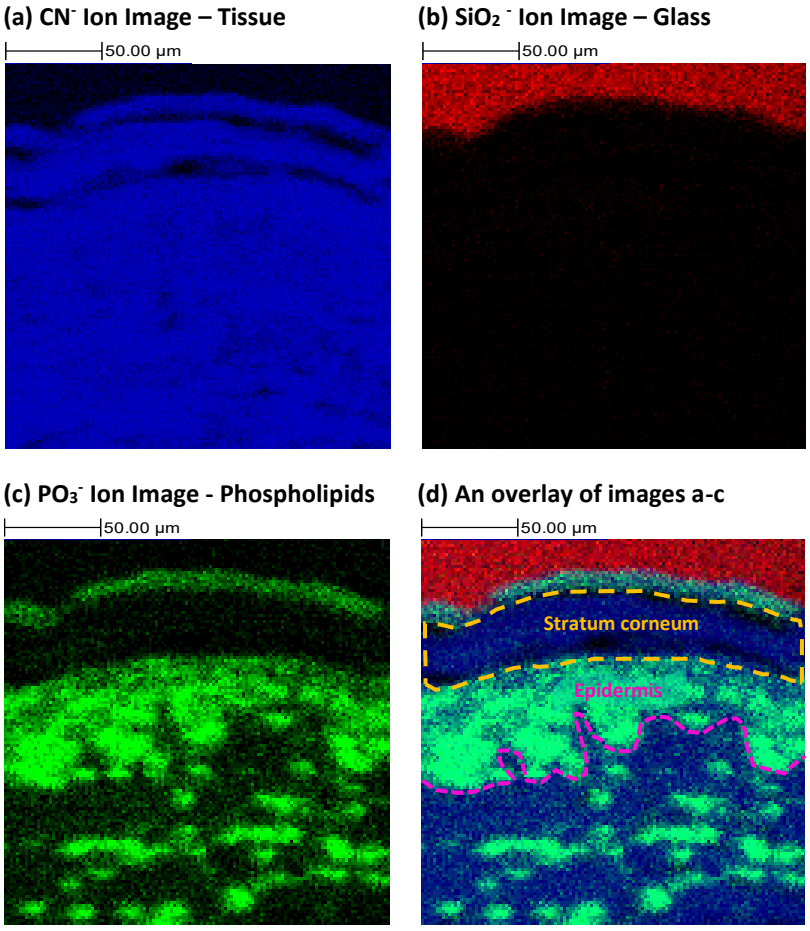

Figure 5.10 ToF-SIMS negative secondary ion images for an example microtomed porcine skin tissue slice, highlighting the spatial distribution of (a) CN^- a tissue marker (b) SiO_2^- a glass marker (c) PO_3^- a phospholipid marker and (d) an overlay of images a-c.

This localised distribution of PO_3^- was observed in all the microtomed samples, with several examples displayed in Figure 5.11. A consistent thickness was observed for both the proposed *stratum corneum* and epidermis regions. Some samples display a small region of PO_3^- intensity directly adjacent to the glass. However, as this is not observed for all of the samples it is proposed to originate from contaminants on the skin surface prior to the embedding process. One important point to note is that the data from these samples was produced using the depth profiling method. Therefore, in order to examine the 2D spatial distribution of these samples, the initial 10 scans from the depth profile were combined to create surface only data.

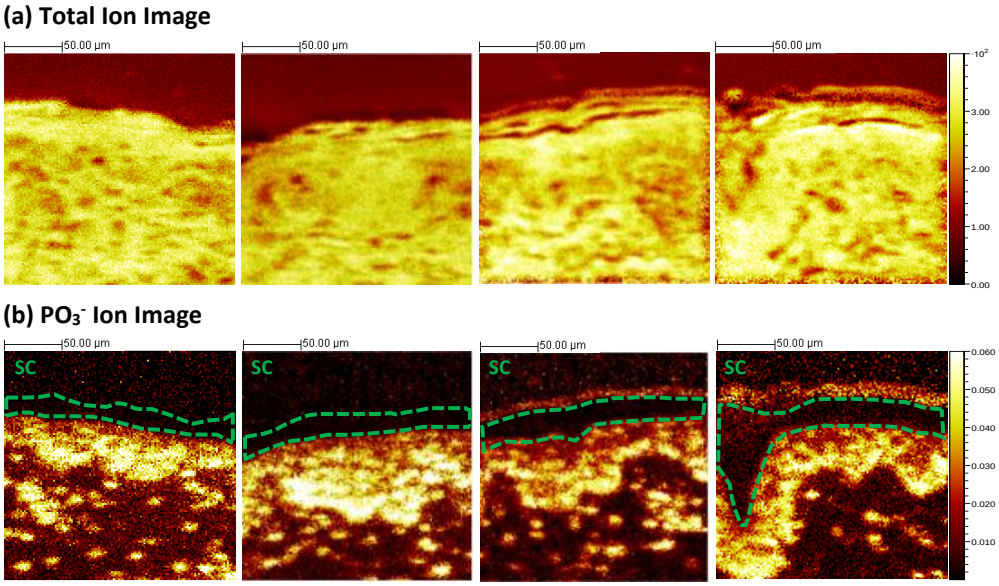

Figure 5.11 Example ToF-SIMS secondary ion images of multiple microtomed slices, illustrating (a) the total ion image and (b) the PO_3^- ion image, with the stratum corneum layer outlined in green.

Unfortunately, there were no ions that were specifically located in the *stratum corneum* but absent in the epidermis. However, as there are no lipid species that are uniquely located within the *stratum corneum*, this lack of distinct diagnostic ions is not entirely unexpected. Recent work by Sjövall *et al.* also demonstrated the use of ToF-SIMS surface analysis to detect localisation of lipid components from microtomed murine skin. They also indicated that phosphate fragments, such as PO_2^-, could be used to show localisation of phospholipids in the viable epidermis region. However, they were also able to show localisation of the negative C24:0 fatty acid molecular ion and other positive ceramide fragments in the *stratum corneum.* These ions were not detected in this study, but this may be due to variation in experimental parameters, including but not isolated to the sample preparation method. The work by Sjövall *et al.* used a cyrofixation method to prepare the samples, while the samples in this study were chemically fixed. In addition, the samples have been acquired from porcine skin, which is physiologically more relevant to human skin than the murine tissue used in their study. These are both factors which may have influenced the distribution of lipid components in the samples.

Some samples displayed a localisation of SO_4H^- in the region assumed to be the dermis, correlating with the decrease in PO_3^- intensity, as highlighted in Figure 5.12a and b. However, as illustrated in Figure 5.12c, this localisation was not apparent in all of the microtomed slices, the reason for which is unknown and would need further exploration.

The absence of the PO_3^- ion is therefore clearly indicative of the *stratum corneum* and its presence in the underlying epidermis reveals the position of the *stratum corneum*/epidermis interface. As the dermis also appears to contain some regions of intensity for this ion, the location of the dermoepidermal junction is less defined.

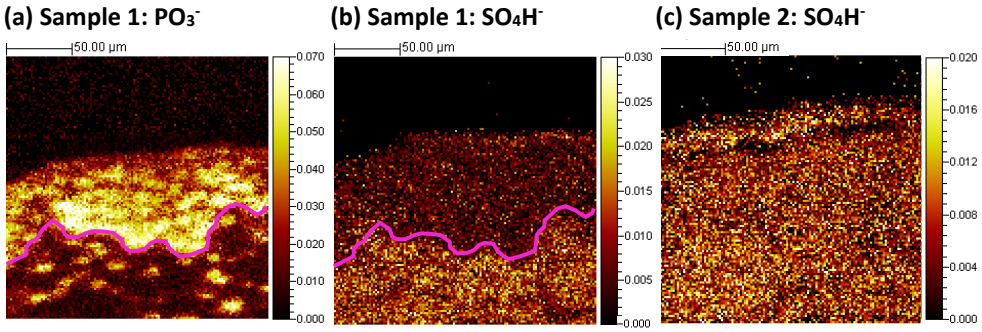

Figure 5.12 ToF-SIMS secondary ion images of two different microtomed slices showing the distribution of (a) PO_3^- in sample 1 (b) SO_4H^- in sample 1 and (c) SO_4H^- in sample 2, highlighting the variability in distribution for the SO_4H^- ion.

Elucidating the location of the *stratum corneum* in these microtomed samples confirmed the previous suggestion that this region was being sputtered slower than the remainder of the tissue. As previously discussed in section 5.3.1.1, the depth profile for the 10 µm slice indicated that the *stratum corneum* region had not been sputtered within the duration of the experiment. This is confirmed through examination of the secondary ion images for this sample. Figure 5.13a shows the PO_3^- ion with the elucidated position of the *stratum corneum* outlined in green. Figure 5.13b and c show both the CNO^- image, indicating the tissue and the SiO_2^- ion, indicating the glass, for the last 10 scans (100 sputter seconds) of the depth profile. As shown, the tissue is clearly still present and the underlying glass clearly still absent for the *stratum*

corneum region. This confirms that this region is being sputtered slower than other areas of the tissue. It was previously discussed that this difference in sputter rate could be the result of a non-uniform thickness within the tissue slice, relating to a problem with the embedding and slicing process. However, these images undoubtedly show that this uneven sputtering follows the shape and positon of the *stratum corneum* region exactly, confirming that this skin layer does sputter slower.

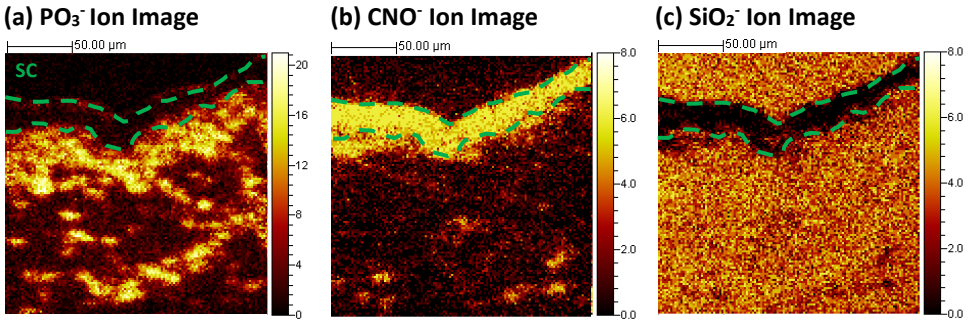

Figure 5.13 ToF-SIMS secondary ion images of a 10 µm microtomed slice, showing the distribution of (a) PO_3^- (b) CNO^- and (c) SiO_2^- for the final 100 sputter seconds of a depth profile. These images highlight the unsputtered stratum corneum region, demonstrating a slower sputter rate for this layer compared to the epidermis and dermis regions.

The positive polarity data also highlights the localisation of specific ions relevant to the layered structure of the skin tissue samples. There are also distinct markers in this polarity which indicate the location of both the glass substrate (Si^+) and the microtomed skin slice ($C_3H_8O^+$). Initial analysis of the secondary ion images suggest that the $C_3H_4S^+$ ion is specifically located in the *stratum corneum* layer, as illustrated in Figure 5.14c. However, overlaying this ion image with ion images for both glass (Fig. 5.14a) and tissue markers (Fig. 5.14b) reveals that in fact this ion is mainly localised on the surface of the microtomed sample, as illustrated in Figure 5.14d. This therefore suggests that it is related to a surface contaminant that was present before the tissue was embedded. Therefore, like the negative polarity, there does not appear to be any ions which are unique to the *stratum corneum* layer.

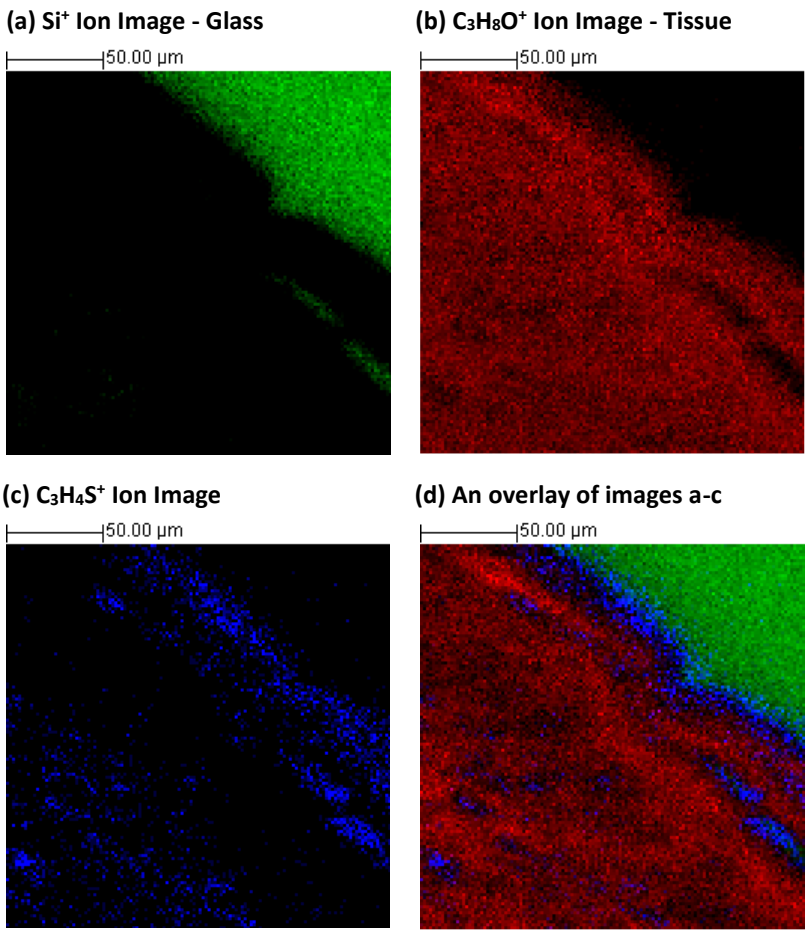

Figure 5.14 ToF-SIMS positive secondary ion images for an example microtomed slice, highlighting the spatial distribution of (a) Si^+ (glass) (b) $C_3H_8O^+$ (tissue) (c) $C_3H_4S^+$ and (d) an overlay of images a-c.

There are, however, ions in the positive polarity that appear to localise in both the proposed epidermis ($NaPO_3H^+$) and dermis ($C_5H_{10}^+$) regions, as highlighted in Figure 5.15. The $NaPO_3H^+$ ion is very similar in structure to the PO_3^- ion observed in the negative polarity and is again suggested to be related to the phospholipid class of compounds. This ion also localises in a region measuring ~ 50 µm (Fig. 5.15b), located in a similar position on the microtomed slice as observed for the PO_3^- ion. This confirms that these phosphate ions can be used to elucidate the location of the phospholipid-rich epidermis and consequently the phospholipid-deficient *stratum corneum.*

The $C_5H_{10}^+$ ion also shows a localised spatial distribution, as demonstrated in Figure 5.15a, in the region which is believed to relate to the dermis. As this fragment is a generic hydrocarbon chain it cannot be uniquely attributed to a

specific compound or even class of lipid. However, as shown in the overlaid image (Fig. 5.15d) the onset of increased intensity for $C_5H_{10}^+$ does correlate with the end of the $NaPO_3H^+$ intensity, which supports the suggestion that the decrease in phosphate intensity is an indication of the dermoepidermal junction. As the negative polarity data was primarily used to correlate sputter time with depth for these microtomed samples, there is only one repeat data set in the positive polarity. However, the localisation of the ions found are closely matched to the repeated trends in the negative polarity data and therefore it can be confidently assumed that these are physiologically relevant findings.

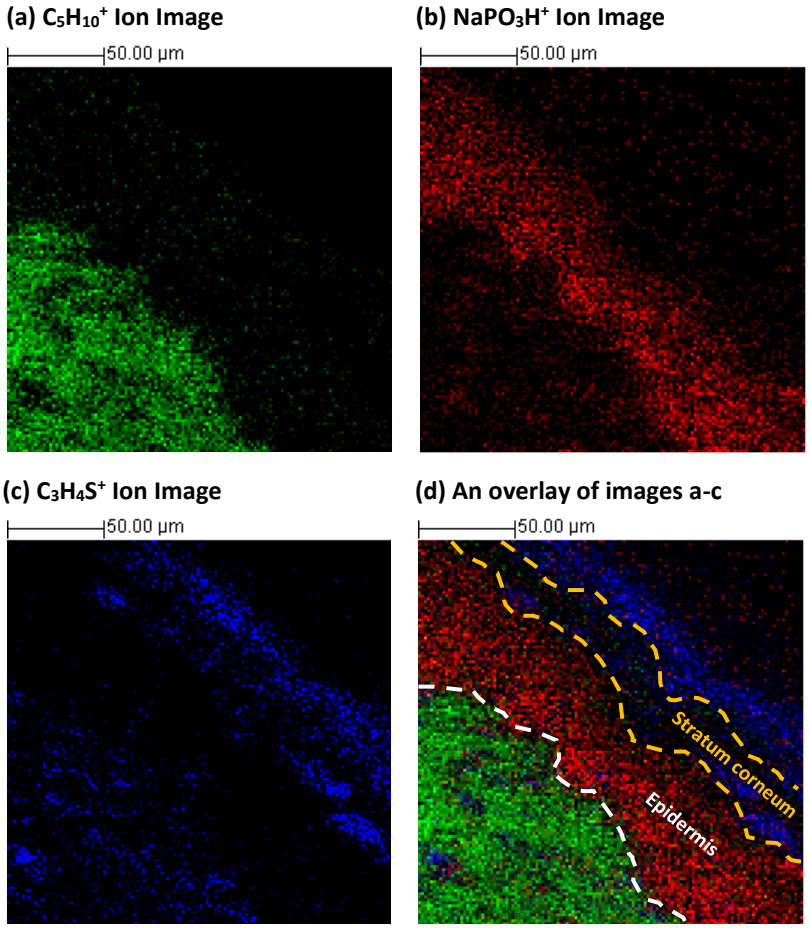

Figure 5.15 ToF-SIMS positive secondary ion images for an example microtomed slice elucidating the different skin layers by highlighting the spatial distribution of (a) $C_5H_{10}^+$ (b) $NaPO_3H^+$ (c) $C_3H_4S^+$ and (d) an overlay of images a-c.

5.3.2.2 Depth profile analysis of whole tissue sections

Following the identification of possible biomarkers from the microtomed samples, depth profile analysis was conducted on whole skin sections to examine whether these ions could also be monitored as a function of tissue depth. Multiple repeat samples were tested using various sputter beam settings, as detailed in section 5.3.3, and for all samples a significant increase in PO_3^- could be observed as a function of depth.

Figure 5.16 shows example negative data acquired from depth profile analysis of *ex vivo* tissue using the final optimised sputter beam settings (20 keV, Ar_{1900}, TC 10 nA). Using these settings, the increase in PO_3^- intensity (Fig. 5.16a) repeatedly occurs at range of sputter times which are close in value to previously reported *stratum corneum* depths, using the sputter rate calculated in section 5.3.1.2 as a guide. For example, the sputter time shown in Figure 5.16a is 295 seconds. Using the previously calculated sputter rate of 0.15 µm/s, this equates to a *stratum corneum* region of 44 µm. Although this is possibly slightly thicker than expected, it is still a reasonable value given that the sputter rate calculated in section 5.3.1.2 is not directly relevant to all samples. This therefore supports the suggestion that PO_3^- can be used as a marker to indicate the *stratum corneum*/epidermis interface in depth profile analysis. As highlighted previously, it is believed that there is a residual layer of phosphate related material on the surface of the skin or possibly absorbed into the early *stratum corneum* layers, resulting from atmospheric contaminants. This would explain the initial high intensity for this ion, which rapidly decreases.

Numerous low mass ions that are abundant in biological material, such as CN^-, CNO^-, CHO_2^- and CH_4N^-, can be used as generic tissue markers. As illustrated in Figure 5.16b, these ions maintain a constant intensity, confirming the presence of tissue material, throughout the sputtering process. This stable ion intensity also confirms that the increase observed for PO_3^- is physiologically relevant and not an artefact of the data.

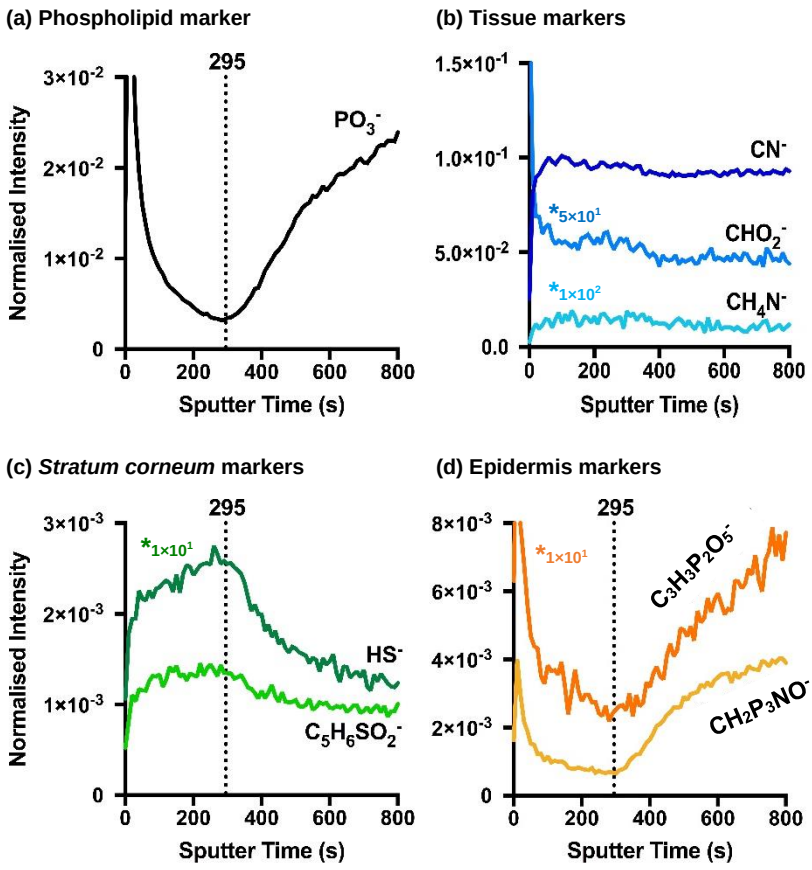

*Figure 5.16 ToF-SIMS negative depth profile data of porcine ex vivo tissue showing the change in ion intensity as a function of depth for (a) PO_3^- (phospholipid marker) and other biomarkers which represent (b) generic tissue (c) the stratum corneum and (d) the epidermis. The * denotes an intensity scaling factor.*

In general, it was difficult to find variations in ion intensity in either polarity that were repeatable across different samples. The lipid classes in the skin are all very similar in structure and, apart from a noticeable phospholipid absence in the *stratum corneum*, they do not differ greatly between different skin layers. Therefore, it is not surprising that there is a lack of significant changes observed with depth. In addition, the non-uniformity in thickness of skin layers across a sample may also conceal any subtle changes.

There are several negative ions, however, that do appear to show repeatable variation in intensity with skin depth. Interestingly, the change in the intensity of these ions occurs at the same sputter time associated with the change in PO_3^- intensity, correlating to the *stratum corneum*/epidermis interface. It is

hard to uniquely identify these fragments as there are numerous possible atom combinations which are within an acceptable ppm deviation from the mass value. However, ions which exhibit a decrease in intensity appear to be sulfur containing fragments, shown in Figure 5.16c. Whereas, the ions that show an increase in intensity are believed to be phosphate related fragments, shown in Figure 5.16d. These phosphate fragments display the same trend as the PO_3^- intensity, which again supports the assignment of this ion to the phospholipid class of compounds.

Several ions exhibited changes in intensity that appeared to be localised within an individual sample and not repeatable across all the samples analysed. It is therefore proposed that these ions are related to non-native species that have contaminated individual samples. Figure 5.17 shows example depth profile data from a proposed contaminated sample. This sample contained several ions that exhibited the same trend, illustrated by the ClO_3H^- ion in Figure 5.17. These ions are all proposed to be Cl containing fragments, as they produced peaks which correlate to the ^{35}Cl and ^{37}Cl isotope pattern. These ions all demonstrated a 'step-like' intensity increase as a function of depth, illustrated by the ClO_3H^- ion in Figure 5.17. As stated, this trend was not observed in other samples. However, as highlighted in Figure 5.17, the initial increase in intensity for these ions occurs at the same sputter time as the increase in phosphate fragments and the decrease in sulfate fragments. The fact that the change in intensity for all of these ions occurs at the same depth within the skin, further supports the idea that this depth is associated with a transition between skin layers, specifically the *stratum corneum*/epidermis interface.

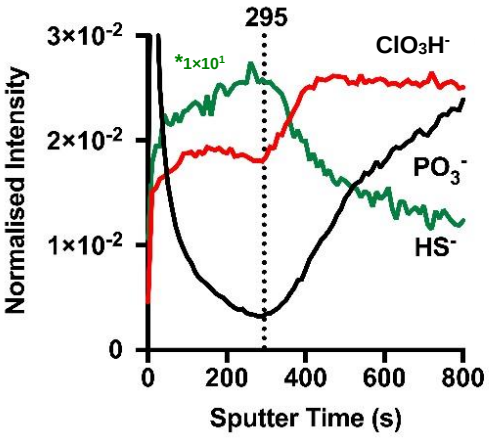

Figure 5.17 ToF-SIMS negative depth profile data from a proposed contaminated sample, highlighting the correlation in intensity for PO_3^-, HS^- and ClO_3H^-.

Unfortunately, no significant trends could be identified in the initial positive depth profile data, including ions highlighted as possible biomarkers in the microtomed sample analysis. The reason for this is unclear, but one possible explanation may be the obstruction of peaks due to the presence of other components within the whole tissue section. The microtomed sample analysis highlighted $NaPO_3H^+$ as a potential biomarker localised within the epidermis region. However, unlike the PO_3^- ion, there is a lack of intensity increase observed, as illustrated in Figure 5.18a. Examination of the spectra indicates that this may be due to the presence of a single broad peak in the whole tissue section, compared to the two resolved peaks in the microtomed sample, as shown in Figure 5.18b.

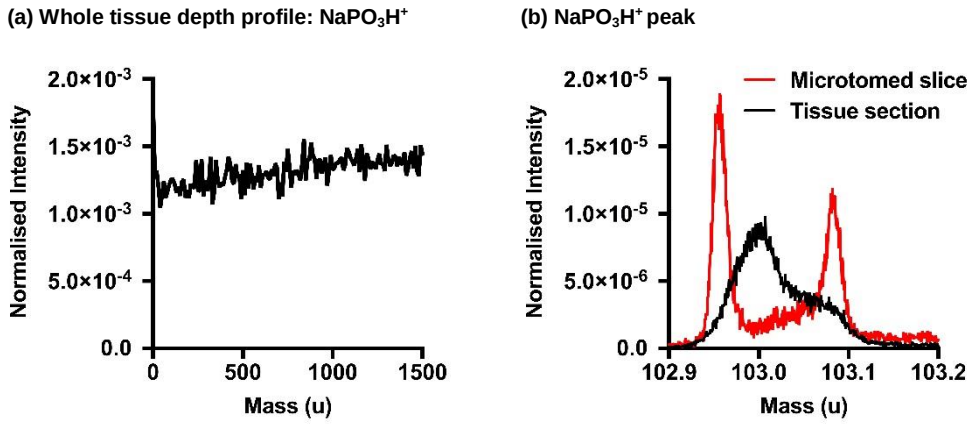

Figure 5.18 ToF-SIMS positive depth profile data for $NaPO_3H^+$ showing (a) the change in intensity as a function of depth and (b) the peak shape for both a microtomed sample and whole tissue section.

The aim of this work was to develop a suitable depth profile method for *ex vivo* skin tissue, to allow the permeation of active compounds to be monitored as a function of depth. Analysis of native lipids as a function of skin depth was therefore not the primary focus. This work has touched upon some interesting trends in ion intensity, but these have not been explored further due to the scope of the project. However, this native analysis has confirmed the use of PO_3^- as an internal biomarker for the end of the *stratum corneum* and the start of the underlying epidermis. This is a hugely important discovery as it removes the need to rely on calculated sputter rates and provides the individual location of the *stratum corneum*/epidermis interface, tailored to each individual sample analysed. However, using the sputter rate calculated in section 5.3.1.2, the PO_3^- increase does correlate to a physiologically relevant depth for the *stratum corneum* which indicates that, although not completely accurate or specific to individual samples, the calculated sputter rate can be used to roughly estimate the sputtered depth.

5.3.3 Optimisation of argon beam settings

The sputter rate of the material can vary significantly depending on the beam settings used. There are four key parameters that can be changed, beam energy, beam current, cluster size and crater area. The sputter rate chosen for a

sample is a fine balance between the analysis time and the depth resolution achieved. A high depth resolution is achieved at the expense of a fast acquisition time, but the lower the resolution the quicker the analysis time. For this work, the aim of conducting depth profile analysis on skin tissue is to compare the permeation of active compounds through the *stratum corneum* and determine whether the compounds pass into the underlying epidermis. In order to establish dynamic SIMS as a viable method to monitor skin permeation, the technique needs to cover a substantial depth in a reasonable time, to allow efficient analysis of multiple repeat samples. However, an adequate depth resolution is also needed to accurately compare the permeation between different samples and also monitor the permeation between different skin layers.

Keeping the sputter area constant at 500 µm × 500 µm, several combinations of beam settings were trialled, in order to find an intermediate sputter rate suitable for profiling to a significant tissue depth, whilst maintaining a high enough resolution to identify the *stratum corneum*/epidermis interface clearly. The initial settings trialled were those employed by Brunelle *et al.* [204] for the analysis of rat brain tissue, specifically a 10 keV Ar_{1455} beam, which produced a measured target current of 8.4 nA. An example skin tissue depth profile using these settings is shown in Figure 5.19a and indicates the onset of the PO_3^- increase at ~ 1900 sputter seconds. Therefore, to profile through the *stratum corneum*, using these settings, the acquisition time would be ~ 45 minutes. Franz cell permeation experiments typically involve multiple repeat samples. In order to objectively compare these samples they would need to be analysed on the same day, to prevent any variability occurring through storage. Multiple analytical repeats would also need to be collected per sample. Therefore, an acquisition time of 45 minutes for one repeat would not enable efficient analysis.

Both the beam energy and cluster size were then increased (Fig. 5.19b-d) which increased the measured target current and subsequently decreased the sputter time associated with the PO_3^- increase. The highest beam energy and cluster size combination produced a target current of 20 nA and an increase in PO_3^- intensity after ~ 60 sputter seconds (Fig. 5.19d), which experimentally is

a more acceptable time to enable efficient analysis of multiple samples. However, this sputter time equates to the collection of 6 data points for the whole *stratum corneum* which, assuming a *stratum corneum* depth of ~ 20-30 µm, is in the region of one data point every 3-5 µm. Typically reported corneocyte layer thicknesses have shown to be ~ 1 µm (section 1.2.1) and therefore these settings would not enable the collection of data on a layer-by-layer basis. To maintain an efficient speed the high beam energy and cluster size were kept constant and instead the target current was manually reduced (Fig. 5.19e-f) until an acceptable sputter time for the PO_3^- increase was achieved. The final optimised settings are a beam energy of 20 keV, cluster size of 1900 atoms and a specified target current of 10 nA. As shown in Figure 5.19f, this results in a sputter time of ~ 170 seconds needed to pass the *stratum corneum*, which theoretically should offer a depth resolution closer to the layer-by-layer analysis required. These settings were all tested on different porcine ear samples, which may explain why there was no significant difference in sputter time observed between the profiles shown in Figure 5.19e and f.

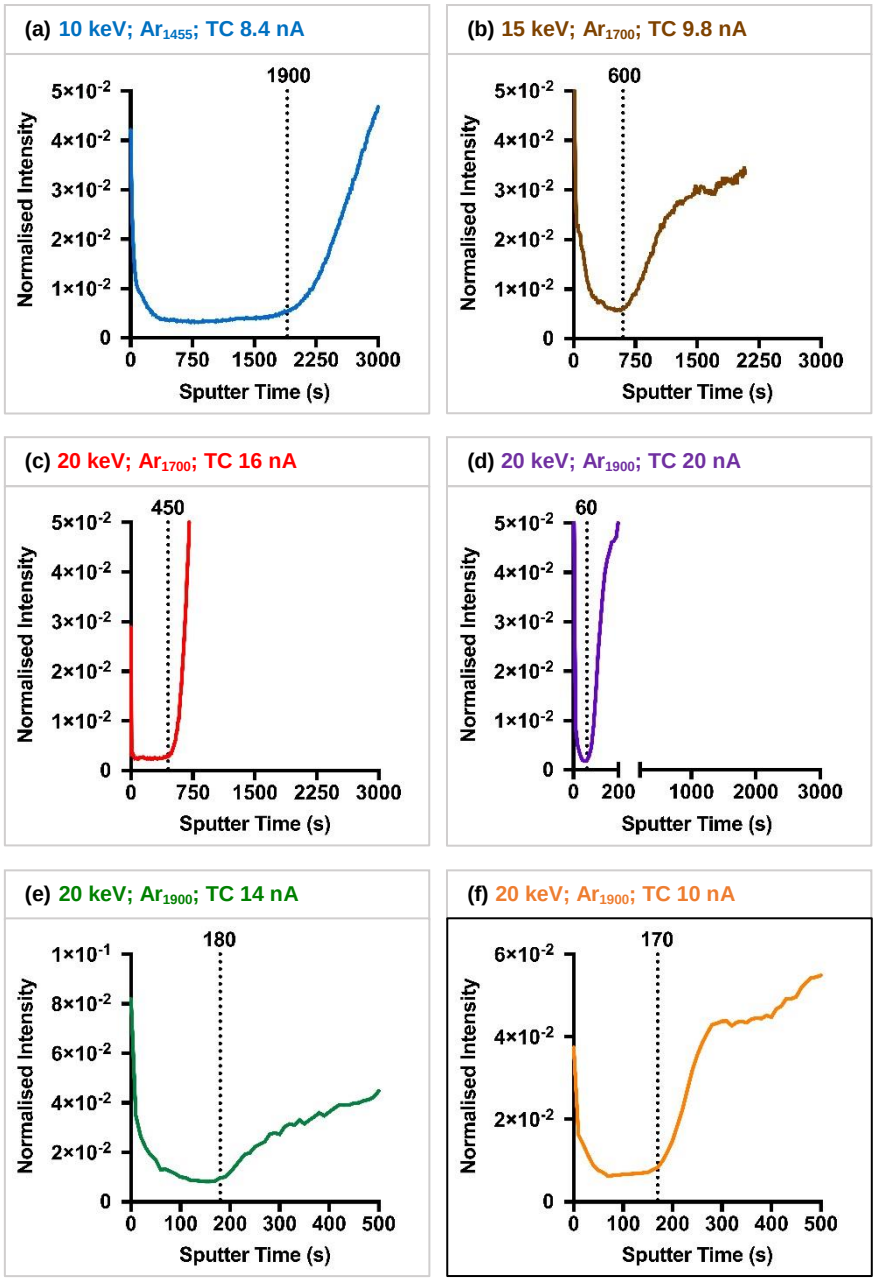

Figure 5.19 ToF-SIMS depth profile data for porcine ear tissue displaying the change in intensity with sputter time for PO_3^- using six different argon beam settings.

5.3.4 Frozen hydrated vs. dehydrated samples

One of the main disadvantages regarding ToF-SIMS analysis of biological materials is the ultra-high vacuum conditions required. As discussed in section 5.1, the use of a cyro-SIMS method to analyse frozen hydrated samples has shown to enhance the detection of native biological species. Therefore, a frozen hydrated sample was compared to a standard dehydrated sample, to

understand whether the cyro-SIMS method offered any advantages for the analysis of the skin tissue samples used in this project. The final optimised argon beam settings (20 keV, Ar_{1900}, TC 10 nA) were used for both samples and data was acquired in both the positive and negative polarities. In order to minimise variability originating from the sample, analysis was conducted on adjacent sections of a single skin tissue sample. A visual comparison was conducted between the depth profiles produced and also between the spectra for individual skin layers.

Negative depth profile data obtained for both the dehydrated (Fig. 5.20a) and frozen hydrated (Fig. 5.20b) samples demonstrates that both methods produced the significant increase in PO_3^- intensity attributed to the *stratum corneum*/epidermis interface. In addition, this increase was observed at roughly the same depth for both samples.

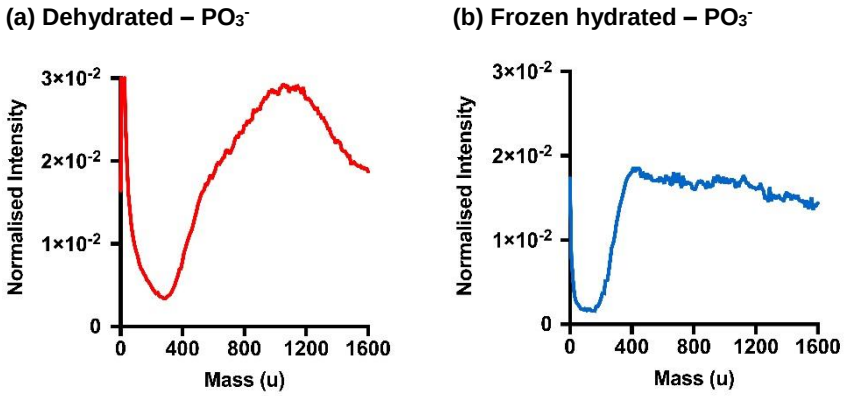

Figure 5.20 ToF-SIMS depth profile data showing the change in intensity for PO_3^- as a function of depth for (a) a dehydrated and (b) a frozen hydrated porcine skin sample.

In order to compare the spectral information for different skin layers, data was exported from various points within the depth profile, guided by the change in PO_3^- intensity. The spectra for these samples are dominated by lower mass peaks, with no significant peaks observed above *m/z* = 200 for either polarity. The negative spectra only has been presented for the *stratum corneum* and epidermis regions, shown in Figure 5.21 and Figure 5.22 respectively. The spectra has been split into two smaller sections of *m/z* 0-100 and 100-200 to enable a more detailed comparison. Visual inspection of both polarities

revealed that for both skin layers, there were no significant differences between the two sample types, with no new or absent peaks apparent. The ion yields were also relatively similar between the two samples with no obvious enhancement for any of the peaks in either data set.

It was therefore decided not to use the frozen hydrated preparation method, as there were no apparent advantages from the initial data. If the main focus of this work was to characterise the lipid composition of the skin as a function of tissue depth, then a more detailed study would have been needed to fully investigate the effects of the sample preparation method. However, as the focus of this work is to monitor the permeation of an active compound through the tissue, as long as all the samples are prepared using the same method, any comparisons made between samples are deemed to be relevant.

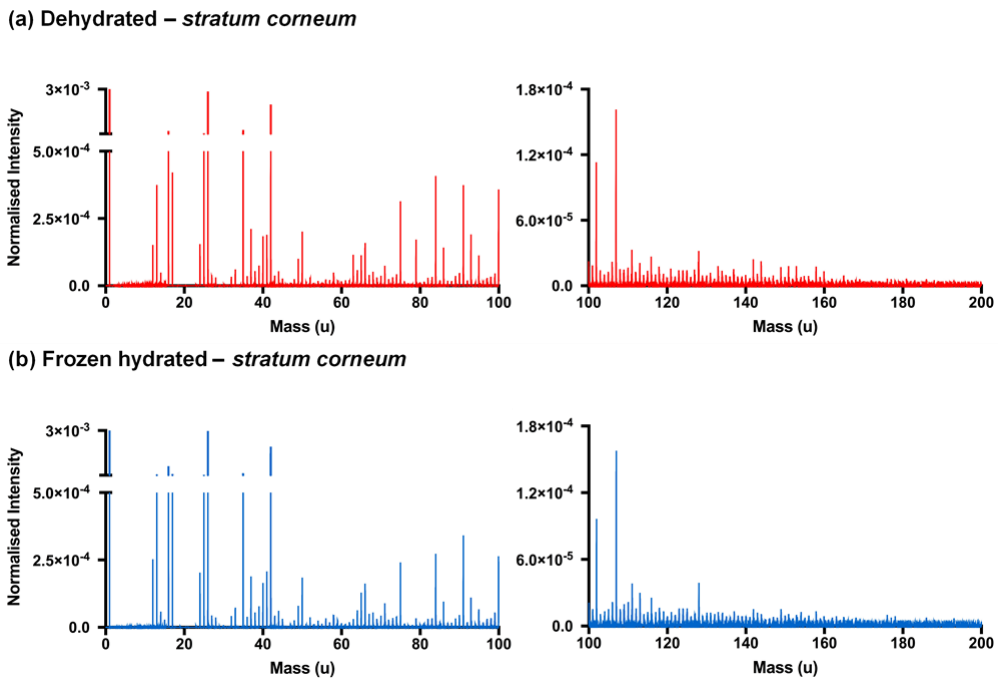

Figure 5.21 ToF-SIMS negative spectra acquired from the stratum corneum region of a (a) dehydrated and (b) frozen hydrated porcine skin sample following depth profile analysis.

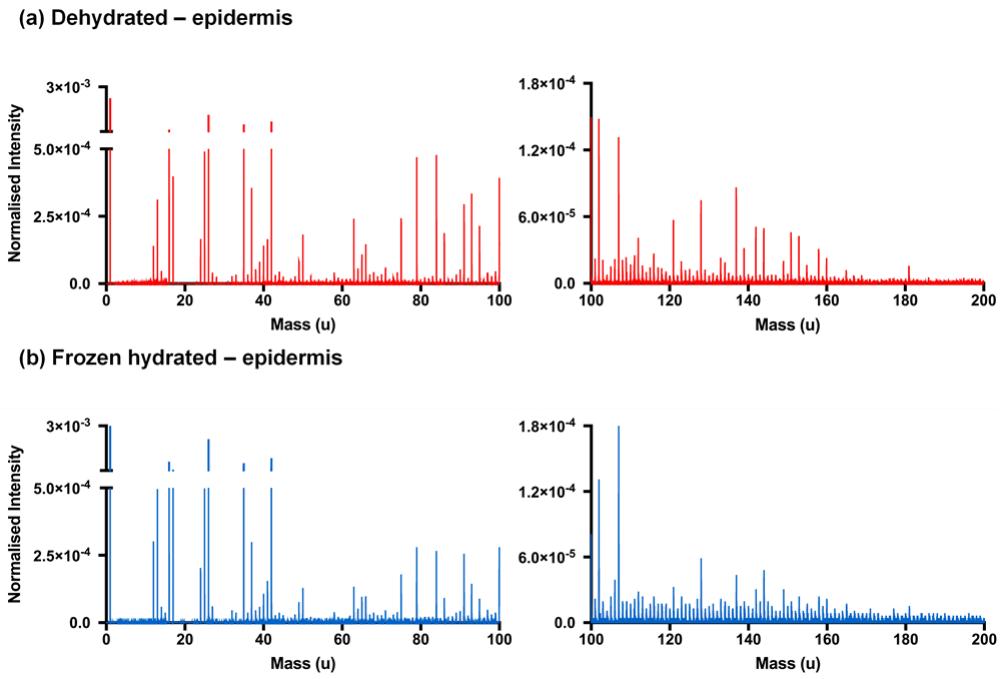

Figure 5.22 ToF-SIMS negative spectra acquired from the epidermis region of a (a) dehydrated and (b) frozen hydrated porcine skin sample following depth profile analysis.

5.4 Conclusions

This study has demonstrated that dual beam dynamic SIMS can be successfully applied to produce a 3D chemical profile of *ex vivo* skin tissue.

Optimisation of several experimental parameters, such as beam energy and beam cluster size, was achieved and it was demonstrated that there were no chemical differences between skin tissue samples that had been dehydrated or analysed as frozen hydrated.

In order to accurately relate this chemical information to the depth of skin tissue analysed, an attempt was made to measure the sputter rate using two different approaches. The use of optical profilometry to measure the sputtered crater appeared to provide a consistent sputter rate, despite inherent variation in tissue depth, both within an individual sample and between samples. However, analysis of microtomed skin slices suggested a slower sputter rate for the *stratum corneum* layer, suggesting that a single sputter rate applied to the whole depth profile may not be accurate.

ToF-SIMS surface analysis of microtomed slices containing multiple skin layers illustrated the localised presence of phospholipid related ions in the viable epidermis, which were absent in the *stratum corneum*, correlating to the known physiological composition of the skin. It was then demonstrated that these phospholipid related ions could be used as inherent markers in the depth profile analysis, due to an increase in the intensity of these ions correlating to the *stratum corneum*/epidermis interface.

This study has therefore established a suitable protocol for the depth profile analysis of *ex vivo* skin tissue, which can now be applied to monitor the permeation of exogenous compounds into the skin following permeation studies.

Chapter 6: Monitoring the permeation of vitamin C derivatives through both *ex vivo* and *in vivo* skin tissue

6.1 Introduction

The current method employed to assess the permeation of a topically applied active ingredient, both pharmaceutical and cosmetic, is to conduct an *in vitro* permeation study using *ex vivo* tissue (section 1.3.2). These studies offer a platform for the initial assessment of topical actives and formulations, especially those containing pharmaceuticals that may have not yet proved toxicologically safe for *in vivo* human application. *In vitro* studies also allow quick, large scale investigations to be carried out on multiple repeat samples without the need to recruit large numbers of human volunteers. Typically, a liquid chromatography mass spectrometry based technique is subsequently employed to quantify the amount of compound that has permeated through the tissue into the receptor solution, remained in the viable tissue layers, partitioned into the *stratum corneum* and remained in the donor solution. This analysis is termed skin fractionation.

One disadvantage of this currently used *in vitro* technique relates to the analysis of the *stratum corneum* layer. This layer is the biggest challenge facing the permeation of most compounds, yet a detailed permeation profile of a compound through this layer into the underlying epidermis is not obtained. The concentration of a compound within individual tape strips is typically under the limit of detection for chromatographic analysis and therefore sequential tape strips are pooled to quantify the concentration of compound in the total *stratum corneum* layer. In addition, these chromatographic based methods do not provide any information on the spatial distribution of a compound within the skin tissue. These are both important considerations in the design of cosmetic formulations in particular. These formulations require permeation and localisation of a compound into the upper layers of the skin only and the uniformity in distribution of the compound within the skin layer is important for its efficacy as a cosmetic.

The development of cosmetic anti-aging formulations is a growing market. These formulations aim to exploit the use of naturally occurring skin components to rejuvenate the clinical appearance of aging skin, with varying success. One commonly used active ingredient in these formulations is vitamin C (ascorbic acid). This compound is well established as a natural antioxidant within skin tissue [275] and numerous studies have demonstrated its protective role against UV and oxidative stress [276-278]. Additionally, it has shown regenerative effects on aged tissue when applied topically to the skin via the stimulation of collagen synthesis [279,280] and clinical improvements in the microstructure of the skin [281,282]. Due to its proficiency as an antioxidant it is readily oxidised, especially in aqueous solutions. Therefore, when formulated for topical application, rapid degradation of the compound occurs, which drastically reduces the shelf life of the product. There have been numerous studies to try and improve the stability of this compound for delivery to the skin, including incorporation into novel delivery vehicles such as liposomes [283] and encapsulations [284,285]. The most popular method employed in the cosmetics industry is the use of ascorbic acid derivatives [286]. These are typically ester derivatives that are proposed to be enzymatically converted to ascorbic acid within the skin. The clinical effects of some of these derivatives have been demonstrated, as reviewed by Farris [287], with some already used in cosmetic products on the market. However, their permeation efficiencies and mechanisms of action are still largely unknown.

This study looks to assess the permeation of ascorbic acid and three ester derivatives of varying weights and lipophilicities, specifically ascorbyl glucoside, ethyl ascorbic acid and sodium ascorbyl phosphate. The structures and corresponding molecular weights of these four compounds of interest are illustrated in Figure 6.1

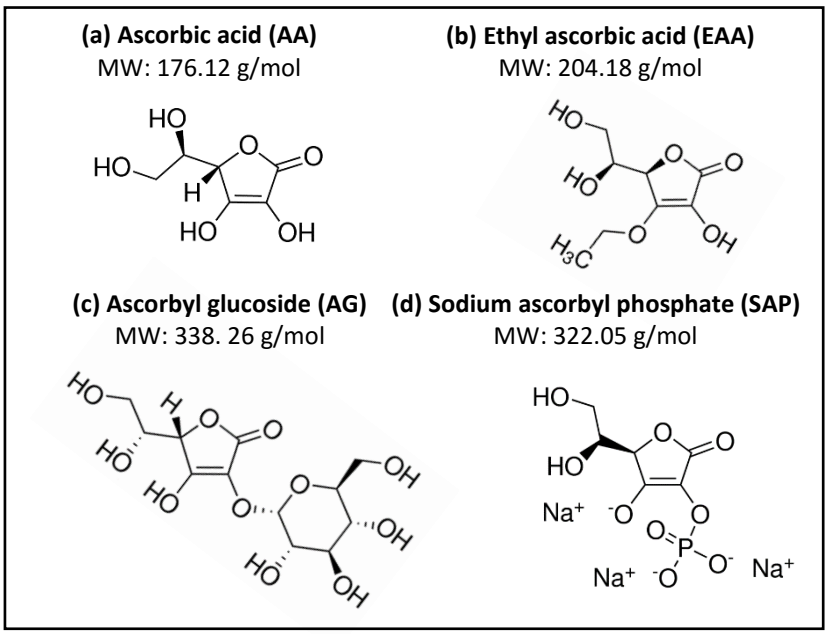

Figure 6.1 The chemical structures and molecular weights (MW) of the four compounds of interest (a) ascorbic acid (b) ethyl ascorbic acid (c) ascorbyl glucoside and (d) sodium ascorbyl phosphate.

Differences in the permeation efficiency of these four compounds have been acknowledged within the cosmetics industry [288]. However, there is no published data which demonstrates a direct comparison between all four. All four compounds have been shown to permeate into the skin to some extent in *ex vivo* tissue, as discussed in a review by Stamford [289]. Ascorbic acid has demonstrated rapid permeation into skin tissue despite its hydrophilicity [290]. Although Foco *et al.* demonstrated the permeation of sodium ascorbyl phosphate through heat separated porcine epidermis [291] it is recognised as poorly permeating in comparison to ascorbic acid [288,289]. Ethyl ascorbic acid is the most novel of the four compounds and has not yet been formulated into a cosmetic product. Although it has been shown to offer increased permeation over ascorbyl glucoside [292] there is no data comparing either of these two derivatives relative to ascorbic acid. It is clear therefore that the permeation efficiencies of these derivatives are still relatively unexplored and further investigation is needed into both their permeation and mechanism of action to facilitate improved design of cosmetic formulations.

6.2 Chapter aims

The main aim of this study is to explore whether the permeation of an exogenous compound can be monitored through *ex vivo* skin tissue using the dynamic SIMS method developed in chapter 5, following a traditional permeation experiment.

This study will explore whether this novel application of ToF-SIMS can provide relevant depth information to discriminate between the permeation profiles of several structurally related cosmetic ingredients with known differences in permeation efficiency. These compounds of interest are ascorbic acid and three derivatives, specifically ascorbyl glucoside, ethyl ascorbic acid and sodium ascorbyl phosphate.

The use of this technique will also be applied to assess the delivery of ascorbic acid to the skin from three different formulations, one laboratory based formulation (phosphate buffered saline), one novel formulation (a supramolecular gel) and one established 'off-the-shelf' cosmetic formulation (The Body Shop® Vitamin C 10 Day Glow Boosting Concentrate).

The permeation of ascorbic acid, from an 'off-the-shelf' cosmetic product, applied *in vivo* to human volunteers will then be monitored using the static SIMS method to analyse sequential *stratum corneum* tape strips.

6.3 Results and discussion

The dual beam dynamic SIMS method developed in chapter 5 demonstrated the successful depth profile analysis of native *ex vivo* skin. It was therefore proposed that this method could also be applied to post-Franz cell *ex vivo* skin, in order to detect the permeation a compound as a function of skin depth. This would offer the potential to acquire a detailed permeation profile for a compound through the *stratum corneum* and underlying epidermis, as well as provide spatial distribution information, both advantages over typically employed chromatographic methods.

As detailed in section 6.1 the compounds of interest chosen for this study were ascorbic acid, ethyl ascorbic acid, ascorbyl glucoside and sodium ascorbyl phosphate (Fig. 6.1a-d respectively). From hereon in they shall be abbreviated to AA, EAA, AG and SAP as denoted in Figure 6.1. The ToF-SIMS depth profile method was therefore applied to *ex vivo* tissue that had been treated with these four compounds in order to establish whether their different permeation efficiencies could be elucidated using this method.

6.3.1 Reference spectra acquisition for the compounds of interest

Before depth profile analysis was conducted it was first necessary to establish diagnostic ions in the ToF-SIMS spectra for all of the four compounds. Surface analysis was initially conducted on the raw materials in both negative and positive polarity (Figures A-2 and A-3). For AA, AG and EAA the negative spectra produced distinct peaks for the molecular ion $[M-H]^-$. However, the $[M+H]^+$ molecular ion in the positive spectra was only present for AG. The molecular ion for SAP was not present in either the negative or the positive spectra. The spectra for this compound was instead dominated by peaks at $m/z < 200$ relating to various phosphate fragments. As the PO_3^- ion intensity is used to indicate the *stratum corneum*/epidermis interface and as most of the compounds ionised more efficiently in the negative polarity, it was decided that the negative polarity only would be used to conduct the depth profile analysis.

The spectrum produced for a compound can often vary greatly between the raw material and the compound within its specified environment. This environment can enhance or suppress the intensity of ions or even change the fragmentation pattern of a compound, a phenomenon termed the matrix effect, discussed in section 1.5.6. Therefore, it was important to establish whether the diagnostic ions present in the raw material spectra were also detectable once the compound was within a skin tissue matrix. ToF-SIMS analysis therefore needed to be conducted on these compounds in a skin tissue environment. Superficially doping a skin sample with a compound solution was not considered an adequate method. This method may lead to a deposited layer of the compound on the surface which, due to the surface sensitivity of ToF-SIMS, would result in analysis of the compound outside the tissue matrix. A tissue homogenisation method was therefore developed in house, described in section 2.2.2.5, which enabled the uniform mixing of a skin tissue homogenate with a compound solution. Evaporation of the solvent produced a dry material containing the compound embedded within a skin tissue matrix, which was then subjected to ToF-SIMS surface analysis. In order to compare the relative ion intensities for the diagnostic ions of each compound, the samples were prepared using the same compound concentration, which after solvent evaporation equated to a compound/tissue ratio of 0.08 mg/1 mg.

The spectra produced for the four compound/skin homogenate samples confirmed that the diagnostic ions produced in the raw material spectra were still detectable from the compound within a skin matrix. The peaks from these diagnostic ions are displayed in Figure 6.2, alongside spectral data produced from a skin tissue sample treated with PBS, the chosen Franz cell medium. As the intensity of the peak is calculated by the total area under the curve and not the peak height, the intensity value for each peak is also displayed. The molecular ion is still present at a significant intensity for AA ($C_6H_7O_6^-$), AG ($C_{12}H_{17}O_{11}^-$) and EAA ($C_8H_{11}O_6^-$) as shown in Figure 6.2a-c respectively. Importantly, there is a negligible intensity produced for each of these ions in the PBS-treated sample, which confirms that they can be used diagnostically to indicate the presence of the respective compounds within skin. An ion diagnostic of SAP was harder to determine in the negative polarity, as the

spectra was largely dominated by phosphate fragments which were also present to some extent in the PBS-treated skin spectrum. The ion chosen to represent SAP in this study was $NaPO_3H^-$ (Fig. 6.2d). A larger fragment is typically preferred as a diagnostic ion, as it represents a more intact structure and is therefore less likely to originate from another source. However, this particular ion was one of the few in the spectrum that displayed a significant intensity compared to the PBS-treated tissue sample.

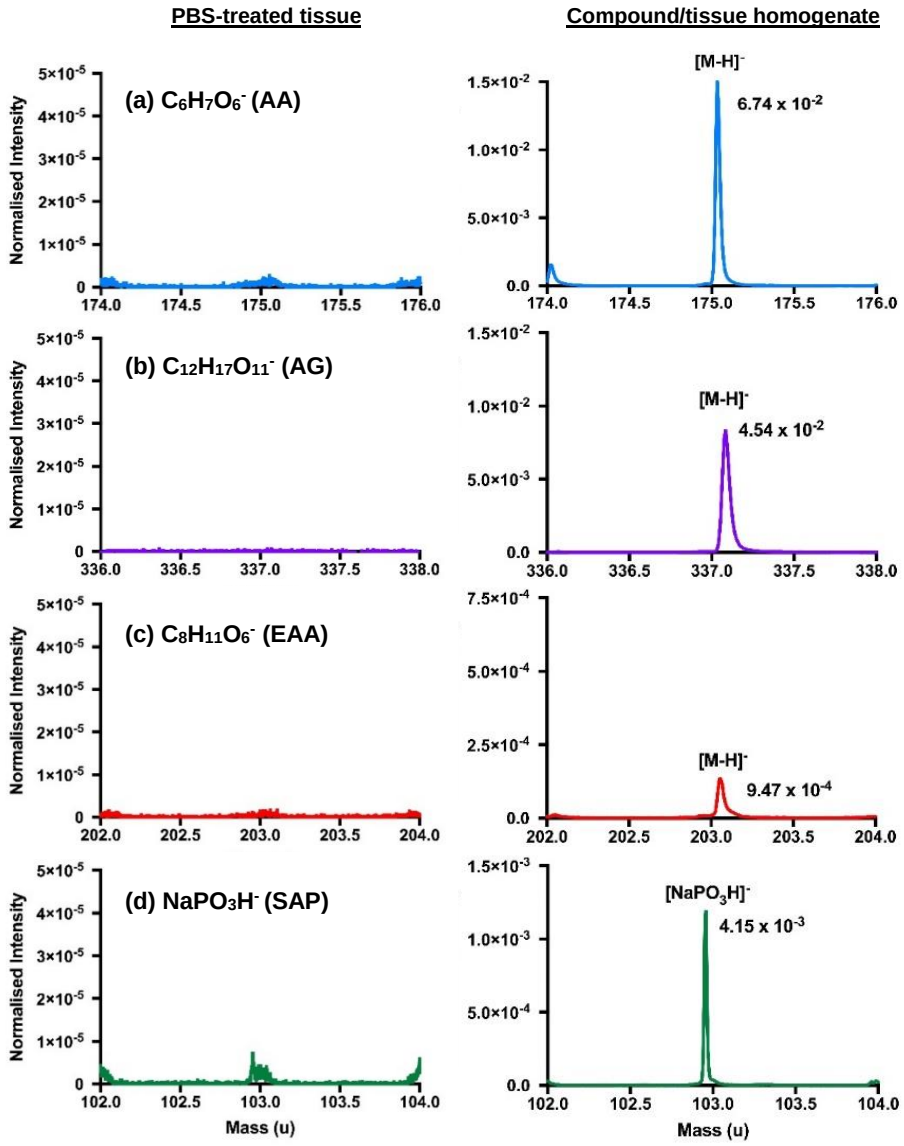

Figure 6.2 ToF-SIMS spectra acquired from surface analysis of porcine ear skin/compound homogenate reference samples for the four different compounds of interest compared to a PBS-treated skin sample, showing the peak intensities for the diagnostic ions (a) $C_6H_7O_6^-$ (AA), *(b) $C_{12}H_{17}O_{11}^-$ (AG), (c) $C_8H_{11}O_6^-$ (EAA) and (d) $NaPO_3H^-$ (SAP).*

Comparing the relative intensity of each ion, it is apparent that both AA and AG produce an ion intensity at least one order of magnitude greater than EAA and SAP. As the concentration of the compounds are all equal, this suggests that within skin tissue AA and AG exhibit a greater ionisation efficiency than EAA and SAP. This therefore must be taken into account when attempting to compare the permeation of these compounds using ToF-SIMS.

6.3.2 The effects of PBS on the native PO_3^- ion

As established in chapter 5 (section 5.3.2.2), when conducting depth profile analysis of *ex vivo* skin tissue, an increase in the phospholipid related PO_3^- ion identifies the *stratum corneum*/epidermis interface. As the *stratum corneum* contains no phospholipids, an increase in the intensity of this ion is observed when the sputter beam has penetrated into the relatively phospholipid-rich underlying epidermis. Assessing the ion intensity of a compound after this observed PO_3^- increase can therefore determine whether it has permeated beyond the skin's most significant barrier, the *stratum corneum*.

The chosen medium for the Franz cell permeation studies is phosphate buffered saline (PBS). At a pH of 7.4, this is a physiologically relevant medium typically employed in permeation studies, especially those involving hydrophilic compounds [111]. However, PBS contains sodium hydrogen phosphate ($Na_2HPO_4^-$) amongst other salts and it was therefore anticipated that the presence of this compound in the tissue may contribute to the PO_3^- intensity observed. Preliminary analysis was therefore conducted to determine whether the presence of PBS in the tissue would affect the PO_3^- ion intensity change as a function of depth.

Depth profile analysis was conducted on both a blank control tissue sample and one that had been treated with PBS in a Franz cell experiment. As demonstrated in chapter 5, variation in tissue depth occurs both within an individual porcine ear and between different ears. In order to minimise any difference in PO_3^- ion intensity caused by biological variance, the two samples were prepared from adjacent sections of the same pig ear and three analytical repeats were conducted per sample. Figure 6.3a illustrates depth profile data

produced for the blank control sample, showing the intensity of PO_3^- as a function of depth. The vertical grey region between the two dotted lines indicates the time period in which the increase in PO_3^- ion is observed for the three analytical repeats, hence the possible location of the *stratum corneum*/epidermis interface. Figure 6.3b displays the PO_3^- depth profiles for the PBS-treated sample, with the *stratum corneum*/epidermis interface for the blank control sample also shown. The profiles for the PBS-treated sample demonstrate that the increase in PO_3^- ion does not correlate to that shown for the control sample and in fact only one of the three repeats appears to show any increase at all in PO_3^- intensity within the timescale of the experiment. This therefore suggests that the phosphate components of the PBS solution present in the tissue are affecting the change in PO_3^- intensity. This is most likely due to the presence of conflicting trends between the PO_3^- ions present in the native tissue and the PO_3^- ions originating from the PBS. The PBS related PO_3^- ions will decrease in intensity due to a reduction in permeation as a function of tissue depth, whereas the native PO_3^- ions relating to the phospholipid compounds will increase with depth once the underlying epidermis is reached.

As the application of PBS to the tissue appears to mask the PO_3^- intensity increase, it was decided that, for analysis of treated tissue samples, the region correlating to the PO_3^- increase will be established using a blank control sample. To ensure that the *stratum corneum*/epidermis interface is as accurate as possible, a control sample taken from the same porcine ear as the compound-treated samples will be analysed for every experiment. This will be displayed on the depth profiles as a vertical grey region between two dotted lines, representing the possible location of the *stratum corneum*/epidermis interface, determined by three repeat areas.

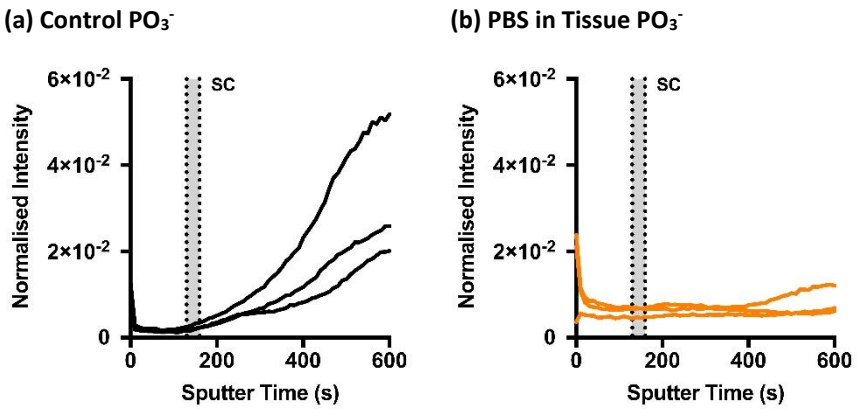

Figure 6.3 ToF-SIMS depth profiles showing the change in PO_3^- intensity as a function of sputter time for (a) a blank control sample and (b) a sample treated with PBS solution. The stratum corneum/epidermis interface is indicated by the light grey vertical region, calculated from the corresponding control sample. Three analytical repeats were collected per sample.

6.3.3 The permeation of vitamin C derivatives through *ex vivo* tissue

The data acquired in this study demonstrates that ToF-SIMS can successfully detect and monitor the permeation of compounds through *ex vivo* skin tissue using the depth profile method established in this project (chapter 5). In addition, the use of ToF-SIMS to obtain a 3D chemical profile of an exogenous compound within biological tissue is currently unprecedented.

Franz cell experiments were conducted by applying an infinite dose of each compound in PBS, at a concentration of 5% (w/v), onto skin samples taken from full thickness porcine ear tissue. Typically, the compounds of interest are used in cosmetic formulations at a concentration of 2% or lower. It was hoped therefore that a chosen concentration of 5% would offer a balance between obtaining suitable ToF-SIMS ion intensity whilst maintaining commercial relevance. The Franz cell experiments ran for a 24 hour period, following which the samples were analysed using the ToF-SIMS depth profile method developed in chapter 5.

Figure 6.4 contains example data from a tissue sample treated with 5% AA (w/v) in PBS, showing depth profiles (Fig. 6.4a and b) which illustrate the

change in ion intensity and secondary ion images (Fig. 6.4c-f) which highlight the spatial distribution of ions, both as a function of tissue depth.

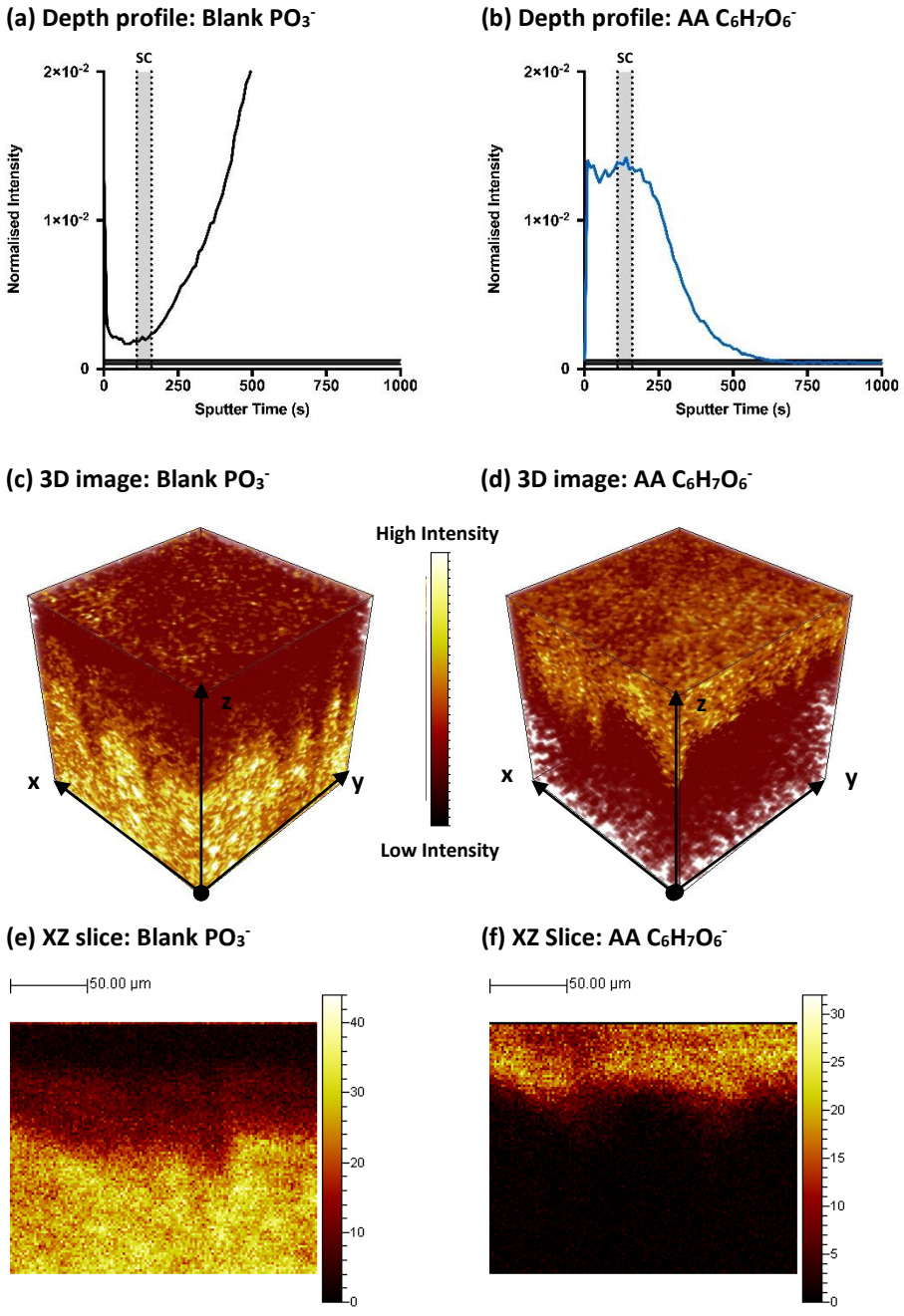

Figure 6.4 Example ToF-SIMS depth profile data showing (a-b) the change in ion intensity and (c-f) the ion spatial distribution as a function of tissue depth. The ions shown are PO_3^-, indicating the stratum corneum/epidermis interface and $C_6H_7O_6^-$, showing permeation of AA following the application of an AA 5% (w/v) PBS solution.

As previously mentioned, a blank control sample is used to locate the *stratum corneum*/epidermis interface using the increase in PO_3^- intensity (Fig. 6.4a). This is then highlighted on the corresponding depth profiles for the treated samples, as a vertical grey region (Fig. 6.4b), to demonstrate whether the compound has permeated into the underlying epidermis. The baseline level of ion intensity is also determined from this blank sample and is highlighted on the depth profiles as a horizontal black region. This indicates when the diagnostic ion of the compound has reached an intensity level that is indistinguishable from the native intensity. Therefore, if the compound is still present at an intensity above the control level after the vertical grey region highlighted on the profile, as shown for AA in Figure 6.4b, then it is proposed to have passed through the *stratum corneum* into the underlying epidermis.

ToF-SIMS also has the ability to map the spatial distribution of ions as a function of depth, both native ions, such as the phospholipid related PO_3^- (Fig. 6.4c and e) and ions from exogenous compounds like AA, indicated by $C_6H_7O_6^-$ (Fig. 6.4d and f). As observed in Figure 6.4, both 3D ion images and 2D slice images prove useful in elucidating the spatial distribution of these specific ions. Figures 6.4d and f demonstrate both the detection of the applied AA and its subsequent permeation into the upper layers of the skin tissue and comparison with the PO_3^- images highlights permeation into the phospholipid-rich epidermis.

For each compound of interest, three analytical repeats were conducted on each of the three experimental repeat samples (section 2.4.1.3), totalling nine individual depth profile data sets. For brevity, only the depth profiles, not the secondary ion images, will be compared in detail. The nine depth profiles for each compound are illustrated in Figure 6.5 showing the change in diagnostic ion intensity as a function of sputter time for $C_6H_7O_6^-$ (AA), $C_{12}H_{17}O_{11}^-$ (AG), $C_8H_{11}O_6^-$ (EAA), and $NaPO_3H^-$ (SAP).

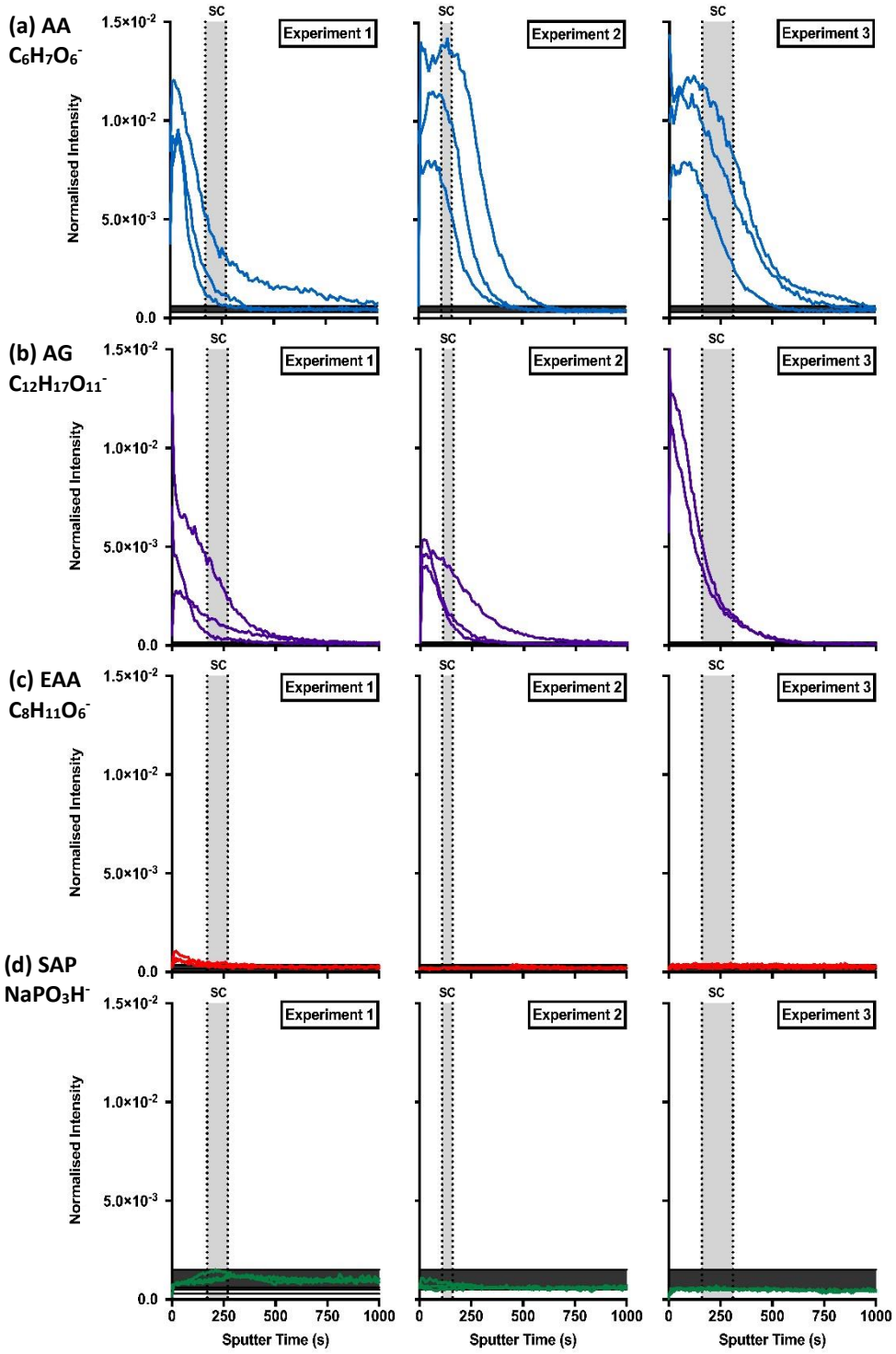

Figure 6.5 ToF-SIMS depth profiles showing the change in ion intensity as a function of sputter time for samples treated with (a) AA (b) AG (c) EAA and (d) SAP in a 24 hour Franz cell experiment. Three experimental repeats and three analytical repeats were conducted for each compound. The stratum corneum interface is indicated by the light grey vertical region and the baseline ion intensity is represented by the black horizontal region, parameters calculated from the corresponding control sample.

A comparison of the depth profiles for the four compounds of interest highlights some significant differences, particularly between compounds that permeate into the skin, specifically AA (Fig. 6.4a) and AG (Fig. 6.4b), and those that appear to not permeate at all, specifically EAA (Fig. 6.4c) and SAP (Fig. 6.4d). Both AA and AG display a significant initial ion intensity that is easily detected, demonstrating an expected decrease as a function of depth until a control level is reached. A similarity in ion intensity is observed between the analytical repeats and the experimental repeats for each compound, highlighting the ability of the method to provide repeatable measurements. Although the calculated depth of the *stratum corneum* is not specific to each sample and therefore must be viewed with some caution, the data does indicate that these compounds consistently permeate past the *stratum corneum* layer into the underlying epidermis. The nine depth profiles for each compound do differ in the point at which the compounds reach a control level, ranging from ~ 400 - 750 sputter seconds. Using the sputter rate calculated in section 5.3.1.2 as a guide, this roughly correlates to a skin depth of between 60 - 112.5 µm. This suggests a localisation of the compounds in the viable epidermal layer, with some possible permeation into the upper dermal layer. However, this cannot be confirmed from these profiles alone and can only be estimated using the calculated sputter rate.

In contrast, the profiles for EAA (Fig. 6.4c) and SAP (Fig. 6.4d) show an ion intensity that remains constant and at a control level throughout the depth profiles. There are several possible reasons for this observed lack of ion intensity. Although full thickness skin was employed in these experiments, in order to limit the acquisition time per sample each depth profile was run for a fixed sputter time of 1000 seconds. It could be argued therefore that these compounds have permeated deeper into the skin, past the point of analysis. However, this does not correlate with the known permeation efficiency of SAP, which suggests that this explanation is not likely [288,289].

A more reasonable explanation would be that these two derivatives have failed to permeate into even the superficial layers of the skin. This would correlate with the accepted poor permeation profile of SAP [288,289] but contradicts data demonstrating that EAA permeated to a greater extent than AG [292]. It may also

be possible that the lack of observed intensity is due to the detection limits of the instrument. Both EAA and SAP produced diagnostic ions at a significant intensity above the control level in the compound/skin homogenate references samples (section 6.3.1). However, the reference ion intensities for EAA and SAP were one order of magnitude lower than the corresponding ions for AA and AG. Therefore, it may be that at reduced concentrations the ion intensities for EAA and SAP are indistinguishable from the control levels. It could also be that EAA and SAP have permeated into the skin at a much lower concentration than AA and AG, producing an intensity which cannot be detected above the control. However, as both the clinical effects *in vivo* and the mode of action for these vitamin C derivatives is still largely unknown, it is hard to speculate further.

If the absence of ion intensity observed for EAA and SAP was due to a lack of permeation, then traditional skin fractionation analysis using chromatography coupled with mass spectrometry (section 1.3.2) would have helped to elucidate this by detecting the percentage of applied compound remaining in the donor solution. However, if the lack of observed intensity is due to a reduced concentration of EAA and SAP within the *stratum corneum* then ToF-SIMS is better equipped to detect the presence of these compounds, due to a significantly greater sensitivity. Future work is planned to explore the detection limit for each compound, using the compound/skin homogenate method (section 2.2.2.5) to produce a microarray of decreasing concentrations. ToF-SIMS surface analysis of these microarrays would then elucidate the highest concentration at which each compound produces a detectable ion intensity in the spectra.

These results illustrate the first use of dynamic SIMS to monitor the permeation of compounds through *ex vivo* skin tissue and have demonstrated the use of this technique to indicate a distinct difference in skin permeation between four compounds of interest. AA and AG have shown to consistently permeate past the *stratum corneum*, whereas the lack of observed intensity for EAA and SAP can be attributed to either a failure to permeate or permeation at a lower than detectable concentration. Importantly, the data shows that a detailed 3D profile of the compound can be obtained as a function of skin

tissue depth, illustrating the transition of the compounds through the *stratum corneum* layer into the underlying epidermis. This information cannot be obtained from traditional chromatographic techniques.

6.3.4 Monitoring the permeation of ascorbic acid following skin delivery using different formulations

The preliminary depth profile data demonstrated that it was possible to monitor the permeation of AA through *ex vivo* tissue using the developed ToF-SIMS method. However, in a commercial product active ingredients are incorporated into a complex formulation, not applied as an aqueous solution. Therefore, the next stage of the study was to elucidate whether this method could detect AA when it was delivered to the skin in an alternative, more commercially relevant formulation. Ideally, several 'off-the-shelf' products would have been chosen, incorporating a range of formulations such as creams, serums and gels. However, due to the instability of AA, this is not the preferred form of vitamin C incorporated into many commercial products. In addition, in order to cross-compare the level of AA delivered to the skin from different formulations, products containing 5% (w/v) concentration were needed to match the previously applied 5% (w/v) PBS solution. However, this high concentration is not typically used in commercial products and therefore the choice was limited.

6.3.4.1 Ascorbic acid delivery from an 'off-the-shelf' cosmetic formulation

One product that did contain ascorbic acid in a 5% concentration was a product from The Body Shop®, namely Vitamin C 10 Day Glow Boosting Concentrate. This product requires the final formulation step to be carried out by the consumer, in which a powder material is mixed into a base solution within a sealed container. The aim is evidently to prevent the premature degradation of AA before the consumer has opened the product. This was useful for this study, as it enabled the formulation to be prepared fresh and removed the possibility of sample degradation effects. Franz cell experiments were conducted as detailed in section 2.4.1.3 comparing the cosmetic product

to the original 5% (w/v) AA in PBS. Due to time restraints only one experimental repeat was conducted for this analysis. The depth profiles from this study are displayed in Figure 6.6 and unexpectedly show no observed ion intensity above the control level for the cosmetic product (Fig. 6.6b). These results suggests that the cosmetic product failed to deliver any AA to the skin, a surprising result considering the profiles for the PBS solution which show clear permeation of AA into the tissue. (Fig. 6.6a). There is no obvious explanation for this lack of permeation and complementary tape strip analysis, discussed later, also illustrates poor permeation of AA from the cosmetic product. Therefore, it is believed that this method is reliable and accurately shows a lack of AA permeation, the reason for which would need to be further investigated through repeat experiments.

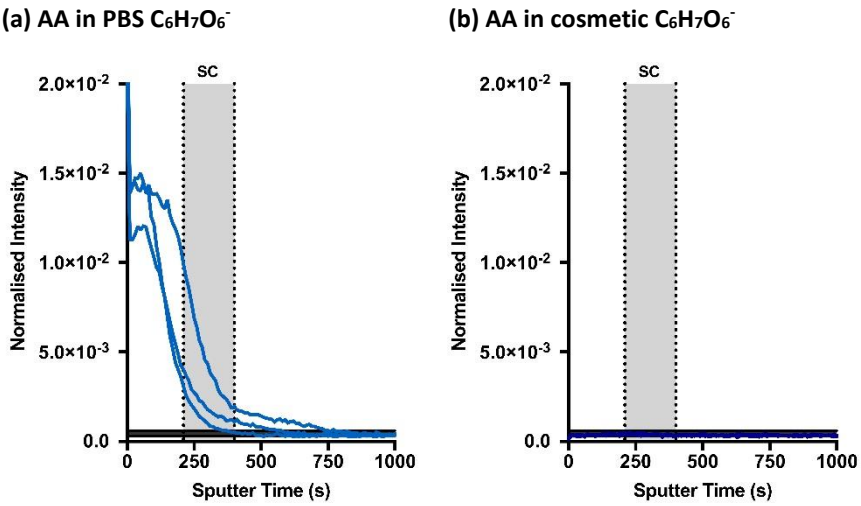

Figure 6.6 ToF-SIMS depth profiles showing the change in C6H7O6- intensity as a function of sputter time for samples treated with (a) 5% (w/v) AA in PBS (b) 5% (w/v) AA in an 'off-the-shelf' cosmetic formulation. The stratum corneum interface is indicated by the light grey vertical region and the baseline ion intensity is represented by the black horizontal region, parameters calculated from the corresponding control sample. Three analytical repeats were collected per sample.

6.3.4.2 Ascorbic acid delivery from a supramolecular gel formulation

In addition to the cosmetic product from The Body Shop®, it was also decided to analyse the permeation of AA from a novel gel delivery system. Dr. Pérez-

García and her research group from the University of Barcelona have developed gels based on a gemini imidazolium amphiphile that have the ability to incorporate an anionic drug compound [220]. However, the group have currently only studied the incorporation of medicinal drugs with a pharmaceutical application and therefore a collaboration was agreed to explore the possibility of incorporating and delivering to the skin a cosmetic ingredient, specifically AA.

It was quickly established that AA could successfully be incorporated into the gel formulation and importantly this formulation could be prepared from a 5% (w/v) solution of AA, as detailed in section 2.4.1.2, hence retaining the same concentration as both the PBS solution and cosmetic product. Three repeat Franz cell experiments were undertaken as detailed in section 2.1.4.3, producing three analytical repeats for each sample. For each separate experiment the gel formulation was prepared immediately prior to application, in order to minimise the possibility of sample degradation effects. The depth profiles produced for this study are shown in Figure 6.7, illustrating the change in $C_6H_7O_6^-$ (AA) intensity from both the PBS (Fig. 6.7a) and gel (6.7b) formulations.

The depth profiles produced for the gel formulation (Fig. 6.7b) show a significant ion intensity for AA, detectable throughout the analysis period, which indicates that the gel formulation did successfully deliver AA to the skin. Interestingly, the ion intensities for the gel formulation (Fig. 6.7b) equate to roughly double of those observed for the PBS solution (Fig. 6.7a). In addition, the ion intensity for the PBS formulation consistently reaches a control level within the analysis period, between 250-750 sputter seconds. Whereas in the gel profiles, the ion intensity remains at a level significantly higher than the control for the corresponding sputter region. These results therefore indicate a possible permeation enhancing effect for the gel formulation.

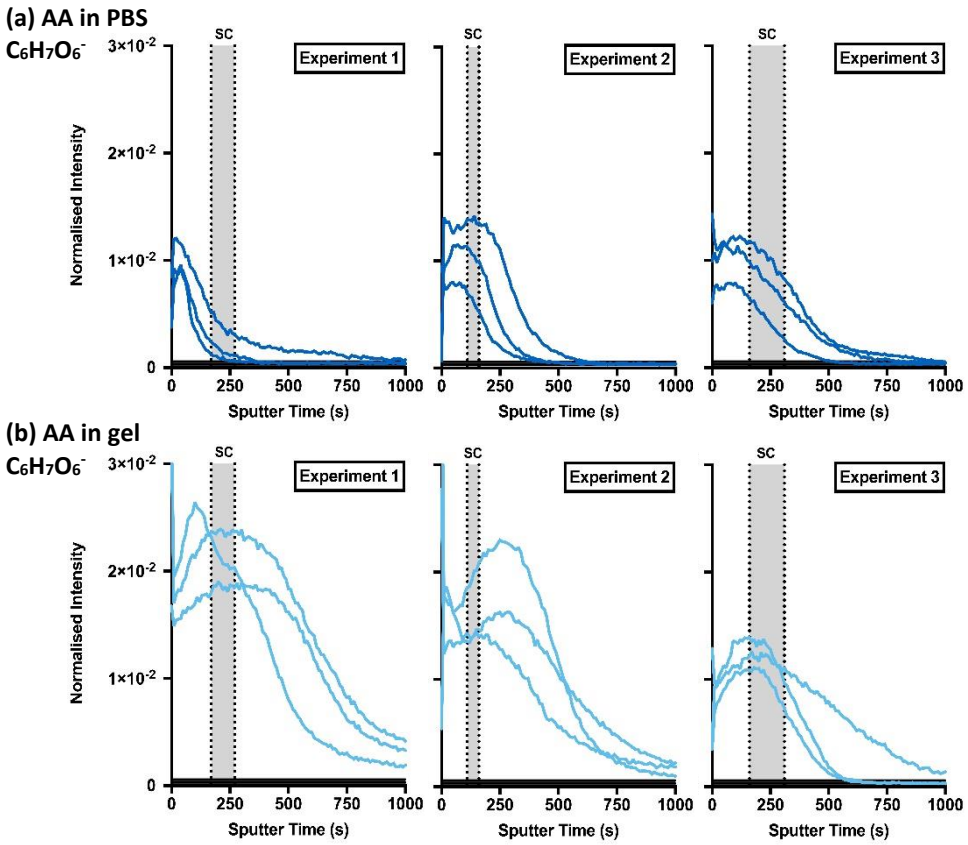

Figure 6.7 ToF-SIMS depth profiles showing the change in $C_6H_7O_6^-$ intensity as a function of sputter time for samples treated with (a) 5% (w/v) AA in PBS and (b) a 5% (w/v) AA supramolecular gel formulation. Three experimental repeats and three analytical repeats were conducted for each sample. The stratum corneum interface is indicated by the light grey vertical region and the baseline ion intensity is represented by the black horizontal region, parameters calculated from the corresponding control sample.

This enhancement effect can also be observed in the ToF-SIMS secondary ion images produced from the depth profiles. Example depth profile images are illustrated in Figure 6.8 and show the spatial distribution of AA in both a sample treated with a 5% PBS solution (Fig. 6.8a and c) and a gel formulation (Fig. 6.8b and d). Both the 3D and the 2D slice images illustrate that AA has permeated significantly further in the sample treated with the gel formulation, supporting the information gained from the depth profiles (Fig. 6.7). The images also highlight an inhomogeneity in the distribution of AA permeation for the gel treated sample. The sample treated with the 5% PBS solution (Fig. 6.8a and c) shows a uniformly distributed layer of AA which has permeated

into the upper region of the tissue. However, the images associated with the gel treated sample (Fig. 6.8b and d) indicate that AA has permeated to different depths of the tissue within the analysis area, despite appearing to be uniformly distributed on the surface of the skin. The reason for this inhomogeneity in permeation is unknown and would need to be further explored. One reason may be the inhomogeneous distribution of the AA compound within the gel matrix. Yet it could also be related to the permeation pathway of AA through the deeper tissue layers, both of which are unknown entities. These images therefore highlight the ability of ToF-SIMS to investigate compound permeation in more detail through the skin, especially the *stratum corneum* barrier layer, which offers the potential to further explore the mechanisms of permeation associated with different compounds and formulations.

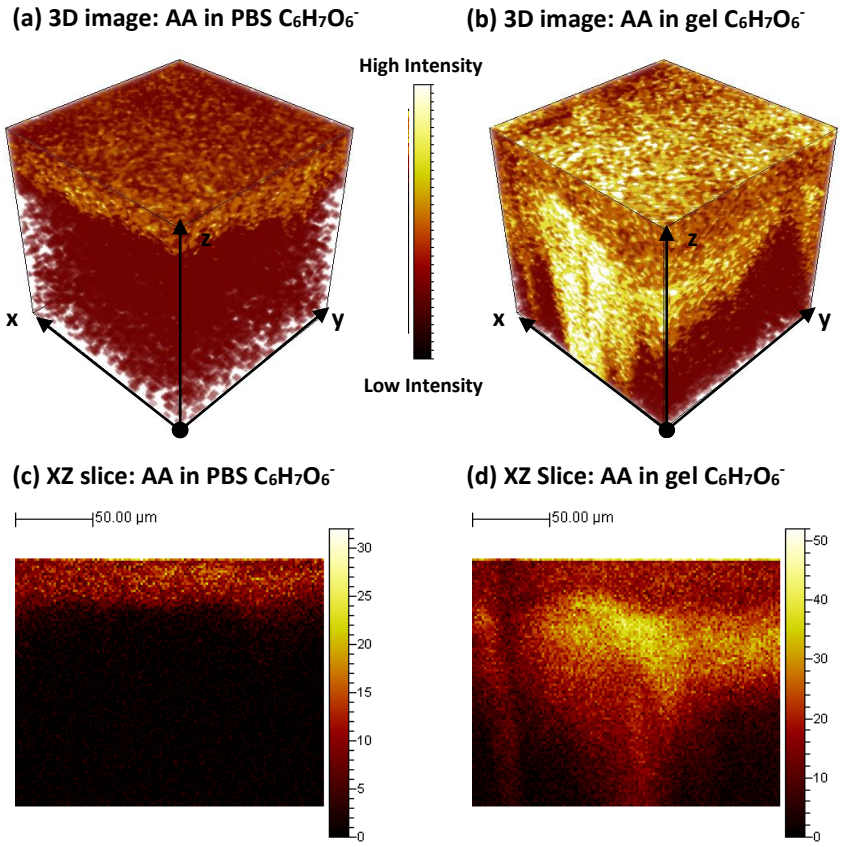

Figure 6.8 Example ToF-SIMS 2D and 3D secondary ion images showing the spatial distribution of $C_6H_7O_6^-$ (AA) as a function of tissue depth for samples treated with (a/c) a 5% AA (w/v) PBS solution (b/d) AA in the novel gel formulation.

The profiles produced for the gel formulation for experiment 3 specifically does not show this permeation enhancement. As shown in Figure 6.7b, the gel formulation depth profiles for experiment 3 are not consistent with the previous two, as the AA ion intensity observed for the gel formulation does not exceed that observed for the PBS solution. In addition, the intensity for two out of the three analytical repeats for the gel formulation reach a control level at the same time as the PBS formulation. On application of the gel formulation to the skin for this experiment, the gel was observed to be more fluid than the previous experiments. It is proposed therefore that the reduced AA permeation may be due to an instability in gel structure, potentially caused by differences in the laboratory environment. It is known that subtle changes in solvent ratio can affect the efficiency of the gelation process and it has been acknowledged by Dr. Pérez-García [293] that changes in other parameters, such as the temperature or humidity of the laboratory environment, may also have an effect. Therefore, it is possible that a variation in conditions on the day of the third experiment have resulted in a sub-optimal gel formation which has affected the permeation enhancing effect of the gel. Alternatively, this loss of enhancement may relate to a partial degradation of the gel, caused by the Franz cell experimental conditions. The calculated melting temperature for the pure gel without any incorporated compounds is 38.5 °C [220]. However, it has been shown that this melting temperature varies on incorporation of compounds, with examples showing both a melting temperature increase and decrease [220]. Although the water bath for the Franz cell experiment is kept at a fixed temperature, changes in the laboratory environment on that particular day may have caused a subtle increase in skin temperature, tipping it past the melting temperature of the gel. Yet, on removal of the gel, following the Franz cell experiment, it appeared to have regained the appropriate viscosity. Therefore, it is likely that an initial instability in the gel formulation has resulted in a poorer AA permeation.

As the gel is produced through a combination of ethanol and water solutions, it could be argued that the permeation enhancement effect of the gel formulation is the result of residual ethanol, which has been shown to enhance skin permeation [294-296]. Therefore, to understand whether the ethanol content of the

gel was having any effect on the permeation of AA, the permeation of a 5% AA (w/v) ethanol: water (2:3) solution was also tested. It was ensured that the ratio of ethanol to water was matched to that used for the gel preparation. Owing to time restraints, only one repeat experiment was conducted for this study. The depth profiles, shown in Figure 6.9, show no observed ion intensity above the control level for the ethanol/water solution (Fig. 6.9b), which suggests that the ethanol used to formulate the gel is not contributing to the enhanced permeation of AA observed with this formulation (Fig. 6.9a). However, the observed complete lack of permeation for this ethanol/water formulation was unexpected and therefore further repeats would have to be conducted to confirm this.

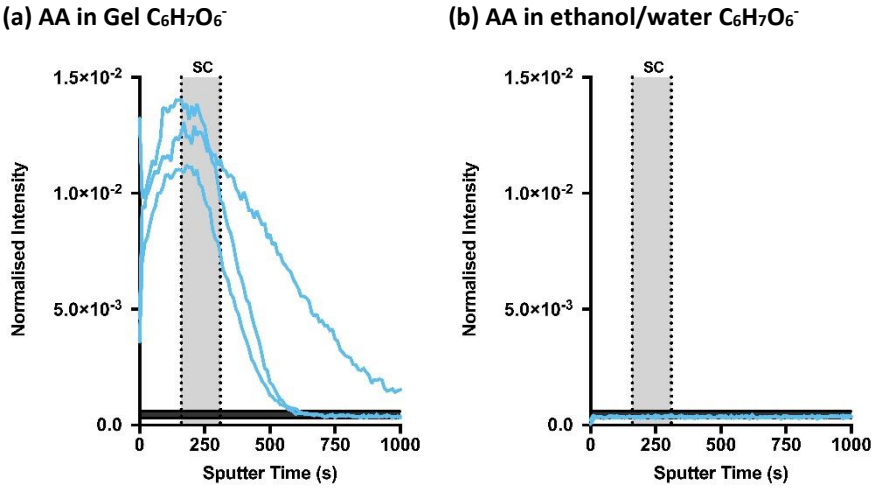

Figure 6.9 ToF-SIMS depth profiles showing the change in $C_6H_7O_6^-$ intensity as a function of sputter time for samples treated with (a) a 5% (w/v) AA supramolecular gel formulation (b) 5% (w/v) AA in a ethanol:water (2:3) solution. Three analytical repeats were collected per sample.The stratum corneum interface is indicated by the light grey vertical region and the baseline ion intensity is represented by the black horizontal region, parameters calculated from the corresponding control sample.

This study has therefore illustrated the successful delivery of a cosmetic ingredient to the skin using this novel supramolecular gel formulation. The data has also indicated a potential permeation enhancing effect resulting from this formulation. The mechanism behind this is currently unexplored but is outside the scope of this project. However, the obvious explanation would be

an improved partition coefficient [2] resulting from a poorer AA association in the gel formulation compared to the PBS solution. This newly developed ToF-SIMS method has offered insight into compound permeation through the *stratum corneum* following delivery using these novel gel formulations. The acquisition of a detailed permeation profile through this barrier layer therefore offers the potential to further explore the delivery mechanisms of novel systems such as these.

6.3.5 Validation of the depth profile method through cross comparison with tape strip analysis

Due to the unprecedented nature of this ToF-SIMS depth profile technique for permeation analysis, it was decided to cross-compare the results from the AA formulation study by conducting ToF-SIMS analysis of tape stripped samples. As the tape strip process involves the physical removal of skin layers from the sample, it can also confirm that the enhanced AA permeation profiles observed for the gel formulation are not a consequence of a superficial gel layer present on the skin surface. Although ToF-SIMS analysis of tape stripped skin is in itself a newly established method, the results published by Judd *et al.* [83] demonstrated a good correlation with microtomed slice analysis, confirming the reliability of the data.

A Franz cell experiment was therefore conducted using the same experimental parameters as before (section 2.1.4.3), but instead of using the dynamic SIMS profiling method on the whole tissue sample, 15 sequential tape strips were collected and analysed using ToF-SIMS surface analysis, as detailed in section 2.4.2. This is the same method employed by Judd *et al.* to monitor chlorhexidine permeation [83]. Strips 2, 6, 10 and 14 were chosen for analysis in order to provide data from regular intervals within the *stratum corneum*. Unfortunately, the porcine ear tissue proved problematic to tape strip and this resulted in the whole *stratum corneum* removal for both the PBS solution (after tape strip 2) and the gel formulation (after tape strip 10) and therefore these data sets are incomplete. One reason for this may have been insufficient drying of the tissue before stripping.

Figure 6.10 shows the exported $C_6H_7O_6^-$ (AA) peak intensities presented for each of the PBS, gel and cosmetic formulations alongside a blank sample. The intensities for tape strip 2 demonstrate that the level of AA present is highest for the gel formulation, followed by PBS, with the cosmetic formulation producing an intensity only marginally above the control level, as highlighted by the inset graph. This suggests that the gel has delivered a higher concentration of AA into the upper *stratum corneum* compared to the PBS formulation and demonstrates an unexpectedly low AA permeation from the cosmetic product. The intensity of $C_6H_7O_6^-$ (AA) for the gel formulation is shown to still be two orders of magnitude greater than the control level at tape strip 10, which relates to the latter portion of the *stratum corneum*. The trends observed therefore mirror the results acquired using the dynamic SIMS method (section 6.3.4.2). In addition, the observed peak intensities displayed in Figure 6.10 are within the same intensity range as those observed from the dynamic SIMS method, further confirming the correlation between the two methods.

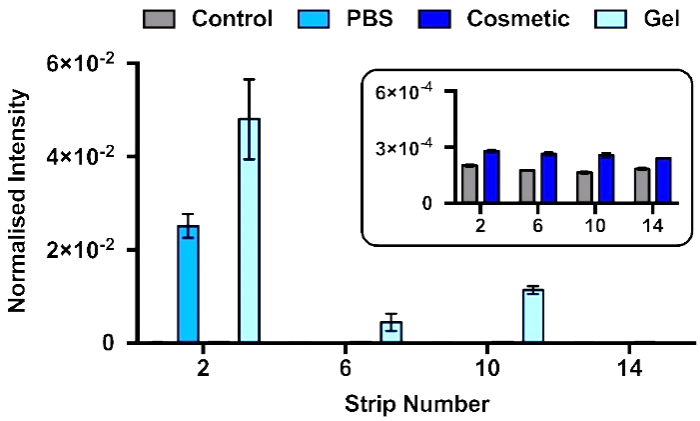

Figure 6.10 ToF-SIMS surface analysis data of tape stripped porcine ear samples, collected following a Franz cell experiment to compare the permeation of AA in three formulations, 5% (w/v) in PBS, a supramolecular gel formulation and an 'off-the-shelf' cosmetic serum. The data shows the exported peak intensities for $C_6H_7O_6^-$ present in tape strips 2, 6, 10 and 14. The PBS and gel intensities are incomplete after strip 2 and 10 respectively.

6.3.6 Detection of ascorbic acid *in vivo* following topical application of a cosmetic product

The work by Judd *et al.* is currently the only published study to focus on the use of ToF-SIMS analysis to monitor permeation of an active compound through the *stratum corneum* [83]. Their analysis was conducted on tape stripped samples collected from porcine tissue following *in vitro* Franz cell experiments. These *in vitro* permeation studies are useful for several reasons, as discussed in section 6.1. However, the ultimate aim is to show the efficiency of an active compound *in vivo*, using human volunteers.

As shown in chapters 3 and 4, the tape stripping process can easily be applied to collect samples from human volunteers *in vivo* and the data shown by both Judd. *et al.* and in section 6.3.5 demonstrates that ToF-SIMS can monitor exogenous compounds as a function of *stratum corneum* depth from tape stripped samples. The combination of these two techniques therefore offers the opportunity to monitor the permeation of an active compound following topical application to human volunteers *in vivo*. This is especially achievable for cosmetic products, even in the early stages of testing as, due to regulation, they can only contain specific ingredients at specific concentrations proven to pose no toxicological threat from topical application. It was therefore decided to conduct a small *in vivo* study to determine whether AA could be detected from the tape stripped samples of human volunteers, following the application of the cosmetic product from The Body Shop® previously used.

The *in vivo* testing was carried out as described in detail in section 2.4.2. Three female, < 27 volunteers were chosen and an infinite dose was applied to the inner forearm of each volunteer, ensuring a uniform coverage across the area to be stripped. Tape strip samples were collected after a 30 minute application time and a blank control area from an adjacent site on the arm was also stripped. Tape strips 2, 6, 10 and 14 were analysed and the exported peak intensities for the AA marker $C_6H_7O_6^-$ are shown in Figure 6.11.

These results show that for all volunteers the $C_6H_7O_6^-$ ion could be detected at a significant intensity above the control level for all tape strips, even tape strip 14. This therefore suggests that this cosmetic product does deliver AA through

the *stratum corneum*, which contradicts the lack of observed permeation shown in the *in vitro* studies (section 6.3.4.1). However, it must be noted that the application time of the cosmetic product in the *in vivo* study was significantly shorter, which may indicate a possible reason for the lack of observed signal after the 24 hour Franz cell study. Tape strip number 14 theoretically correlates to a layer within the deepest section of the *stratum corneum*. Therefore, the observed presence of AA in this layer, at a level significantly above the control, suggests that the cosmetic product most likely delivers some AA past the *stratum corneum* into the viable epidermis, which is the desired result.

The observed ion intensities shown in Figure 6.11 are within the same order of magnitude observed for the PBS formulation in both the depth profile and *in vitro* tape strip data (sections 6.3.3 and 6.3.4), which indicates that the permeation profile of AA is consistent across different analysis methods. Figure 6.11 highlights some slight variability between the three volunteers, both in terms of the total ion intensities and the trends observed between strip numbers. However, variance between volunteers is expected, especially for human volunteers, as demonstrated by the native analysis conducted in chapter 4. These results highlight that topically applied products do permeate to different levels in different consumers, an important consideration for both the pharmaceutical and cosmetic industry in the design of new products.

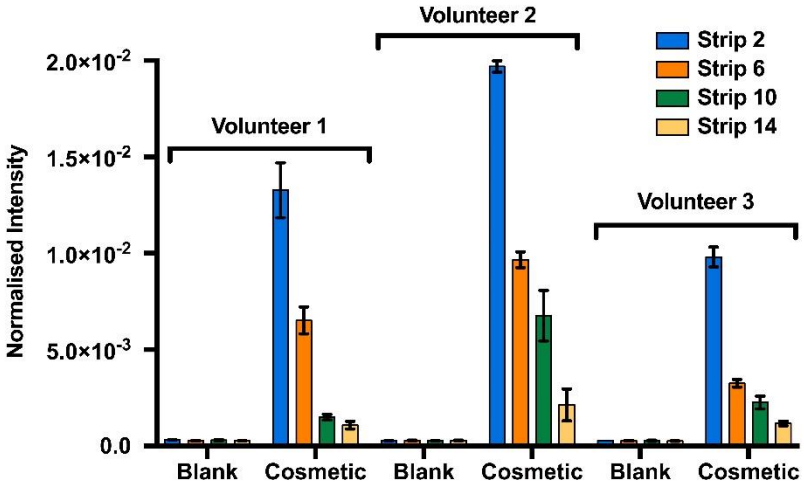

Figure 6.11 ToF-SIMS exported peak intensities showing the level of $C_6H_7O_6^-$ present in tape strips 2, 6, 10 and 14 collected in vivo from n=3 human volunteers. Samples were collected from a blank control area and one that had been subjected to a 30 minute application of an AA containing cosmetic product.

These results therefore illustrate that ToF-SIMS surface analysis can successfully detect AA from the individual tape stripped layers collected and hence can provide information on the permeation as a function of *stratum corneum* depth. This study is unprecedented as it is the first to show the use of ToF-SIMS to monitor permeation from human samples collected *in vivo*. Importantly, this was also achieved following the application of a complex 'off-the-shelf' cosmetic product. This highlights the huge potential of ToF-SIMS to provide detailed, commercially relevant information regarding permeation across the *stratum corneum*, the biggest barrier facing topically applied products.

One important advantage offered by ToF-SIMS for tape strip analysis is the ability to map the spatial distribution of specific ions, allowing the distribution of compounds within the skin to be elucidated following permeation. As previously mentioned, this is information that cannot be gained from traditional chromatographic analysis. Figure 6.12 illustrates the ToF-SIMS secondary ion images for strips 2, 6, 10 and 14 for one volunteer from the study, highlighting the spatial distribution of both a tissue marker CN^- (Fig. 6.12a) and the AA ion $C_6H_7O_6^-$ (Fig. 6.12b). For tape strip number 2, the AA

distribution clearly matches that of the tissue, with the observed furrows present in the tissue image mirrored also in the AA image. However, not only do tape strips 6, 10 and 14 show a clear reduction in the intensity of AA present in the sample, they also highlight a distribution pattern that is no longer homogeneous within the tissue region. However, there does appear to be some regularity in the pattern produced in the AA images, which suggests that this inhomogeneity in distribution is not merely a difference in permeation efficiency between one area of the sample and another. This regularity may point to a particular permeation pathway for AA through the *stratum corneum*. However, the spatial resolution for these images, which have been collected using the high current bunched mode, is not high enough to further elucidate these suggestions. It may therefore be beneficial for future analysis to also use the burst alignment mode to determine whether any additional features can be determined from an enhanced image resolution.

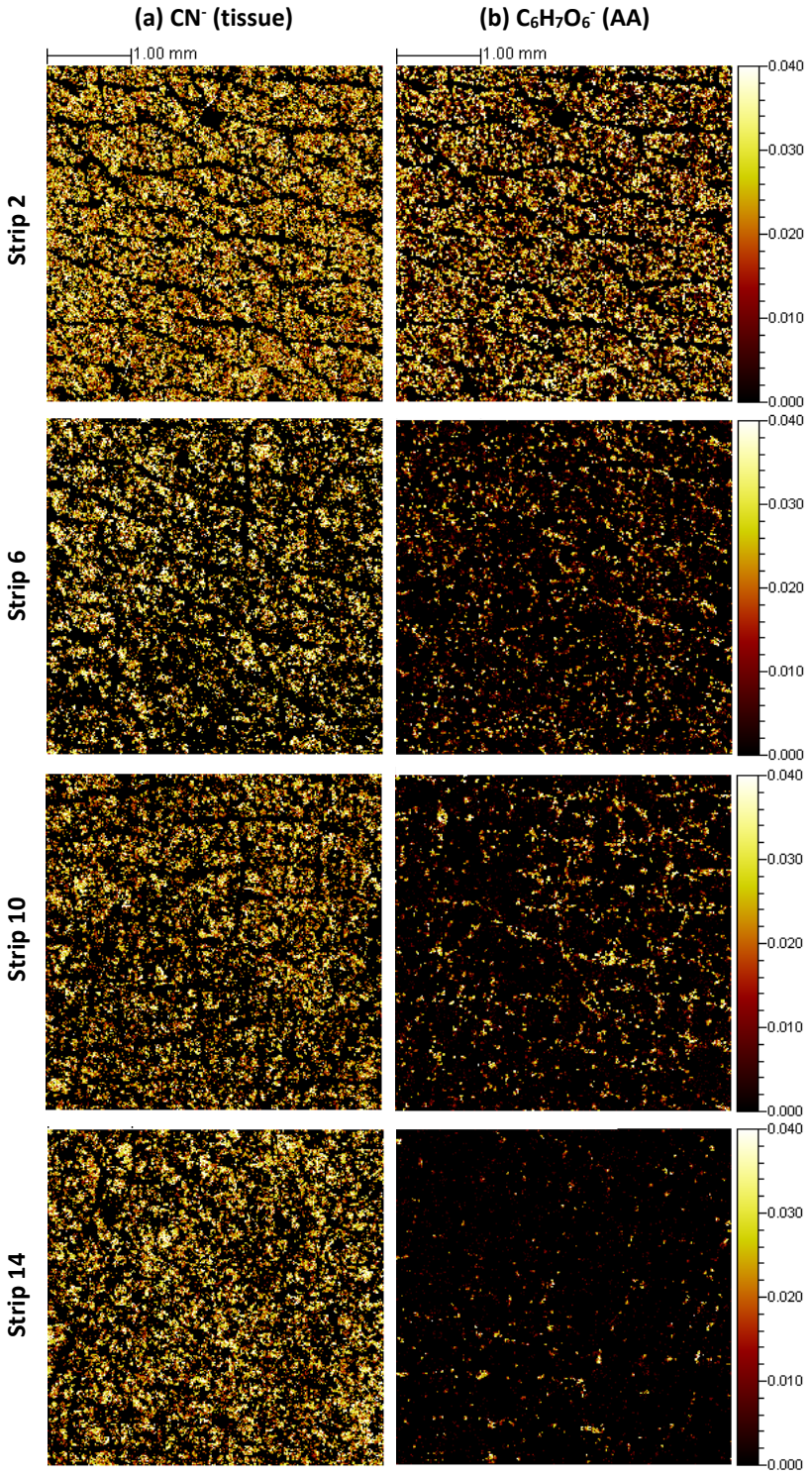

Figure 6.12 ToF-SIMS secondary ions images of tape stripped samples collected in vivo from human volunteers showing the spatial distribution of (a) CN^- a tissue marker and (b) $C_6H_7O_6^-$ the AA molecular ion for tape strip number 2, 4, 6 and 10.

6.4 Conclusions

This chapter has demonstrated the successful analysis of *ex vivo* skin tissue to monitor the permeation of exogenous compounds as a function of skin depth, using the dynamic SIMS method developed in chapter 5. The method was able to discriminate between the permeation efficiencies of four vitamin C related compounds, showing consistent permeation beyond the *stratum corneum* for both ascorbic acid and ascorbyl glucoside and a lack of permeation for sodium ascorbyl phosphate and unexpectedly, ethyl ascorbic acid.

This analysis yielded novel 3D chemical profiles, elucidating the distribution of an exogenous compound within biological tissue. This has previously only been achieved using ToF-SIMS for individual cells and so is believed to be the first successful application to whole tissue samples.

Ascorbic acid delivery to the skin following the application of several different formulations *in vitro* was also assessed in this study, elucidating the permeation enhancing effects of a novel supramolecular gel formulation. The *in vitro* permeation of an 'off-the-shelf' cosmetic product was also tested, which showed an unexpected lack of ascorbic acid delivery to the skin. ToF-SIMS surface analysis of collected tape strips was also employed to assess the permeation of these different formulations, which confirmed the trends observed and validated the use of the developed dynamic SIMS method.

The final aspect of this study used the method developed in chapter 3 to successfully monitor the permeation of ascorbic acid through human *stratum corneum* following application of a cosmetic product *in vivo.* This study presents the first analysis of permeation following *in vivo* human sampling achieved using ToF-SIMS.

Chapter 7: Conclusions and future work

7.1 Research summary

The novel application of ToF-SIMS analysis to study human *stratum corneum* described in this work has demonstrated the ability to obtain information on both native lipids and permeated exogenous species. Human *stratum corneum* collected *in vivo* was examined using an optimised surface analysis method and demonstrated the ability to detect subtle changes in individual tape stripped layers relating to skin aging. Changes in the levels of both cholesterol sulfate and long chain fatty acids were observed as a consequence of both intrinsic and extrinsic aging, offering previously unreported insights into aging mechanisms. This method was also used to successfully monitor the permeation of a cosmetic ingredient through the *stratum corneum* of human volunteers, following *in vivo* application of an 'off-the-shelf' cosmetic product.

Unprecedented 3D chemical depth profiles elucidating the distribution of a cosmetic ingredient within *ex vivo* porcine tissue were obtained using an extensively developed dynamic SIMS method. This method was used to discriminate between the permeation efficiencies of several vitamin C related compounds and also between different vehicle formulations. This is currently the only study to successfully use the dynamic SIMS technique to map the 3D distribution of an exogenous compound in a biological tissue sample.

7.2 Characterisation of tape stripped native human *stratum corneum* (Chapter 3)

Surface analysis of tape stripped *stratum corneum* using ToF-SIMS has recently been pioneered by Judd *et al.* for the detection of a topical product in *ex vivo* porcine skin [83]. The first chapter of this work therefore aimed to further develop this technique to enable the analysis of native human *stratum corneum* collected *in vivo*. This method development investigated instrumental parameters to optimise the detection of native lipid species from individual tape strips. It was established that a Bi_3^+ liquid metal ion gun (LMIG), used in the high current bunched (HC-BU) focusing mode, provided the optimal ion beam settings for these sample types, facilitating the detection of native lipid species, including the intact structures of several fatty acids and cholesterol sulfate. The absence of cholesterol in the spectra was unexpected, especially due to its high levels in the *stratum corneum.* However, the unpredictability in behaviour of this molecule under vacuum has been previously demonstrated and the influence of the matrix effect for these sample types is unknown. Anticipated intact structures of ceramides were also absent but this is proposed to be due to fragmentation of these large species. These preliminary results have therefore shown that ToF-SIMS has the potential to characterise the lipid composition of the *stratum corneum*, with further investigation into the absence of cholesterol and a more complete comparison of the ions present in the spectra required.

This chapter also demonstrated the measurement of several physical parameters of the tape stripped samples. Scanning electron microscopy (SEM) was demonstrated to be a suitable technique to study both the confluency of the *stratum corneum* layer and the size and morphology of the individual corneocytes. In combination with ToF-SIMS analysis, this technique was used to establish that optimal sample preparation involved loading the samples directly into the ToF-SIMS instrument with no prior dehydration. Multivariate data analysis was applied to discover a degradation of these sample types over a six month period and revealed that this was prevented by storing the samples in conditions less than 4 °C.

The depth of *stratum corneum* removed per tape strip has been shown to vary as a consequence of both experimental and inherent physiological influences. Optical profilometry and atomic force microscopy (AFM) were used to measure the thickness of the removed layer, with the latter proving the most successful in providing a consistent and physiologically relevant value. The values obtained were found to be variable from previous studies also using atomic force microscopy, emphasising the inconsistencies encountered in measuring corneocyte properties.

7.3 Age-related changes to human *stratum corneum* collected *in vivo* (Chapter 4)

The work in this chapter demonstrated the successful application of ToF-SIMS surface analysis to detect subtle age-related changes in human *stratum corneum* collected using the tape stripping method. An *in vivo* study was conducted using human volunteers and changes to the lipid composition resulting from both intrinsic and extrinsic aging were investigated. Using the methods established in chapter 3, the presence of several lipid species were shown to vary as a result of both intrinsic and extrinsic aging, specifically cholesterol sulfate and both lignoceric acid and hexacosanoic acid. The age-related increase in cholesterol sulfate observed agreed with both previously reported age-related changes in mouse tissue and established knowledge regarding the clinical effects related to an accumulation of this molecule. This is the first work to experimentally demonstrate this increase in human *stratum corneum* samples, thereby confirming existing theory. The observed intrinsic aging increase in the level of lignoceric acid appears to correlate with the only other study describing age-related effects on *stratum corneum* fatty acids. There are currently no other studies that have examined the effect of extrinsic aging on *stratum corneum* fatty acids and therefore this reported decrease in lignoceric acid and hexacosanoic acid is unprecedented. These findings correlate to studies showing a decrease in total fatty acid content in human epidermis relating to both acute UV exposure and long term photoaging effects. Analysis of sequential strips also elucidated trends in these three lipids as a function of *stratum corneum* depth, which agreed with limited work suggesting the presence of a *stratum corneum* lipid gradient.

The imaging capabilities of ToF-SIMS provided a significant advantage over the typically employed chromatographic methods for analysis of these sample types, where the secondary ion images were used to elucidate a previously unreported age-related localised increase in cholesterol sulfate.

The use of the previously developed SEM and AFM methods were employed to measure age-related physical effects on the *stratum corneum,* conducting analysis on the corneocyte surface area and thickness per strip respectively.

The corneocyte surface area demonstrated an increase and decrease related to intrinsic and extrinsic aging respectively, in agreement with previous studies, and confirmed the presence of age-related changes within an individual tape stripped layer. AFM analysis established that there was no statistically significant difference in the depth of *stratum corneum* removed per strip resulting from either intrinsic or extrinsic influences. This confirmed that the age-related chemical changes observed using ToF-SIMS, through cross comparison of individual tape strips, could be confidently attributed to actual physiological differences rather than a variation in sample depth.

7.4 Method development of dual beam dynamic SIMS for depth profile analysis of *ex vivo* skin (Chapter 5)

Although dynamic SIMS has been applied to a range of biological tissues, the technique has not yet been established for the analysis of skin. The work detailed in this chapter has therefore developed and optimised a protocol for dual beam dynamic SIMS analysis of *ex vivo* porcine tissue and has demonstrated the first use of ToF-SIMS to produce a 3D chemical profile of skin tissue. The optimisation of several experimental parameters was achieved, including the chosen beam energy and cluster size. The choice of these parameters demonstrated a significant effect on the sputter rate of the skin tissue samples. Hence, the optimisation of these parameters enabled the establishment of a sputter rate that would provide a balance between high depth resolution and an efficient sample throughput. Despite previous studies demonstrating an enhanced signal for biological species using a cyro-SIMS method to analyse a frozen hydrated sample, this study found no difference in the spectra of a frozen hydrated and a dehydrated sample. This indicates that no significant chemical change occurs for *ex vivo* skin tissue on dehydration of the sample.

An important factor in developing a dynamic SIMS protocol is the calibration of a sample specific sputter rate to correlate the chemical information acquired with a relevant sample depth. This can be achieved by conducting analysis on samples with a known thickness or by measuring the depth of a sputtered crater. Attempts to calculate a sputter rate using these methods highlighted a significant variation in the topography of the porcine skin. This variation occurred within a single tissue section and between sections taken from different tissues, which complicated the calculation of an accurate sputter rate that could be universally applied to all skin tissue samples. The analysis of microtomed skin demonstrated a reduced sputter rate for the *stratum corneum* layer compared to the underlying epidermis and dermis regions, which emphasised the complexity in calculating a generic sputter rate for biological samples with inhomogeneous multilayer structures.

This study showed that an inherent chemical marker, relating to the phospholipid class of compounds, could be used to indicate the *stratum corneum*/epidermis interface for each individual sample analysed. This diagnostic ion proved ideal to indicate when compounds of interest had passed the most significant barrier in the skin, the *stratum corneum.*

7.5 Monitoring the permeation of vitamin C derivatives through both *ex vivo* and *in vivo* skin tissue (Chapter 6)

The work in this chapter utilised both the static SIMS method developed in chapter 3 and the dynamic SIMS method developed in chapter 5 to successfully monitor the permeation of cosmetic ingredients through human *stratum corneum* collected *in vivo* and *ex vivo* porcine skin respectively.

Permeation studies were conducted for several vitamin C related compounds and subsequently the whole *ex vivo* tissue sample was successfully analysed using the dynamic SIMS method developed in chapter 5. This yielded a novel 3D chemical profile elucidating the distribution of the exogenous compound within the skin tissue as a function of depth. This has previously only been achieved for individual cells and so is believed to be the first successful application to whole tissue samples. Discrimination between the permeation efficiencies of these vitamin C related compounds was successfully achieved. Ascorbic acid and ascorbyl glucoside showed consistent permeation beyond the *stratum corneum*, whereas sodium ascorbyl phosphate, and unexpectedly ethyl ascorbic acid, appeared not to permeate the skin at all.

Ascorbic acid delivery to the skin following the *in vitro* application of several different formulations was also assessed in this study, elucidating the permeation enhancing effects of a novel supramolecular gel formulation. This research highlighted the potential of ToF-SIMS to provide detailed information regarding both the extent and the spatial distribution of permeation across the *stratum corneum* for novel formulations. This information cannot be acquired from traditional techniques such as chromatographic analysis. The permeation of an 'off-the-shelf' cosmetic product was also tested, which showed an unexpected lack of ascorbic acid delivery to the skin. The lack of permeation for the cosmetic formulation and the enhancement effects of the gel were also analysed using ToF-SIMS surface analysis of tape strips collected from the *ex vivo* tissue. This method for monitoring permeation was previously developed and validated by Judd *et al.* [83] and it confirmed the trends observed using the dynamic SIMS depth profile method.

The final aspect of this study used the method developed in chapter 3 to successfully monitor the permeation of ascorbic acid through human *stratum corneum* following application of a cosmetic product *in vivo.* This study presents the first analysis of permeation following *in vivo* human sampling achieved using ToF-SIMS. The imaging capabilities of ToF-SIMS again proved beneficial to map the spatial distribution of the active ingredient within the *stratum corneum* layers. The ToF-SIMS secondary ion images highlighted a homogeneity in distribution within the tissue for the initial tape strips, which varied in the deeper layers of the *stratum corneum.* Although the ascorbic acid was no longer homogeneously distributed within the tissue for these layers, it did still exhibit a regularity in the pattern produced across the sample, which may indicate a particular permeation pathway for ascorbic acid through the *stratum corneum.*

This study demonstrates the successful use of ToF-SIMS to monitor the skin permeation of topical products and highlights the potential of the technique to provide information that cannot be gained from traditionally used methods. However, currently the cost and specialised training needed to collect and analyse the data makes this technique impractical for widespread use as an industrial screening method. Nonetheless, it can offer both the pharmaceutical and cosmetic industries the chance to investigate, in unprecedented detail, compounds or formulations of particular interest.

7.6 Implications for skin research and future work

In conclusion, this work has provided important insights into both the aging mechanisms of the skin and the effective delivery of anti-aging ingredients across the skin barrier. Importantly, it has also established a solid foundation for further analysis of skin tissue using ToF-SIMS, demonstrating the ability of this technique to obtain specific information from samples obtained both *in vivo* and *ex vivo*.

As demonstrated, ToF-SIMS has the required sensitivity to detect changes in the lipid composition of tape stripped samples, something which is not easily achievable using the traditional chromatographic methods. This offers the potential to study this lipid composition as a function of *stratum corneum* depth, an area which until now has been poorly researched. Obtaining information regarding changes to this lipid composition at such a detailed level can help to elucidate the fundamental molecular mechanisms behind the skin's barrier function and offer further insight into the effects of both inherent and external influences. One area for further work would be to conduct a more detailed examination of the spectra and the numerous fragment ions produced, in order to elucidate peaks which can confidently be assigned to other lipid species beyond cholesterol sulfate and fatty acid components. However, due to the similarity in structure of lipids present in the *stratum corneum*, the origin of many peaks in the spectra could not be uniquely identified due to an overlap of *m/z* assignments. Analysis of complex samples such as these could be improved through the use of a ToF-SIMS instrument with higher mass resolution. The National Physical Laboratory (NPL) are currently leading a consortium, including ION-TOF, The University of Nottingham, The University of Illinois and GlaxoSmithKline, to design a revolutionary instrument which will incorporate a Thermo Scientific™ Orbitrap™ mass analyser [297]. This instrument will offer enhanced sensitivity in the region of two orders of magnitude and ultra high mass resolution which, combined with the ability to conduct tandem mass spectrometry analysis, will greatly improve compound identification. It would therefore prove useful to employ an instrument such as this to analyse the tape stripped *stratum corneum* samples, in order to achieve more distinct peak assignments.

In addition, this work only briefly analysed the presence of a lipid gradient in the *stratum corneum*, detected from the alternate strips (1-15) of two volunteers. This study could therefore be expanded to incorporate more volunteers and the whole set of sequential strips could be analysed, in order to offer a more complete understanding of the fluctuation of lipid levels throughout the *stratum corneum.* This lipid gradient could also be examined through the depth profile analysis of *ex vivo* tissue, using the dynamic SIMS method developed in this work. However, optimisation of this method would be required to facilitate a higher depth resolution for the *stratum corneum* layer specifically. The imaging capabilities for the tape strip analysis could also be utilised further. For instance, employing the burst alignment mode of the ToF-SIMS technique to produce higher resolution images which may aid in the examination of both lipid localisation effects, as observed with cholesterol sulfate, and also the spatial distribution of a permeated compound.

The development of a dynamic SIMS method to produce 3D chemical depth profiles of *ex vivo* skin tissue is a huge advancement in the field of skin research. No other technique is able to obtain the combination of high chemical specificity, mass resolution and both lateral and axial resolution offered by this technique. This work has shown the potential to use this method following permeation studies, in order to provide detailed information about the distribution of a compound within skin tissue, in particular its permeation profile across the skin's greatest barrier, the *stratum corneum*. The discovery of an inherent marker to indicate the location of the *stratum corneum*/epidermis interface is crucial for avoiding the extensive variability in skin layer depth, offering permeation analysis through each sample on an individual basis. However, a significant limitation to this technique with regards to monitoring the permeation of a compound is the lack of quantitative data that can be obtained. Therefore, the main aim for any future work is to establish a calibration method, which will enable the correlation of ion intensity with a relevant compound concentration. The development of a novel method to produce homogenised skin/compound mixtures offers significant potential for this area. Work is currently ongoing to optimise a microarray printing methodology for these samples, to allow a high throughput

assessment of a series of different sample/compound concentrations. ToF-SIMS analysis of these concentration series for each compound would then enable the intensity visualised in the depth profile to be attributed to a relevant compound concentration.

Chapter 8: References

(1) Haake, A.; Scott, G. A. and Holbrook, K. A. In *The Biology of the Skin*; Freinkel, R. K. and Woodley, D. T., Eds.; Taylor & Francis: 2001, 19-45.

(2) Benson, H. A. E. In *Topical and Transdermal Drug Delivery*; John Wiley & Sons, Inc.: 2012, 1-22.

(3) Kligman, A. M. and Christophers, E. *Arch. Dermatol.* **1963**, *88,* 702-5.

(4) Kashibuchi, N.; Hirai, Y.; O'Goshi, K. and Tagami, H. *Skin Res. Technol.* **2002**, *8,* 203-11.

(5) Fluhr, J. W.; Pelosi, A.; Lazzerini, S.; Dikstein, S. and Berardesca, E. *Skin Pharmacol. Appl. Skin Physiol.* **2001**, *14,* 10-6.

(6) Saijo, S. and Hashimoto-Kumasaka, K. *J. Soc. Cosmet. Chem.* **1991**, *42,* 379-83.

(7) Plewig, G. *J. Invest. Dermatol.* **1970**, *54,* 19-23.

(8) Marks, R. *Br. J. Dermatol.* **1981**, *104,* 627-33.

(9) Machado, M.; Salgado, T. M.; Hadgraft, J. and Lane, M. E. *Int. J. Pharm.* **2010**, *384,* 73-7.

(10) Marks, R. and Barton, S. P. In *Stratum Corneum*; Marks, R. and Plewig, G., Eds.; Springer Berlin Heidelberg: Berlin, Heidelberg, 1983, 161-70.

(11) Al-Jaberi, H. and Marks, R. *Br. J. Dermatol.* **1984**, *111,* 437-43.

(12) Corcuff, P. and Leveque, J. L. *Photodermatol.* **1988**, *5,* 110-5.

(13) Stucker, M.; Licht, M. and Heise, H. M. *J. Diabetes Metab.* **2015**, *6:9 (603).*

(14) Fredonnet, J.; Gasc, G.; Serre, G.; Séverac, C. and Simon, M. *J. Dermatol. Sci.* **2014**, *75,* 63-5.

(15) Richter, T.; Peuckert, C.; Sattler, M.; Koenig, K.; Riemann, I.; Hintze, U.; Wittern, K. P.; Wiesendanger, R. and Wepf, R. *Skin Pharmacol. Physiol.* **2004**, *17,* 246-57.

(16) Holbrook, K. A. and Odland, G. F. *J. Invest. Dermatol.* **1974**, *62,* 415-22.

(17) Watanabe, M.; Tagami, H.; Horii, I.; Takahashi, M. and Kligman, A. M. *Arch. Dermatol.* **1991**, *127,* 1689-92.

(18) Weigand, D. A.; Haygood, C. and Gaylor, J. R. *J. Invest. Dermatol.* **1974**, *62,* 563-8.

(19) Ya-Xian, Z.; Suetake, T. and Tagami, H. *Arch. Dermatol. Res.* **1999**, *291,* 555-9.

(20) Elias, P. M.; Cooper, E. R.; Korc, A. and Brown, B. E. *J. Invest. Dermatol.* **1981**, *76,* 297-301.

(21) Pirot, F.; Berardesca, E.; Kalia, Y. N.; Singh, M.; Maibach, H. I. and Guy, R. H. *Pharm. Res.* **1998**, *15,* 492-4.

(22) Egawa, M.; Hirao, T. and Takahashi, M. *Acta. Derm. Venereol.* **2007**, *87*, 4-8.

(23) Böhling, A.; Bielfeldt, S.; Himmelmann, A.; Keskin, M. and Wilhelm, K. P. *Skin Res. Technol.* **2014**, *20*, 50-7.

(24) Sandby-Moller, J.; Poulsen, T. and Wulf, H. C. *Acta. Derm. Venereol.* **2003**, *83*, 410-3.

(25) Elias, P. M. *J. Invest. Dermatol.* **1983**, *80*.

(26) Elias, P. M.; Gruber, R.; Crumrine, D.; Menon, G.; Williams, M. L.; Wakefield, J. S.; Holleran, W. M. and Uchida, Y. *Biochim. Biophys. Acta* **2014**, *1841*, 314-8.

(27) Niehues, H.; van Vlijmen-Willems, I. M. J. J.; Bergboer, J. G. M.; Kersten, F. F. J.; Narita, M.; Hendriks, W. J. A. J.; van den Bogaard, E. H.; Zeeuwen, P. L. J. M. and Schalkwijk, J. *Br. J. Dermatol.* **2016**, *174*, 795-802.

(28) Rawlings, A. V. and Harding, C. R. *Dermatol. Ther.* **2004**, *17*, 43-8.

(29) Elias, P. M. and Friend, D. S. *J. Cell Biol.* **1975**, *65*, 180-91.

(30) Elias, P. M.; Goerke, J. and Friend, D. S. *J. Invest. Dermatol.* **1977**, *69*, 535-46.

(31) Elias, P. M.; McNutt, N. S. and Friend, D. S. *Anat. Rec.* **1977**, *189*, 577-93.

(32) Talreja, P.; Kleene, N. K.; Pickens, W. L.; Wang, T. F. and Kasting, G. B. *AAPS PharmSci.* **2001**, *3*, 48–56.

(33) P. M. Elias, K. R. F., M. Denda In *Dermal Absorption and Toxicity Assessment, Second Edition*; Roberts, M. S., Ed.; CRC Press: 2007, 79-87.

(34) Harding, C. R. *Dermatol. Ther.* **2004**, *17*, 6-15.

(35) Madison, K. C.; Swartzendruber, D. C.; Wertz, P. W. and Downing, D. T. *J. Invest. Dermatol.* **1987**, *88*, 714-8.

(36) Bouwstra, J.; Gooris, G. and Ponec, M. *J. Biol. Phys.* **2002**, *28*, 211-23.

(37) Lampe, M. A.; Williams, M. L. and Elias, P. M. *J. Lipid Res.* **1983**, *24*, 131-40.

(38) Epstein, E. H.; Williams, M. L. and Elias, P. M. *J. Am. Acad. Dermatol.* **1984**, *10*, 866-8.

(39) Picardo, M.; Ottaviani, M.; Camera, E. and Mastrofrancesco, A. *Dermatoendocrinol.* **2009**, *1*, 68-71.

(40) Pappas, A.; Johnsen, S.; Liu, J.-C. and Eisinger, M. *Dermatoendocrinol.* **2009**, *1*, 157-61.

(41) van Smeden, J.; Hoppel, L.; van der Heijden, R.; Hankemeier, T.; Vreeken, R. J. and Bouwstra, J. A. *J. Lipid Res.* **2011**, *52*, 1211-21.

(42) Weerheim, A. and Ponec, M. *Arch. Dermatol. Res.* **2001**, *293*, 191-9.

(43) Zbytovská, J.; Kiselev, M. A.; Funari, S. S.; Garamus, V. M.; Wartewig, S.; Palát, K. and Neubert, R. *Colloids Surf. A Physicochem. Eng. Asp.* **2008**, *328*, 90-9.

(44) Norlen, L.; Nicander, I.; Lundsjo, A.; Cronholm, T. and Forslind, B. *Arch. Dermatol. Res.* **1998**, *290*, 508-16.

(45) van Smeden, J.; Boiten, W. A.; Hankemeier, T.; Rissmann, R.; Bouwstra, J. A. and Vreeken, R. J. *Biochim. Biophys. Acta.* **2014**, *1841*, 70-9.

(46) Rogers, J.; Harding, C.; Mayo, A.; Banks, J. and Rawlings, A. *Arch. Dermatol. Res.* **1996**, *288*, 765-70.

(47) Bonte, F.; Saunois, A.; Pinguet, P. and Meybeck, A. *Arch. Dermatol. Res.* **1997**, *289*, 78-82.

(48) Elias, P. M.; Williams, M. L.; Maloney, M. E.; Bonifas, J. A.; Brown, B. E.; Grayson, S. and Epstein, E. H. *J. Clin. Invest.* **1984**, *74*, 1414-21.

(49) Sato, J.; Denda, M.; Nakanishi, J.; Nomura, J. and Koyama, J. *J. Invest. Dermatol.* **1998**, *111*, 189-93.

(50) Zettersten, E.; Man, M.-Q.; Farrell, A.; Ghadially, R.; Williams, M. L.; Feingold, K. R.; Elias, P. M.; Sato, J. and Denda, M. *J. Invest. Dermatol.*, *111*, 784-90.

(51) Paige, D. G.; Morse-Fisher, N. and Harper, J. I. *Br. J. Dermatol.* **1994**, *131*, 23-7.

(52) Lavrijsen, A. P.; Bouwstra, J. A.; Gooris, G. S.; Weerheim, A.; Bodde, H. E. and Ponec, M. *J. Invest. Dermatol.* **1995**, *105*, 619-24.

(53) Pilgram, G. S. K.; Vissers, D. C. J.; Van Der Meulen, H.; Pavel, S.; Lavrijsen, S. P. M.; Bouwstra, J. A. and Koerten, H. K. *J. Invest. Dermatol.* **2001**, *117*, 710-7.

(54) Motta, S.; Monti, M.; Sesana, S.; Caputo, R.; Carelli, S. and Ghidoni, R. *Biochim. Biophys. Acta* **1993**, *1182*, 147-51.

(55) Motta, S.; Monti, M.; Sesana, S.; Mellesi, L.; Ghidoni, R. and Caputo, R. *Arch. Dermatol.* **1994**, *130*, 452-6.

(56) van Smeden, J.; Janssens, M.; Boiten, W. A.; van Drongelen, V.; Furio, L.; Vreeken, R. J.; Hovnanian, A. and Bouwstra, J. A. *J. Invest. Dermatol.* **2014**, *134*, 1238-45.

(57) Di Nardo, A.; Wertz, P.; Giannetti, A. and Seidenari, S. *Acta. Derm. Venereol.* **1998**, *78*, 27-30.

(58) Imokawa, G.; Abe, A.; Jin, K.; Higaki, Y.; Kawashima, M. and Hidano, A. *J. Invest. Dermatol.* **1991**, *96*, 523-6.

(59) Angelova-Fischer, I.; Mannheimer, A. C.; Hinder, A.; Ruether, A.; Franke, A.; Neubert, R. H.; Fischer, T. W. and Zillikens, D. *Exp. Dermatol.* **2011**, *20*, 351-6.

(60) van Smeden, J.; Janssens, M.; Kaye, E. C.; Caspers, P. J.; Lavrijsen, A. P.; Vreeken, R. J. and Bouwstra, J. A. *Exp. Dermatol.* **2014**, *23*, 45-52.

(61) Demerjian, M.; Crumrine, D. A.; Milstone, L. M.; Williams, M. L. and Elias, P. M. *J. Invest. Dermatol.* **2006**, *126*, 2032-8.

(62) Goto-Inoue, N.; Hayasaka, T.; Zaima, N.; Nakajima, K.; Holleran, W. M.; Sano, S.; Uchida, Y. and Setou, M. *PLoS One* **2012**, *7*.

(63) Williams, M. L. and Elias, P. M. *J. Clin. Invest.* **1981**, *68,* 1404-10.

(64) Folch, J.; Lees, M. and Sloane-Stanley, G. *J. Biol. Chem.* **1957**, *226,* 497-509.

(65) Bligh, E. G. and Dyer, W. J. *Can. J. Biochem. Physiol.* **1959**, *37,* 911-7.

(66) Sheppard, A. J. *J. Am. Oil Chem. Soc.* **1963**, *40,* 545-8.

(67) Opitz, A.; Wirtz, M.; Melchior, D.; Mehling, A.; Kling, H.-W. and Neubert, R. H. H. *Chromatographia* **2011**, *73,* 559-65.

(68) Radin, N. S. In *Methods Enzymol.*; Academic Press: 1981; Vol. Volume 72, 5-7.

(69) Jungersted, J. M.; Bomholt, J.; Bajraktari, N.; Hansen, J. S.; Klærke, D. A.; Pedersen, P. A.; Hedfalk, K.; Nielsen, K. H.; Agner, T. and Hélix-Nielsen, C. *Arch. Dermatol. Res.* **2013**, *305,* 699-704.

(70) Marks, R. and Dawber, R. P. *Br. J. Dermatol.* **1971**, *84,* 117-23.

(71) Nakagawa, K. *Lipids* **2010**, *45,* 91-6.

(72) Cho, H. J.; Chung, B. Y.; Lee, H. B.; Kim, H. O.; Park, C. W. and Lee, C. H. *J. Dermatol. Sci.* **2012**, *39,* 295-300.

(73) Tazrart, A.; Bolzinger, M. A.; Moureau, A.; Molina, T.; Coudert, S.; Angulo, J. F.; Briancon, S. and Griffiths, N. M. *Chem. Biol. Interact.*

(74) Wolf, J. *Z. Mikr. Anat. Forsch.* **1939**, *46*.

(75) Pinkus, H. *J. Invest. Dermatol.* **1951**, *16,* 383-6.

(76) Schwarb, F. P.; Gabard, B.; Rufli, T. and Surber, C. *Dermatology* **1999**, *198,* 44-51.

(77) Cambon, M.; Issachar, N.; Castelli, D. and Robert, C. *J. Cosmet. Sci.* **2001**, *52,* 1-11.

(78) Beisson, F.; Aoubala, M.; Marull, S.; Moustacas-Gardies, A. M.; Voultoury, R.; Verger, R. and Arondel, V. *Anal. Biochem.* **2001**, *290,* 179-85.

(79) Sarveiya, V.; Risk, S. and Benson, H. A. E. *J. Chromatogr. B* **2004**, *803,* 225-31.

(80) Dupuis, D.; Rougier, A.; Roguet, R.; Lotte, C. and Kalopissis, G. *J. Invest. Dermatol.* **1984**, *82,* 353-6.

(81) Pellett, M. A.; Roberts, M. S. and Hadgraft, J. *Int. J. Pharm.* **1997**, *151,* 91-8.

(82) Wagner, H.; Kostka, K.-H.; Lehr, C.-M. and Schaefer, U. F. *Pharm. Res.* **2000**, *17,* 1475-81.

(83) Judd, A. M.; Scurr, D. J.; Heylings, J. R.; Wan, K.-W. and Moss, G. P. *Pharm. Res.* **2013**, *30,* 1896-905.

(84) de Jalon, E. G.; Blanco-Prieto, M. J.; Ygartua, P. and Santoyo, S. *J. Control. Release* **2001**, *75,* 191-7.

(85) Gamer, A. O.; Leibold, E. and van Ravenzwaay, B. *Toxicol. In Vitro* **2006**, *20,* 301-7.

(86) Breternitz, M.; Flach, M.; Präßler, J.; Elsner, P. and Fluhr, J. W. *Br. J. Dermatol.* **2007**, *156*, 231-40.

(87) Bashir, S. J.; Chew, A.-L.; Anigbogu, A.; Dreher, F. and Maibach, H. I. *Skin Res. Technol.* **2001**, *7*, 40-8.

(88) Lademann, J.; Weigmann, H.-J.; Schanzer, S.; Richter, H.; Audring, H.; Antoniou, C.; Tsikrikas, G.; Gers-Barlag, H. and Sterry, W. *J. Biomed. Opt.* **2005**, *10*.

(89) Jacobi, U.; Meykadeh, N.; Sterry, W. and Lademann, J. *J. Dtsch Dermatol. Ges.* **2003**, *1*, 884-9.

(90) Jui-Chen, T.; Cappel, M. J.; Weiner, N. D.; Flynn, G. L. and Ferry, J. *Int. J. Pharm.* **1991**, *68*, 127-33.

(91) Weigand, D. A. and Gaylor, J. R. *J. Invest. Dermatol.* **1973**, *60*, 84-7.

(92) Teichmann, A.; Jacobi, U.; Ossadnik, M.; Richter, H.; Koch, S.; Sterry, W. and Lademann, J. *J. Invest. Dermatol.* **2005**, *125*, 264-9.

(93) Lademann, J.; Jacobi, U.; Surber, C.; Weigmann, H. J. and Fluhr, J. W. *Eur. J. Pharm. Biopharm.* **2009**, *72*, 317-23.

(94) Chao, Y. E. and Nylander-French, L. A. *Annals of Occupational Hygiene* **2004**, *48*, 65-73.

(95) Wiedersberg, S. and Nicoli, S. In *Topical and Transdermal Drug Delivery*; John Wiley & Sons, Inc.: 2012, 109-30.

(96) Dreher, F.; Arens, A.; Hostynek, J. J.; Mudumba, S.; Ademola, J. and Maibach, H. I. *Acta. Derm. Venereol.* **1998**, *78*, 186-9.

(97) Lindemann, U.; Wilken, K.; Weigmann, H.-J. r.; Schaefer, H.; Sterry, W. and Lademann, J. *J. Biomed. Opt.* **2003**, *8*, 601-7.

(98) Weigmann, H. J.; Lindemann, U.; Antoniou, C.; Tsikrikas, G. N.; Stratigos, A. I.; Katsambas, A.; Sterry, W. and Lademann, J. *Skin Pharmacol. Physiol.* **2003**, *16*, 217-27.

(99) Klang, V.; Schwarz, J. C.; Hartl, A. and Valenta, C. *Skin Pharmacol. Physiol.* **2011**, *24*, 256-68.

(100) Voegeli, R.; Heiland, J.; Doppler, S.; Rawlings, A. V. and Schreier, T. *Skin Res. Technol.* **2007**, *13*, 242-51.

(101) van der Molen, G. R.; Spies, F.; van 't Noordende, M. J.; Boelsma, E.; Mommaas, M. A. and Koerten, K. H. *Arch. Dermatol. Res.* **1997**, *289*, 514-8.

(102) M. R. Prausnitz, P. M. E., T. J. Franz, M. Schmuth, J. C. Tsai, G. K. Menon, W. M. Holleran, K. R. Feingold In *Dermatology* Bolognia, J., Jorizzo, J. L. and Schaffer, J. V., Eds.; Elsevier/Saunders: 2012, 2065-73.

(103) Bolzinger, M.-A.; Briançon, S.; Pelletier, J. and Chevalier, Y. *Current Opinion in Colloid & Interface Science* **2012**, *17*, 156-65.

(104) Schaefer, F. U.; Hansen, S.; Schneider, M.; Contreras, L. J. and Lehr, C.-M. In *Drug Absorption Studies: In Situ, In Vitro and In Silico Models*; Ehrhardt, C. and Kim, K.-J., Eds.; Springer US: Boston, MA, 2008, 3-33.

(105) Otberg, N.; Teichmann, A.; Rasuljev, U.; Sinkgraven, R.; Sterry, W. and Lademann, J. *Skin Pharmacol. Physiol.* **2007**, *20*, 195-8.

(106) Lademann, J.; Richter, H.; Schaefer, U. F.; Blume-Peytavi, U.; Teichmann, A.; Otberg, N. and Sterry, W. *Skin Pharmacol. Physiol.* **2006**, *19*, 232-6.

(107) Franz, T. J. *J. Invest. Dermatol.* **1975**, *64*, 190-5.

(108) SCCS, The Scientific Committee on Consumer Safety. *Basic criteria for the in vitro assessment of dermal absorption of cosmetic ingredients.* Updated, 2010; SCCS/1358/10.

(109) Heylings, J. R. In *Topical and Transdermal Drug Delivery*; John Wiley & Sons, Inc.: 2012, 183-99.

(110) Ng, S.-F.; Rouse, J. J.; Sanderson, F. D.; Meidan, V. and Eccleston, G. M. *AAPS PharmSciTech* **2010**, *11*, 1432-41.

(111) OECD, Organisation for Economic Co-operation and Development, Paris. *2004a, Guidance Document No. 28. The Conduct of Skin Absorption Studies.* Updated, 2004.

(112) Jung, E. C. and Maibach, H. I. *J. Appl. Toxicol.* **2015**, *35*, 1-10.

(113) Gray, G. M. and Yardley, H. J. *J. Lipid Res.* **1975**, *16*, 434-40.

(114) Barbero, A. M. and Frasch, H. F. *Toxicol. In Vitro* **2009**, *23*, 1-13.

(115) Dick, I. P. and Scott, R. C. *J. Pharm. Pharmacol.* **1992**, *44*, 640-5.

(116) Bhatia, K. S. and Singh, J. *Pharm. Pharmacol. Commun.* **1996**, *2*, 275-6.

(117) Sekkat, N.; Kalia, Y. N. and Guy, R. H. *J. Pharm. Sci.* **2002**, *91*, 2376-81.

(118) Singh, S.; Zhao, K. and Singh, J. *Drug Chem. Toxicol.* **2002**, *25*, 83-92.

(119) Boudry, I.; Blanck, O.; Cruz, C.; Blanck, M.; Vallet, V.; Bazire, A.; Capt, A.; Josse, D. and Lallement, G. *J. Appl. Toxicol.* **2008**, *28*, 645-57.

(120) Bronaugh, R. L.; Stewart, R. F. and Congdon, E. R. *Toxicol. Appl. Pharmacol.* **1982**, *62*, 481-8.

(121) OECD, Organisation for Economic Co-operation and Development, Paris. *Guidance notes on dermal absorption.* Updated, 2010.

(122) Davies, D. J.; Ward, R. J. and Heylings, J. R. *Toxicol. in Vitro* **2004**, *18*, 351-8.

(123) Dragicevic-Curic, N.; Scheglmann, D.; Albrecht, V. and Fahr, A. *J. Control. Release* **2008**, *127*, 59-69.

(124) Paula, D. D.; Martins, C. A. and Bentley, M. V. L. B. *Biomed. Chromatogr.* **2008**, *22*, 1416-23.

(125) Hasler-Nguyen, N.; Shelton, D.; Ponard, G.; Bader, M.; Schaffrik, M. and Mallefet, P. *BMC Dermatol.* **2009**, *9*, 3.

(126) Hasler-Nguyen, N. and Fotopoulos, G. *BMC Res. Notes* **2012**, *5*, 1-5.

(127) Robinson, M.; Visscher, M.; Laruffa, A. and Wickett, R. *J. Cosmet. Sci.* **2010**, *61*, 13-22.

(128) Denda, M.; Koyama, J.; Hori, J.; Horii, I.; Takahashi, M.; Hara, M. and Tagami, H. *Arch. Dermatol. Res.* **1993**, *285*, 415-7.

(129) Denda, M.; Hori, J.; Koyama, J.; Yoshida, S.; Nanba, R.; Takahashi, M.; Horii, I. and Yamamoto, A. *Arch. Dermatol. Res.* **1992**, *284*, 363-7.

(130) Neerken, S.; Lucassen, G. W.; Bisschop, M. A.; Lenderink, E. and Nuijs, T. *J. Biomed. Opt.* **2004**, *9*, 274-81.

(131) Rajadhyaksha, M.; Grossman, M.; Esterowitz, D.; Webb, R. H. and Rox Anderson, R. *J. Invest. Dermatol.* **1995**, *104*, 946-52.

(132) Verma, D. D.; Verma, S.; Blume, G. and Fahr, A. *Eur. J. Pharm. Biopharm.* **2003**, *55*, 271-7.

(133) Campbell, C. S. J.; Contreras-Rojas, L. R.; Delgado-Charro, M. B. and Guy, R. H. *J. Control. Release* **2012**, *162*, 201-7.

(134) Gerger, A.; Koller, S.; Weger, W.; Richtig, E.; Kerl, H.; Samonigg, H.; Krippl, P. and Smolle, J. *Cancer* **2006**, *107*, 193-200.

(135) Sakuyama, S.; Hirabayashi, C.; Hasegawa, J. and Yoshida, S. *Skin Res. Technol.* **2010**, *16*, 151-60.

(136) Wong, P. T. T.; Goldstein, S. M.; Grekin, R. C.; Godwin, T. A.; Pivik, C. and Rigas, B. *Cancer Res.* **1993**, *53*, 762-5.

(137) Bommannan, D.; Potts, R. O. and Guy, R. H. *J. Invest. Dermatol.* **1990**, *95*, 403-8.

(138) Bommannan, D.; Potts, R. O. and Guy, R. H. *J. Control. Release* **1991**, *16*, 299-304.

(139) Tsai, J. C.; Lo, Y. L.; Lin, C. Y.; Sheu, H. M. and Lin, J. C. *J. Spectrosc.* **2004**, *18*, 423-31.

(140) Tanojo, H.; Junginger, H. E. and Boddé, H. E. *J. Control. Release* **1997**, *47*, 31-9.

(141) Naik, A.; Pechtold, L. A. R. M.; Potts, R. O. and Guy, R. H. *J. Control. Release* **1995**, *37*, 299-306.

(142) Notingher, I. and Imhof, R. E. *Skin Res. Technol.* **2004**, *10*, 113-21.

(143) Marcott, C.; Lo, M.; Kjoller, K.; Domanov, Y.; Balooch, G. and Luengo, G. S. *Exp. Dermatol.* **2013**, *22*, 419-21.

(144) McIntosh, L. M.; Summers, R.; Jackson, M.; Mantsch, H. H.; Mansfield, J. R.; Howlett, M.; Crowson, A. N. and Toole, J. W. P. *J. Invest. Dermatol.* **2001**, *116*, 175-81.

(145) Boireau-Adamezyk, E.; Baillet-Guffroy, A. and Stamatas, G. N. *Skin Res. Technol.* **2014**, *20*, 409-15.

(146) Egawa, M. and Tagami, H. *Br. J. Dermatol.* **2008**, *158*, 251-60.

(147) Tosato, M. G.; Orallo, D. E.; Ali, S. M.; Churio, M. S.; Martin, A. A. and Dicelio, L. *J. Photochem. Photobiol.* **2015**, *153*, 51-8.

(148) Pyatski, Y.; Zhang, Q.; Mendelsohn, R. and Flach, C. R. *Int. J. Pharm.* **2016**, *505*, 319-28.

(149) Essendoubi, M.; Gobinet, C.; Reynaud, R.; Angiboust, J. F.; Manfait, M. and Piot, O. *Skin Res. Technol.* **2016**, *22*, 55-62.

(150) Saar, B. G.; Contreras-Rojas, L. R.; Xie, X. S. and Guy, R. H. *Mol. Pharm.* **2011**, *8*, 969-75.

(151) Freudiger, C. W.; Min, W.; Saar, B. G.; Lu, S.; Holtom, G. R.; He, C.; Tsai, J. C.; Kang, J. X. and Xie, X. S. *Science* **2008**, *322*, 1857-61.

(152) Mogilevych, B.; Isensee, D.; Rangel, J. L.; Dal Pizzol, C.; Martinello, V. C. A.; Dieamant, G. C. and Martin, A. A., *Biophotonics South America*, Conference Proceedings, May 23, 2015

(153) Franzen, L.; Selzer, D.; Fluhr, J. W.; Schaefer, U. F. and Windbergs, M. *Eur. J. Pharm. Biopharm.* **2013**, *84*, 437-44.

(154) Saar, B. G.; Freudiger, C. W.; Reichman, J.; Stanley, C. M.; Holtom, G. R. and Xie, X. S. *Science* **2010**, *330*, 1368-70.

(155) Mateus, R.; Moore, D. J.; Hadgraft, J. and Lane, M. E. *Int. J. Pharm.* **2014**, *475*, 471-4.

(156) Enthaler, B.; Trusch, M.; Fischer, M.; Rapp, C.; Pruns, J. K. and Vietzke, J.-P. *Anal. Bioanal. Chem.* **2013**, *405*, 1159-70.

(157) de Macedo, C. S.; Anderson, D. M.; Pascarelli, B. M.; Spraggins, J. M.; Sarno, E. N.; Schey, K. L. and Pessolani, M. C. *J. Mass Spectrom.* **2015**, *50*, 1374-85.

(158) Hart, P. J.; Francese, S.; Claude, E.; Woodroofe, M. N. and Clench, M. R. *Anal. Bioanal. Chem.* **2011**, *401*, 115-25.

(159) Touboul, D.; Roy, S.; Germain, D. P.; Chaminade, P.; Brunelle, A. and Laprévote, O. *Int. J. Mass Spectrom.* **2007**, *260*, 158-65.

(160) Lagarrigue, M.; Becker, M.; Lavigne, R.; Deininger, S.-O.; Walch, A.; Aubry, F.; Suckau, D. and Pineau, C. *Mol. Cell. Proteomics* **2011**, *10*.

(161) D'Alvise, J.; Mortensen, R.; Hansen, S. H. and Janfelt, C. *Anal. Bioanal. Chem.* **2014**, *406*, 3735-42.

(162) Cersoy, S.; Richardin, P.; Walter, P. and Brunelle, A. *J. Mass Spectrom.* **2012**, *47*, 338-46.

(163) Kezutyte, T.; Desbenoit, N.; Brunelle, A. and Briedis, V. *Biointerphases* **2013**, *8*, 3.

(164) Okamoto, M.; Tanji, N.; Katayama, Y. and Okada, J. *Appl. Surf. Sci.* **2006**, *252*, 6805-8.

(165) Monteiro-Riviere, N. A.; Wiench, K.; Landsiedel, R.; Schulte, S.; Inman, A. O. and Riviere, J. E. *Toxicol. Sci.* **2011**.

(166) Aoyagi, S.; Matsuzaki, T.; Kato, N. and Kudo, M. *J. Surf. Anal.* **2011**, *17*, 346-9.

(167) Herzog, R. F. K. and Viehböck, F. P. *Phys. Rev.* **1949**, *76*, 855-6.

(168) Liebl, H. J. and Herzog, R. F. K. *J. Appl. Phys.* **1963**, *34*, 2893-6.

(169) Vickerman, J. C. and Gilmore, I. *Surface Analysis: The Principal Techniques*; Wiley, 2009.

(170) Benninghoven, P.-D. A. *Z. Phys.* **1970**, *230*, 403-17.

(171) Hofmann, J. P.; Rohnke, M. and Weckhuysen, B. M. *Phys. Chem. Chem. Phys.* **2014**, *16*, 5465-74.

(172) Hagenhoff, B.; Kersting, R. and Rading, D. In *Handbook of Surface and Interface Analysis: Methods for Problem-Solving*; Riviere, J. C. and Myhra, S., Eds.; CRC Press: 2009.

(173) Kirkpatrick, A. *Nucl. Instrum. Methods Phys. Res. B* **2003**, *206*, 830-7.

(174) Postawa, Z.; Czerwinski, B.; Szewczyk, M.; Smiley, E. J.; Winograd, N. and Garrison, B. J. *J. Phys. Chem. B* **2004**, *108*, 7831-8.

(175) Winograd, N. *Anal. Chem.* **2005**, *77*, 142 A-9 A.

(176) Weibel, D. E.; Lockyer, N. and Vickerman, J. C. *Appl. Surf. Sci.* **2004**, *231–232*, 146-52.

(177) Rabbani, S.; Barber, A. M.; Fletcher, J. S.; Lockyer, N. P. and Vickerman, J. C. *Anal. Chem.* **2011**, *83*, 3793-800.

(178) Gnaser, H.; Ichiki, K. and Matsuo, J. *Rapid Commun. Mass. Spectrom.* **2012**, *26*, 1-8.

(179) Yokoyama, Y.; Aoyagi, S.; Fujii, M.; Matsuo, J.; Fletcher, J. S.; Lockyer, N. P.; Vickerman, J. C.; Passarelli, M. K.; Havelund, R. and Seah, M. P. *Anal. Chem.* **2016**, *88*, 3592-7.

(180) Hagenhoff, B.; van Leyen, D.; Niehuis, E. and Benninghoven, A. *J. Vac. Sci. Technol., A*, **1989**, *7*, 3056-64.

(181) Gilmore, I. S. and Seah, M. P. *Appl. Surf. Sci.* **2002**, *187*, 89-100.

(182) Sodhi, R. N. S. *Analyst* **2004**, *129*, 483-7.

(183) Vickerman, J. C. In *TOF-SIMS: Materials Analysis by Mass Spectrometry*; Vickerman, J. C. and Briggs, D., Eds.; SurfaceSpectra/IM Publications: 2013.

(184) Jones, E. A.; Lockyer, N. P. and Vickerman, J. C. *Int. J. Mass Spectrom.* **2007**, *260*, 146-57.

(185) Cheng, J. and Winograd, N. *Anal. Chem.* **2005**, *77*, 3651-9.

(186) Kobayashi, D.; Yamamoto, Y. and Isemura, T. *Surf. Interface Anal.* **2013**, *45*, 113-6.

(187) Mouhib, T.; Delcorte, A.; Poleunis, C.; Henry, M. and Bertrand, P. *Surf. Interface Anal.* **2010**, *42*, 641-4.

(188) Shard, A. G.; Green, F. M.; Brewer, P. J.; Seah, M. P. and Gilmore, I. S. *J. Phys. Chem. B* **2008**, *112*, 2596-605.

(189) Jones, E. A.; Lockyer, N. P. and Vickerman, J. C. *Anal. Chem.* **2008**, *80*, 2125-32.

(190) Lu, C.; Wucher, A. and Winograd, N. *Anal. Chem.* **2010**, *83*, 351-8.

(191) Iida, S. i.; Miyayama, T.; Sanada, N.; Suzuki, M.; Fisher, G. L. and Bryan, S. R. *Surf. Interface Anal.* **2011**, *43*, 214-6.

(192) Wucher, A.; Sun, S.; Szakal, C. and Winograd, N. *Anal. Chem.* **2004**, *76*, 7234-42.

(193) Robinson, M. A.; Graham, D. J. and Castner, D. G. *Anal. Chem.* **2012**, *84*, 4880-5.

(194) Lee, J. L. S.; Ninomiya, S.; Matsuo, J.; Gilmore, I. S.; Seah, M. P. and Shard, A. G. *Anal. Chem.* **2010**, *82*, 98-105.

(195) Bailey, J.; Havelund, R.; Shard, A. G.; Gilmore, I. S.; Alexander, M. R.; Sharp, J. S. and Scurr, D. J. *ACS Appl. Mater. Interfaces* **2015**, *7*, 2654-9.

(196) Wehbe, N.; Tabarrant, T.; Brison, J.; Mouhib, T.; Delcorte, A.; Bertrand, P.; Moellers, R.; Niehuis, E. and Houssiau, L. *Surf. Interface Anal.* **2013**, *45*, 178-80.

(197) Wang, Y.-C. and Castner, D. G. *Microsc. Microanal.* **2016**, *22*, 346-7.

(198) Foster, R. N.; Harrison, E. T. and Castner, D. G. *Langmuir* **2016**, *32*, 3207-16.

(199) Sjövall, P.; Johansson, B. and Lausmaa, J. *Appl. Surf. Sci.* **2006**, *252*, 6966-74.

(200) Malmberg, P.; Nygren, H.; Richter, K.; Chen, Y.; Dangardt, F.; Friberg, P. and Magnusson, Y. *Microsc. Res. Tech.* **2007**, *70*, 828-35.

(201) Malmberg, P.; Börner, K.; Chen, Y.; Friberg, P.; Hagenhoff, B.; Månsson, J.-E. and Nygren, H. *Biochim. Biophys. Acta, Mol. Cell. Biol. Lipids* **2007**, *1771*, 185-95.

(202) Nygren, H.; Malmberg, P.; Kriegeskotte, C. and Arlinghaus, H. F. *FEBS Lett.* **2004**, *566*, 291-3.

(203) Mas, S.; Touboul, D.; Brunelle, A.; Aragoncillo, P.; Egido, J.; Laprevote, O. and Vivanco, F. *Analyst* **2007**, *132*, 24-6.

(204) Bich, C.; Havelund, R.; Moellers, R.; Touboul, D.; Kollmer, F.; Niehuis, E.; Gilmore, I. S. and Brunelle, A. *Anal. Chem.* **2013**, *85*, 7745-52.

(205) Nygren, H.; Börner, K.; Hagenhoff, B.; Malmberg, P. and Månsson, J.-E. *Biochim. Biophys. Acta, Mol. Cell. Biol. Lipids* **2005**, *1737*, 102-10.

(206) Lazar, A. N.; Bich, C.; Panchal, M.; Desbenoit, N.; Petit, V. W.; Touboul, D.; Dauphinot, L.; Marquer, C.; Laprévote, O.; Brunelle, A. and Duyckaerts, C. *Acta Neuropathol.* **2013**, *125*, 133-44.

(207) Sjövall, P.; Johansson, B.; Belazi, D.; Stenvinkel, P.; Lindholm, B.; Lausmaa, J. and Schalling, M. *Appl. Surf. Sci.* **2008**, *255*, 1177-80.

(208) Debois, D.; Bralet, M.-P.; Le Naour, F.; Brunelle, A. and Laprévote, O. *Anal. Chem.* **2009**, *81*, 2823-31.

(209) Robinson, M. A. and Castner, D. G. *Biointerphases* **2013**, *8*, 15.

(210) Fletcher, J. S.; Lockyer, N. P.; Vaidyanathan, S. and Vickerman, J. C. *Anal. Chem.* **2007**, *79*, 2199-206.

(211) Van Nuffel, S.; Parmenter, C.; Scurr, D. J.; Russell, N. A. and Zelzer, M. *Analyst* **2016**, *141*, 90-5.

(212) Passarelli, M. K.; Newman, C. F.; Marshall, P. S.; West, A.; Gilmore, I. S.; Bunch, J.; Alexander, M. R. and Dollery, C. T. *Anal. Chem.* **2015**, *87*, 6696-702.

(213) Wehrli, P. M.; Lindberg, E.; Angerer, T. B.; Wold, A. E.; Gottfries, J. and Fletcher, J. S. *Surf. Interface Anal.* **2014**, *46*, 173-6.

(214) Nygren, H.; Dahlen, G. and Malmberg, P. *Basic Clin. Pharmacol. Toxicol.* **2014**, *115*, 129-33.

(215) Tuccitto, N.; Marletta, G.; Carnazza, S.; Grasso, L.; Caratozzolo, M.; Guglielmino, S. and Licciardello, A. *Surf. Interface Anal.* **2011**, *43*, 370-5.

(216) Graham, D. J.; Wilson, J. T.; Lai, J. J.; Stayton, P. S. and Castner, D. G. *Biointerphases* **2016**, *11*.

(217) Kokesch-Himmelreich, J.; Woltmann, B.; Torger, B.; Rohnke, M.; Arnhold, S.; Hempel, U.; Müller, M. and Janek, J. *Anal. Bioanal. Chem.* **2015**, *407*, 4555-65.

(218) Vanbellingen, Q. P.; Castellanos, A.; Rodriguez-Silva, M.; Paudel, I.; Chambers, J. W. and Fernandez-Lima, F. A. *J. Am. Soc. Mass Spectrom.* **2016**1-8.

(219) Fitzpatrick, T. B. *Arch. Dermatol.* **1988**, *124*, 869-71.

(220) Rodrigues, M.; Calpena, A. C.; Amabilino, D. B.; Garduno-Ramirez, M. L. and Pérez-García, L. *J. Mater. Chem. B* **2014**, *2*, 5419-29.

(221) Meyer, W. and Zschemisch, N. H. *Berl. Munch. Tierarztl. Wochenschr.* **2002**, *115*, 401-6.

(222) Jacobi, U.; Kaiser, M.; Toll, R.; Mangelsdorf, S.; Audring, H.; Otberg, N.; Sterry, W. and Lademann, J. *Skin Res. Technol.* **2007**, *13*, 19-24.

(223) Graham, D. J. and Castner, D. G. *Biointerphases* **2012**, *7*, 49.

(224) Worley, B. and Powers, R. *Curr. Metabolomics* **2013**, *1*, 92-107.

(225) Boccard, J. and Rutledge, D. N. *Anal. Chim. Acta* **2013**, *769*, 30-9.

(226) Bylesjö, M.; Rantalainen, M.; Cloarec, O.; Nicholson, J. K.; Holmes, E. and Trygg, J. *J. Chemometrics* **2006**, *20*, 341-51.

(227) van den Berg, R. A.; Hoefsloot, H. C. J.; Westerhuis, J. A.; Smilde, A. K. and van der Werf, M. J. *BMC Genom.* **2006**, *7*, 142-.

(228) Tian, H.; Wucher, A. and Winograd, N. *Surf. Interface Anal.* **2014**, *46*, 115-7.

(229) Sjövall, P.; Greve, T. M.; Clausen, S. K.; Moller, K.; Eirefelt, S.; Johansson, B. and Nielsen, K. T. *Anal. Chem.* **2014**, *86*, 3443-52.

(230) Kubo, A.; Ishizaki, I.; Kubo, A.; Kawasaki, H.; Nagao, K.; Ohashi, Y. and Amagai, M. *Sci. Rep.* **2013**, *3*.

(231) Passarelli, M. K. and Winograd, N. *Biochim. Biophys. Acta* **2011**, *1811*, 976-90.

(232) Ashtikar, M.; Matthäus, C.; Schmitt, M.; Krafft, C.; Fahr, A. and Popp, J. *Eur. J. Pharm. Sci.* **2013**, *50*, 601-8.

(233) Caspers, P. J.; Lucassen, G. W.; Wolthuis, R.; Bruining, H. A. and Puppels, G. J. *Biospectroscopy* **1998**, *4*, S31-9.

(234) Keller, B. O.; Sui, J.; Young, A. B. and Whittal, R. M. *Anal. Chim. Acta.* **2008**, *627*, 71-81.

(235) Farage, M. A.; Miller, K. W.; Elsner, P. and Maibach, H. I. *Int. J. Cosmet. Sci.* **2008**, *30*, 87-95.

(236) Marrot, L. and Meunier, J. R. *J. Am. Acad. Dermatol.* **2008**, *58*, S139-48.

(237) McCullough, J. L. and Kelly, K. M. *Ann. N. Y. Acad. Sci.* **2006**, *1067*, 323-31.

(238) Flament, F.; Bazin, R.; Laquieze, S.; Rubert, V.; Simonpietri, E. and Piot, B. *Clin. Cosmet. Investig. Dermatol.* **2013**, *6*, 221-32.

(239) Wilhelm, K. P.; Cua, A. B. and Maibach, H. I. *Arch. Dermatol.* **1991**, *127*, 1806-9.

(240) Luebberding, S.; Krueger, N. and Kerscher, M. *Int. J. Cosmet. Sci.* **2013**, *35*, 183-90.

(241) Conti, A.; Schiavi, M. E. and Seidenari, S. *Int. J. Cosmet. Sci.* **1995**, *17*, 77-85.

(242) Eisner, P.; Wilhelm, D. and Maibach, H. I. *Dermatology* **1990**, *181*, 88-91.

(243) Roskos, K. V. and Guy, R. H. *Pharm. Res.* **1989**, *6*, 949-53.

(244) Man, M. Q.; Xin, S. J.; Song, S. P.; Cho, S. Y.; Zhang, X. J.; Tu, C. X.; Feingold, K. R. and Elias, P. M. *Skin Pharmacol. Physiol.* **2009**, *22*, 190-9.

(245) Choi, E.-H.; Man, M.-Q.; Xu, P.; Xin, S.; Liu, Z.; Crumrine, D. A.; Jiang, Y. J.; Fluhr, J. W.; Feingold, K. R. and Elias, P. M. *J. Invest. Dermatol.* **2007**, *127*, 2847-56.

(246) Pochi, P. E.; Strauss, J. S. and Downing, D. T. *J. Invest. Dermatol.* **1979**, *73*, 108-11.

(247) Pappas, A.; Fantasia, J. and Chen, T. *Dermatoendocrinol.* **2013**, *5*, 319-24.

(248) Tagami, H. *Arch. Dermatol. Res.* **2008**, *300 Suppl 1*, S1-6.

(249) Rougier, A.; Lotte, C.; Corcuff, P. and Maibach, H. I. *J. Soc. Cosmet. Chem.* **1988**, *39*, 15-26.

(250) Grove, G. L. and Kligman, A. M. In *Stratum Corneum*; Marks, R. and Plewig, G., Eds.; Springer Berlin Heidelberg: Berlin, Heidelberg, 1983, 191-5.

(251) Giangreco, A.; Qin, M.; Pintar, J. E. and Watt, F. M. *Aging Cell* **2008**, *7*, 250-9.

(252) Gilhar, A.; Ullmann, Y.; Karry, R.; Shalaginov, R.; Assy, B.; Serafimovich, S. and Kalish, R. S. *J. Gerontol. A Biol. Sci. Med. Sci.* **2004**, *59*, 411-5.

(253) Engelke, M.; Jensen, J. M.; Ekanayake-Mudiyanselage, S. and Proksch, E. *Br. J. Dermatol.* **1997**, *137*, 219-25.

(254) Lee, J. H.; An, H. T.; Chung, J. H.; Kim, K. H.; Eun, H. C. and Cho, K. H. *Photodermatol. Photoimmunol. Photomed.* **2002**, *18*, 253-61.

(255) El-Abaseri, T. B.; Putta, S. and Hansen, L. A. *Carcinogenesis* **2006**, *27*, 225-31.

(256) Lock-Andersen, J.; Therkildsen, P.; de Fine Olivarius, F.; Gniadecka, M.; Dahlstrom, K.; Poulsen, T. and Wulf, H. C. *Photodermatol. Photoimmunol. Photomed.* **1997**, *13*, 153-8.

(257) Bhawan, J.; Andersen, W.; Lee, J.; Labadie, R. and Solares, G. *J. Cutan. Pathol.* **1995**, *22*, 154-9.

(258) Pearse, A. D.; Gaskell, S. A. and Marks, R. *J. Invest. Dermatol.* **1987**, *88*, 83-7.

(259) Jungersted, J. M.; Hellgren, L. I.; Høgh, J. K.; Drachmann, T.; Jemec, G. B. and Agner, T. *Acta Derm. Venereol.* **2010**, *90*, 350-3.

(260) Bak, H.; Hong, S. P.; Jeong, S. K.; Choi, E. H.; Lee, S. E.; Lee, S. H. and Ahn, S. K. *Int. J. Dermatol.* **2011**, *50*, 832-7.

(261) Haratake, A.; Komiya, A.; Horikoshi, T.; Uchiwa, H. and Watanabe, S. *Skin Pharmacol. Physiol.* **2006**, *19*, 275-82.

(262) Kim, E. J.; Jin, X. J.; Kim, Y. K.; Oh, I. K.; Kim, J. E.; Park, C. H. and Chung, J. H. *J. Dermatol. Sci.* **2010**, *57*, 19-26.

(263) Harvey, A.; Carr, C. M. and Pereira, A. *J. Cosmet. Sci.* **2004**, *55*, 265-79.

(264) Poleunis, C.; Everaert, E. P.; Delcorte, A. and Bertrand, P. *Appl. Surf. Sci.* **2006**, *252*, 6761-4.

(265) Bouwstra, J. A.; Gooris, G. S.; Dubbelaar, F. E. and Ponec, M. *J. Lipid Res.* **1999**, *40*, 2303-12.

(266) Cumpson, P. J.; Portoles, J. F. and Sano, N. *J. Vac. Sci. Technol., A*, **2013**, *31*, 020605.

(267) Fletcher, J. S.; Conlan, X. A.; Jones, E. A.; Biddulph, G.; Lockyer, N. P. and Vickerman, J. C. *Anal. Chem.* **2006**, *78*, 1827-31.

(268) Grehl, T.; Möllers, R. and Niehuis, E. *Appl. Surf. Sci.* **2003**, *203–204*, 277-80.

(269) Wang, Z.; Liu, B.; Zhao, E. W.; Jin, K.; Du, Y.; Neeway, J. J.; Ryan, J. V.; Hu, D.; Zhang, K. H. L.; Hong, M.; Le Guernic, S.; Thevuthasan, S.; Wang, F. and Zhu, Z. *J. Am. Soc. Mass Spectrom.* **2015**, *26*, 1283-90.

(270) Taylor, A. J.; Graham, D. J. and Castner, D. G. *Analyst* **2015**, *140*, 6005-14.

(271) Seah, M. P.; Havelund, R.; Shard, A. G. and Gilmore, I. S. *J. Phys. Chem. B* **2015**, *119*, 13433-9.

(272) Gamble, L. J.; Graham, D. J.; Bluestein, B.; Whitehead, N. P.; Hockenbery, D.; Morrish, F. and Porter, P. *Biointerphases* **2015**, *10*, 019008.

(273) Malm, J.; Giannaras, D.; Riehle, M. O.; Gadegaard, N. and Sjövall, P. *Anal. Chem.* **2009**, *81*, 7197-205.

(274) Chandra, S.; Bernius, M. T. and Morrison, G. H. *Anal. Chem.* **1986**, *58*, 493-6.

(275) Bendich, A.; Machlin, L. J.; Scandurra, O.; Burton, G. W. and Wayner, D. D. M. *Adv. Free Radic. Biol. Med.* **1986**, *2*, 419-44.

(276) Offord, E. A.; Gautier, J.-C.; Avanti, O.; Scaletta, C.; Runge, F.; Krämer, K. and Applegate, L. A. *Free Radic. Biol. Med.* **2002**, *32*, 1293-303.

(277) Darr, D.; Combs, S.; Dunston, S.; Manning, T. and Pinnell, S. *Br. J. Dermatol.* **1992**, *127*, 247-53.

(278) Raschke, T.; Koop, U.; Düsing, H. J.; Filbry, A.; Sauermann, K.; Jaspers, S.; Wenck, H. and Wittern, K. P. *Skin Pharmacol. Physiol.* **2004**, *17*, 200-6.

(279) Murad, S.; Tajima, S.; Johnson, G. R.; Sivarajah, A. and Pinnell, S. R. *J. Invest. Dermatol.* **1983**, *81*, 158-62.

(280) Phillips, C. L.; Combs, S. B. and Pinnell, S. R. *J. Invest. Dermatol.* **1994**, *103*, 228-32.

(281) Humbert, P. G.; Haftek, M.; Creidi, P.; Lapière, C.; Nusgens, B.; Richard, A.; Schmitt, D.; Rougier, A. and Zahouani, H. *Exp. Dermatol.* **2003**, *12*, 237-44.

(282) Traikovich, S. S. *Arch. Otolaryngol. Head Neck Surg.* **1999**, *125*, 1091-8.

(283) Zhou, W.; Liu, W.; Zou, L.; Liu, W.; Liu, C.; Liang, R. and Chen, J. *Colloids Surf., B* **2014**, *117*, 330-7.

(284) Desai, K. and Park, H. J. *J. Microencapsul.* **2005**, *22*, 179-92.

(285) Kirby, C.; Whittle, C.; Rigby, N.; Coxon, D. and Law, B. *Int. J. Food Sci. Tech.* **1991**, *26*, 437-49.

(286) Austria, R.; Semenzato, A. and Bettero, A. *J. Pharm. Biomed. Anal.* **1997**, *15*, 795-801.

(287) Farris, P. K. *Dermatol. Surg.* **2005**, *31*, 814-8.

(288) Bell, M., Skincare Scientific Advisor, Walgreens Boots Alliance, Nottingham, UK, Personal Communication, **2016.**

(289) Lee, A. R. C. and Tojo, K. *Chem. Pharm. Bull.* **1998**, *46*, 174-7.

(290) Stamford, N. P. J. *J. Cosmet. Dermatol.* **2012**, *11*, 310-7.

(291) Foco, A.; Gasperlin, M. and Kristl, J. *Int. J. Pharm.* **2005**, *291*, 21-9.

(292) Hsiao, C. Y.; Huang, C. H.; Hu, S.; Ko, Y. S.; Sung, H. C. and Huang, S. Y. *Lasers Med. Sci.* **2011**, *26*, 369-76.

(293) Pérez-García, L., University of Barcelona, Barcelona, Spain, Personal Communication, **2016.**

(294) Kurihara-Bergstrom, T.; Knutson, K.; DeNoble, L. J. and Goates, C. Y. *Pharm. Res.* **1990**, *7,* 762-6.

(295) Ghanem, A.-H.; Mahmoud, H.; Higuchi, W. l.; Rohr, U. D.; Borsadia, S.; Liu, P.; Fox, J. L. and Good, W. R. *J. Control. Release* **1987**, *6,* 75-83.

(296) Pershing, L. K.; Lambert, L. D. and Knutson, K. *Pharm. Res.* **1990**, *7,* 170-5.

(297) 3D nanoSIMS - label-free molecular imaging, http://www.npl.co.uk/news/3d-nanosims-label-free-molecular-imaging (Accessed 25th October, 2016).

Chapter 9: Appendix

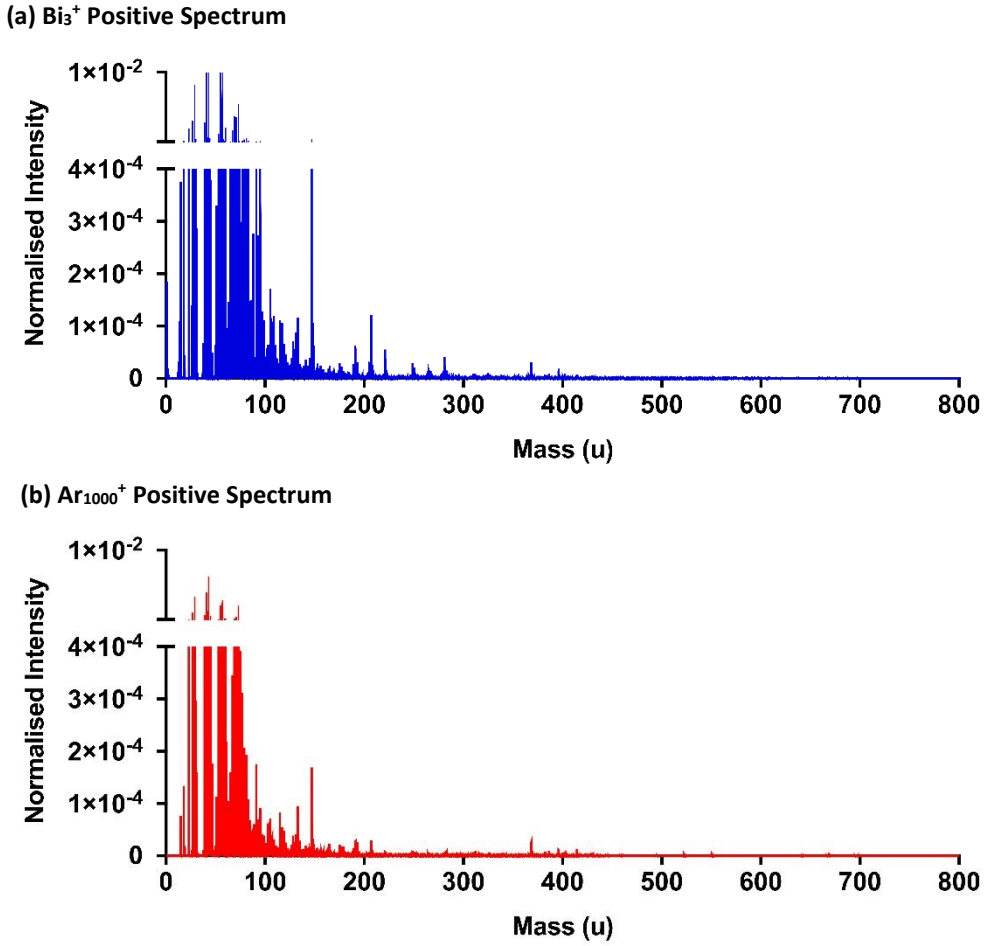

Figure A-1 ToF-SIMS positive spectra collected using a (a) Bi_3^+ and (b) Ar_{1000}^+ primary ion analysis beam.

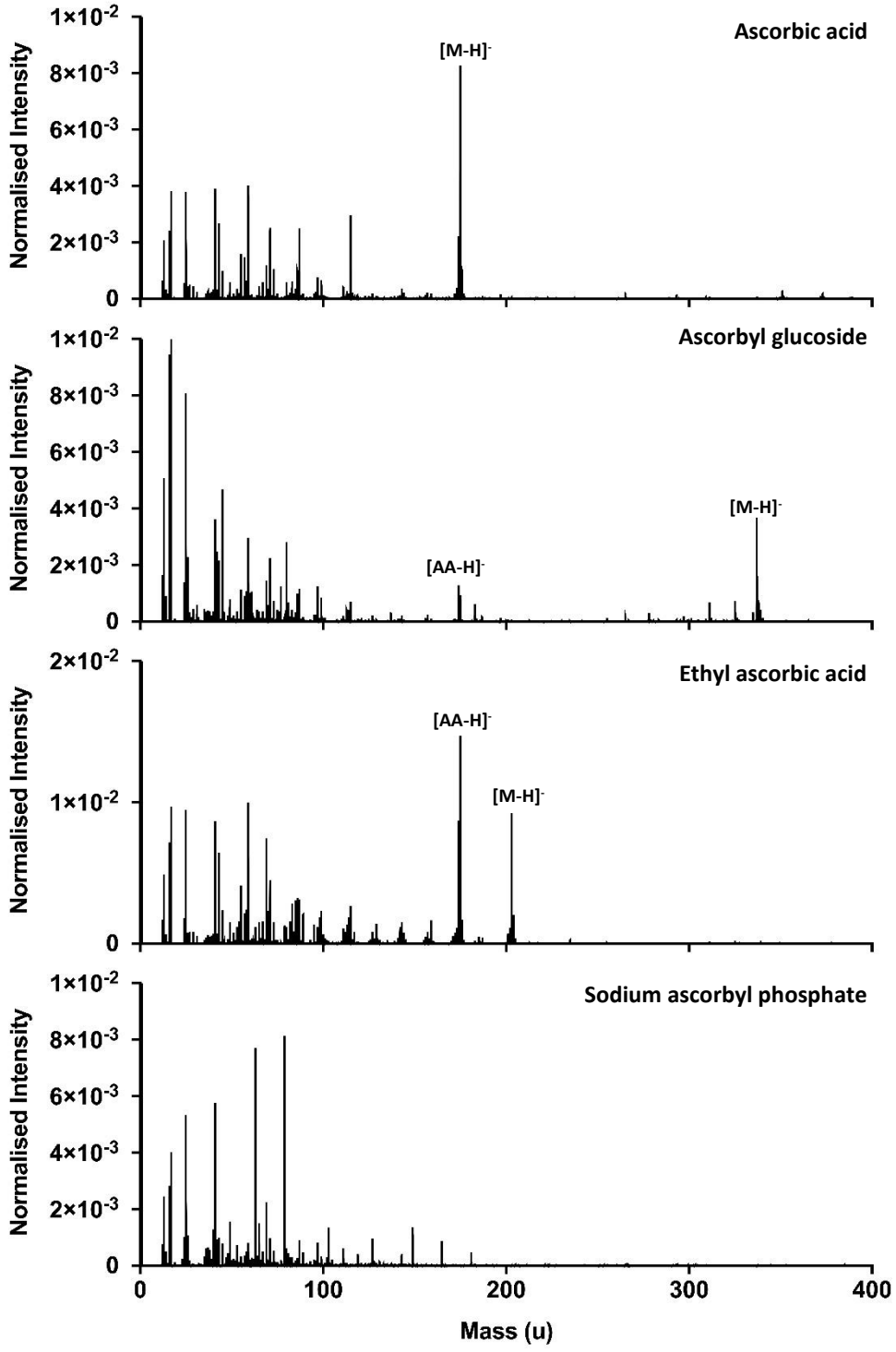

Figure A-2 ToF-SIMS negative reference spectra for the four vitamin C related compounds.

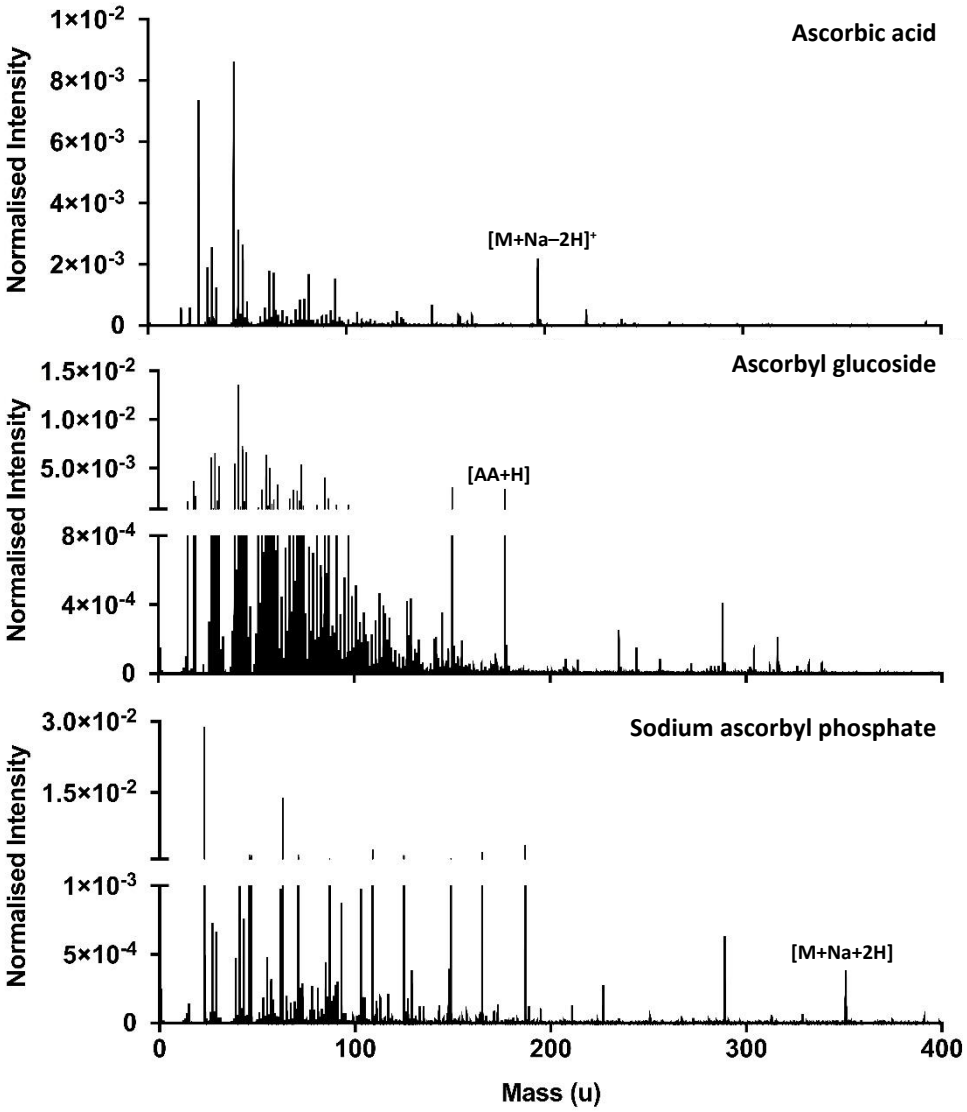

Figure A-3 ToF-SIMS positive reference spectra for three vitamin C related compounds.